

NDOT Research Report

Report No. 078-13-803

**Post-Tensioning Duct Air Pressure Testing
Effects on Web Cracking**

January 2015

**Nevada Department of Transportation
1263 South Stewart Street
Carson City, NV 89712**



Disclaimer

This work was sponsored by the Nevada Department of Transportation. The contents of this report reflect the views of the authors, who are responsible for the facts and the accuracy of the data presented herein. The contents do not necessarily reflect the official views or policies of the State of Nevada at the time of publication. This report does not constitute a standard, specification, or regulation.

Report No. CCEER 15-02

**POST-TENSIONING DUCT AIR PRESSURE TESTING EFFECTS ON WEB
CRACKING**

Brett M. Allen
David H. Sanders

A report sponsored by the Nevada Department of Transportation
Contract Number NDOT P078-13-803

Center for Civil Engineering Earthquake Research

University of Nevada, Reno
Department of Civil and Environmental Engineering, MS 258
1664 N. Virginia St.
Reno, NV 89557

January 2015

Abstract

Nevada Department of Transportation (NDOT) post-tensioned concrete bridges have experienced web cracking near the post-tensioning ducts during the construction process. The ducts were air pressure tested to ensure the duct can successfully be grouted for a bonded post-tensioned system. During the air pressure testing, tendon stressing and grouting, web cracks form that cause delamination of the concrete in the web that lead to repairs.

The research presented in this report focused on recreating the web cracking issue to understand why the problem exists and to create a solution for the web cracking. The project consisted of four main components: recreating the web cracking using three large-scale experimental beams, updated design details to minimize/eliminate web cracking in three large-scale experimental beams, an extensive parametric study, and develop design recommendations.

Beam studies included the design and construction of six large-scale (0.7) concrete bridge beams. Three beams studied the effects of curvature on web cracking using existing NDOT details and three beams updated design details such as increased spacing between post-tensioning ducts and inclusion of duct tie reinforcement bars between post-tensioning ducts. All beams were designed with the same dimensions and tested to NDOT standards. Results indicate that the greatest impact on web cracking was the air pressure testing. Post-tensioning curvature also has an effect on web cracking. Increasing the duct spacing and inclusion of duct tie reinforcement bars increased the performance of the beams.

A detailed parametric study using the ATENA nonlinear analysis software investigated various design parameters including current NDOT details. Various parameters included web width, duct spacing, duct tie reinforcement, number of ducts and location of duct within the web. Through the experimental beams and the analytical studies, design equations were developed to reduce web cracking. Recommendations regarding additional reinforcement, duct layout and duct details were developed to reduce damage and increase the performance of post-tensioned bridge beams.

Acknowledgement

This report is based on the thesis of “Post-Tensioning Duct Air Pressure Testing Effects on Web Cracking” by Brett M. Allen. The research presented in this study was funded by Nevada Department of Transportation (NDOT). The support and guidance of Michael Taylor and Troy Martin, the NDOT project managers, is appreciated. The comments and interest provided by Nathan Harrison are also appreciated. The conclusions and recommendations presented in this report are those of the authors and should not be construed to be endorsed by NDOT.

Thanks are given to UNR’s laboratory staff, Dr. Patrick Laplace, Chad Lyttle, and Todd Lyttle, for their efforts and coordination with testing. Special thanks are given to Mark Lattin for his help and support in post-tensioning and overall testing. Mr. Don Newman, Brendan Morris, and Dave Lopez are noted for their interest and construction efforts.

During the course of this research, the National Science Foundation provided the opportunity to work with Erin Segal as an N.E.E.S. REU (Research Experience for Undergrads) student. Erin’s work throughout the program is greatly appreciated. Lastly, the love, support and guidance provided by my parents. I would not be where I am today without them.

Table of Contents

1.0	Introduction.....	1
1.1	Problem Statement	1
1.2	Previous Research	2
1.3	Scope and Objective.....	3
2.0	Preliminary Analysis and Experimental Program.....	4
2.1	Introduction	4
2.2	Testing Configuration Details	4
2.2.1	Overall Beam Design.....	4
2.2.2	Test Setup.....	10
2.2.3	Loading Protocol.....	13
2.3	Round A Experimental Beams	16
2.3.1	C1 – Largest Radius.....	16
2.3.1.1	Design.....	16
2.3.2	C3 – Smallest Radius	17
2.3.2.1	Design.....	17
2.3.3	C2 – Medium Radius	18
2.3.3.1	Design.....	18
2.4	Preliminary Finite Element Analysis	19
2.5	Round B Experimental Beams	23
2.5.1	C4 – Increased Duct Spacing	23
2.5.1.1	Design.....	23
2.5.2	C5 – Increased Duct Spacing and 17.5” Duct Reinforcement.....	24
2.5.2.1	Design.....	24
2.5.3	C6 – Increased Duct Spacing and 7.0” Duct Reinforcement.....	25
2.5.3.1	Design.....	25
2.6	Instrumentation.....	26
2.6.1	Reinforcement Strain Gauges	27
2.6.2	Embedded Concrete Strain Gauges	29
2.6.3	Concrete Surface Strain Gauges	31
2.6.4	Displacement Transducers	33
2.6.5	Pressure Transducers	34
2.7	Construction	34
2.8	Materials.....	37
2.8.1	Conventional Concrete.....	37
2.8.2	Reinforcing Steel	38
2.8.3	Prestressing Steel	39
3.0	Experimental Beam Results.....	40
3.1	Introduction	40
3.2	Round A Experimental Beams	40
3.2.1	Configuration 1	40
3.2.1.1	Embedded Concrete Strain Gauges	40
3.2.1.2	Concrete Surface Strain Gauges	45
3.2.1.3	Cross Sectional Cracks	47
3.2.1.4	Shear Reinforcement Strain Gauges.....	48
3.2.1.5	Beam End Displacements.....	50

3.2.1.6	C1 Results Overview	52
3.2.2	Configuration 2	52
3.2.2.1	Embedded Concrete Strain Gauges	52
3.2.2.2	Concrete Surface Strain Gauges	55
3.2.2.3	Cross Sectional Cracks	58
3.2.2.4	Shear Reinforcement Gauges and Beam End Displacement.....	59
3.2.2.5	C2 Results Overview	59
3.2.3	Configuration 3	59
3.2.3.1	Embedded Concrete Strain Gauges	59
3.2.3.2	Concrete Surface Strain Gauges	64
3.2.3.3	Cross Sectional Cracks	70
3.2.3.4	Web Bulging.....	71
3.2.3.5	Shear Reinforcement Gauges and Beam End Displacement.....	73
3.2.3.6	C3 Results Overview	73
3.2.4	Round A Results Overview	74
3.3	Round B Experimental Beams	74
3.3.1	Configuration 4	74
3.3.1.1	Embedded Concrete Strain Gauges	74
3.3.1.2	Concrete Surface Strain Gauges	83
3.3.1.3	Cross Sectional Cracks	89
3.3.1.4	Web Bulging.....	90
3.3.1.5	Shear Reinforcement Gauges and Beam End Displacement.....	92
3.3.1.6	C4 Results Overview	92
3.3.2	Configuration 5	93
3.3.2.1	Embedded Concrete Strain Gauges	93
3.3.2.2	Concrete Surface Strain Gauges	102
3.3.2.3	Cross Sectional Cracks	108
3.3.2.4	Duct Tie Reinforcement Gauges	109
3.3.2.5	Web Bulging.....	114
3.3.2.6	Shear Reinforcement Gauges and Beam End Displacement.....	116
3.3.2.7	C5 Results Overview	116
3.3.3	Configuration 6	117
3.3.3.1	Embedded Concrete Strain Gauges	117
3.3.3.2	Concrete Surface Strain Gauges	126
3.3.3.3	Cross Sectional Cracks	132
3.3.3.4	Duct Tie Reinforcement Gauges	133
3.3.3.5	Web Bulging.....	139
3.3.3.6	Shear Reinforcement Gauges and Beam End Displacement.....	141
3.3.3.7	C6 Results Overview	141
3.3.4	Round B Results Overview.....	142
3.4	Beam Comparisons	142
3.4.1	Curvature Parameter	142
3.4.1.1	Embedded Concrete Strain Gauges at Centerline.....	142
3.4.1.2	Embedded Concrete Strain Gauges at 30 inches from Centerline....	143
3.4.2	Duct Spacing and Duct Tie Reinforcement	145
3.4.2.1	Embedded Concrete Strain Gauges at Centerline.....	145

3.4.2.2	Embedded Concrete Strain Gauges at 30 inches from Centerline.....	146
3.4.2.3	Web Bulging.....	147
3.4.3	Web Cracking	149
4.0	Analytical Parametric Study	150
4.1	Introduction	150
4.2	Parametric Model	151
4.3	Model Verification	156
4.4	Duct Curvatures and Duct Tie Reinforcement Models	157
4.5	Artificial Crack Models.....	168
4.5.1	Scaled Version (0.7 scale).....	168
4.5.2	Full scale version (1.0 scale).....	175
4.6	Number of Ducts Models	178
4.7	Duct Locations Models	180
4.8	Results Overview	182
5.0	Conclusions and Recommendations	184
5.1	Experimental Conclusions.....	184
5.2	Parametric Study Conclusions	184
5.3	Recommendations	185
6.0	References.....	187
	Appendix A: Experimental Tables.....	188
	Appendix B: Experimental Figures	199
	Appendix C: Atena Results.....	211

List of Tables

Table 2-1: Comparison between NDOT bridges and UNR designed bridge.....	5
Table 2-2: Comparison between NDOT bridges and experimental beams.	6
Table 2-3: Stress comparisons between NDOT bridges and UNR bridges.	13
Table 2-4: Stressing ram gauge pressure and load data.	14
Table 2-5: Stressing ram gauge pressure for each loading step.	15
Table 2-6: Results from increasing the web width.	20
Table 2-7: Results from increasing the spacing between the ducts.	20
Table 2-8: Results from various duct tie reinforcement spacings.	23
Table 2-9: Instrumentation list for all 6 beams.	27
Table 2-10: Slump test results.	36
Table 2-11: Concrete Cylinder Test Averages.	38
Table 2-12: Reinforcement Strengths.	38
Table 3-1: Y-axis values for each loading stage.	42
Table 3-2: C1 embedded concrete strain at 0" O.C. at each load stage.	44
Table 3-3: C1 concrete surface gauges at each loading stage.	47
Table 3-4: C1 shear reinforcement gauges at each loading stage.	50
Table 3-5: C1 beam end displacements at each loading stage.	51
Table 3-6: C2 embedded concrete gauges at each loading stage.	54
Table 3-7: C2 concrete surface gauges at each loading stage.	57
Table 3-8: C3 embedded concrete gauges at each loading stage.	64
Table 3-9: C3 concrete west surface strain at each loading stage.	68
Table 3-10: C3 concrete east surface strain at each loading stage.	69
Table 3-11: C3 web bulge values at each loading stage.	73
Table 3-12: C4 embedded concrete strain at 0" O.C. for each loading stage.	77
Table 3-13: C4 embedded concrete strain at 15" O.C. for each loading stage.	80
Table 3-14: C4 embedded concrete strain at 30" O.C. for each loading stage.	83
Table 3-15: C4 concrete west surface strain at each loading stage.	87
Table 3-16: C4 concrete east surface strain at each loading stage.	88
Table 3-17: C4 web bulge values at each loading stage.	92
Table 3-18: C5 embedded concrete strain at 0" O.C. at each loading stage.	96
Table 3-19: C5 embedded concrete strain at 15" O.C. at each loading stage.	97
Table 3-20: C5 embedded concrete strain at 30" O.C. at each loading stage.	102
Table 3-21: C5 concrete west surface strain at each loading stage.	106
Table 3-22: C5 concrete east surface strain at each loading stage.	107
Table 3-23: C5 duct tie strain -8.75" at each loading stage.	112
Table 3-24: C5 duct tie strain +8.75" at each loading stage.	113
Table 3-25: C5 duct tie strain +26.25" at each loading stage.	114
Table 3-26: C5 web bulging at each loading stage.	116
Table 3-27: C6 embedded concrete strain at 0" O.C. at each loading stage.	120
Table 3-28: C6 embedded concrete strain at 15" O.C. at each loading stage.	123
Table 3-29: C6 embedded concrete strain at 30" O.C. at each loading stage.	126
Table 3-30: C6 concrete west surface strain at each loading stage.	130
Table 3-31: C6 concrete east surface strain at each loading stage.	131
Table 3-32: C6 duct ties at -1.75" at each loading stage.	137
Table 3-33: C6 duct ties at +5.25" at each loading stage.	138

Table 3-34: C6 duct ties at +26.25" at each loading stage.....	139
Table 3-35: C6 web bulging at each loading stage.....	141
Table 3-36: Embedded concrete strain 0" O.C. at 50 psi after 0.75fpu.....	143
Table 3-37: Embedded concrete strain 30" O.C. at 50 psi after 0.75fpu.....	144
Table 3-38: Embedded concrete strain 0" O.C. at 50 psi after 0.75fpu.....	146
Table 3-39: Embedded concrete strain 30" O.C. at 50 psi after 0.75fpu.....	147
Table 3-40: Total middle web bulge values for C3, C4, C5 and C6.	149
Table 3-41: Appearance of cracks on web face.....	149
Table 3-42: Maximum crack widths throughout the beam.....	149
Table 4-1: Parametric Study at 0.7 scale and duct spacing at 1.05"	150
Table 4-2: Atena models with the artificial crack between the ducts.	151
Table 4-3: Macroelement Atena mesh detail, refinements and material properties.	153
Table 4-4: Atena loads and locations.....	154
Table 4-5: COM between Atena and experimental results (0.75fpu-top duct).	156
Table 4-6: COM between Atena and experimental results (125psi AP - 0.85fpu).....	156
Table 4-7: Extreme fiber stress between NDOT estimates and Atena.	157
Table 4-8: Experimental vs. Atena duct tie results (100psi Top - 0.75fpu).....	157
Table 4-9: Duct curvatures and duct tie reinforcement Atena model outline.....	158
Table 4-10 Duct tie spacing versus duct tie stress	175
Table 4-11: Maximum stresses for 2, 3 and 4 duct beams.....	179
Table 4-12: Number of ducts with and without duct tie reinforcement.....	180
Table 4-13: Cross section stresses - ducts in the top, middle and bottom.	182
Table A-1: C2 shear reinforcement strain values.	188
Table A-2: C2 beam end displacements.	188
Table A-3: C3 shear reinforcement strain values.	189
Table A-4: C3 beam end displacements.	190
Table A-5: C4 shear reinforcement strain values.	191
Table A-6: C4 beam end displacements.	192
Table A-7: C5 shear reinforcement strain values.	193
Table A-8: C5 beam end displacements.	194
Table A-9: C6 shear reinforcement strain values.	195
Table A-10: C6 beam end displacements.	196
Table A-11: C6 duct tie reinforcement at 12.25" right of centerline.....	197
Table A-12: C6 duct tie reinforcement at 19.25" right of centerline.....	198
Table C-1: Load and associated steps in Atena software.	211

List of Figures

Figure 1-1: NDOT Bridge web cracking.	1
Figure 1-2: NDOT Bridge cut section after cracking occurred.	2
Figure 2-1: Longitudinal Area of Interest.	4
Figure 2-2: Cross Sectional Area of Interest.	5
Figure 2-3: UNR beam design detail and cross sections.	7
Figure 2-4: Cross sectionals reinforcement details.	9
Figure 2-5: Plan view skin reinforcement detail.	9
Figure 2-6: Shear along the length of the beam.	10
Figure 2-7: Elevation view of test setup with reaction block representing the column.	11
Figure 2-8: Plan view of test setup.	11
Figure 2-9: Laboratory experimental test setup.	12
Figure 2-10: Stressing and non-stressing ends of the beam.	12
Figure 2-11: Air pressure testing setup on the ends of the beams.	15
Figure 2-12: C1 design detail.	17
Figure 2-13: C3 design detail.	18
Figure 2-14: C2 design detail.	19
Figure 2-15: Principal stresses around ducts with 0.7" spacing (C2 loading).	21
Figure 2-16: Principal stresses around ducts with 1.05" spacing (C2 loading).	21
Figure 2-17 : Duct Tie Reinforcement Detail.	22
Figure 2-18: C4 design detail.	24
Figure 2-19: C5 duct tie reinforcement locations.	25
Figure 2-20: C5 design detail.	25
Figure 2-21: C6 duct tie reinforcement locations.	26
Figure 2-22: C6 design detail.	26
Figure 2-23: Reinforcement and concrete surface strain gauge locations.	27
Figure 2-24: Reinforcement strain gauge locations and labels.	28
Figure 2-25: Shear reinforcement strain gauges installed on beam.	28
Figure 2-26: Duct tie reinforcement bar strain gauges installed.	29
Figure 2-27: Embedded concrete strain gauge.	29
Figure 2-28: Round A embedded concrete strain gauge locations.	30
Figure 2-29: Embedded concrete strain gauges installed between ducts.	31
Figure 2-30: Round A embedded concrete strain gauge locations and labels.	31
Figure 2-31: Round B embedded concrete strain gauge locations and labels.	31
Figure 2-32: C1 and C2 concrete surface strain gauge locations and labels.	32
Figure 2-33: Concrete surface strain gauges installed on web face.	32
Figure 2-34: C3, C4, C5 and C6 concrete strain gauge location and labels.	33
Figure 2-35: Example of the web bulging and concrete surface gauges.	33
Figure 2-36: One side of forms and shear reinforcement during construction.	34
Figure 2-37: Installation of post-tensioning steel ducts.	35
Figure 2-38: Progression of construction.	35
Figure 2-39: Duct tie reinforcement detail with the direction of ties altered.	36
Figure 2-40: Duct tie reinforcement bars installed in the beam.	37
Figure 2-41: Stress-strain curve for conventional reinforcement bars.	39
Figure 3-1: C1 embedded concrete strain at centerline.	41
Figure 3-2: C1 embedded concrete strain versus time.	43

Figure 3-3: C1 embedded concrete strain at +30" from centerline.....	45
Figure 3-4: C1 concrete surface strain gauges.....	46
Figure 3-5: C1 web face after completion of all loading with no cracks.....	47
Figure 3-6: Cutting the beam in half to look at cross section.....	48
Figure 3-7: C1 cut beam cross section with no cracks.....	48
Figure 3-8: C1 shear reinforcement gauges.....	49
Figure 3-9: C1 displacement on ends of the beam.....	51
Figure 3-10: C2 embedded concrete strain at centerline.....	52
Figure 3-11: C2 embedded concrete strain versus time.....	53
Figure 3-12: C2 embedded concrete strain at +30" from centerline.....	55
Figure 3-13: C2 concrete surface strain gauges.....	56
Figure 3-14: Surface strain gauge compression explanation.....	57
Figure 3-15: C2 crack appearance at 0.75fpuB.....	58
Figure 3-16: C2 web face after loading with cracks highlighted for clarity.....	58
Figure 3-17: C2 cut beam cross section.....	59
Figure 3-18: Repair of concrete rock in the web of C3.....	60
Figure 3-19: C3 embedded concrete strain at centerline.....	61
Figure 3-20: C3 embedded concrete strain versus time.....	62
Figure 3-21: C3 embedded concrete strain at +30" from centerline.....	63
Figure 3-22: C3 concrete surface strain at -12 inches.....	65
Figure 3-23: C3 concrete surface strain at centerline.....	66
Figure 3-24: C3 concrete surface strain at +12 inches.....	67
Figure 3-25: C3 crack appearance at 0.75fpuB.....	70
Figure 3-26: C3 web face after loading with cracks shown for clarity.....	70
Figure 3-27: C3 cut beam cross section.....	71
Figure 3-28: C3 web bulge.....	72
Figure 3-29: C4 embedded concrete strain at centerline.....	75
Figure 3-30: C4 embedded concrete strain versus time.....	76
Figure 3-31: C4 embedded concrete strain at -15" from centerline.....	78
Figure 3-32: C4 embedded concrete strain at +15" from centerline.....	79
Figure 3-33: C4 embedded concrete strain at -30" from centerline.....	81
Figure 3-34: C4 embedded concrete strain at +30" from centerline.....	82
Figure 3-35: C4 concrete surface strain at -6" from centerline.....	84
Figure 3-36: C4 concrete surface strain at centerline.....	85
Figure 3-37: C4 concrete surface strain at +6" from centerline.....	86
Figure 3-38: C4 crack appearance at 100psiB after 0.75fpu.....	89
Figure 3-39: C4 web face after loading with cracks shown for clarity.....	89
Figure 3-40: C4 cut beam cross section.....	90
Figure 3-41: C4 web bulge.....	91
Figure 3-42: C5 embedded concrete strain at centerline.....	94
Figure 3-43: C5 embedded concrete strain versus time.....	95
Figure 3-44: C5 embedded concrete strain at -15" from centerline.....	98
Figure 3-45: C5 embedded concrete strain at +15" from centerline.....	99
Figure 3-46: C5 embedded concrete strain at -30" from centerline.....	100
Figure 3-47: C5 embedded concrete strain at +30" from centerline.....	101
Figure 3-48: C5 concrete surface strain at -6" from centerline.....	103

Figure 3-49: C5 concrete surface strain at centerline.	104
Figure 3-50: C5 concrete surface strain at +6" from centerline.....	105
Figure 3-51: C5 appearance of cracks at 75psiB after 0.75fpu.....	108
Figure 3-52: C5 cracking after loading with cracks highlighted for clarity.	108
Figure 3-53: C5 cut beam cross section.....	108
Figure 3-54: C5 duct tie reinforcement strain at -8.75" from centerline.	109
Figure 3-55: C5 duct tie reinforcement strain at +8.75" from centerline.	110
Figure 3-56: C5 duct tie reinforcement strain at +26.25" from centerline.	111
Figure 3-57: C5 web bulge.	115
Figure 3-58: C6 embedded concrete strain at centerline.	118
Figure 3-59: C6 embedded concrete strain versus time.....	119
Figure 3-60: C6 embedded concrete strain at -15" from centerline.....	121
Figure 3-61: C6 embedded concrete strain at +15" from centerline.....	122
Figure 3-62: C6 embedded concrete strain at -30" from centerline.....	124
Figure 3-63: C6 embedded concrete strain at +30" from centerline.....	125
Figure 3-64: C6 concrete surface strain at -12" from centerline.	127
Figure 3-65: C6 concrete surface strain at centerline.	128
Figure 3-66: C6 concrete surface strain at +12" from centerline.....	129
Figure 3-67: C6 appearance of cracks at 125psiB after 0.75fpu.....	132
Figure 3-68: C6 cracking after loading with cracks highlighted for clarity.	132
Figure 3-69: C6 cut beam cross section with no cracks.....	133
Figure 3-70: C6 duct tie reinforcement strain at -1.75" from centerline.	134
Figure 3-71: C6 duct tie reinforcement strain at +5.25" from centerline.	135
Figure 3-72: C6 duct tie reinforcement strain at +26.25" from centerline.	136
Figure 3-73: C6 web bulge.	140
Figure 3-74: Round A embedded concrete strain at centerline.....	143
Figure 3-75: Round A embedded concrete strain at +30" from centerline.....	144
Figure 3-76: Embedded concrete comparisons at centerline.	145
Figure 3-77: Embedded concrete comparisons at +30" from centerline.	147
Figure 3-78: Web bulge comparisons at 50psi after 0.75fpu.....	148
Figure 3-79: Web bulge comparisons at 125psi after 0.85fpu.....	148
Figure 4-1: Atena boundary conditions.	152
Figure 4-2: Atena model macroelement assignments.....	152
Figure 4-3: Duct loading configuration.	154
Figure 4-4: Analytical model dead loading.	155
Figure 4-5: Principal stresses at centerline for C2 with no reinforcement.	159
Figure 4-6: Principal stresses at centerline for C2 with reinforcement at 10.5".....	159
Figure 4-7: Duct tie stress vs. curvature (No artificial crack).....	160
Figure 4-8: Duct tie stress vs. duct tie spacing (No artificial crack).....	161
Figure 4-9: Total web bulge vs. curvatures (No artificial crack).....	161
Figure 4-10: Total web bulge vs. duct tie spacings (No artificial crack).....	162
Figure 4-11: Crack width (MB) vs. curvatures (No artificial crack).	162
Figure 4-12: Crack width (MB) vs. duct tie spacing (No artificial crack).....	163
Figure 4-13: Crack width vs. duct tie stress (No artificial crack).....	163
Figure 4-14: Web bulging at each loading step for C2 with no reinforcement.	164
Figure 4-15: Crack size at each loading step for C2 with no reinforcement.	165

Figure 4-16: Web bulging at each loading step (C2 – duct tie 10.5" spacing).	166
Figure 4-17: Crack size at each loading step (C2 – duct tie 10.5" spacing).	167
Figure 4-18: Artificial cracks with applied air pressures from ducts.....	168
Figure 4-19: Bar stress vs. duct tie spacing (with artificial crack).	170
Figure 4-20: Bar stress vs. equivalent curvature loads (with artificial crack).	170
Figure 4-21: Bar stress vs. tie spacing for no AC and AC (Artificial Crack).....	171
Figure 4-22: No AC and AC for bar stress vs. curvatures (Artificial Crack).	171
Figure 4-23: Post-tensioning equation descriptions.....	172
Figure 4-24: Reinforcement ratio vs. equivalent curvature force (0.7 scale).	173
Figure 4-25: Atena spacing vs. equivalent curvature (0.7 scale).	174
Figure 4-26: Reinforcement ratio vs. equivalent curvature load (1.0 scale).....	176
Figure 4-27: Atena spacing vs. equivalent curvature (1.0 scale).	177
Figure 4-28: 2, 3 and 4 ducts in the web.....	178
Figure 4-29: Parametric study with 2 ducts in the web at midspan of the beam.	178
Figure 4-30: Parametric study with 3 ducts in the web at midspan of the beam.	179
Figure 4-31: Parametric study with 4 ducts in the web at midspan of the beam.	179
Figure 4-32: Support conditions for ducts in the middle and bottom of the web.	181
Figure 4-33: Principal stresses at centerline (ducts in the middle of the web).	181
Figure 4-34: Principal stress at centerline (ducts at the bottom of the web).....	182
Figure 5-1: Duct tie reinforcement design detail.	185
Figure B-1: C2 shear reinforcement.	199
Figure B-2: C2 beam end displacement.....	200
Figure B-3: C3 shear reinforcement.	201
Figure B-4: C3 beam end displacements.	202
Figure B-5: C4 shear reinforcement.	203
Figure B-6: C4 beam end displacements.	204
Figure B-7: C5 shear reinforcement.	205
Figure B-8: C5 beam end displacements.	206
Figure B-9: C6 shear reinforcement.	207
Figure B-10: C6 beam end displacements.	208
Figure B-11: C6 duct tie reinforcement 12.25" right of centerline.....	209
Figure B-12: C6 duct tie reinforcement 19.25" right of centerline.....	210
Figure C-1: C1 (11.5 k/ft.) crack width at CL between ducts (no duct ties).	212
Figure C-2: C1 (11.5 k/ft.) max. web bulge on each face (no duct ties).....	213
Figure C-3: C1 (11.5 k/ft.) crack width at CL between ducts (1.05" spacing).	214
Figure C-4: C1 (11.5 k/ft.) max. web bulge on each face (1.05" spacing).	215
Figure C-5: C2 (19.12 k/ft.) crack width at CL between ducts (no duct ties).	216
Figure C-6: C2 (19.12 k/ft.) max. web bulge on each face (no duct ties).....	217
Figure C-7: C2 (19.12 k/ft.) crack width at CL between ducts (1.05" spacing).	218
Figure C-8: C2 (19.12 k/ft.) max. web bulge on each face (1.05" spacing).	219
Figure C-9: Avg. C2 & C3 (22.60 k/ft.) crack width at CL (no duct ties).....	220
Figure C-10: Avg. C2 & C3 (22.60 k/ft.) max. web bulge (no duct ties).	221
Figure C-11: Avg. C2 & C3 (22.60 k/ft.) crack width at CL (1.05" spacing).	222
Figure C-12: Avg. of C2 & C3 (22.60 k/ft.) max. web bulge (1.05" spacing).	223
Figure C-13: C3 (26.10 k/ft.) crack width at CL between ducts (no duct ties).	224
Figure C-14: C3 (26.10 k/ft.) max. web bulge on each face (no duct ties).....	225

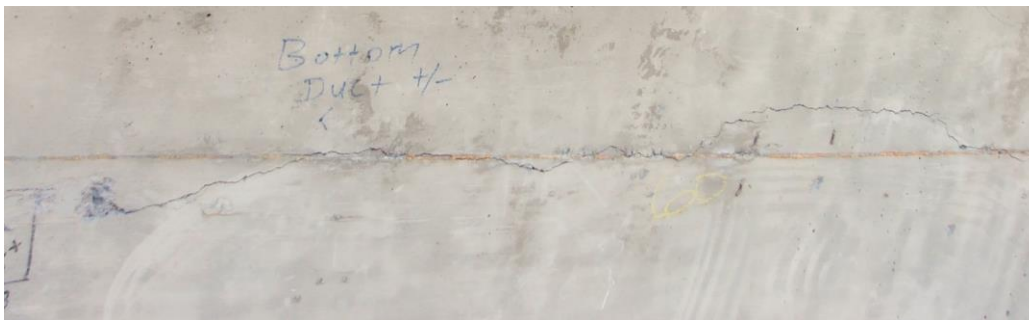
Figure C-15: C3 (26.10 k/ft.) crack width at CL between ducts (1.05" spacing).	226
Figure C-16: C3 (26.10 k/ft.) max. web bulge on each face (1.05" spacing).	227
Figure C-17: C3+ (29.7 k/ft.) crack at CL between ducts (no duct ties).	228
Figure C-18: C3+ (29.7 k/ft.) max. web bulge on each face (no duct ties).	229
Figure C-19: C3+ (29.7 k/ft.) crack width at CL between the ducts (1.05" spacing).	230
Figure C-20: C3+ (29.7 k/ft.) max. web bulge on each face (1.05" spacing).	231
Figure C-21: C1 (11.5 k/ft.) AC bar stress MB (17.5" spacing).	232
Figure C-22: C1 (11.5 k/ft.) AC bar stress MB (7" spacing).	233
Figure C-23: C2 (19.12 k/ft.) AC bar stress MB (17.5" spacing).	234
Figure C-24: C2 (19.12 k/ft.) AC bar stress MB (3.5" spacing).	235
Figure C-25: C3 (26.10 k/ft.) AC bar stress MB (17.5" spacing).	236
Figure C-26: C3 (26.10 k/ft.) AC bar stress MB (3.5" spacing).	237
Figure C-27: C3+ (29.7 k/ft.) AC bar stress MB (17.5" spacing).	238
Figure C-28: C3+ (29.7 k/ft.) AC bar stress MB (3.5" spacing).	239

1.0 Introduction

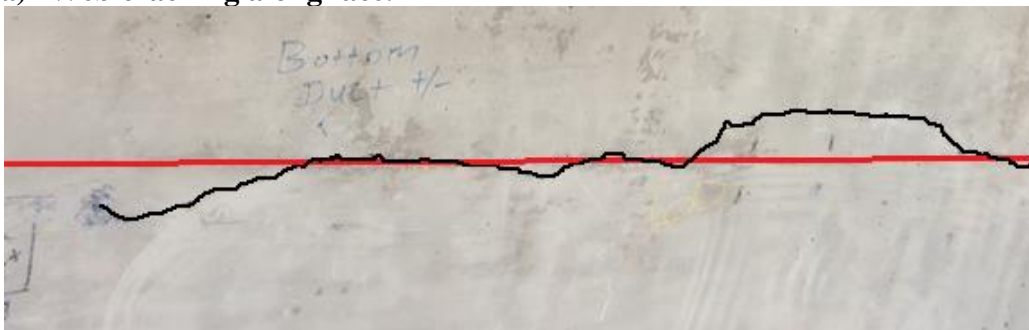
1.1 Problem Statement

During the construction process of a post-tensioning bridge, one of the most critical aspects is the grouting of the tendons. An unsuccessful grouting of the tendons can lead to tremendous problems. In order to help ensure that there can be proper grouting, the Nevada Department of Transportation (NDOT) has adopted the procedure of air pressuring the ducts before stressing the tendons and then again after the tendons have been stressed. The purpose of this is to ensure the post-tensioning system is able to be grouted as well as revealing any concrete defects and potential issues with the various post-tensioning components.

During the construction of the Steamboat Hills and Galena Creek bridges, cracking occurred along the web during the construction process that led to repairs shown in Figure 1-1. During the process of stressing the tendons, air pressure testing and grouting of the ducts, web cracks formed around the ducts and transferred to the web surface leading to delamination and repairs. Figure 1-1a shows the cracks along the outside surface of the exterior inclined girder web of Steamboat Hills Bridge. The crack occurred along the bottom duct and is highlighted in Figure 1-1b above the column and adjacent to the pier cap. Cracking extended beyond both sides of the pier cap on both the outside and inside surfaces of the exterior-inclined girder web. The post-tensioning curvatures are larger for inclined girders to create the same vertical post-tensioning forces as the vertical interior girders. The cracking directly negates one of the prime reasons for post-tensioning, to minimize service load cracking and also raised concern of the integrity of the structure (Stone & Breen, 1981).



a) Web cracking along face.



b) Web cracking along face with duct and crack outlined.

Figure 1-1: NDOT Bridge web cracking.

Upon discovery of the surface cracks shown in Figure 1-1, the cracks were regarded as detrimental to the longevity and performance of the bridge. Cracks that reach the steel ducts can cause corrosion of the ducts and eventually the post-tensioning tendons from moisture that can lead to failure of the bridge. The web face was cut open to examine the concrete around the ducts to evaluate the significance of the cracking, shown in Figure 1-2. Concrete cracking between the ducts and below the ducts can be seen leading to the cracking along the web surface in Figure 1-2. As seen in Figure 1-2, the cracking along the web surface is following the outline of the bottom duct. The cracks were filled with high-strength epoxy to repair the beam.

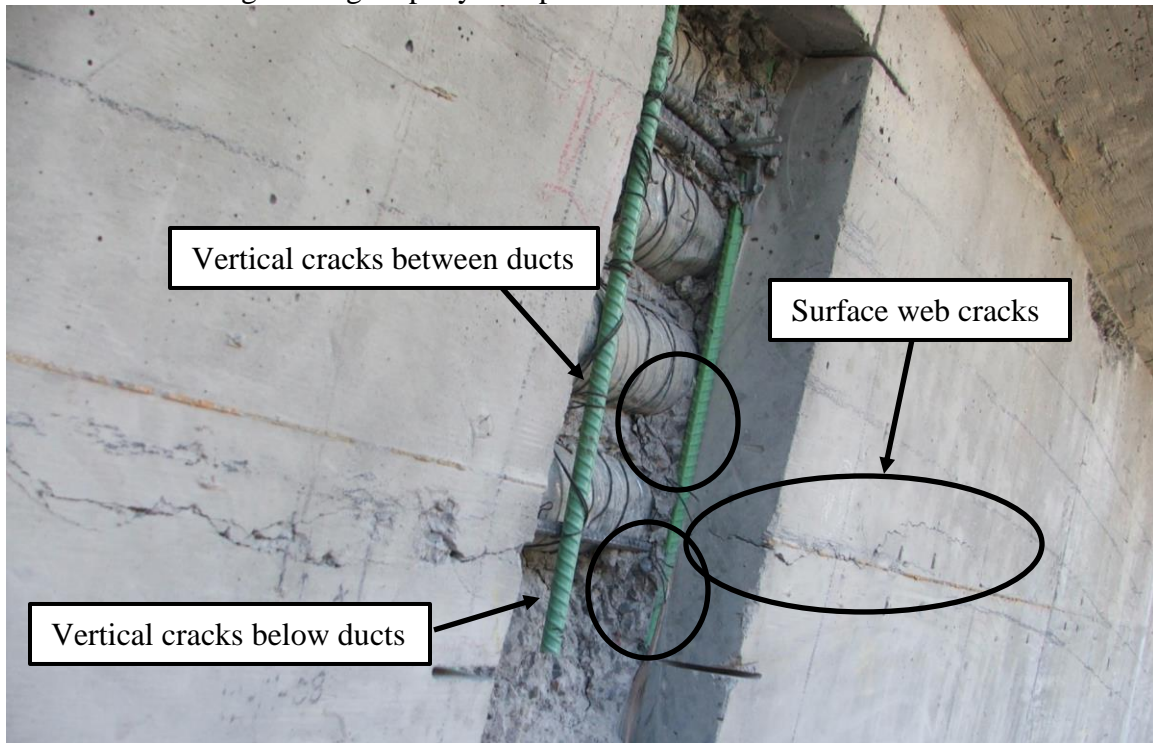


Figure 1-2: NDOT Bridge cut section after cracking occurred.

1.2 Previous Research

Podolny Jr. (1985) studied the cause of web cracking in horizontally curved bridges and designed retrofit procedures. The horizontally post-tensioned curved bridge was cracking and spalling along the web due to the lateral prestressing force. The concrete damage was counteracted by adding hoops around the ducts and reinforcement hooks above and below the ducts connecting to the shear reinforcement. The inclusion of duct ties contained the post-tension tendons.

No research was identified on the impact of vertical curvature in prestressing tendons in combination with air pressure testing of post-tensioning ducts. With no previous research being conducted on the effects of combined post-tensioning and air pressure testing on concrete, web cracking in vertically curved tendon paths, it is vital to study the effects and propose solutions for NDOT.

1.3 Scope and Objective

The main objective of this study is understanding the development of concrete web cracking induced from the post-tensioning and air pressure testing of the ducts. Once understood, bridge design procedures can be altered to minimize concrete cracking.

The project consists of two major components: large-scale experimental laboratory testing and an analytical parametric study. Six 0.7 scale post-tensioned concrete bridge beams with various design details were designed, constructed and tested. Post-tensioned beams were designed similar to NDOT's Rancho Drive Bridge and Steamboat Hills Bridge. Rancho Drive Bridge had no web cracking whereas Steamboat Hills Bridge had web cracking. The analytical studies consisted of varying multiple design details and then using Atena 3D finite element program to study the effects. Both the experimental and analytical models were used to determine design procedures and details that have an effect on reducing the damage caused by the post-tensioning and the air pressure testing during the construction process.

2.0 Preliminary Analysis and Experimental Program

2.1 Introduction

To replicate NDOT's web cracking issue, 3 experimental beams were constructed based on current NDOT bridges interior girders. The experimental beams were designed at 0.7 scale for laboratory testing. The 3 beams had varying duct curvatures ranging from low curvature to high curvatures when compared with existing NDOT bridges. Based on the results from round A and a preliminary analysis using Atena 3D Finite Element Modeling (FEM) program, 3 more beams were designed and constructed that included various design changes to reduce the web cracking. Therefore, a total of 6 beams were designed with 3 beams being modeled after current NDOT and 3 more beams with various design changes intended to reduce the cracking.

2.2 Testing Configuration Details

2.2.1 Overall Beam Design

With the web cracking occurring over the column in NDOT bridges, the experimental beam design focused on the region above the column in the superstructure. Bridges located at Rancho Drive and Steamboat Hills are considered to be a typical bridges. The dimensions of the bridge were compiled into a table for design purposes of the experimental beams. The equivalent curvature of Rancho Drive is at the lower end of the spectrum for NDOT bridges. The equivalent curvature of Steamboat Hills is on the higher side. Steamboat Hills was also chosen since it experienced web cracking issues. Whereas the Rancho Drive Bridge did not experience any web cracking damage. Since the area of concern is the negative curvature of the prestressing layout, the experimental beam is only modeled after the negative curvature and is cut at the inflection points of the tendons as seen in Figure 2-1.

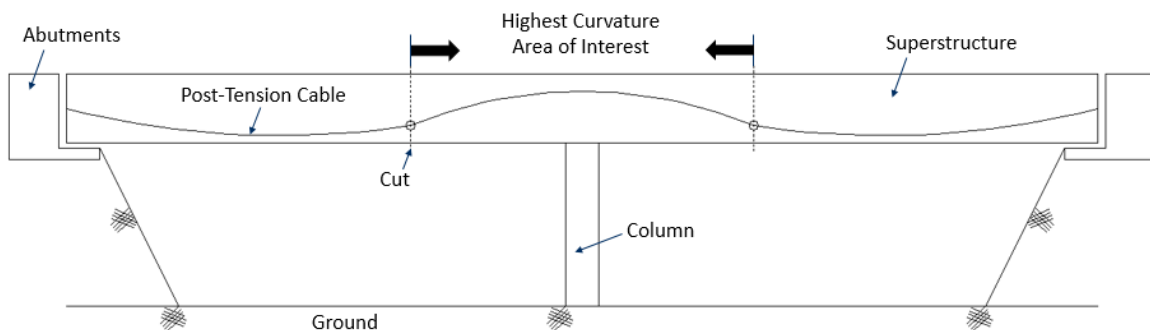


Figure 2-1: Longitudinal Area of Interest.

Cutting the beam at the inflection points and only running experiments on the negative curvature of the beam allowed for ease of testing and transportation from the construction/casting site into the laboratory. In addition to the length being shortened, the cross section of the box girder was also limited to only one web of the complete box girder as seen in Figure 2-2.

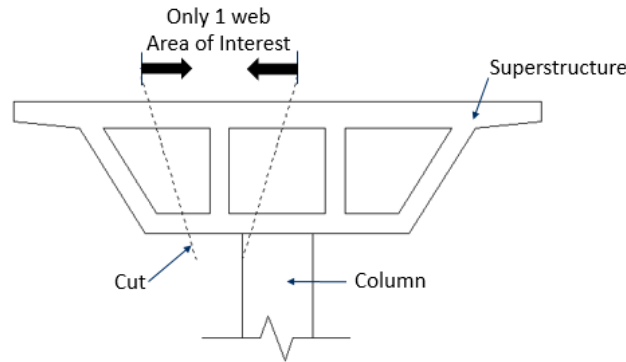


Figure 2-2: Cross Sectional Area of Interest.

The size of the flanges were chosen based on dividing the flanges at the midpoint between the webs. This creates the cross section where the top flange is wider than the bottom flange as the majority of box girders have a skewed outside girder and leads to the experimental beam having an I-shaped cross section. With the design narrowed down to the negative curvature and the cross section consisting of one web, an “I” section, the experimental beam was able to be modeled comparatively to a typical NDOT bridge scaled to 0.7 scale.

Table 2-1 provides the basic dimensions of the NDOT bridges and the corresponding 0.7 scale. Comparing Rancho Drive and Steamboat Hills bridges, it was more feasible to model the dimensions after Rancho Drive as the length and depth are more suitable for laboratory testing.

Table 2-1: Comparison between NDOT bridges and UNR designed bridge.

		NDOT Bridge		NDOT 0.7 Scaled		UNR Design
		Rancho	Steamboat	Rancho	Steamboat	0.7 Scale
	Length, ft.	28.00	45.00	19.60	31.50	17.50
	Depth, in.	68.00	117.60	47.60	82.32	42.00
Top Flange	Width, in.	123.00	141.60	86.10	99.12	50.50
	Height, in.	9.00	9.00	6.30	6.30	6.00
Bot. Flange	Width, in.	113.00	136.20	79.10	95.34	33.50
	Height, in.	6.00	7.87	4.20	5.51	4.50
Web	Width, in.	12.00	11.76	8.40	8.23	8.40
	Height, in.	53.00	100.73	37.10	70.51	31.50
	Area, in.²	2421.00	3531.13	1694.70	2471.79	718.35
	Volume, cyd	18.83	43.46	13.18	30.42	4.56
	Center of Gravity, in.	41.11	65.28	28.78	45.70	24.38

As seen in Table 2-1, the beam designed by UNR is representative of the Rancho Drive Bridge. The main difference in the design can be noticed in the flanges on the beam. The flanges were chosen to be narrower when compared to NDOT’s Bridge, as having a wide flange does not impact the flow of forces in the web and the smaller flange

does reduce construction costs. The web thickness was decided to remain kept at 8.4 inches as cracking was present in the web for Steamboat Hills Bridge and the web is of primary importance. Web cracking was not present in Rancho Drive Bridge. The center of gravity measured from the base also remains at a similar ratio to the beam depth when comparing both the UNR beams and the Rancho Drive beam. Length of the beam was determined based on being similar to the length of Rancho's length and to have the ends of the beams close to the holes located in the strong floor in the laboratory, which will be necessary for the test setup. Keeping the beam ends above the strong floor holes allows for the vertical dead load to be applied. The dead load is discussed further in section 2.2.2.

In order to make the specimens representative of the actual beams, the cross-sectional properties were compared to the actual bridge properties. Table 2-2 provides the values relating Rancho Drive and Steamboat Hills bridges to the bridges designed at UNR. The beams designed at UNR are comparable in terms of the equivalent prestress force in the first row with C1 being similar to the Rancho Drive Bridge and C3 to the Steamboat Hills Bridge.

The controlling factor for the determination of the radii's and amount of tendons per duct was matching the equivalent distributed prestress force. Knowing the amount of equivalent prestress force needed, nine tendons per duct were chosen. As stated in section 2.2.3, the tendons were planned to be overstressed to 0.85fpu. With the overstressing, it was decided to use twelve tendons instead of nine tendons to add an extra safety factor with the tendon stresses only reaching 0.6375fpu at 0.85fpu nine tendon load. With an equivalent nine tendons being stressed, the radii's could be chosen to produce an equivalent prestress force comparable to Rancho Drive and Steamboat Springs. Another determining factor for the radii's was keeping the duct spacing in the center of the beam at 0.7 inches and maintaining the allowable spacing of the post-tensioning anchorage devices. The smaller radii's allowed for a smaller prestressing force, P_{tot} , to be applied while still providing the proper forces. P_{tot} takes into account an assumed 10% friction loss. The reinforcement was designed to meet AASHTO (2012) LRFD Specifications while attempting to have a similar reinforcement percentage as in the Nevada bridges. Table 2-2 shows the equivalent prestress force for each beam which is taking the average tendon amplitude, a_{avg} , for multiple tendon paths as opposed to a single amplitude, "a", for a single tendon path.

Table 2-2: Comparison between NDOT bridges and experimental beams.

	NDOT Bridge		NDOT 0.7 Scale		UNR 0.7 Scale		
	Rancho	S.S.	Rancho	S.S.	C1	C2	C3
PS Force, kip/ft.	16.48	35.7	11.53	24.99	11.76	19.12	26.09
Avg. Radii, ft.	144	124	100.8	86.8	97.83	46.32	30.88
Flange % of Rein.	Top	0.606	0.505	0.606	0.505	0.594	
	Bot.	0.752	0.371	0.752	0.371	0.683	
P_{tot} , kip	2373	4463.6	1162.8	2187.2	711.869		
Duct Spacing, in	1		0.7		0.7		

Figure 2-3 is the basic beam configuration with cross sections in the area of interest and the anchorage zones. In between the ducts was a clear spacing of 0.7 inches. Standard NDOT bridges use 1.0 inches and therefore, a scaling factor of 0.7 provides 0.7 inches. As noticed in Figure 2-3, the web gets wider at the ends of the beam. This is the anchorage zone area and has to account for the large forces being applied from the post-tensioning and secured by the anchorages.

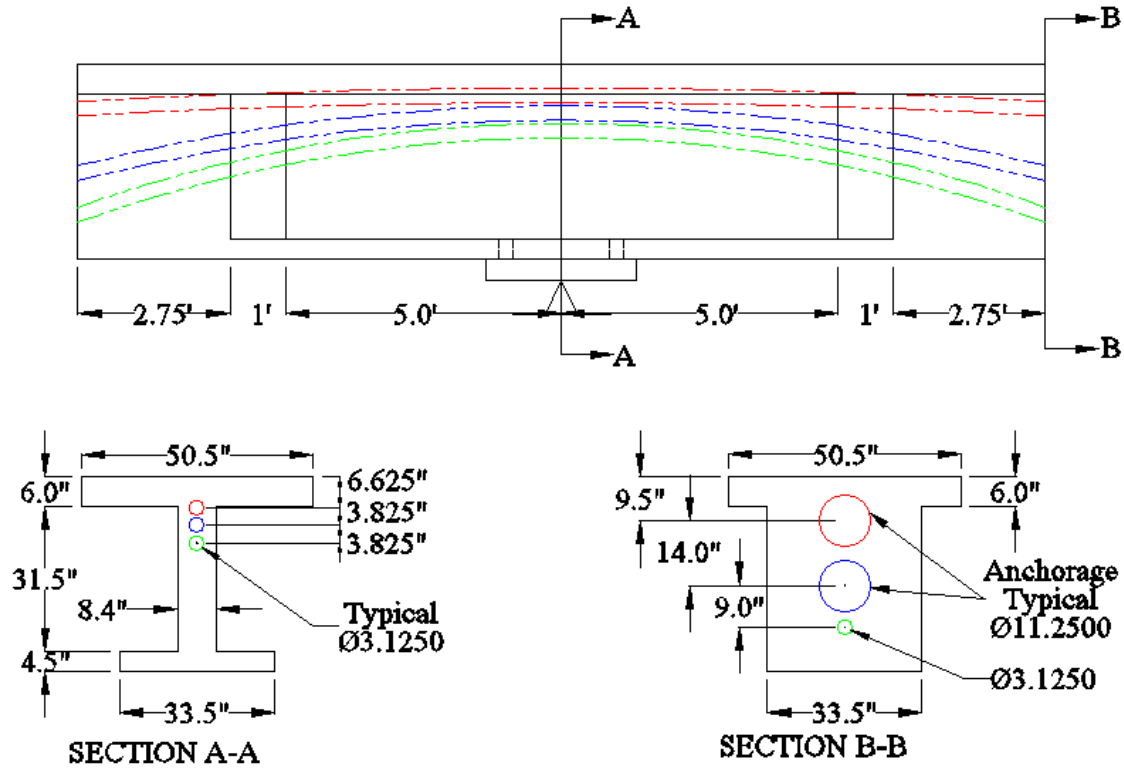


Figure 2-3: UNR beam design detail and cross sections.

As the overall design was similar between all the beams, the reinforcement was chosen based on AASHTO LRFD Bridge Design (2012) as well as NDOT bridges as a standard reference for matching reinforcement percentages. The longitudinal reinforcement was designed for the dead load and then compared to the reinforcement percentages in the NDOT bridges. The following equations were used in determining the proper amount of longitudinal reinforcement from AASHTO section 5.7.3.3.2.

$$M_{cr} = \gamma_3 [(\gamma_1 f_r + \gamma_2 |f_{cpe}|) S_c - M_{dnc} \left(\frac{S_c}{S_c} - 1 \right)] \quad (2-1)$$

Where:

γ_1 = flexural cracking variability factor

γ_2 = prestress variability factor

γ_3 = ratio of minimum yield strength to ultimate tensile strength of reinforcement

f_r = modulus of rupture, AASHTO 5.4.2.6

f_{cpe} = compressive stress in concrete

S_c = section modulus

M_{dnc} = total un-factored dead load moment

Equation (2-1) was used to calculate the cracking moment of the beam. From the cracking moment, it was determined if the beam had an adequate prestressing moment in the section. If the prestressing moment was higher than the cracking moment than the section was deemed adequate. If it is not, then the remaining of the cracking moment needed to be accounted for in the flexural reinforcement as seen in equation (2-2) with M_{target} being the moment the reinforcement needs to account for.

$$M_{target} = M_{cr} - M_{ps} \quad (2-2)$$

The nominal moment capacity for the prestressed and reinforced concrete section is as follows based on AASHTO equation 5.7.3.2.2-1:

$$M_n = A_{ps}f_{ps} \left(d_p - \frac{a}{2} \right) + A_s f_s \left(d_s - \frac{a}{2} \right) + 0.85f'_c (b - b_w) h_f \left(\frac{a}{2} - \frac{h_f}{2} \right) \quad (2-3)$$

Where:

A_{ps} = area of prestressing steel

f_{ps} = stress in prestressing steel, AASHTO Eq. 5.7.3.1.1-1

d_p = distance from extreme compression fiber to centroid of prestressing tendons

a = depth of the compression block

A_s = area of conventional flexural reinforcement

f_s = stress in conventional flexural reinforcement

d_s = distance from extreme compression fiber to centroid of conventional reinforcement

f'_c = concrete compression strength

b = width of compression flange

b_w = web width

h_f = height/thickness of flange

The nominal moment capacity of equation (2-3) needs to be checked against the cracking moment as shown in equation (2-5).

$$\phi M_n \geq M_{cr} \quad (2-5)$$

The longitudinal reinforcement was chosen based on NDOT's Rancho Drive and Steamboat Hills reinforcement percentage and checked against the cracking and maximum moments from AASHTO equations. The longitudinal reinforcement percentages are shown in Table 2-2 with UNR designed beams having 0.594% for the top flange and 0.683% for the bottom flange with Rancho Drive Bridge reinforcement percentage at 0.606% for the top flange and 0.752% for bottom flange. Based on the aforementioned equations, the longitudinal reinforcement was chosen for both the top and bottom flanges. The top flange had a total of nine-#5 bars spread throughout the width of the flange whereas the bottom flange had ten-#4 bars throughout the entire bottom flange width as seen in Figure 2-4.

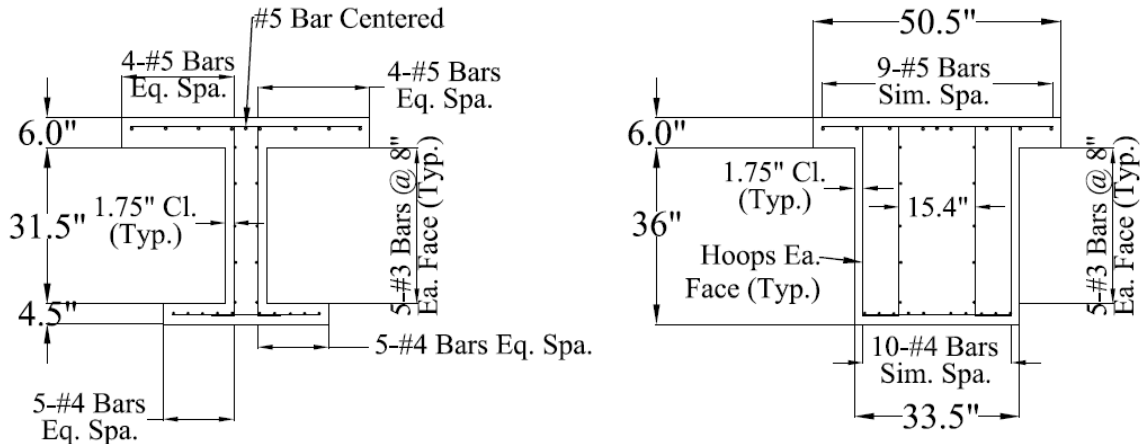


Figure 2-4: Cross sectionals reinforcement details.

The next step for calculating the reinforcement within the beam was to determine the longitudinal reinforcement needed within the web, known as skin reinforcement. The skin reinforcement's main purpose is crack control in the web. The equation for the skin reinforcement is attained from AASHTO 5.7 and is show in equation (2-5).

$$A_{sk} = \max[0.012(d - 30), \frac{A_s + A_{ps}}{4}] \quad (2-5)$$

Figure 2-5 shows the layout for the skin reinforcement with sizes and dimensions coordinating with Figure 2-4.

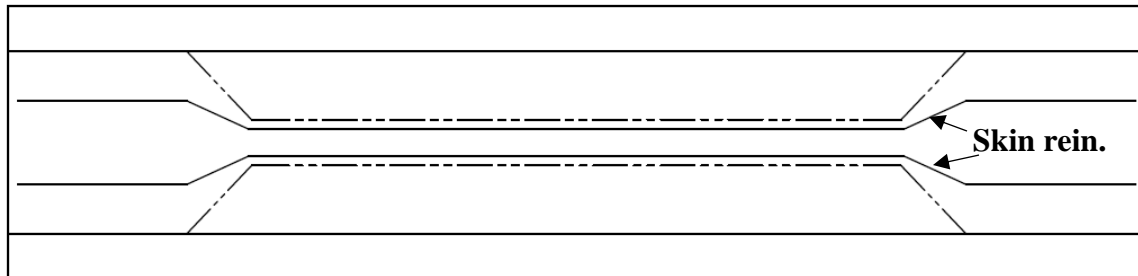


Figure 2-5: Plan view skin reinforcement detail.

The shear equations were used from AASHTO 5.8.3 with the shear capacity coming from both the concrete and the reinforcement contribution.

$$V_c = 0.0316 \beta \sqrt{f_c} b_v d_v \quad (2-6)$$

With:

V_c = concrete shear contribution, kip

β = Stress variable, AASHTO 5.8.3

b_v = effective web width, in.

d_v = 0.8h or distance from extreme compression fiber to centroid of prestressing reinforcement, whichever is greater, in.

Equation (2-6) provides the shear contribution from the concrete. If the shear from the concrete was deemed adequate compared to the shear demand, then shear reinforcement was not needed. In the design of the experimental beams, the concrete alone was not satisfactory so shear reinforcement was needed.

$$V_s = \frac{A_v f_y d}{s} \quad (2-7)$$

With:

V_s = reinforcement shear contribution, kip

A_v = area of shear reinforcement chosen, in.²

f_y = yield strength of steel reinforcement, psi

s = spacing of shear reinforcement

Equation (2-8) shows the shear capacity of the beams with both the concrete and reinforcement taken into account where it needs to be larger than the shear demand shown in equation (2-9).

$$\phi V_n = \phi V_c + \phi V_s \quad (2-8)$$

$$\phi V_n > V_u \quad (2-9)$$

Figure 2-6 shows the shear along the length of the beam with the concrete shear contribution being less than the shear demand along locations of the beam. To determine the appropriate shear reinforcement spacing, the spacing had to provide enough capacity for the beam to withstand the shear demand on the ends of the beam of 210 kips and almost 100 kips at the center of the beam, where the beam is supported. The shear reinforcement was chosen to be #3 bars at 3.5 inches along the length of the beam while providing adequate concrete cover throughout.

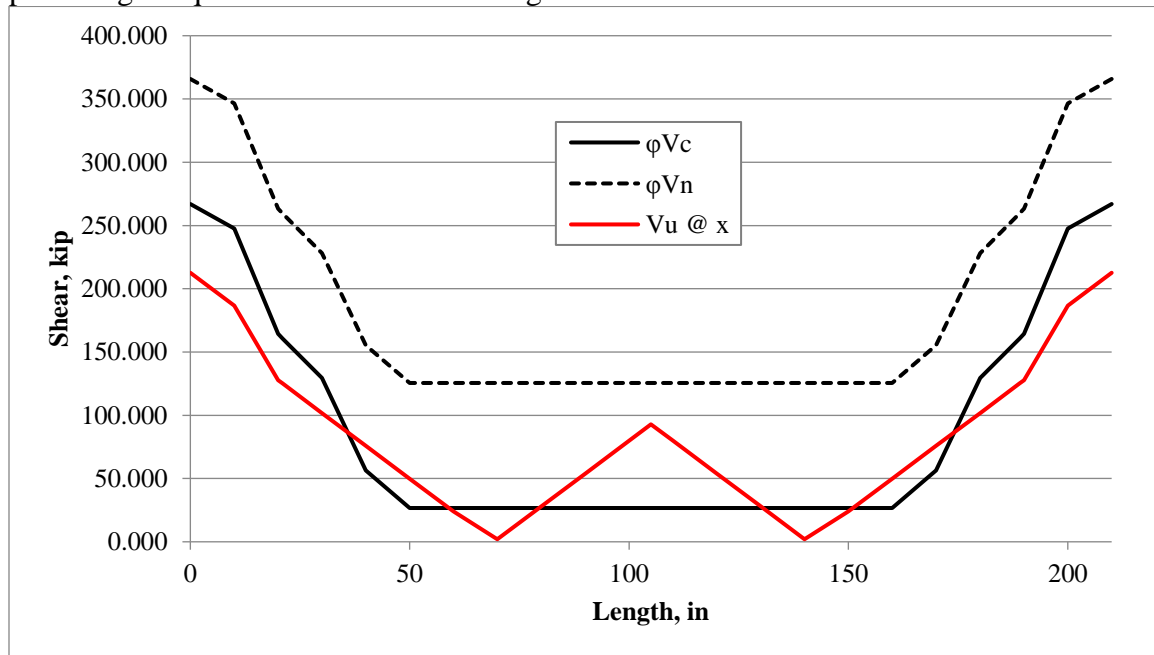


Figure 2-6: Shear along the length of the beam.

2.2.2 Test Setup

The beam design was based on the segment over the support as shown in Figure 2-1. The experimental beams were arranged where the beam was supported in the center with each end hanging freely. This setup is similar to a full scale beam cut at the inflection points while keeping it supported by the column. To represent the column in the experimental beams, a large 4x4x8 ft. reaction block was positioned on the strong floor of the laboratory with the beam placed on top of the reaction block. The beam was secured to the reaction block and the strong floor through the use of four Dywidag bars

extending through the bottom flange of the beam. The bars were not post-tensioned, only hand tight to lock the beam in place, see Figure 2-7.

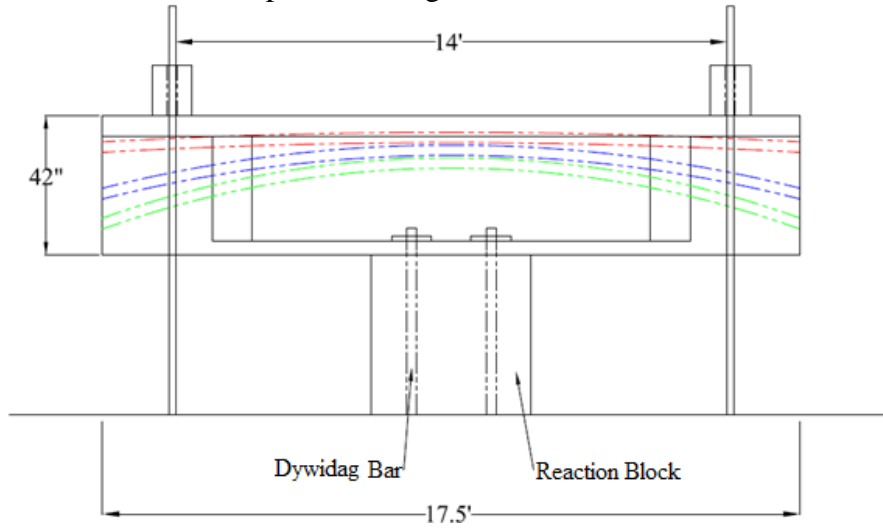


Figure 2-7: Elevation view of test setup with reaction block representing the column.

Figure 2-7 also shows the applied vertical dead load towards the ends of the beams, see Figure 2-1. The self-weight from the remaining span has to be accounted for to get proper stress condition at the center of the beam. As shown in Figure 2-8, the dead load was applied with the use of spreader beams spanning the entire width of the experimental beam and pressure jacks on each end of the spreader beam. The load was applied at a distance of 7 ft. off-center on both beam ends. The load location was limited based on the spacing of the holes in the strong floor. All four of the pressure jacks were connected to an accumulator to ensure each jack was exerting the same force on the ends of the beams.

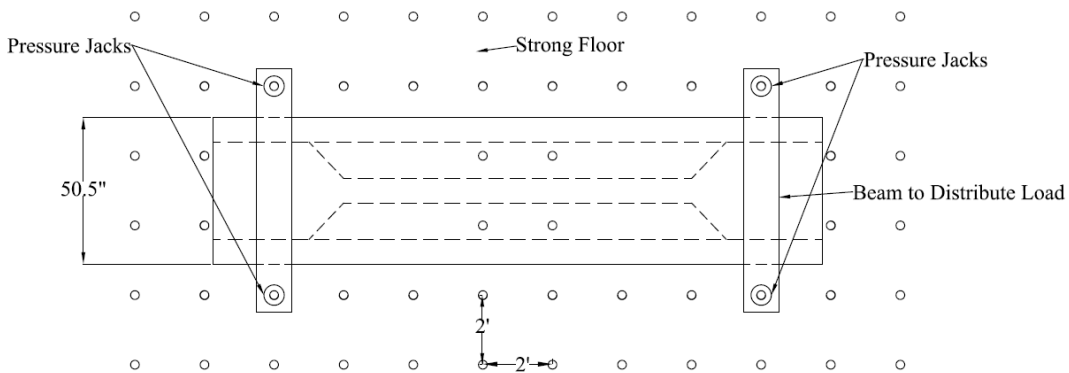


Figure 2-8: Plan view of test setup.

The amount of dead load applied to the ends of the beams was determined based on the Rancho Drive Bridge. As the negative curvature of Rancho Drive Bridge was used for modeling the experimental beams, the continuing span for the rest of the beam (the positive curvatures and abutments) was calculated based on effective flange width on either side of one web of the box girder. Dead load was applied to each end of the beam to create the same shear and moment in the section as would be found in the Rancho

Drive Bridge. The required dead load was calculated to be 22.5 kip from the Rancho Drive drawings. Figure 2-9 shows the reaction block in the center of the beam with both ends being unsupported with a dead load application towards the ends of the beams.

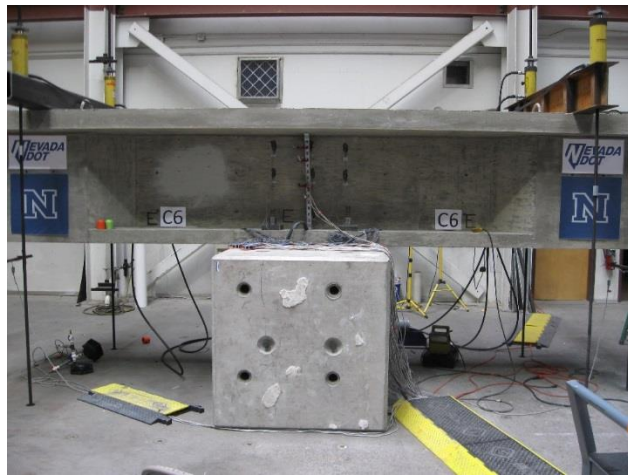
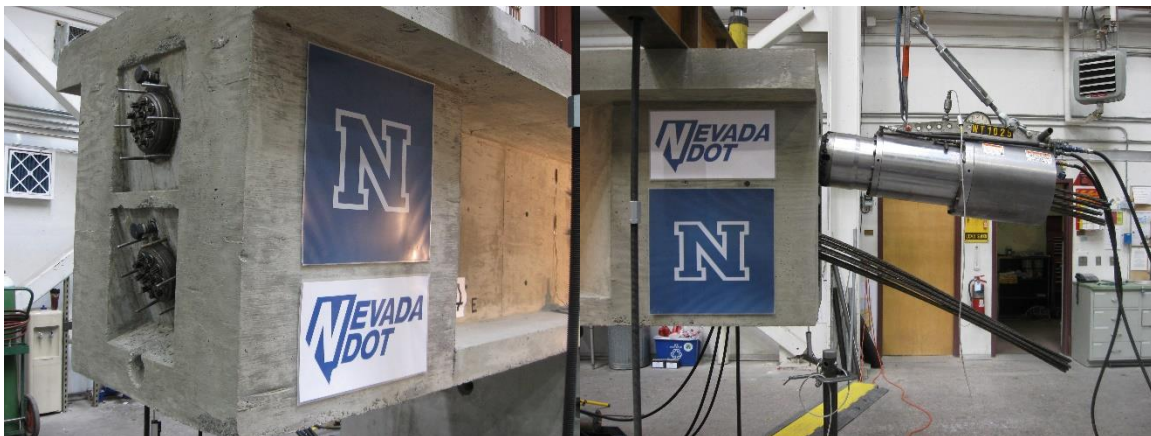


Figure 2-9: Laboratory experimental test setup.

The beams were designed with a post-tensioning force of 0.75fpu for a nine strand system. Shown in Section 2.2.3, the loading protocol is based on using a maximum load of 0.85fpu. As this reduces the safety factor of the tendons failing, the experiment used twelve strands to be able to apply a larger post-tensioning force to the bridge. This allowed for a higher factor of safety and a lower chance of tendon failure. The wedge plates were matched on both ends of the beam with the strands being in the same wedge plate hole on each end. This was performed to minimize winding of the tendons in the middle of the beam to try and eliminate any unknowns.



a) Post-tensioning non-stressing end. b) Post-tensioning end of beam.

Figure 2-10: Stressing and non-stressing ends of the beam.

Once the wedge plates were installed, the wedge grips were positioned on the tendons leaving the dead end having minimal strand sticking out the end as seen in Figure 2-10a and the live end providing enough strand for the post-tensioning jack to grip the strands shown in Figure 2-10b with the post-tensioning jack placed on the top duct. The

post-tensioning jack was a Dywidag Systems International (DSI) 12-0.6” multistrand stressing ram with the matching multistrand hydraulic pump with power seating equipped for seating of the wedges.

This test setup was determined to be adequate in representing the real bridge as the extreme fiber stress state over the column were comparable to the real bridges as seen in Table 2-3. The stresses were determined for the UNR specimens from the Atena 3D finite element models. The test setup in Atena was the same as the experimental setup with the appropriate forces applied to the beams. The complete details of the finite element models are provided in Chapter 4.0.

Table 2-3: Stress comparisons between NDOT bridges and UNR bridges.

	NDOT		NDOT 0.7 Scale		0.7 Scaled UNR Model		
	Rancho	S.S.	Rancho	S.S.	C1	C2	C3
Equivalent PS Dist., kip/ft.	16.48	35.7	11.53	24.99	11.76	19.12	26.09
Stress Top, psi	-819	-1299	-819	-1299	-1205	-1120	-1074
over pier Bot., psi	-615	-437	-615	-437	-402	-378	-358

In accordance with NDOT, the ratio of the flexural top stress to the bottom stress is typically, but not required, 3 to 1 over a column. Steamboat Hills follows this general assumption, while Rancho Drive does not. Each post-tensioning curvature provided the 3:1 ratio of top stresses to bottom stresses over the column. The stresses were at the center of the beam at midspan. The loading followed the loading protocol stated in section 2.2.3 with the stresses shown being at the end of all prestressing and air pressure loading. With the stresses being in accordance to a stress ratio of 3:1 (top:bottom), the test setup for the experimental beams was deemed adequate.

2.2.3 Loading Protocol

Loading was determined based on NDOT’s Standard Specifications for Road and Bridge Construction (2014) protocols. NDOT standard procedure starts with air-pressuring all post-tensioning ducts to 50 psi to ensure no major deficiencies are present before post-tensioning occurs. If the air pressure does not drop below 25 psi air pressure within one-minute, the ducts/post-tensioning system are deemed adequate. Upon finishing the air-pressure testing of the ducts, the post-tensioning can commence.

Post-tensioning values are based on an ultimate strength of 270 ksi (fpu) and assuming only 9 strands per tendon (even though there were actually 12 strands as explained in section 2.2.2). The first 11 steps are in accordance to the loading protocol that would be used in the field including a maximum air pressure of 50 psi. The remaining steps were added to determine the level of safety in the beam. The full loading protocol is as follows:

1. *Apply dead load on beam (22.5 kips on each end)*
2. *50 psi air pressure test middle duct (locked off with no more than half of original pressure lost in one-minute)*
3. *50 psi air pressure test top duct (same procedure as step 2)*
4. *0.15 fpu stress of middle duct (to take slack out of strands)*

5. *0.15 fpu stress of top duct (to take slack out of strands)*
6. *0.45 fpu stress of middle duct*
7. *0.45 fpu stress of top duct*
8. *0.75 fpu stress of middle duct*
9. *0.75 fpu stress of top duct*
10. *50 psi air pressure test middle duct*
11. *50 psi air pressure test top duct*
12. 75 psi air pressure test middle duct
13. 75 psi air pressure test top duct
14. 100 psi air pressure test middle duct
15. 100 psi air pressure test top duct
16. 125 psi air pressure test middle duct
17. 125 psi air pressure test top duct
18. 0.85 fpu stress of middle duct
19. 0.85 fpu stress of top duct
20. 50 psi air pressure test middle duct
21. 50 psi air pressure test top duct
22. 75 psi air pressure test middle duct
23. 75 psi air pressure test top duct
24. 100 psi air pressure test middle duct if capable*
25. 100 psi air pressure test top duct if capable*
26. 125 psi air pressure test middle duct if capable*
27. 125 psi air pressure test top duct if capable*

*If ducts cannot hold air pressure per step 2 (locked off with no more than half of original pressure lost in one minute), a constant pressure is applied for one minute.

After step 11, the loading was increased to determine the leading cause of the web cracking and the factor of safety over standard loading. To model the overloading, the beams were post-tensioned to 0.85 fpu and the air pressure was increased to 125 psi for both the middle and top ducts. Provided with the stressing ram, the calibration sheets provided a gauge pressure for a desired load as seen in Table 2-4.

Table 2-4: Stressing ram gauge pressure and load data.

Gauge pressure, psi		Load, kip
Round A	Round B	
0	0	0
1217	1300	100
2442	2567	200
3700	3817	300
5000	5083	400
7000	7117	562

Round A and Round B gauge pressures are slightly different because the beams were tested at different times and had different stressing rams. With the provided data, equations were able to be formulated to calculate the specific gauge pressure based on the

exact load required. Equation (2-10) is for Round a stressing ram and equation (2-11) is related to round B stressing ram.

$$P = \frac{L - 2.1644}{0.08} \quad (2-10)$$

$$P = \frac{L + 1.7769}{0.0791} \quad (2-11)$$

With: P = gauge pressure, psi and L = prestressing load, kips

With the Equations (2-10) and (2-11), the gauge pressure for each loading sequence was calculated. Table 2-5 shows the gauge pressure values needed for both stressing rams used in the experimental testing to reach the appropriate forces.

Table 2-5: Stressing ram gauge pressure for each loading step.

fpu=	270	ksi	Gauge Pressure	
			Round A	Round B
A=	0.217	in. ²		
P _{ult} (9)=	527.31	kip	6564.32	6688.84
0.15fpu=	79.10	kip	961.65	1022.42
0.45fpu=	237.29	kip	2939.06	3022.33
0.75fpu=	395.48	kip	4916.48	5022.24
0.85fpu=	448.21	kip	5575.61	5688.88

Air pressure was applied to the ducts via the loading protocol outlined previously. Grout caps were used on one end of the beam, the dead end, whereas an air pressure trumpet was designed for the opposing side, the live end, so the tendons did not have to be cut. If the tendons were to be cut, the stressing ram would not be able to grab the tendons to overstress the beam to 0.85fpu. The caps used during air pressure testing of the beams are shown in Figure 2-11 with Figure 2-11a being the provided grout caps fitted for the 12-strand anchorage device and Figure 2-11b being the steel trumpet caps to fit around the strand extending out of the beam.



a) Air pressure/grout caps. b) Steel trumpet used for air pressure testing.

Figure 2-11: Air pressure testing setup on the ends of the beams.

2.3 Round A Experimental Beams

Round A experimental beams consist of the first three configurations (C1, C2, C3) each having varying curvatures from low to high. Round A was designed and tested first to see how the radius of curvature affects the amount of cracking. Round A consisted of existing details. Round B, which will be described later, looked a ways to improve detailing.

2.3.1 C1 – Largest Radius

C1 was selected to have the same equivalent curvature load as the Rancho Drive Bridge. It was the largest radius (smallest curvature) and therefore would provide the smallest forces exerted on the beam due to the following equation:

$$w = \frac{8Pa}{L^2} \quad (2-12)$$

Where:

w = equivalent curvature load due to prestressing, kip/ft.

P = equivalent end load, kip

a = amplitude of tendon profile, ft.

L = length of beam, ft.

With the equivalent end load and the length remaining constant, the amplitude of the tendon profile can increase or decrease the forces exerted from prestressing depending on the amplitude of tendon profile.

2.3.1.1 Design

The design was carefully chosen for C1 to have an average distributed load from the prestressing similar to NDOT's Rancho Drive Bridge. The total distributed load of Rancho Drive bridge was determined based on the detailed construction plans provided by NDOT. Once the distributed load for the post-tensioning ducts were calculated to be 16.48 kip/ft. for the Rancho Drive Bridge, that value was scaled down to 11.54 kips/ft. to match the scaling factor (0.7) of the experimental beams. The radius of curvatures for C1 were able to be determined to be similar to 0.7 scale of Rancho Drive Bridge. Based on achieving the same average distributed load and limitations due to the anchorage sizes, the curvatures of the ducts were determined. The loads were calculated assuming a 10% tendon initial loss due to anchorage set, elastic shortening and friction as well as taking into account the Z-value or tendon-duct offset (0.375 inches). The design details of C1 are outlined in Figure 2-12. The prestress effective distributed load for C1, from the design prestress force (9 0.6" tendons x 0.217 in² x 0.75*270 ksi = 395.4 kips) was determined as follows: $8*395.4*0.9*((2.875 \text{ in.} - 0.375 \text{ in.}) + (13.05 \text{ in.} - 0.375 \text{ in.})) / (17.5 \text{ ft}^2 * 12 \text{ in/ft}) = 11.75 \text{ kip/ft}$ which is near the target of 11.54 kip/ft.

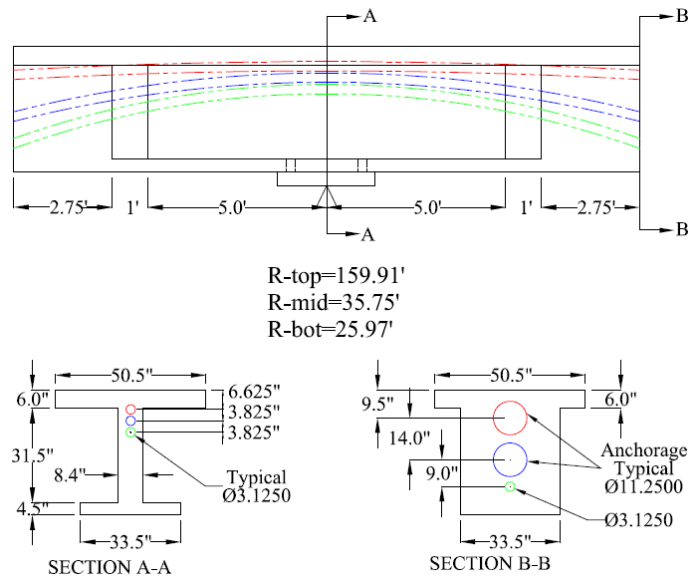


Figure 2-12: C1 design detail.

2.3.2 C3 – Smallest Radius

C3 is the most extreme case for the duct curvature having the largest forces from the post-tensioning. C3 was modeled comparably to Steamboat Hills Bridge that NDOT previously constructed. The bridge at Steamboat Hills had smaller radii's leading to a larger distributed load due to the prestressing.

2.3.2.1 Design

Design of C3 was chosen based on the bridge NDOT designed that had smaller radii's for the post-tensioning. As the radius is directly related to the distributed force due to the prestressing from equation (2-12), the equivalent distributed force from the post-tensioning layout was larger than that of Rancho Drive Bridge which C1 was designed after. Steamboat Hills Bridge had a total distributed load of 35.7 kip/ft. before scaling compared to that of Rancho that had an average of 16.5 kip/ft. The force was scaled (0.7) down to 25.0 kip/ft. which was the target distributed force for C3. Similarly to C1 design, the loads were calculated with an assumed 10% initial loss due to anchorage set, elastic shortening and friction as well as taking into account the Z-value or tendon-duct offset (0.375 inches). Table 2-2 shows a comparison between the NDOT bridges (scaled and unscaled) alongside the beams designed for the experimental testing at UNR. Figure 2-13 shows the design detail for C3. The bottom duct was securely capped off once getting into the anchorage zone area as there was not enough room on the ends of the beams with the curvature being much larger on this configuration. The prestress effective distributed load for C2, from the design prestress force (9 0.6" tendons x 0.217 in² x 0.75*270 ksi = 395.4 kips) was determined as follows: $8 * 395.4 * 0.9 * ((11.375 \text{ in.} - 0.375 \text{ in.}) + (23.050 \text{ in.} - 0.375 \text{ in.})) / (17.5 \text{ ft}^2 * 12 \text{ in/ft}) = 26.1 \text{ kip/ft}$ which is near the target of 25.0 kip/ft.

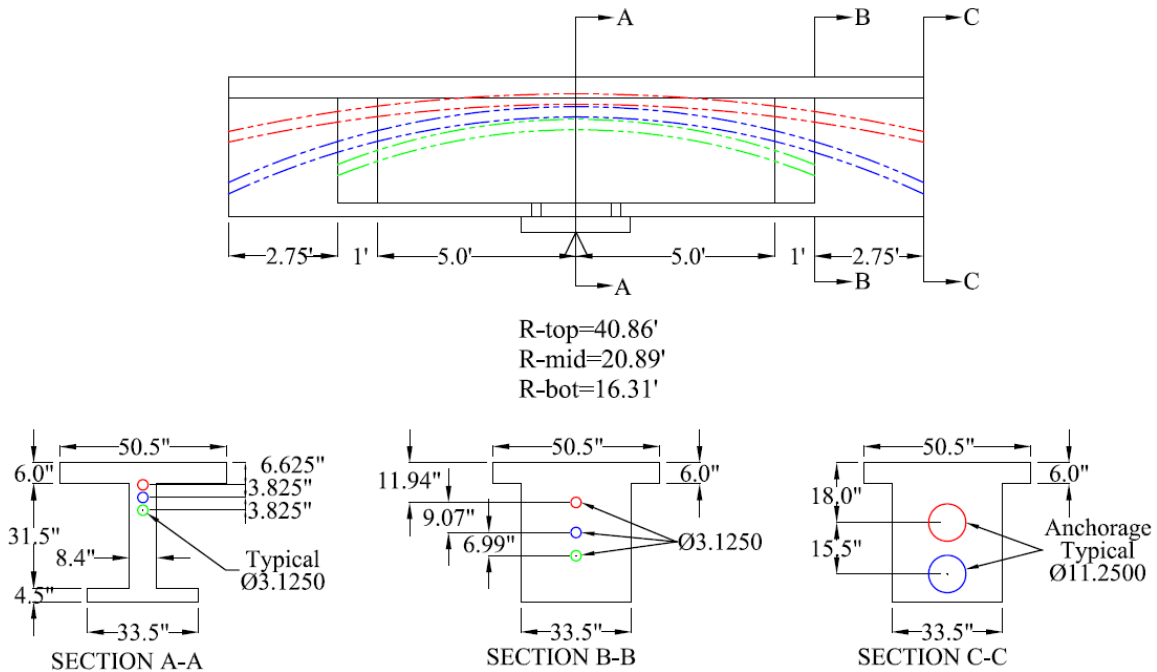


Figure 2-13: C3 design detail.

2.3.3 C2 – Medium Radius

C2 was designed similarly as of equation (2-12). The design objective of C2 was to achieve an equivalent curvature load that averaged the value for NDOT bridge (low forces) (C1) and a more extreme radius NDOT bridge (high forces) (C3).

2.3.3.1 Design

The general design is the same for C2 as it was for C1 with the only difference being the change in curvature of the applied prestressing. Similar to C1 and C3, the loads were calculated assuming a 10% tendon initial loss due to anchorage set, elastic shortening and friction as well as taking into account the Z-value or tendon-duct offset (0.375 inches). Based on the desired distributed load, the radius of curvature and anchorage locations were determined. C2 design detail is outlined in Figure 2-14. The prestress effective distributed load for C1, from the design prestress force (9 0.6" tendons x 0.217 in² x 0.75*270 ksi = 395.4 kips) was determined as follows: $8 * 395.4 * 0.9 * ((6.875 \text{ in.} - 0.375 \text{ in.}) + (18.55 \text{ in.} - 0.375 \text{ in.})) / (17.5 \text{ ft}^2 * 12 \text{ in/ft}) = 19.12 \text{ kip/ft}$.

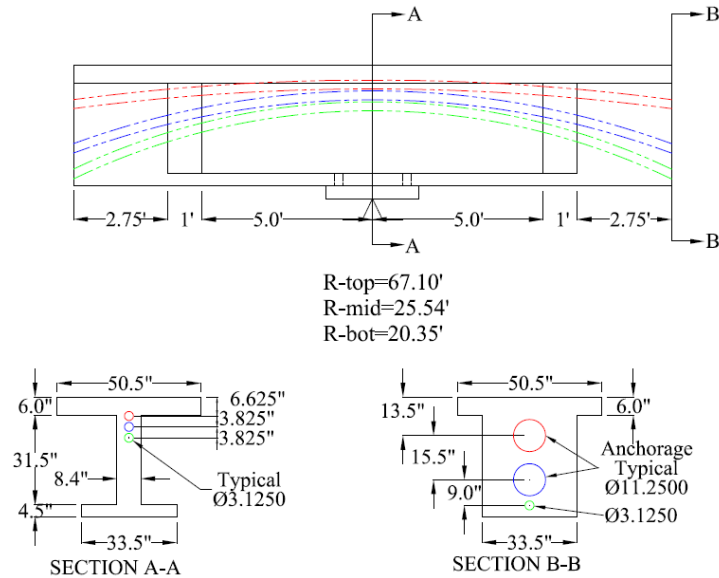


Figure 2-14: C2 design detail.

2.4 Preliminary Finite Element Analysis

A preliminary analysis with Atena 3D finite element (FE) modeling software was conducted to facilitate the design of the Round B specimens. Atena 3D software was chosen because it was designed specifically for concrete structural modeling with the capability of capturing concrete cracking. Atena uses the Rankine-fracturing model for concrete cracking. The process of crack formation is divided into three stages: uncracked, process zone, and cracked zone. The crack formation takes place during the process zone with a decrease in tensile stress. Once the crack is formed, a full release of stress is seen (Cervenka et al, 2014). The full detail of the FE model is further discussed in Chapter 4.0 Analytical Parametric Study. The preliminary analysis has no artificial cracks included in the models, further discussed in Chapter 4.0.

As the first 3 beams were being directly modeled after current NDOT bridges, the preliminary analysis could be calibrated against observed behavior in the field. For the second round of testing, Round B, a much more intense preliminary analysis was completed to determine the proper design changes that were needed in order to improve performance. Round B design possibilities consisted of increasing the web width, increasing the spacing between the ducts, including reinforcement between the ducts at various spacing (duct ties), and the location of the duct tie reinforcing ties. Running the various parameters provided the opportunity to modify the experimental design to test the parameters that would make the biggest impact to reducing the cracking. The preliminary analysis consisted of running curvatures the same as C2, being that C2 is the average of C1 and C3, the extremes of curvatures for NDOT, explained in further detail in section 2.3.3. The curvature of C2 is the most common curvature in the field according to NDOT.

Upon completing the preliminary analysis of the increased web width, increased spacing between ducts, and the inclusion of duct ties, it was determined that increasing the web width did not have a large effect in overall beam performance as seen in Table 2-6. When only the web width was changed, increasing from 8.375 inches to 10.5 inches,

this is denoted by 8.375W and 10.5W with “W” symbolizing the web width. Increasing the web width by 25% led to minimal crack reduction where it would lead to a much larger cost and weight to the bridge due to the extra concrete. The 25% increase in web width, would lead to an increase in the web width for a typical NDOT bridge from 12 inches to 15 inches. This increase of 3 inches would lead to a cost increase due to increase material and increased dead load.

Table 2-6: Results from increasing the web width.

	PS Curvatures, kip/ft.	Rein. Spacing, in.	M-B Concrete Stress, ksi	Max Web bulge, in.	M-B Crack Width, in.
C2 - 8.375W	19.12	NA	0.449	0.0136	0.0084
C2 - 10.5W	19.12	NA	0.449	0.0138	0.0061

Increasing the spacing between the ducts was the first priority as this allowed for more concrete to be present between the ducts which would in turn lead to an increase in tension capacity between the ducts. Increasing the spacing from the 0.70 inches spacing to 0.875 inches and 1.05 inches, in the scale model, would determine how much the increase spacing was effective. The 25% increase to 0.875 inch for the duct spacing, the stresses were not much lower when compared to 0.70 inch leading to an additional increase to 1.05 inch spacing between the ducts. As expected, the 50% increase in duct spacing led to lower stresses compared to both the 0.70 inch and 0.875 inch spacing. Table 2-7 provides the results comparing the increase in spacing between ducts. The concrete stress is comparable in between the middle and bottom ducts in the x-direction (transverse of the beam). The web bulge decreased with the increase in spacing was more apparent with the 1.05 inch duct spacing. The web bulge and crack between the middle and bottom ducts indicate a similar trend with decreasing with an increase in duct spacing.

Table 2-7: Results from increasing the spacing between the ducts.

	PS Curvatures, kip/ft.	Duct Spacing, in.	M-B Concrete Stress, ksi	Max Web bulge, in.	M-B Crack Width, in.
C2 - 0.7D	19.12	0.7	0.449	0.0136	0.0084
C2 - 0.875D	19.12	0.875	0.451	0.0081	0.0059
C2 - 1.05D	19.12	1.05	0.451	0.00192	0.0027

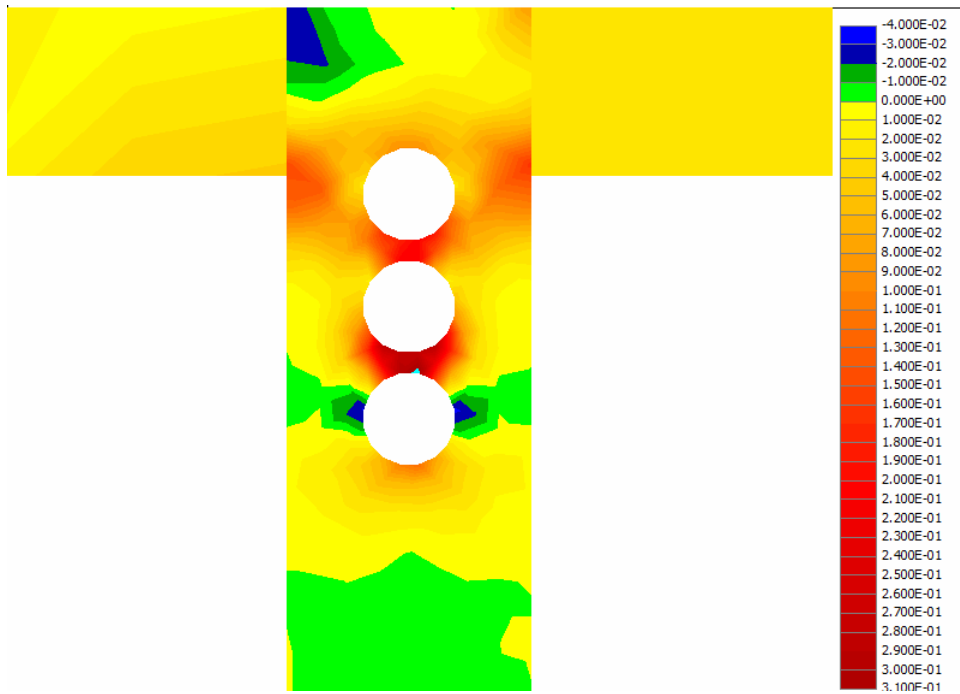


Figure 2-15: Principal stresses around ducts with 0.7" spacing (C2 loading).

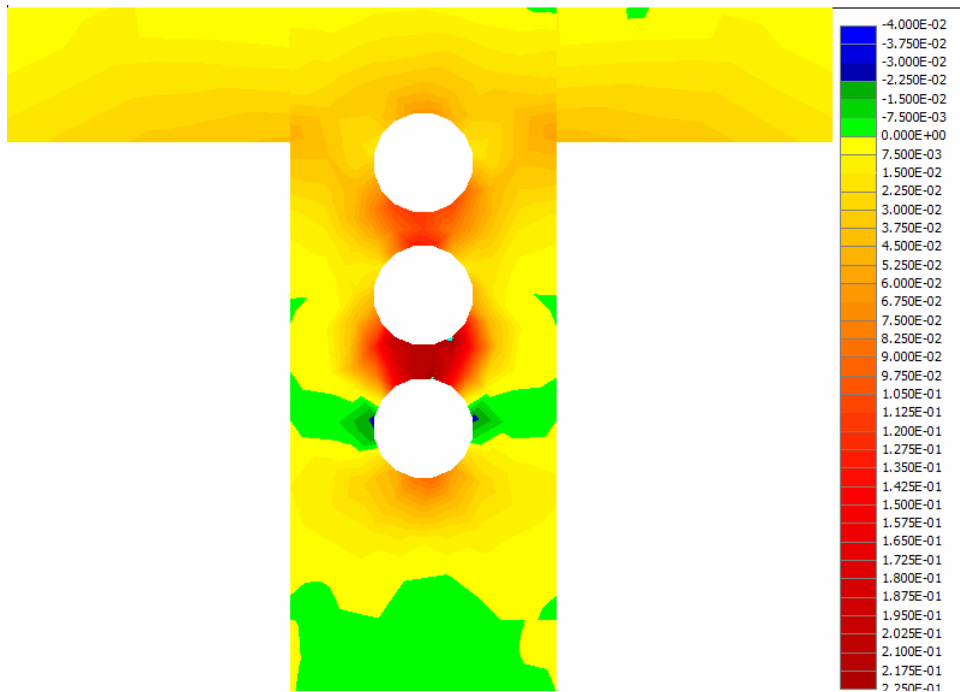


Figure 2-16: Principal stresses around ducts with 1.05" spacing (C2 loading).

Figure 2-15 and Figure 2-16 show the difference between the spacing increase between the ducts after 0.75 fpu and before air pressure was applied with the stresses overall being lower throughout the section, especially amid the ducts. The stresses between the middle and bottom ducts for 0.7 inch spacing was 0.370 ksi and for 1.05 inch

spacing, the stress was 0.225 ksi. The duct spacing of 1.05 inches provided the largest performance increase, and therefore it was determined to use 1.05 inch spacing, a 50% increase, between the ducts for the experimental testing. 1.05 inch duct spacing was chosen over 0.875 inch spacing as this would be on the upper end of duct spacing and should provide a better understanding of how the performance varies with increasing the duct spacing.

The next parameter of interest was the inclusion of duct tie reinforcement. Duct tie reinforcement was necessary because of the poor tension capacity of concrete. Adding reinforcement between the ducts was included to carry the tension forces once the concrete cracks and to keep the crack size small between the ducts. Figure 2-17 provides the details of the duct tie reinforcement. The duct ties have one leg that is 90 degrees and the opposite leg is 135 degrees. Each duct tie is secured to the vertical shear reinforcement with one tie between each duct, one tie below the bottom duct at each spacing and one tie above the top duct. As the duct ties are secured to the vertical shear reinforcement, the spacing between the duct ties are determined based on the shear reinforcement.

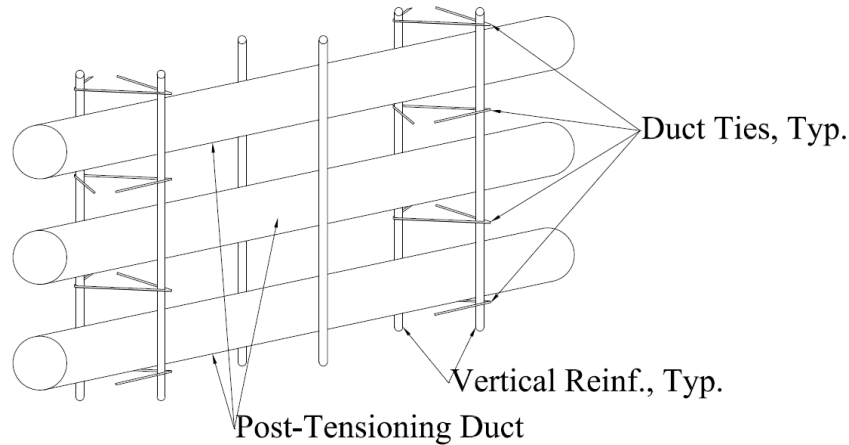


Figure 2-17 : Duct Tie Reinforcement Detail.

After NDOT had web cracking in a bridge, NDOT started including #4 rebar duct tie reinforcement at 24-inch spacing to ensure no cracking. Based on the NDOT spacing of 24 inches, an analysis was run in the scale model at 17.5 inch (#3 bar), which is equivalent to 25 inches in the real bridge. A 17.5 inch spacing of number #3 rebar was used because of the 3.5 inch shear reinforcement spacing with the reinforcement ratio being 0.556% for NDOT bridges and 0.623% for UNR designed bridges.

With the inclusion of reinforcement in concrete, the concrete can still crack but the cracks will seek out the reinforcement and the reinforcement will arrest the cracks from propagating. Therefore reinforcement spacing is an important parameter. As the previous beam had a duct tie spacing of 25 inches for full-scale, reducing the spacing and having the bars at a closer proximity was included in the Atena analysis. Decreasing the duct tie spacing for 0.7 scale from 17.5 inches down to 3.5 inches, leads to a full scale spacing of 5.0 inches. All of the duct tie spacings were chosen based on the shear reinforcement spacing which is spaced at 3.5 inches, discussed in section 2.2.1. The various duct tie reinforcement spacing are shown in Table 2-8. With the decrease in duct

tie reinforcement spacing, the stress in the duct ties, the web bulge and the crack width all decreased.

Table 2-8: Results from various duct tie reinforcement spacings.

	PS Curvatures, kip/ft.	Rein. Spacing, in.	M-B Concrete Stress, ksi	M-B 1.75OC Bar Stress, ksi	Max Web bulge, in.	M-B Crack Width, in.
C2 - 17.5R	19.12	17.5	0.448	20.2	0.000977	0.00108
C2 - 14.0R	19.12	14.0	0.450	14.1	0.000779	0.00802
C2 - 10.5R	19.12	10.5	0.451	13.4	0.000679	0.000678
C2 - 7.0R	19.12	7.0	0.451	13.1	0.000621	0.000456
C2 - 3.5R	19.12	3.5	0.450	10	0.000502	0.00013
C2	19.12	NA	0.449	NA	0.00192	0.0027

Based on the preliminary analysis using Atena 3D software, Round B laboratory beams were chosen. The fourth configuration (C4) had 1.05 inch spacing between ducts as opposed to previously used 0.7 inch spacing and no duct tie reinforcement. The fifth configuration (C5) was determined to have similar 1.05 inch spacing between ducts to C4 with the inclusion of duct tie reinforcement at a spacing of 17.5 inch on center. Lastly, the sixth configuration (C6) was to have the 1.05 inch spacing as well as the duct tie reinforcement but at a smaller spacing of 7.0 inches on center.

2.5 Round B Experimental Beams

Round B experimental beams consist of the final three configurations (C4, C5, and C6). The scope of Round B beams was to expand on the knowledge attained from Round A beams by altering the design parameters to improve upon the overall performance of the beams. For comparison purposes, Round B beams were designed with the same curvature as C2 since C2 was the intermediate prestress force and provided a reliable comparison beam. C1 and C3 curvatures were the extremes of design for NDOT with C2 being an average and the most common curvature. All three beams in Round B were designed with the same curvature matching that of C2.

2.5.1 C4 – Increased Duct Spacing

As stated previously, C4 has the same radius of curvature for the post-tensioning ducts as C2. The main difference between the two configurations is that C4 has an increased duct spacing compared to C2.

2.5.1.1 Design

C4 design is similar with all dimensions and all the reinforcement being equivalent to that of Round A beams. The modification comes into account with the spacing between the ducts at midspan. C4 increases the spacing between the ducts by 50% from 0.7 inches to 1.05 inches. As the tension capacity of concrete is low compared to the compression capacity, the increase in concrete between the ducts will increase the load capacity between the ducts. As the curvature is kept the same as C2, the ducts and

anchorages are only shifted to account for the additional spacing between the ducts. Figure 2-18 provides the design detail for C4 including the radii's associated with each duct layout.

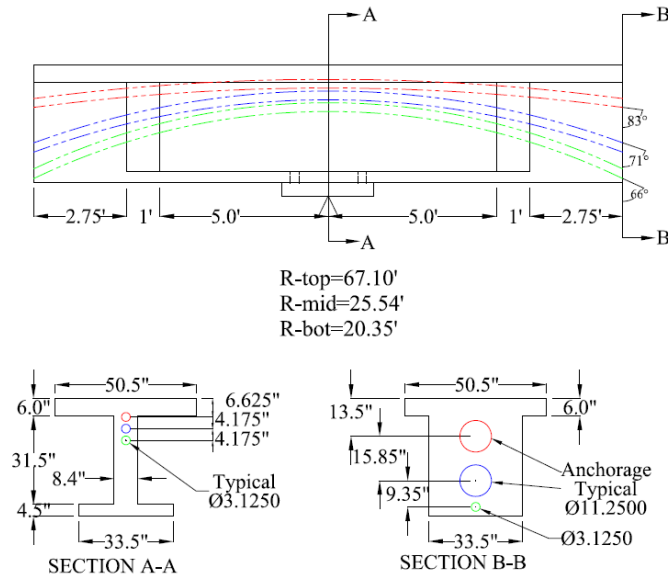


Figure 2-18: C4 design detail.

2.5.2 C5 – Increased Duct Spacing and 17.5” Duct Reinforcement

C5 is the first experimental beam that includes the duct tie reinforcement between the post-tensioning ducts. C5 curvature is the same as C2 and C4’s curvature to understand the effects of added duct ties.

2.5.2.1 Design

The design of C5 is the same as C4 with having the increased duct spacing of 1.05 inches between the ducts but duct tie reinforcement was added between the ducts. The duct ties were placed at a spacing of 17.5 inches which corresponds to the 3.5 inch spacing of the shear reinforcement. In NDOT’s bridges where duct tie reinforcement was included, the spacing of the duct ties were at 24 inches, upon scaling that by the specified 0.7, the spacing declines to 16.8 inches. As the location of the duct ties are limited to the location of the shear reinforcement, 16.8 inch spacing is between two shear reinforcement bars so the spacing was increased to match the shear reinforcement at 17.5 inches. This leads to an unscaled spacing of 25 inches as opposed to the NDOT 24 inches. The duct ties were rotated similarly to Figure 2-39 so the 135° would not be placed on the same bar directly next to each other.

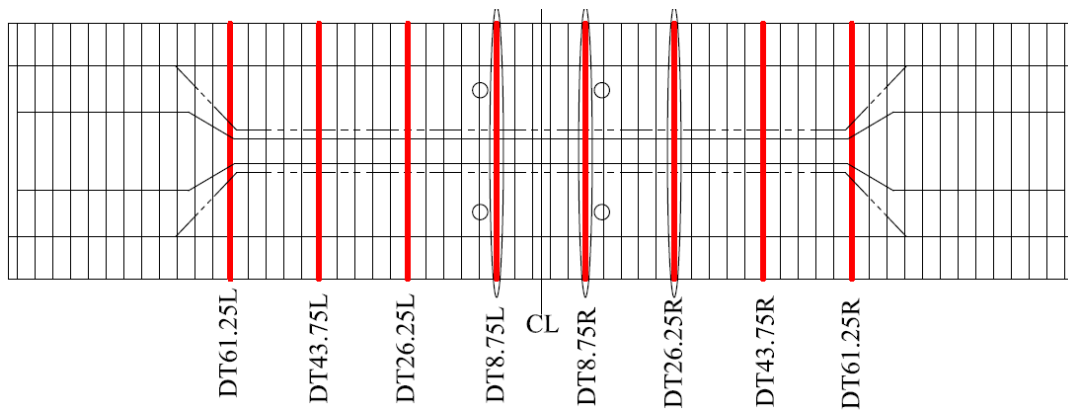


Figure 2-19: C5 duct tie reinforcement locations.

Figure 2-19 provides the location of the duct ties placed along the length of the beam at the 17.5 inch spacing. The red highlighted bars are the locations of the duct ties with having the ties not being located directly at midspan (CL) (the nearest point between ducts) but being offset on each side. As midspan (CL) is the closest point between the ducts, the concrete area is less. Figure 2-20 provides the design detail for C5.

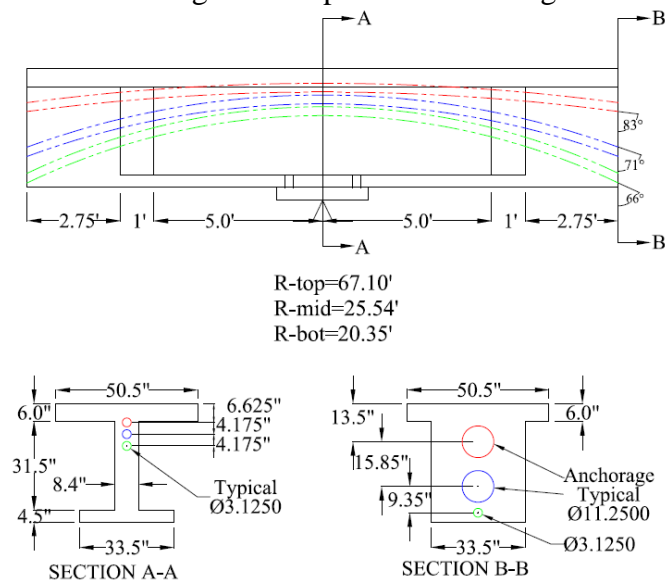


Figure 2-20: C5 design detail.

2.5.3 C6 – Increased Duct Spacing and 7.0” Duct Reinforcement

The final configuration is similar to C5 with the only difference being the duct tie reinforcement is at a closer spacing. The final beam, C6, is to determine how much of an affect the duct tie reinforcement spacing has on preventing the cracks to propagate.

2.5.3.1 Design

The overall design of C6 is the exact same as the previous five beams. The distinction of this beam compared with the others is the duct tie reinforcing bars being at a reduced spacing of 7.0 inches. Once the 7.0 inch spacing is equivalent to an unscaled

spacing of 10.0 inches. This spacing is under half of C5 spacing for the duct tie reinforcement. With the 7.0 inch spacing, the duct ties are installed every second shear bar as seen in Figure 2-21 with the locations being marked red for the duct tie locations.

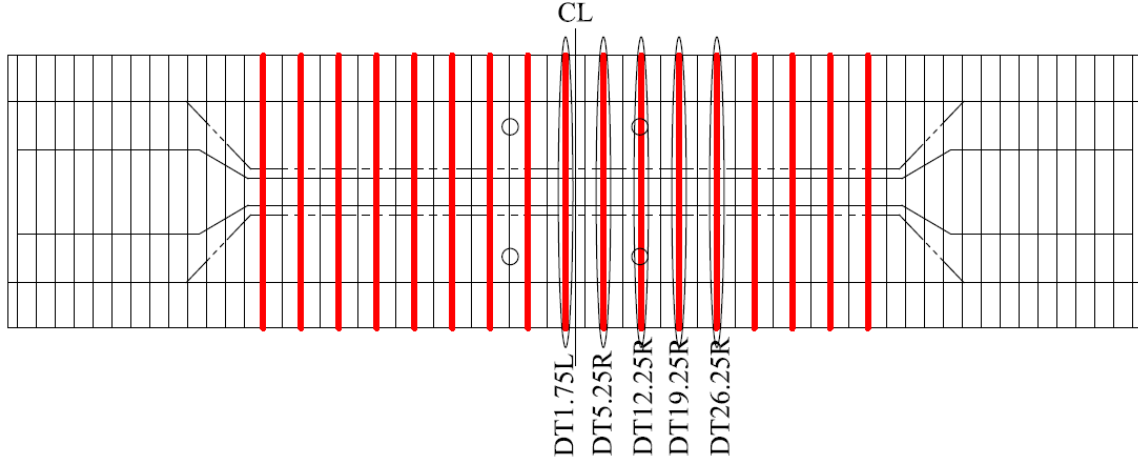


Figure 2-21: C6 duct tie reinforcement locations.

Figure 2-22 provides the overall design of C6 with the radii's listed along with the various sections of the beam.

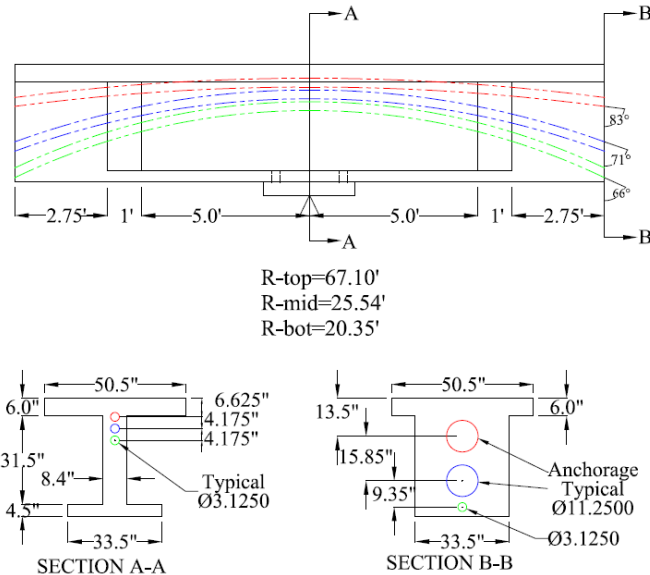


Figure 2-22: C6 design detail.

2.6 Instrumentation

Instrumentation for all six beams consisted of reinforcement strain gauges, embedded concrete strain gauges, concrete surface strain gauges, displacement transducers on the ends of the beams and displacement transducers on the web face to capture the web bulging. The full list of instrumentation for each beam is presented in Table 2-9.

Table 2-9: Instrumentation list for all 6 beams.

Instrument	No. Used					
	C1	C2	C3	C4	C5	C6
Reinforcement strain gauge	6	6	6	6	6	6
Embedded concrete strain gauge	6	6	6	15	15	15
Surface concrete strain gauge	3	3	14	14	14	14
PT Jack pressure transducer	1	1	1	1	1	1
DL pressure transducer	1	1	1	1	1	1
Displacement transducer	2	2	2	2	2	2
Air pressure transducers	-	2	2	2	2	2
Web bulging gauges	-	-	6	6	6	6
Duct tie reinforcement strain gauges	-	-	-	-	12	20
<i>Total</i>	19	21	38	47	59	67

2.6.1 Reinforcement Strain Gauges

There were a total of 6 reinforcement strain gauges placed in two locations along the beam. Three strain gauges were placed at 6 inches off center to the right and another three strain gauges at 6 inches off center to the opposite side. The strain gauges were placed on the shear reinforcement at 3 different heights along the same shear bar. Heights were matched up with the location of the ducts and were symmetric between both sides of center. In Figure 2-23 the locations of the reinforcement strain gauges can be seen and the labels for each strain gauge are provided in Figure 2-24 with: S6 (L, R) (T, M, B) with the S representing steel; 6 being six inches off-center; L and R being for left and right of center; T, M, and B being the top, middle and bottom gauges.

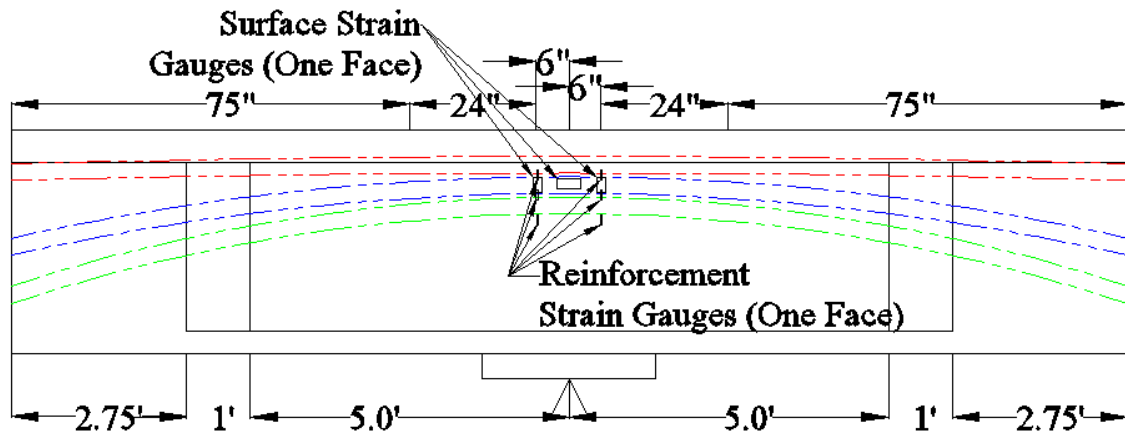


Figure 2-23: Reinforcement and concrete surface strain gauge locations.

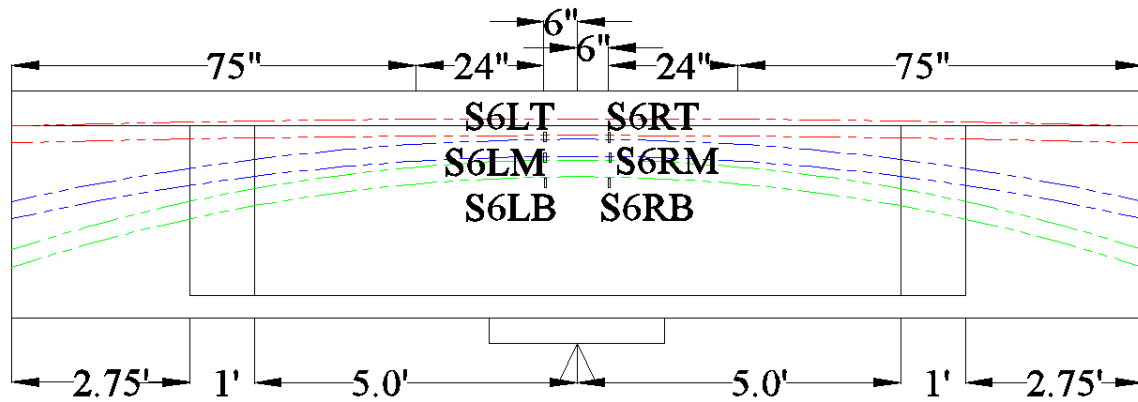


Figure 2-24: Reinforcement strain gauge locations and labels.



Figure 2-25: Shear reinforcement strain gauges installed on beam.

C5 and C6 had additional reinforcement strain gauges that were placed on the duct tie reinforcement bars. The reinforcement strain gauges on the duct tie reinforcement was used to determine the stress the duct ties were undergoing during the loading. The strain gauges were installed at three locations along the beam at all four heights (Figure 2-39) for a total of 12 duct tie reinforcement strain gauges for C5 as shown in Figure 2-19. The duct ties were determined to be gauged on the closest duct ties to the center of the beam as well as the preceding duct tie location on one side. The strain gauges were attached in the center of the bar once an area was ground clean following with a waterproofing agent to ensure an effective gauge during testing. Figure 2-26 shows the duct ties before the strain gauges were affixed and once the duct ties are installed in the beams with a strain gauge attached.



a) Strain gauge installation.

b) Placement between the ducts.

Figure 2-26: Duct tie reinforcement bar strain gauges installed.

With the decrease in duct tie reinforcement spacing for C6, the strain gauges affixed on the duct ties increased to record the same location off-center at 25.75 inches. Figure 2-21 provides the locations of each duct tie strain gauge highlighted by the oval surrounding the corresponding duct ties. The duct tie strain gauges started with instrumenting the duct ties on each side of centerline of the beam and expanding to one side of the beam until 25.75 inches from centerline was reached which corresponds to the duct tie strain gauges for C5 as seen in Figure 2-19.

2.6.2 Embedded Concrete Strain Gauges

The embedded concrete strain gauges were used in between the ducts to capture the strain in the concrete. The embedded concrete gauges were shaped similar to that of a dumbbell (see Figure 2-27) so that when the concrete was undergoing compression or tension, it would pull on the end plates of the dumbbell shaped gauge while the gauge captures the behavior.



Figure 2-27: Embedded concrete strain gauge.

A total of 6 embedded concrete strain gauges were used along the beam for C1, C2 and C3. The number of embedded concrete strain gauges increased for round B beams to a total of 15. The increase is to capture more data along the length of the beam around the ducts. The most important area of consideration, where the ducts are closest at the midspan of the beam, included embedded strain gauges in between the top and middle

duct, between the middle and bottom duct and 0.5 inches below the bottom duct. In addition to 3 embedded gauges being at the center of the beam length, 3 more embedded gauges were used at 30 inches off-center to one side in the same location in respect to the ducts for C1, C2 and C3 as shown in Figure 2-28. The number of embedded concrete gauges was increased for C4, C5 and C6; they included gauges at 15 inches to each side of center plus the centerline gauge and 30 inches to each side that were in C1, C2 and C3.

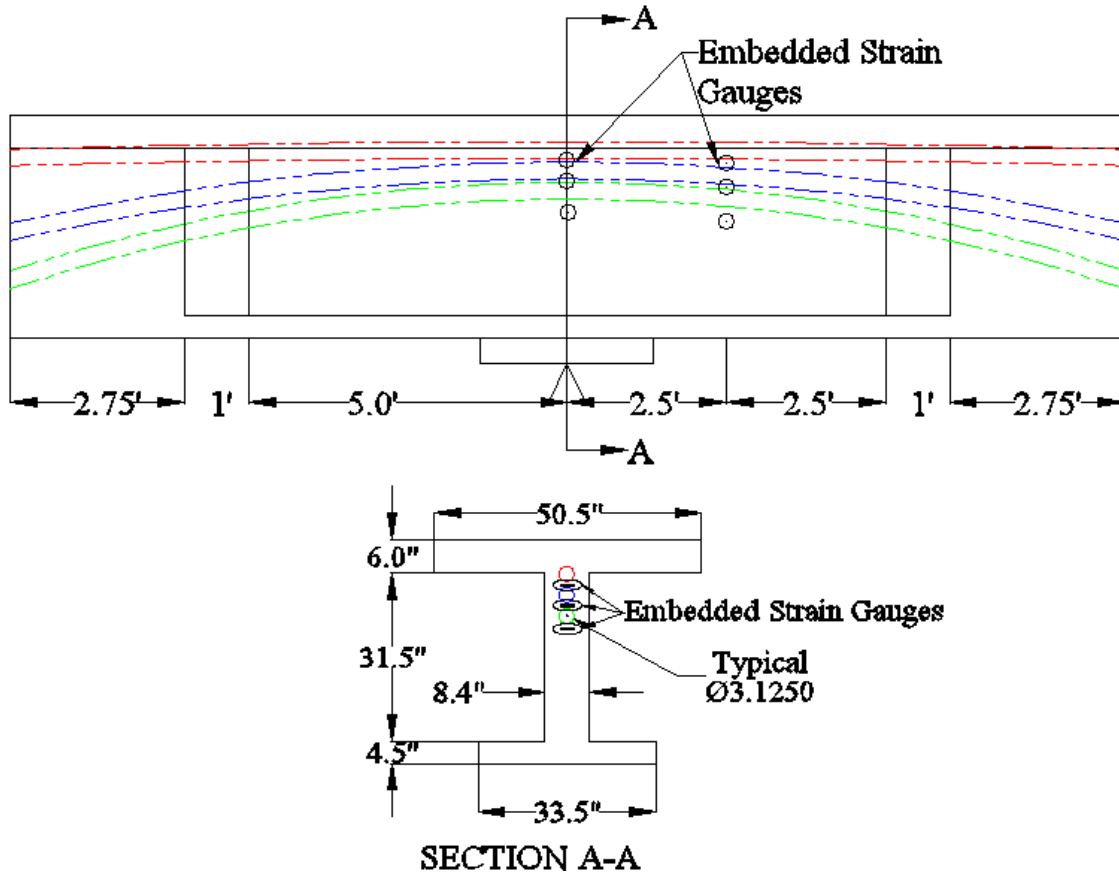


Figure 2-28: Round A embedded concrete strain gauge locations.

The location of the gauges that were not located in the center of the beam were chosen because the reaction block was acting as the column (discussed in Section 2.2.2) had a total width of 4 feet being centered on the beam leading to the reaction block reaching 24 inches off-center. With the gauges being located at 30 inches off-center, the gauges are reaching outside of the column support which can help understand how much the cracks extended outside of the column supported area. Figure 2-29 shows the embedded concrete strain gauges installed around the ducts.



a) Strain gauges tied to shear reinforcement. b) Strain gauges around ducts.
Figure 2-29: Embedded concrete strain gauges installed between ducts.

The embedded concrete strain gauge labels are as follows: C (0, 15, 30) (T, M, B) (L, R) where C stands for embedded concrete; 0, 15 and 30 are for the location off-center; T, M, and B are for the top, middle or bottom gauge; L and R for left and right if applicable. Figure 2-30 shows the locations and associated labels for Round A beams and Figure 2-31 for Round B beams.

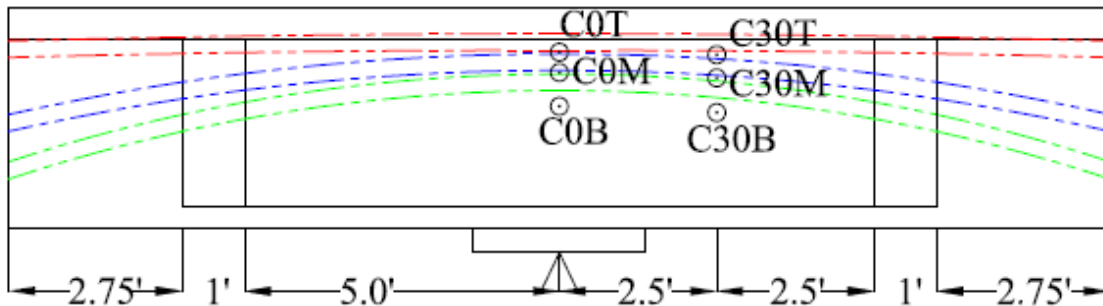


Figure 2-30: Round A embedded concrete strain gauge locations and labels.

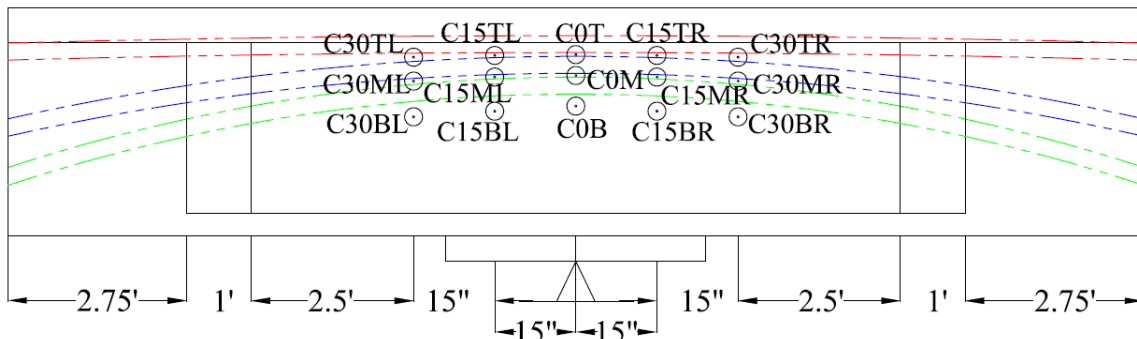


Figure 2-31: Round B embedded concrete strain gauge locations and labels.

2.6.3 Concrete Surface Strain Gauges

The concrete surface strain gauges were used on one web face of the beam. There were a total of 3 surface gauges for C1 and C2, one gauge being at the center of the beam and in the location of the middle duct whereas the following two gauges were at the same

height but place at 6 inches off-center. The two outside gauges were placed vertically and the center gauge was placed horizontally as seen in Figure 2-32. The amount of surface strain gauges increased for beams C3, C4, C5 and C6 to a total of fourteen, seven per side and all placed vertically. The increase in surface strain gauges was to have a better understanding of the distribution of strains in the section.

The concrete surface strain gauges are named as follows: SGS (L, C, R) with SGS being strain gauge surface and L, C, and R standing for left, center and right. Figure 2-32 shows the naming principle in accordance with the location of the gauge for C1 and C2. Figure 2-33 shows the concrete surface strain gauges installed on the web face.

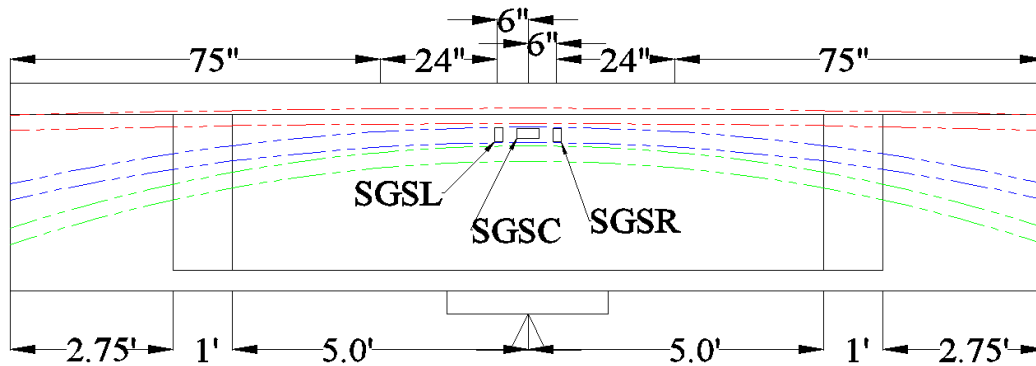
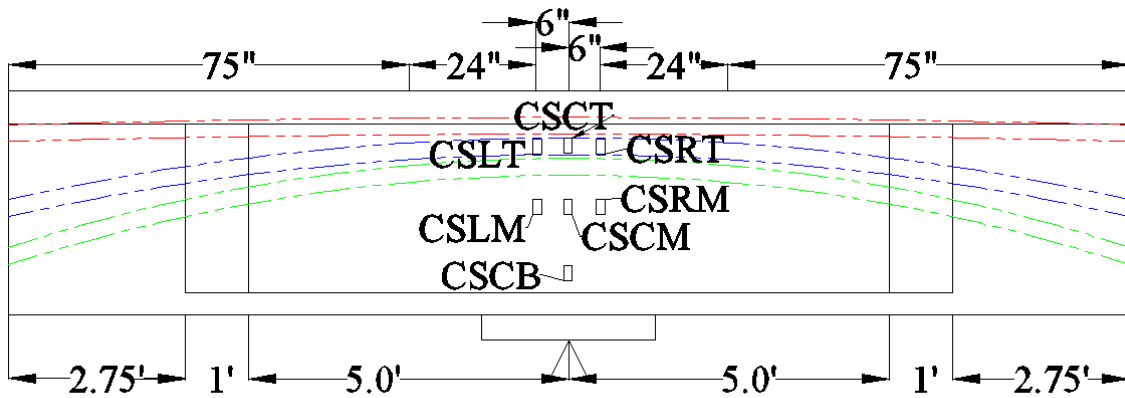


Figure 2-32: C1 and C2 concrete surface strain gauge locations and labels.



Figure 2-33: Concrete surface strain gauges installed on web face.

Figure 2-34 shows the locations of the concrete surface strain gauges relative to the steel ducts for C3, C4, C5 and C6. The naming convention is as follows: CS (L, C, R) (T, M, B) (E, W) where CS stands for concrete surface; L, C, and R are for the location of left, center and right; T, M and B for top, middle, bottom and E, W being for the east and west facing webs of the beam.



*E or W at end donates East and West facing web

Figure 2-34: C3, C4, C5 and C6 concrete strain gauge location and labels.

2.6.4 Displacement Transducers

Displacement transducers were used on the ends of the beams to measure the displacement induced by the post-tensioning and the vertical dead load that was applied. The transducers were capturing the vertical displacement at the beam ends that would be caused by the post-tensioning and to ensure the beam was symmetric between the ends.

For C3, C4, C5 and C6, displacement transducers were added to measure the deformation in the web. The displacement transducers were placed at midspan of the beam at three different heights along the face of both sides of the web. The gauges were placed at the halfway mark of the web, 75% of the height from the top face of the bottom flange and 87.5% of the height from the top face of the bottom flange, shown in Figure 2-35. Capturing how much the web was bulging during the various loading steps was necessary to determine the effect each loading step had on the overall performance of the beam. Figure 2-35 is an example of the web bulging test setup with each displacement transducer along the height of the web. Along with the web bulging gauges, the seven concrete surface gauges can also be seen on the web face.

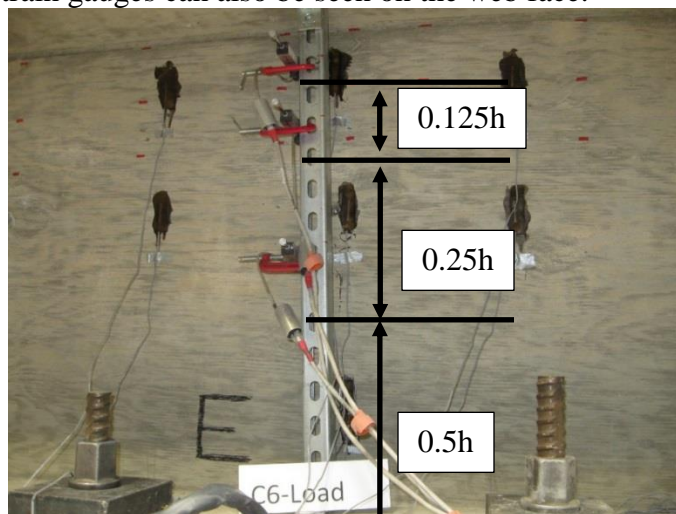


Figure 2-35: Example of the web bulging and concrete surface gauges.

2.6.5 Pressure Transducers

With the experimental beam only being the negative curvature region over a column, the dead load associated with the rest of the bridge that is not being tested needs to be taken into account and was discussed in Section 2.2.1. A pressure transducer was used to capture the applied dead load to the ends of the beam. To capture the post-tensioning jacking force, a pressure transducer was used in line of the hydraulic pump and the jack to capture the corresponding pressure to transform it into an applied force based on jack calibration sheets.

2.7 Construction

Construction of the beam started out with forming one side of the web of the beam. Once one side of the web was positioned, the reinforcement mat for the bottom flange was able to be put in place. Following the bottom mat, one side of the shear reinforcement and web longitudinal reinforcement were able to be placed at the appropriate spacing. After placing the shear reinforcement, the post-tensioning anchorages were able to be placed at the precise heights at the ends of the beams and the steel ducts for post-tensioned were able to be bent to the specified radius for all three ducts.



Figure 2-36: One side of forms and shear reinforcement during construction.

Various techniques were used in bending of the ducts including bending it while putting it in the beam and checking a calculated height per location to bending the ducts before placing them and checking the height. Through many attempts, it was determined that bending the ducts while out of the beam was the most efficient and provided the ducts with the least amount of damage. During the placement of the ducts in the beam, the ducts were tied off to the shear reinforcement that was in place to ensure the ducts kept the specified curvature. Since the ducts were tied to only one face of the shear reinforcement, the ducts were off-center by approximately 15/16 inch.

As the ducts were positioned, special care was taken into the spacing of the ducts at midspan where the ducts would be the closest to each other and keeping the specified 0.7 inch spacing between the ducts. The next step was to add the second face of the shear and web longitudinal reinforcement. After both sides of the shear reinforcement was added, strain gauges were able to be installed. The opposing side of the web form was placed after the web was measured correctly at 8.375 inches. To finish up the construction process, the reinforcement mat for the top flange area was placed.



a) Technique used to bend steel ducts. b) Steel ducts placed in the beam.

Figure 2-37: Installation of post-tensioning steel ducts.



a) All shear reinforcement installed. b) All forms and reinforcement installed.

Figure 2-38: Progression of construction.

After all of the reinforcement, forms, and the internal strain gauges were in place, the next task was to place the concrete. The concrete placement included a concrete vibrator and a vibrator hammer used on the outside of the wood forms on the web to get good consolidation around the ducts with minimal spacing between the ducts. A slump test was performed (ASTM International, 2012) on the concrete to determine the workability of the concrete and shown in

Table 2-10. Concrete cylinders (6"x12") were made for both compression cylinders and split-cylinder tests as noted in section 2.8.1.

Table 2-10: Slump test results.

	Slump, in
C1&C2	2.25
C3	3.5
C4&C5	2.625
C6	2.5

Reinforcement duct ties were designed and placed for C5 and C6. NDOT started using the duct tie reinforcement subsequently to web cracking failure in a bridge to ensure cracking wasn't present, the design of the duct ties were similar to that of NDOT's design. The design of the duct tie reinforcement consisted of one end having a 135° hook and the opposing end having a 90° hook for ease of construction. The duct tie reinforcement was connected around the shear reinforcement while altering the direction of the hooked ends as seen in Figure 2-39.

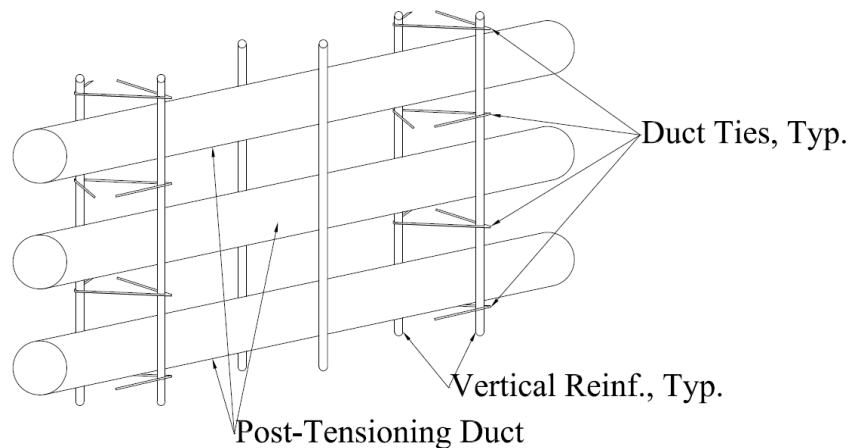


Figure 2-39: Duct tie reinforcement detail with the direction of ties altered.

Attaching the duct tie reinforcement occurred after the ducts were placed and the second side of the shear reinforcement was attached. The duct ties were placed according to the design of both C5 and C6 and following the placement of reinforcement strain gauges on applicable bars discussed in ensuing sections.



Figure 2-40: Duct tie reinforcement bars installed in the beam.

Figure 2-40 shows the duct tie reinforcement bars installed in the beam and the switching of the hooked ends. The duct ties were positioned to be as close to the center between the ducts as possible unless longitudinal reinforcement interfered.

2.8 Materials

2.8.1 Conventional Concrete

With the design being modeled after NDOT bridges, similar concrete properties were also chosen for the laboratory experiments. With NDOT using normal strength concrete in the majority of the bridges, normal strength concrete was also used in the scaled models. For each round of casting (Round A and B), 3 cylinders were compression tested at 7, 14, and 28 days after casting and on the day of the test. Three cylinders were split-cylinder tested on the 28th day and on the day of the test. The specifics for the compression cylinder tests and the split-cylinder tests can be found in Table 2-11. Standard ASTM practice was used for both compression and split-cylinder tests. As the beams were large-scale, two concrete trucks were used with the first truck being used for the first two beams being casted and the second truck being used on the third beam casted for the day.

Table 2-11: Concrete Cylinder Test Averages.

Round A				Round B			
Day		Comp., psi	Tensile, psi	Day		Comp., psi	Tensile, psi
7	C1&C2	2979	-	7	C4&C5	3850	-
	C3	2678	-		C6	4009	-
14	C1&C2	3480	-	14	C4&C5	4368	-
	C3	3609	-		C6	4525	-
28	C1&C2	4111	311.6	28	C4&C5	5581	414.7
	C3	3893	355.6		C6	5615	394
93 - C1 Test		6039	448.8	28 - C4 Test		5451	405.3
101 - C2 Test		5957	449.5	35 - C5 Test		5275	401.6
112 - C3 Test		5852	476.8	43 - C6 Test		6020	433.3

Round A beams were tested at a much later date after concrete casting compared with Round B beams. The large variation is due to schedule availability of the large scale laboratory for both rounds of testing. ASTM C39 – Standard Test Method for Compressive Strength of Cylindrical Concrete Specimens (2014a) was used for the compression strength. ASTM C496 – Standard Test Method for Splitting Tensile Strength of Cylindrical Concrete Specimens (2011) was followed for the tensile strength.

2.8.2 Reinforcing Steel

The reinforcing steel is standard grade A706 60 ksi yield strength. Standard reinforcing steel is commonly used in NDOT bridges and the results from tension tests for the bars are listed on Table 2-12. The tension tests followed ASTM A370 – Standard Test Methods and Definitions for Mechanical Testing of Steel Products (2014).

Table 2-12: Reinforcement Strengths.

Bar Size	Yield, ksi	Ultimate Stress, ksi	Yield Strain
3	68.2	100.5	0.00225
4	68.0	92.9	0.00234
5	67.1	99.5	0.00231

The stress and strain curves for all three bars are shown in Figure 2-41. All three bars have a similar yield point and ultimate stress with the #4 bar being lowest.

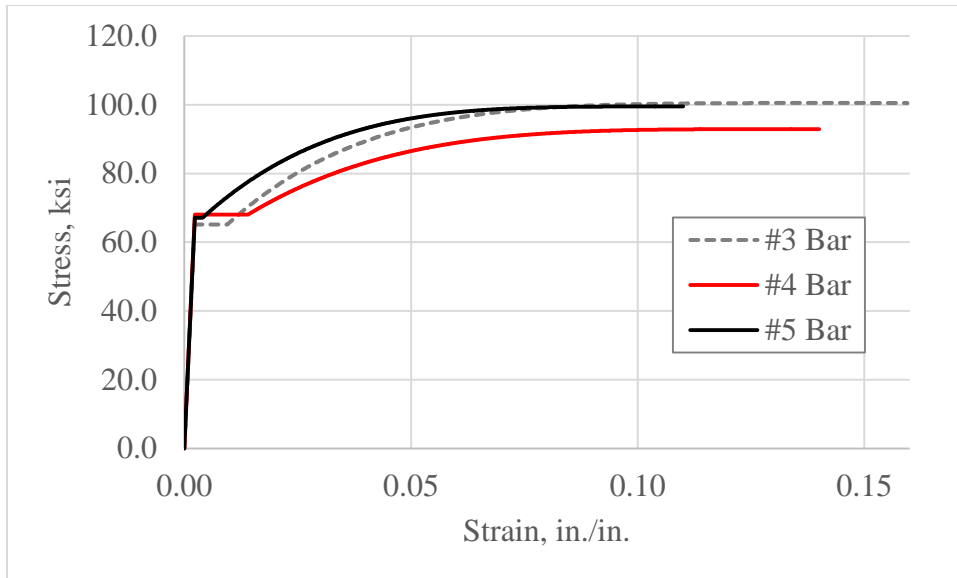


Figure 2-41: Stress-strain curve for conventional reinforcement bars.

2.8.3 Prestressing Steel

The prestressing steel that was used in the experimental beams was the same strength that is commonly used in NDOT bridges, 0.6" diameter seven-wire 270 ksi prestressing low-relax strand. The material properties of the prestressing strand was not needed for the experimental data and modeling so no material tests were completed.

3.0 Experimental Beam Results

3.1 Introduction

The results for each beam described in Chapter 2 are detailed in the following sections. The results are divided into the performance of each individual beam. Each beam has the results from the various instrumentation used as well as the outcome of cutting the beams in half after the experiment was concluded. The beams were cut in half, in the transverse direction, to understand how the stressing and air pressure impacted cracking within the beam.

3.2 Round A Experimental Beams

3.2.1 Configuration 1

3.2.1.1 Embedded Concrete Strain Gauges

C1 beam was the smallest tendon curvature of C1, C2 and C3 with a spacing between the ducts of 0.7 inch (1.0 inch in the full scale). With the instrumentation described in Chapter 2, the embedded concrete strain gauges placed between the post-tensioning ducts proved to be the most valuable gauges used in C1 beam. The embedded concrete strain gauges versus the prestress load on the beam for C1 are provided in Figure 3-1. The y-axis of the figure shows the loading on the beam notated as:

$$\frac{P_{\text{applied}}}{0.75P_{\text{GUTS}}} \quad (3-1)$$

With:

P_{applied} = total applied load to the beam including both top and middle post-tensioning.

Such as: $[(0.15f_{\text{pu}_{\text{middle}}}+0.15f_{\text{pu}_{\text{top}}})A_{\text{ps}}$ or $(0.75f_{\text{pu}_{\text{middle}}}+0.45f_{\text{pu}_{\text{top}}})A_{\text{ps}}$

P_{GUTS} = Guaranteed Ultimate Tensile Strength of both the top and middle ducts.

$[(0.75f_{\text{pu}_{\text{middle}}}+0.75f_{\text{pu}_{\text{top}}})A_{\text{ps}}]$ where A_{ps} is based on nine 0.6" tendons per duct.

Therefore when 0.75fpu is applied on both top and middle ducts this corresponds to a value of 1.0 on the y-axis.

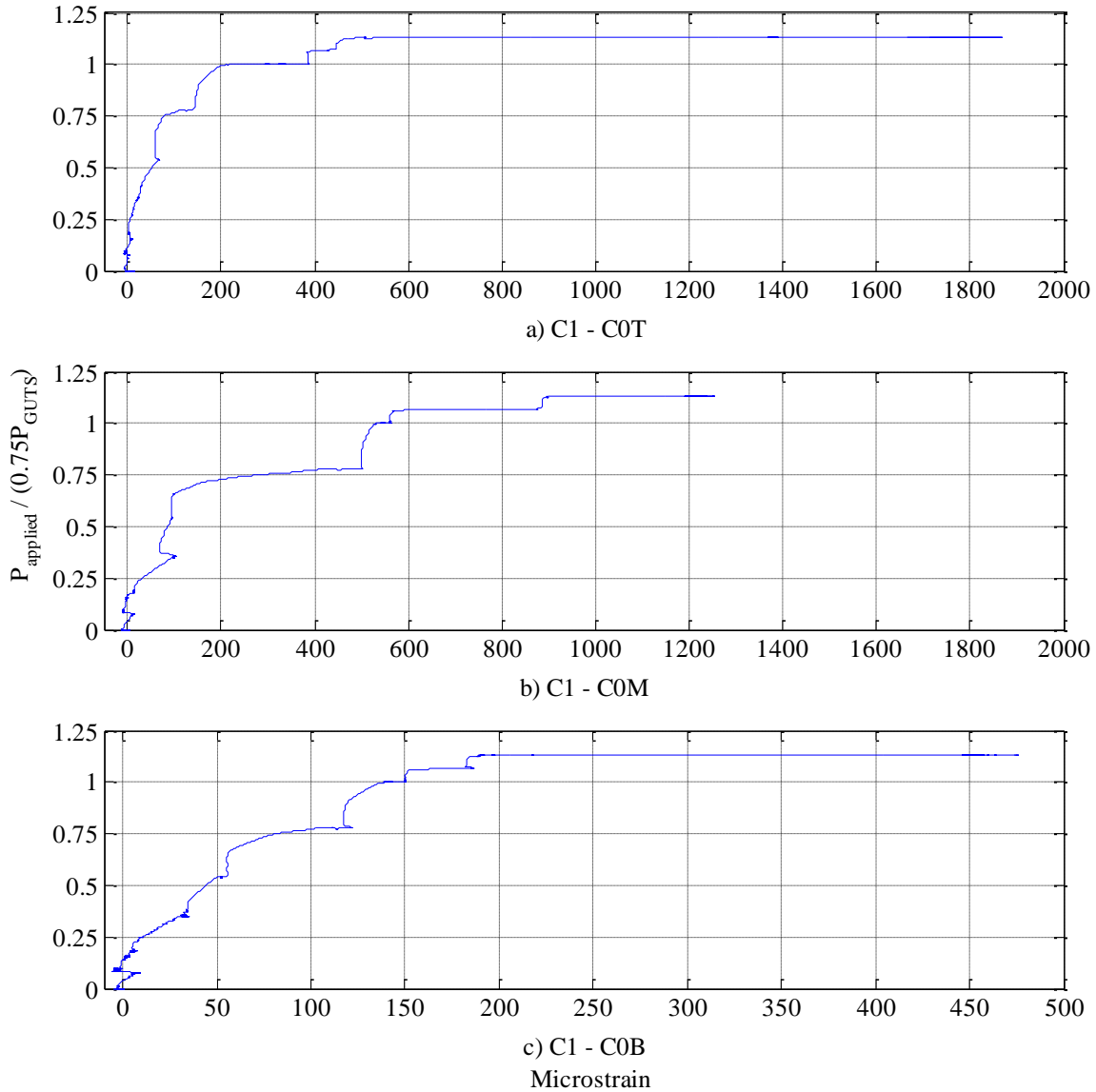


Figure 3-1: C1 embedded concrete strain at centerline.

In Figure 3-1, the loading steps outlined in Section 2.2.3 can be seen with stressing starting with the middle duct and then moving to the top duct for 0.15fpu, 0.45fpu, 0.75fpu, 0.85fpu and the air pressures. As noted previously, 1.0 on the y-axis represents 0.75fpu in the top and middle ducts. Anything less than 1.0 will be all the prestressing leading up to 0.75fpu for both top and middle ducts. At the 1.0 and 1.13 marks, the strain starts growing, as denoted by the horizontal flat lines. This can be attributed to air pressure growing, as denoted by the horizontal flat lines. This can be attributed to air pressure testing of the ducts after the stressing at 0.75fpu and 0.85fpu. Air pressure consisted of 50, 75, 100 and 125psi in the middle duct and then in the top ducts.

The values for each loading stage including all the post-tensioning stressing values as well as the air pressure testing after stressing are outlined in Table 3-1 with each value being calculated in accordance with equation (3-1).

Table 3-1: Y-axis values for each loading stage.

	<u>P_{applied}</u> 0.75P_{GUTS}
0.15fpu_{middle}	0.1
0.15fpu_{middle}+0.15fpu_{top}	0.2
0.45fpu_{middle}+0.15fpu_{top}	0.4
0.45fpu_{middle}+0.45fpu_{top}	0.6
0.75fpu_{middle}+0.45fpu_{top}	0.8
0.75fpu_{middle}+0.75fpu_{top}	1.0
Air Pressure	1.0
0.85fpu_{middle}+0.75fpu_{top}	1.067
0.85fpu_{middle}+0.85fpu_{top}	1.133
Air Pressure	1.133

Figure 3-1 shows that the transverse strain between the ducts decreased when progressing down the height of the web from C0T to C0M and finally reaching C0B with the locations outlined in Section 2.6.2. Stressing up to 0.75fpu produced a larger strain in C0M, between the middle and bottom duct, than C0T and C0B.

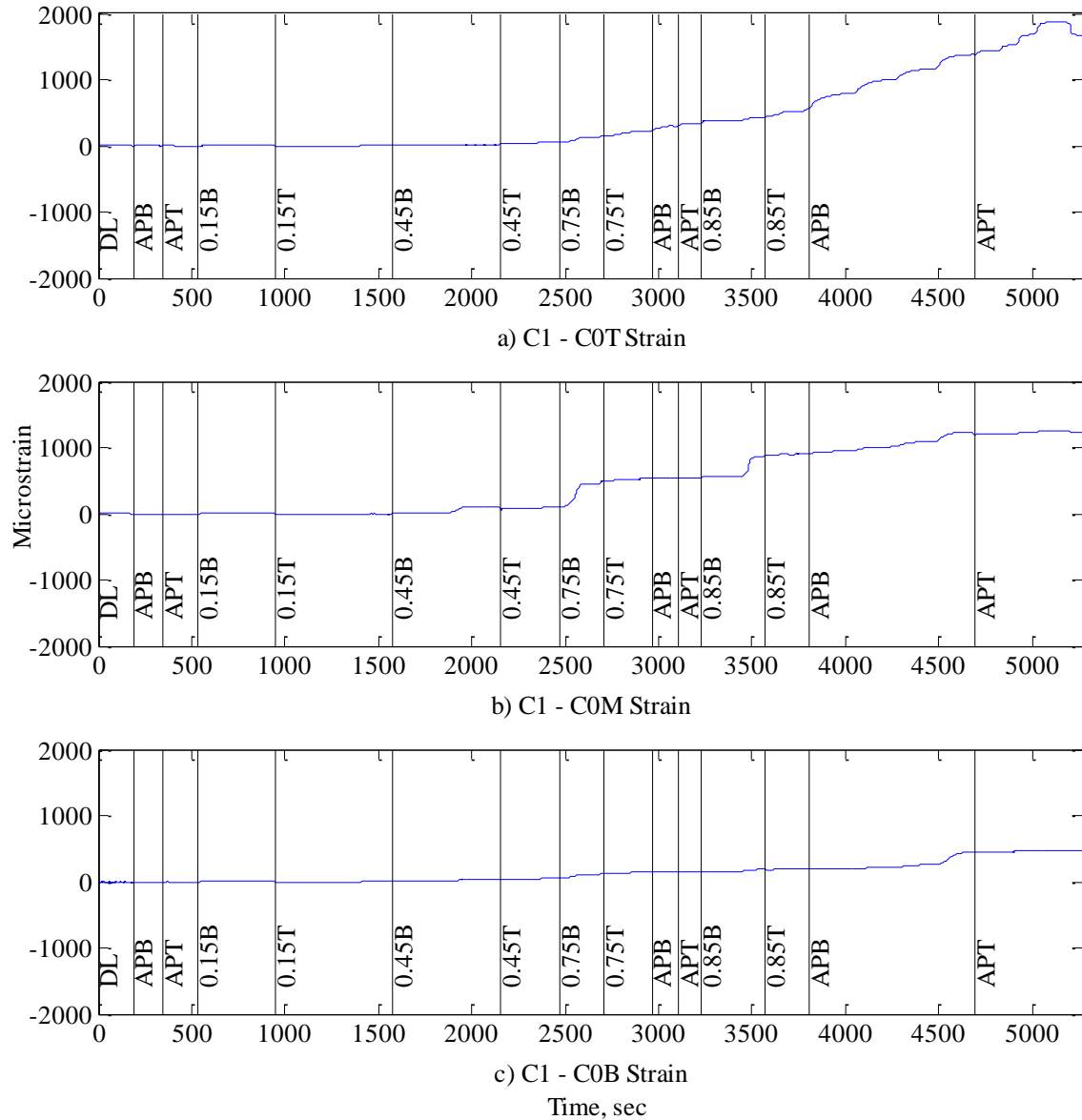


Figure 3-2: C1 embedded concrete strain versus time.

As the various air pressures are hard to differentiate on the loading-strain figures, Figure 3-2 shows the transverse concrete strain versus time where it is easier to determine if the air pressure accounts for the large strain values. The labels located in the figure identify each loading phase. Labels APB and APT represent Air Pressure Bottom tendon and Air Pressure Top tendon, respectively. Air pressure after 0.75fpu produces a large increase in strain compared to the post-tensioning. The air pressure after 0.85fpu shows an increase in concrete strain throughout the web. All of the air pressures (50, 75, 100, 125 psi) were all completed in one run without stopping between each air pressure.

For the embedded concrete strain gauges located at +30 inches from midspan (30 inches toward the stressing end), it can be observed from Figure 3-3 that the strain is drastically lower throughout the height of the web compared to the strain gauges directly at midspan with C0T at 1800 $\mu\epsilon$ versus C30T at 200 $\mu\epsilon$ versus C0M at 1250 $\mu\epsilon$ versus

C30M at 125 $\mu\epsilon$, and C0B at 475 $\mu\epsilon$ versus C30B at 75 $\mu\epsilon$. This is expected as there is a larger spacing between the ducts when extending from the midspan of the beam to the anchorage zones as seen in Figure 2-3. With an increased spacing between the ducts, there is an increase in concrete between the ducts therefore leading to a larger area of concrete to distribute the forces produced from the prestressing. The increase in concrete between the ducts leads to a larger concrete tension capacity. Locations of embedded concrete strain gauges can be seen in Figure 2-30.

Similar to the strain gauges located at the center of the beam, the concrete tension strain is largest in the C30T gauge (between top and middle ducts) at 200 $\mu\epsilon$ and decreases going down the web to C30M (between middle and bottom ducts) at 125 $\mu\epsilon$ and finally reaching C30B (below the bottom duct) 75 $\mu\epsilon$. Comparing Figure 3-1 to Figure 3-3, the gauges that are located at 30 inches from centerline have a significant reduction in strain produced during the air pressure phases when compared to midspan. The large horizontal line on gauge C30T can be attributed to the fact that it is an experimental setup and the gauges might not have perfect bond within the concrete. Also, during concrete casting the gauges could be shifted leading to the gauges being oriented in a different direction than intended even with careful consideration taken into fastening the gauges properly. Table 3-2 provides the values of the embedded concrete gauges in the center of the beam at the end of each loading stage. Air pressure of 50, 75, 100 and 125 psi were all completed during the same run with no break between air pressures.

Table 3-2: C1 embedded concrete strain at 0" O.C. at each load stage.

	C0T, $\mu\epsilon$	C0M, $\mu\epsilon$	C0B, $\mu\epsilon$	C30T, $\mu\epsilon$	C30M, $\mu\epsilon$	C30B, $\mu\epsilon$
APB-50psi	-6.5	-6.5	-6.5	-78.5	0.0	0.0
APT-50psi	6.5	-13.1	-6.5	-72.0	6.5	-6.5
DL	-13.1	-6.5	6.5	-19.6	13.1	6.5
0.15fpuB	6.5	13.1	13.1	0.0	19.6	6.5
0.15fpuT	6.5	-13.1	0.0	-19.6	6.5	6.5
0.45fpuB	39.2	98.1	19.6	-52.3	32.7	19.6
0.45fpuT	66.1	94.1	52.9	128.1	47.4	29.7
0.75fpuB	142.7	501.4	122.4	148.4	80.8	47.4
0.75fpuT	218.7	529.6	140.7	168.7	91.3	55.9
APB-50 to 125psi	294.0	540.7	142.0	165.5	87.3	54.6
APT-50 to125psi	323.5	545.3	142.0	165.5	87.3	57.2
0.85fpuB	428.3	873.4	187.9	178.6	107.0	66.4
0.85fpuT	555.4	900.9	192.4	181.8	107.0	71.6
APB-50 to125psi	1378.8	1204.0	445.2	183.8	83.4	69.0
APT-50 to125psi	1663.7	1229.6	474.0	183.2	82.1	67.7

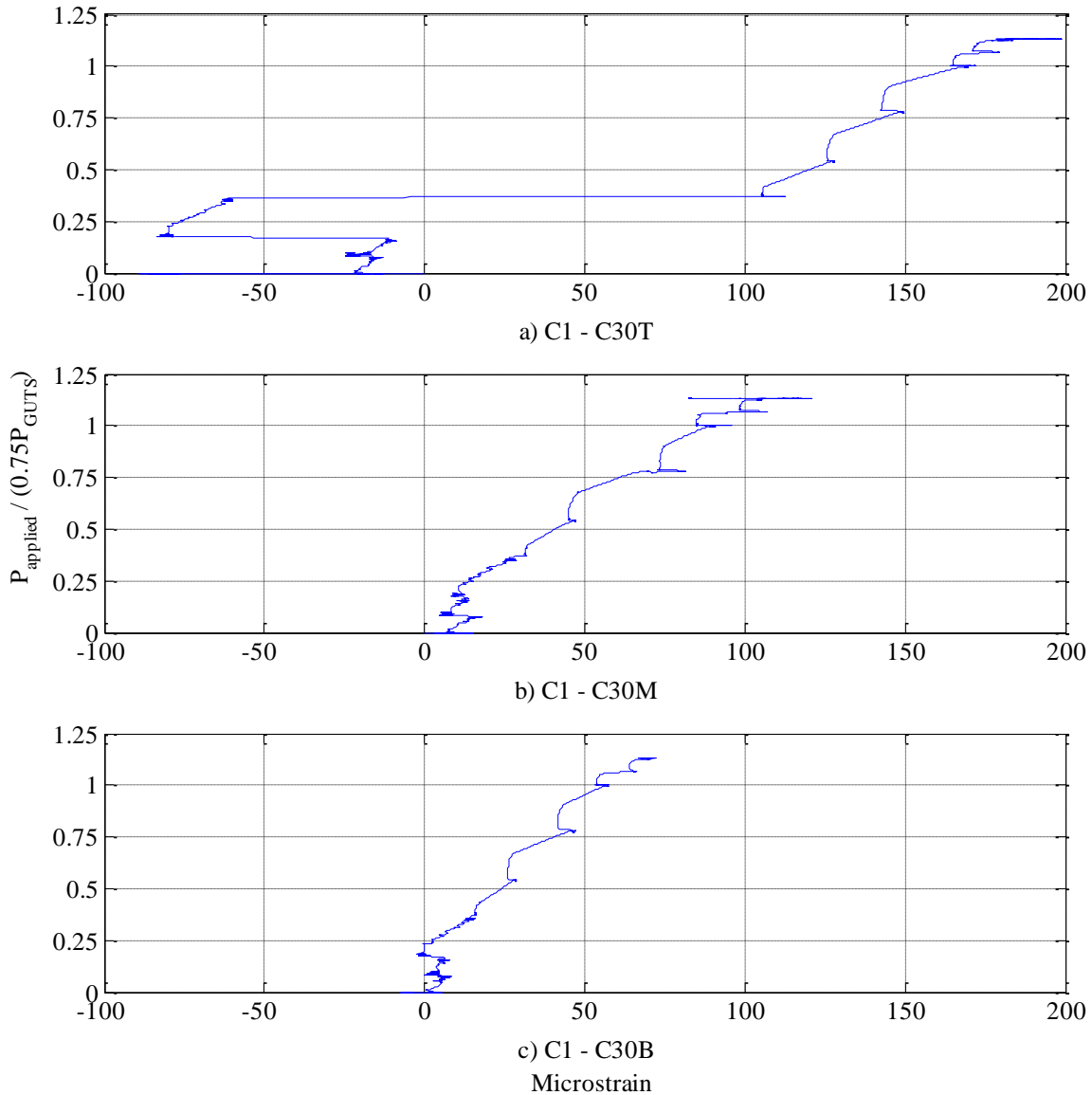


Figure 3-3: C1 embedded concrete strain at +30" from centerline.

3.2.1.2 Concrete Surface Strain Gauges

Figure 3-4 shows the values for the concrete surface strain gauges. The two outside gauges are vertical, and the center gauge is horizontal. Per the orientation of the gauges from Figure 2-32, it makes sense that the center surface strain gauge is in compression as the post-tensioning is putting the beam in compression in the longitudinal direction.

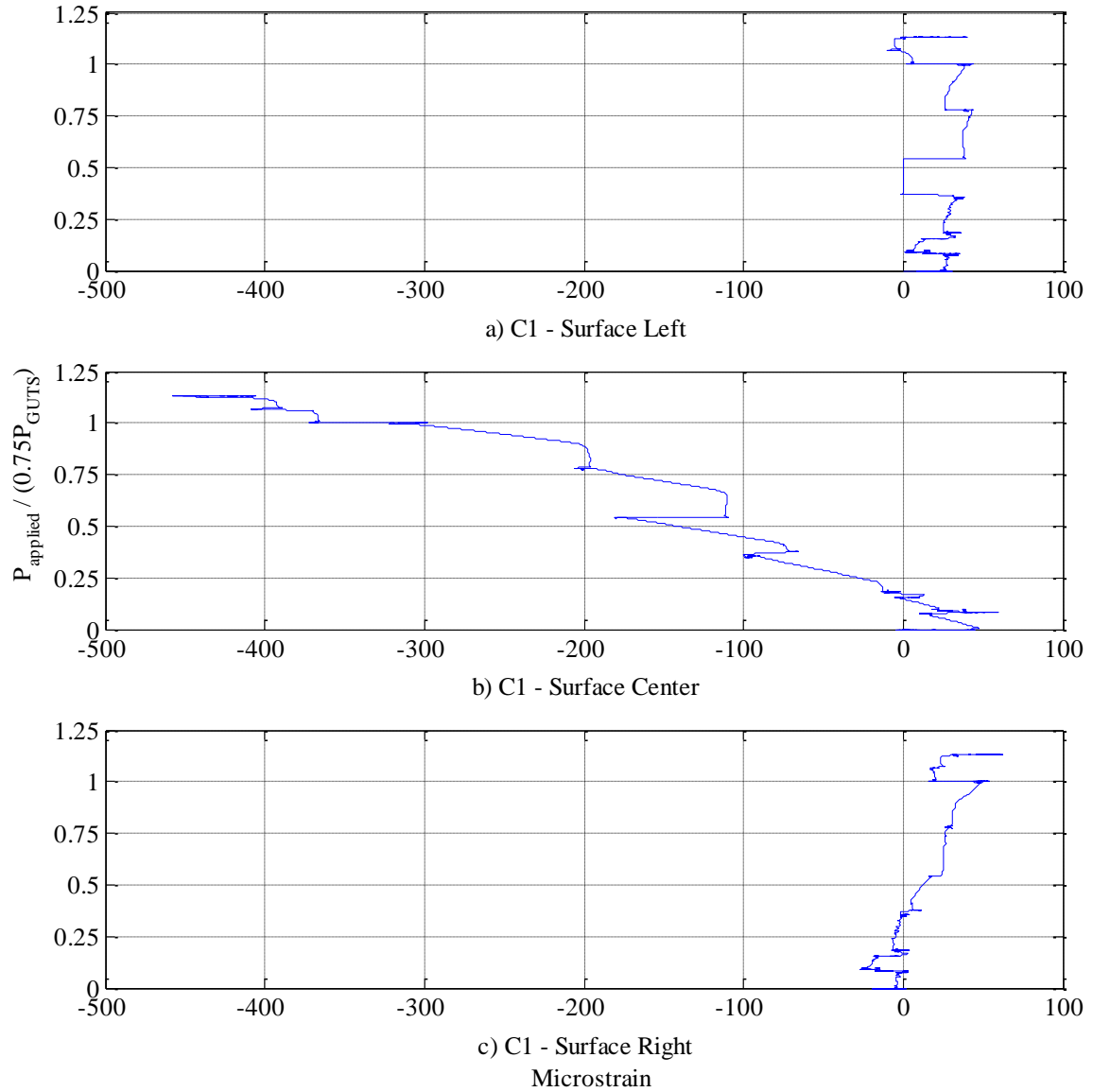


Figure 3-4: C1 concrete surface strain gauges.

Table 3-3 provides the values of the concrete surface strain gauges at the end of each loading stage. C1 beam did not have any cracks that transmitted to the surface of the web throughout the entire loading sequence including post-tensioning stressing as well as the air pressure after 0.75fpu and 0.85fpu. Figure 3-5 shows the web face upon completion of all loading events with no visible cracks present.

Table 3-3: C1 concrete surface gauges at each loading stage.

	SGSL, $\mu\epsilon$	SGSC, $\mu\epsilon$	SGSR, $\mu\epsilon$
APB-50psi	0.0	-6.5	-19.6
APT-50psi	19.6	13.1	-26.2
DL	32.7	52.3	13.1
0.15fpuB	26.2	19.6	0.0
0.15fpuT	32.7	13.1	-6.5
0.45fpuB	32.7	-111.2	0.0
0.45fpuT	0.0	-179.6	16.3
0.75fpuB	26.4	-205.2	25.4
0.75fpuT	40.8	-317.9	49.0
APB-50 to 125psi	34.3	-301.5	44.4
APT-50 to 125psi	37.6	-301.5	49.0
0.85fpuB	-7.6	-405.7	21.5
0.85fpuT	-0.4	-456.1	33.3
APB-50 to 125psi	10.0	-416.2	47.7
APT-50 to 125psi	28.4	-411.6	49.7



Figure 3-5: C1 web face after completion of all loading with no cracks.

3.2.1.3 Cross Sectional Cracks

Once the experimental testing was concluded, the beams were cut in half to determine how the cracking propagated throughout the cross section of the beam as well as understanding if consolidation was properly obtained. A large rotary saw was used on the upper flange and lowered as far into the web as possible and a concrete chainsaw was used to complete the cut as shown in Figure 3-6.



a) Cutting with a rotary saw.



b) Cutting with a concrete chainsaw.

Figure 3-6: Cutting the beam in half to look at cross section.

Inspection of the cross section once cutting was complete showed that only one minor crack appeared. The cut face of the beam can be seen in Figure 3-7 with the only one crack located between the top and middle duct with a width of 0.005 inches.



a) Cross section with minimal cracks.



b) Cross section with cracks drawn.

Figure 3-7: C1 cut beam cross section with no cracks.

3.2.1.4 Shear Reinforcement Strain Gauges

The results for the strain gauges attached to the shear reinforcement are outlined in Figure 3-8. All shown reinforcement strain gauges performed relatively similar with low microstrain values. The locations of the shear reinforcement strain gauges are shown in Figure 2-24.

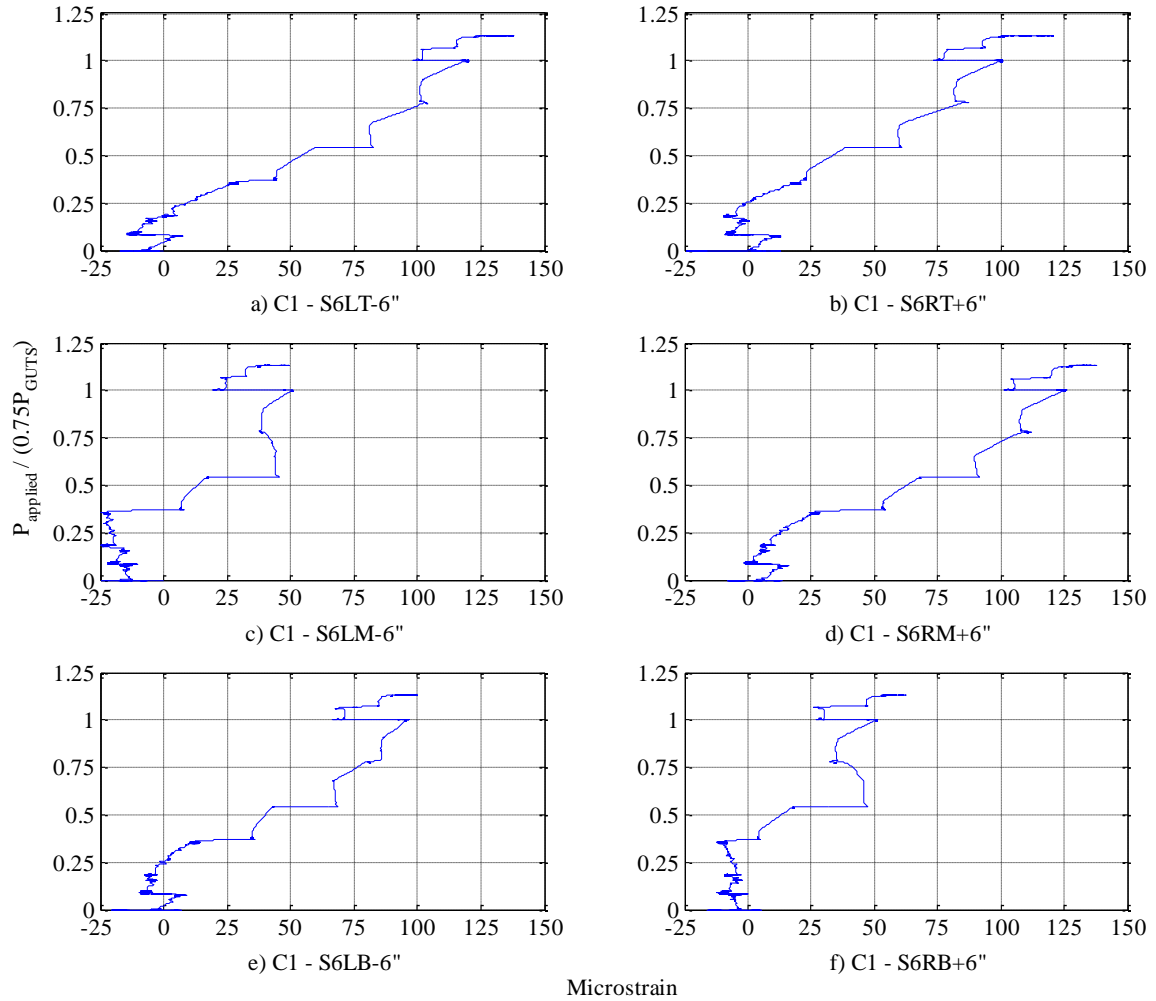


Figure 3-8: C1 shear reinforcement gauges.

Table 3-4 provides values for the shear reinforcement strain gauges at the end of each loading stage for all six gauges.

Table 3-4: C1 shear reinforcement gauges at each loading stage.

	S6LT, με	S6LM, με	S6LB, με	S6RT, με	S6RM, με	S6RB, με
APB-50psi	-6.5	-26.2	-19.6	-26.2	-6.5	-19.6
APT-50psi	-19.6	-32.7	-19.6	-13.1	6.5	-19.6
DL	-13.1	-6.5	0.0	6.5	13.1	0.0
0.15fpuB	0.0	-6.5	13.1	6.5	13.1	0.0
0.15fpuT	0.0	-13.1	-6.5	0.0	6.5	-6.5
0.45fpuB	26.2	-19.6	6.5	13.1	39.2	-13.1
0.45fpuT	60.4	17.8	43.4	37.7	68.0	19.0
0.75fpuB	103.0	38.1	82.7	86.9	111.9	32.8
0.75fpuT	120.1	50.6	95.8	100.6	125.0	50.5
APB-50:125psi	118.1	48.0	93.8	97.4	123.6	47.2
APT-50:125psi	118.8	47.3	93.8	98.0	124.3	48.5
0.85fpuB	115.5	25.0	75.5	94.1	119.1	26.9
0.85fpuT	125.3	40.1	89.9	103.3	128.9	56.4
APB-50:125psi	126.0	40.8	91.2	107.9	129.5	55.1
APT-50:125psi	135.8	49.9	96.5	116.4	133.5	62.9

3.2.1.5 Beam End Displacements

The vertical displacement at the ends of the beams were similar and shown in Figure 3-9 with each displacement reaching a maximum of around 0.03-0.04 inches. The displacement of the ends started going negative (upwards) with the application of the dead load at the ends and the initial post-tensioning.

Table 3-5 shows the beam end displacements at the end of each loading stage.

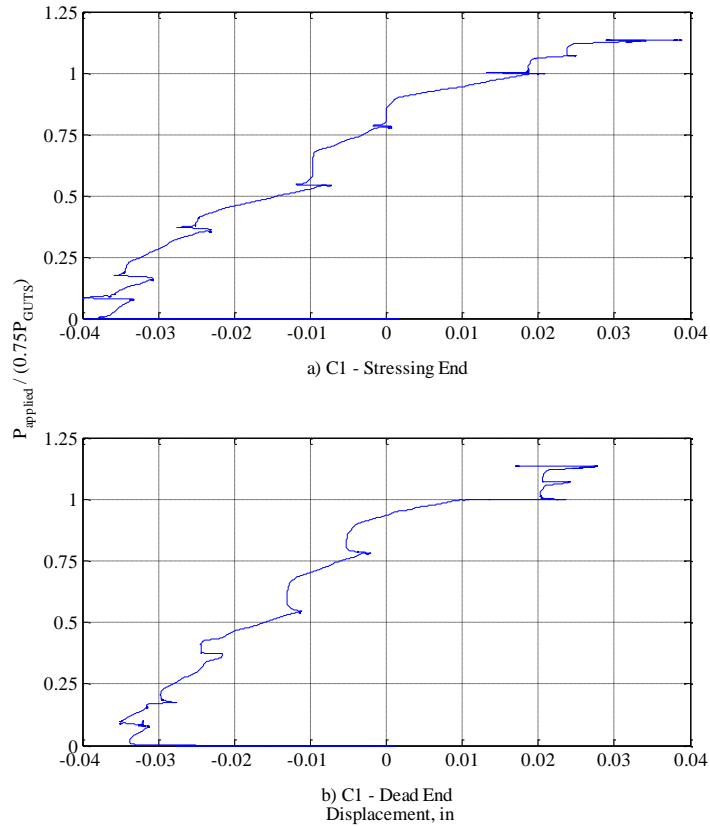


Figure 3-9: C1 displacement on ends of the beam.

Table 3-5: C1 beam end displacements at each loading stage.

	Disp. Stress, in.	Disp. Non-Stress, in.
APB-50psi	0.040	0.025
APT-50psi	0.041	0.028
DL	0.037	0.025
0.15fpuB	0.033	0.031
0.15fpuT	0.031	0.031
0.45fpuB	0.023	0.022
0.45fpuT	0.007	0.011
0.75fpuB	-0.001	0.002
0.75fpuT	-0.021	-0.011
APB-50:125psi	-0.014	-0.013
APT-50:125psi	-0.014	-0.014
0.85fpuB	-0.025	-0.024
0.85fpuT	-0.034	-0.027
APB-50:125psi	-0.029	-0.028
APT-50:125psi	-0.039	-0.017

3.2.1.6 C1 Results Overview

With C1 having largest radii's for the post-tensioning ducts, the vertical distributed load from the post-tensioning was low in comparison to typical NDOT bridges. This low vertical distributed post-tensioning load had minimal effects on the performance of the beam as a whole. There were no cracks present throughout the cross section of the beam as well as the surface of the web. Based on this one experiment, beams with this tendon curvature satisfying minimum tendon duct spacing will perform well.

3.2.2 Configuration 2

3.2.2.1 Embedded Concrete Strain Gauges

C2 had a radius of curvature that provided a post-tensioning force that was average for NDOT bridges with it being between a low curvature of the Rancho Drive Bridge (C1) and a high curvature of the Steamboat Hills Bridge (C3). The spacing between the ducts remained at 0.7 inches (1.0 inch full scale) similarly to C1. The figures presented for C2 are comparable to C1. Figure 3-10 provides the results for the embedded concrete strain gauge at midspan of the beam.

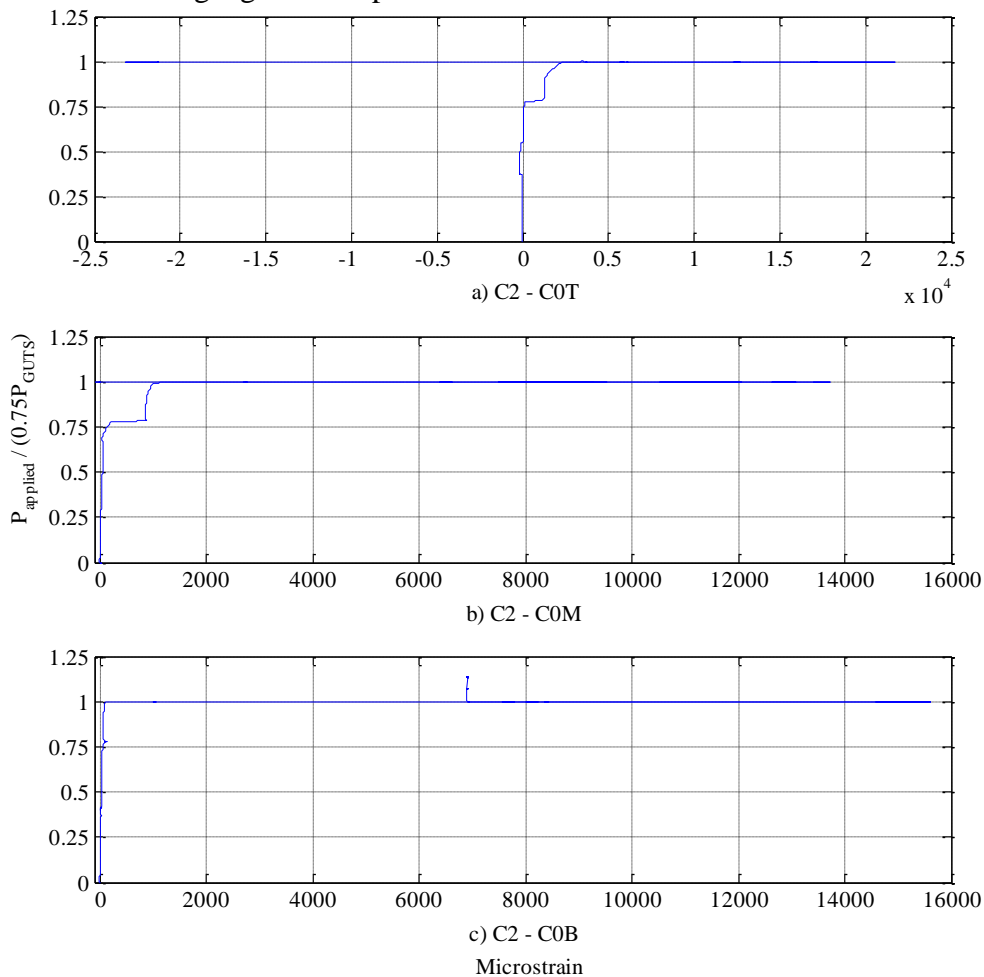


Figure 3-10: C2 embedded concrete strain at centerline.

The tendon stressing phases have minimal strain effect when compared to the air pressure. The top and middle embedded strain gauge reached the limit of the strain gauge (22,000 microstrain) during the air pressure after 0.75fpu phase, therefore it was not possible to capture the values from 0.85fpu and air pressures applied after. The strain in the bottom gauge increased to almost to 16,000 microstrain during the air pressuring after 0.75fpu and then decreased to approximately 7,000 microstrain when the 0.85fpu post-tensioning stressing occurred. Figure 3-10 shows that the air pressure had a much larger effect on the strain between the ducts then the stressing of the post-tensioning tendons and even bringing the strain gauges to their maximum limits.

Figure 3-11 provides the strain-time diagram for C2 to determine the strain variation between the different air pressure loadings. The labels APB and APT represent Air Pressure Bottom and Air Pressure Top, respectively. The value shown right after the APB and APT is the air pressure applied (50, 75, 100, 125psi). As seen in Figure 3-11, the air pressure had a large impact on the strain. The strain escalated from approximately 0 strain to 5,000 microstrain or higher during the air pressure loading in C2 whereas in C1, the air pressure had a more minor effect on the strain.

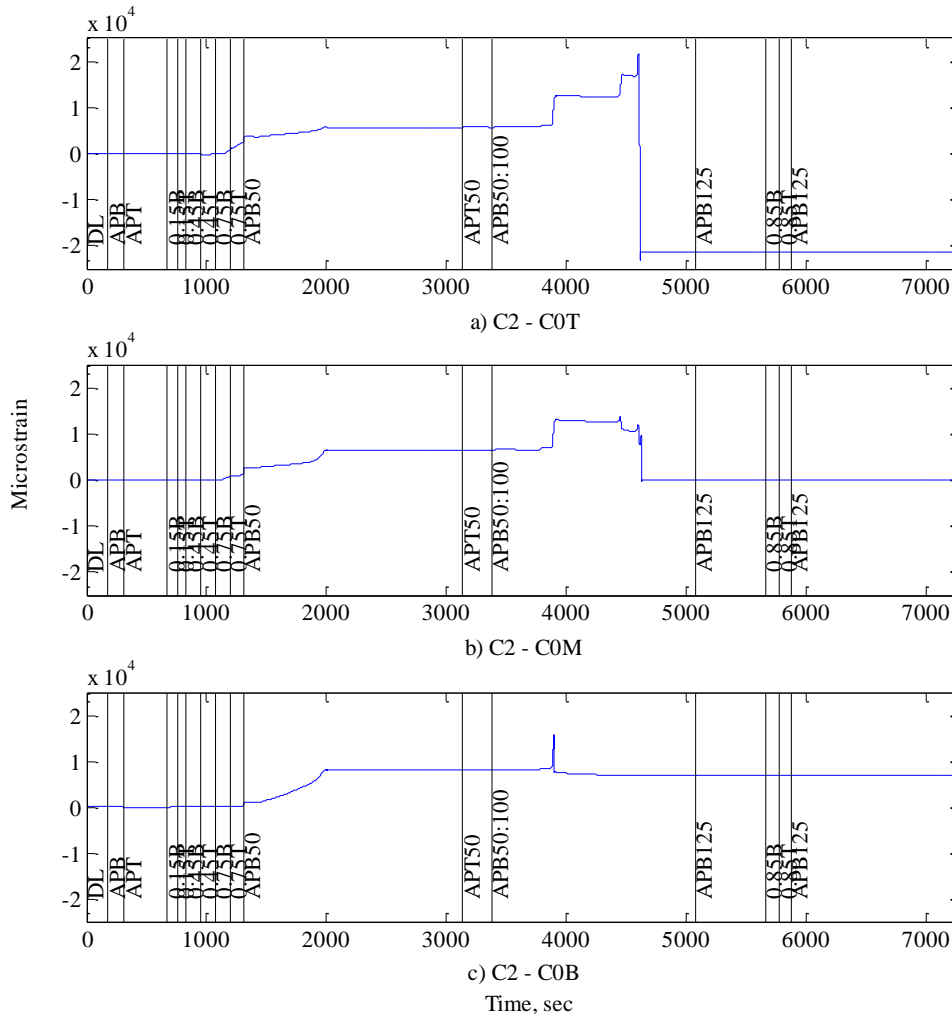


Figure 3-11: C2 embedded concrete strain versus time.

Figure 3-12 provides the results for the embedded concrete strain gauges at +30 inches from the center (30 inches to the stressing side). The top gauge approached the limit of the gauge and decreased before 0.85fpu stressing to around 5,500 microstrain. Unlike the top gauge, the middle gauge reached the limit and broke before the tendons were stressed to 0.85fpu. The bottom gauge had strains almost twice the values of C1. The large strains exceeded the concrete tension capacity, therefore a crack was expected between all three ducts as well as extending below the ducts into the web. The cracking would later be confirmed from the cutting of the beam in half, discussed later. The embedded concrete strain decreased moving away from center of the beam. Table 3-6 shows the strain at the end of each loading stage for the embedded concrete gauges. After 0.85fpu, only 125 psi air pressure testing of the bottom duct was conducted.

Table 3-6: C2 embedded concrete gauges at each loading stage.

	C0T, με	C0M, με	C0B, με	C30T, με	C30M, με	C30B, με
APB-50psi	-3.9	12.5	-0.7	0.0	-3.9	-3.9
APT-50psi	-6.6	16.4	0.7	-2.0	-6.6	-6.6
DL	2.0	-3.9	-3.3	-3.3	2.0	-0.7
0.15fpuB	22.3	8.5	3.3	-1.3	22.3	7.9
0.15fpuT	20.3	19.7	6.6	3.3	20.3	10.5
0.45fpuB	148.8	26.2	25.6	17.7	148.8	28.2
0.45fpuT	143.6	60.3	34.1	23.6	143.6	40.0
0.75fpuB	3835.5	690.5	84.6	61.6	3835.5	79.3
0.75fpuT	3419.2	1087.9	83.3	70.7	3419.2	89.1
APB-50psi	4588.0	6397.7	8030.5	78.0	4588.0	89.1
APT-50psi	4603.7	6399.7	8027.8	76.0	4603.7	91.7
APB-50, 75, 100psi	0.0	0.0	6931.7	22100.0	0.0	106.2
APB-125psi	0.0	0.0	6917.3	5799.5	0.0	110.1
0.85fpuB	0.0	0.0	6912.0	5350.7	0.0	127.1
0.85fpuT	0.0	0.0	6914.0	5349.4	0.0	129.1
APB-125psi	0.0	0.0	6910.7	5040.2	0.0	149.4

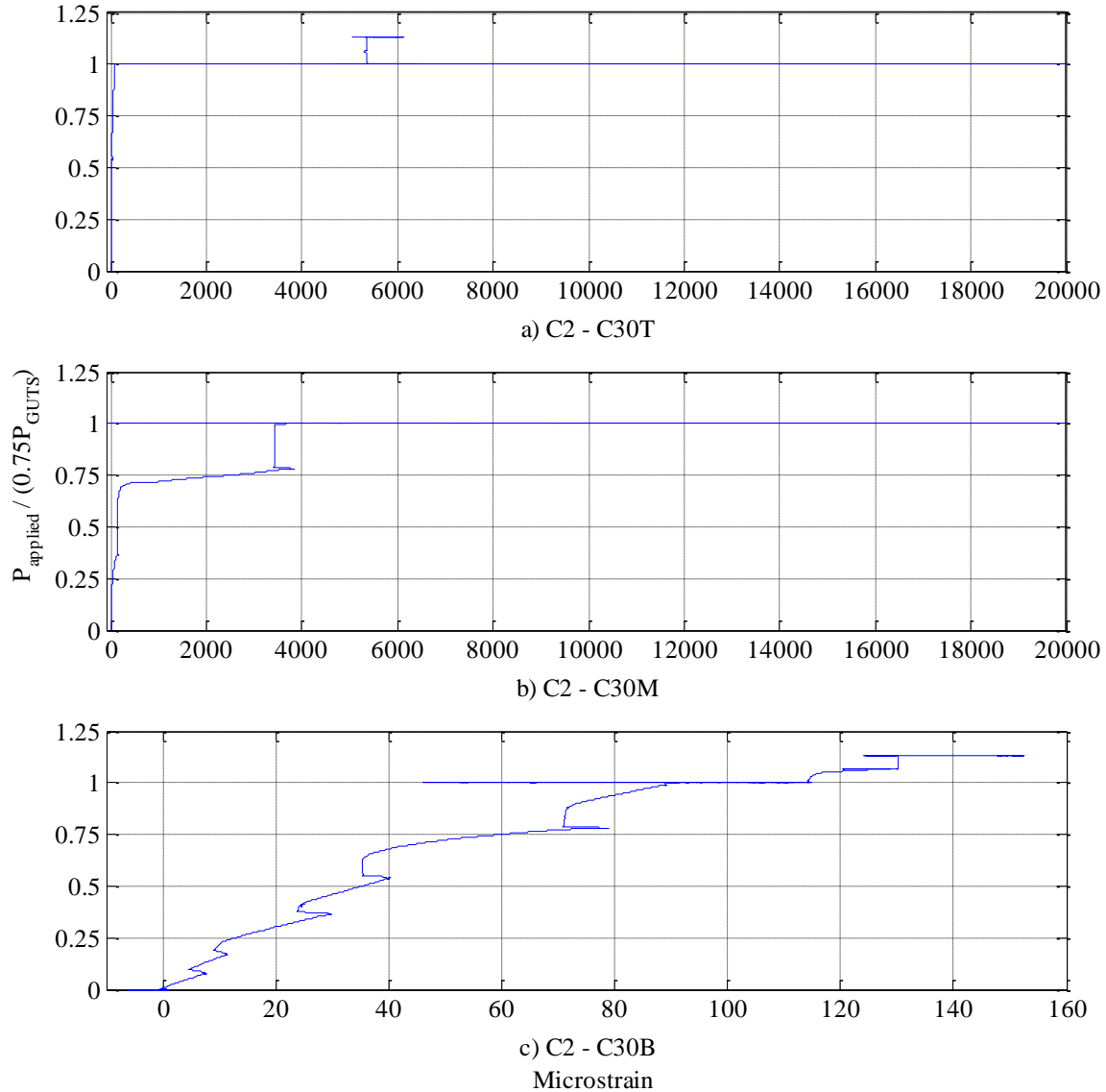


Figure 3-12: C2 embedded concrete strain at +30” from centerline.

3.2.2.2 Concrete Surface Strain Gauges

The concrete surface strain gauges were oriented in the same direction for C2 as they were for C1. The strain gauge that was located in the center of the beam had comparable results to C1 reaching close to 400 microstrain in compression as it was horizontal and in compression during the full testing. For the two outside strain gauges that were positioned vertically, they started in tension during the stressing stages but once air pressure started, the strain became compression and finished around 1,000 microstrain in compression.

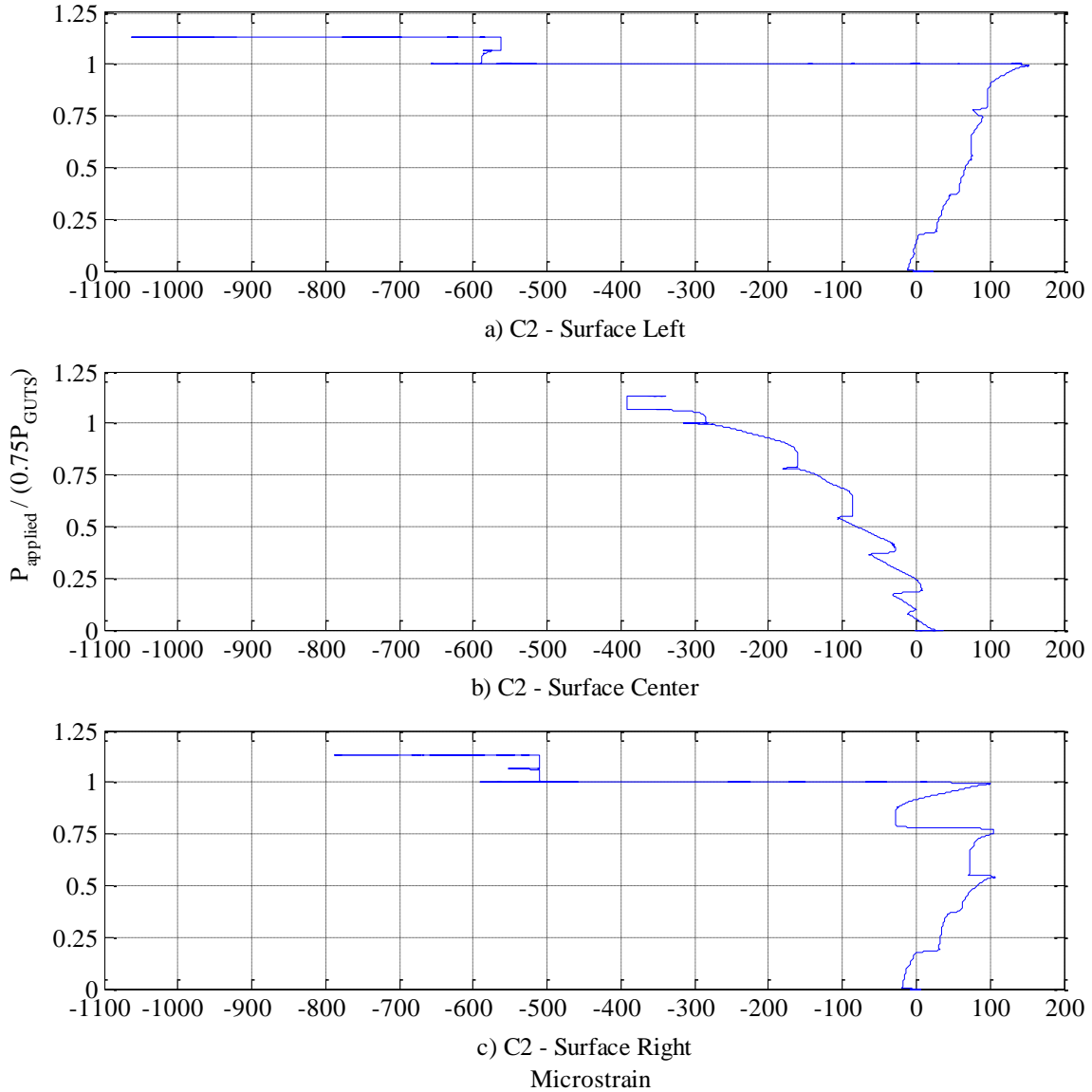


Figure 3-13: C2 concrete surface strain gauges.

The compression on the vertical gauges can be due to the fact that the strain gauges are located between the top and middle ducts whereas the prestressing tendons are exerting a force on the bottom of the top duct and the air pressure is exerting a force in all directions around the middle duct, leading to an area of compression where the strain gauges are located, see Figure 3-14.

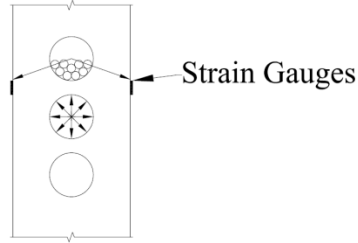


Figure 3-14: Surface strain gauge compression explanation.

Table 3-7 shows the concrete surface strain for all three gauges at the end of each loading stage throughout the testing.

Table 3-7: C2 concrete surface gauges at each loading stage.

	SGSL	SGSC	SGSR
	μϵ	μϵ	μϵ
APB-50psi	-1.3	0.7	-7.2
APT-50psi	17.0	34.1	-0.7
DL	-3.3	23.6	-6.6
0.15fpuB	-2.6	-9.2	-11.8
0.15fpuT	4.6	-28.8	0.0
0.45fpuB	46.5	-64.2	44.6
0.45fpuT	76.0	-104.9	108.8
0.75fpuB	84.5	-178.3	-11.8
0.75fpuT	154.0	-274.7	100.2
APB-50psi	-2.0	-298.3	-55.0
APT-50psi	-2.6	-301.6	-57.7
APB-50, 75, 100psi	-528.8	-285.8	-477.6
APB-125psi	-612.6	-283.2	-535.3
0.85fpuB	-581.2	-351.4	-553.0
0.85fpuT	-562.8	-391.4	-510.4
APB-125psi	-919.3	-363.9	-700.4

As large strains were produced in between the ducts, it was not surprising to see cracks on the surface of the web. Cracks first appeared on the web face during 0.75fpu post-tensioning of the bottom tendon with cracks shown in Figure 3-15.

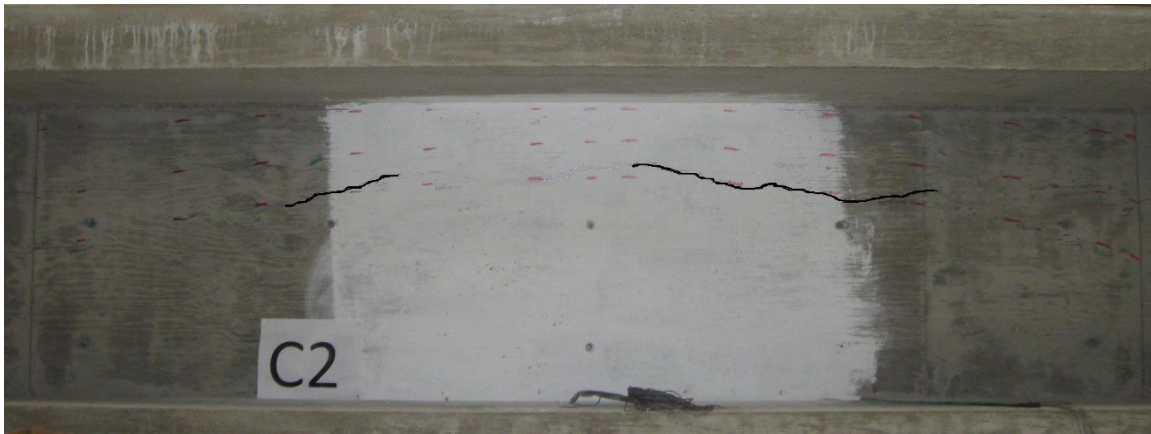


Figure 3-15: C2 crack appearance at 0.75fpuB.

Figure 3-16 shows the cracking along the face of the web. The cracks primarily occurred along the outline of the bottom duct with a maximum crack width of 0.05 inches. The cracks are outlined in Figure 3-16 to better show the results; the line is not representative of the crack width.

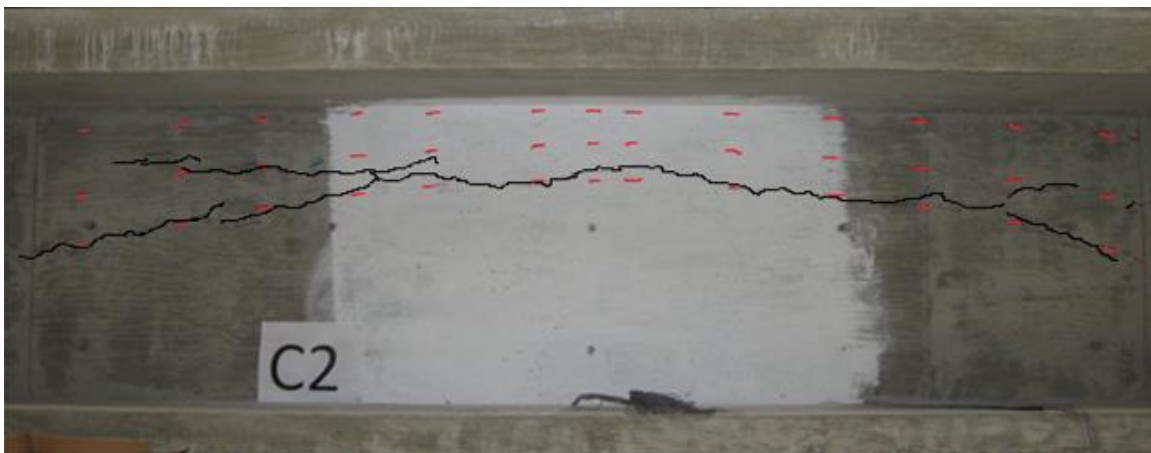


Figure 3-16: C2 web face after loading with cracks highlighted for clarity.

3.2.2.3 Cross Sectional Cracks

With the same procedure as was used in C1, C2 was cut in half to best understand how the cracks propagated throughout the cross section. C2 cross section after cutting the beam in half is shown in Figure 3-17. Compared to C1, C2 has much more notable damage, especially around the middle duct. Between the middle duct and bottom duct, the concrete was heavily damaged. This could be due to the testing procedure of prestressing and air pressurizing plus poor consolidation occurred during the concrete casting with only 0.7 inches between the ducts.



a) Cross section with cracks.



b) Cross section with cracks drawn.

Figure 3-17: C2 cut beam cross section.

More noticeable damage occurred in C2 than C1 as cracks occurred between all the ducts. Cracking was on the web surface as well as migrating down the web below the bottom duct. The crack width was 0.03 inches between the top and middle ducts while increasing between the middle and bottom ducts to 0.15 inches and increasing to 0.20 inches below the bottom duct.

3.2.2.4 Shear Reinforcement Gauges and Beam End Displacement

The strain gauge results from the shear reinforcement and the beam end displacement was not significant to this study. Therefore, refer to Appendices A and B for the results for the shear reinforcement strain gauges and the displacements on the ends of the beams.

3.2.2.5 C2 Results Overview

As the vertical distributed prestressing force increased due to a higher curvature, the damage increased. C2 had cracks that reached the surface of the web as well as cracking throughout the height of the web. In addition to the increase in cracking, the middle and bottom ducts were also damaged during the experimental testing. The damage to the ducts is most likely due to the fact that the spacing between the ducts was 0.7 inches which can lead to issues achieving proper consolidation between the ducts.

3.2.3 Configuration 3

3.2.3.1 Embedded Concrete Strain Gauges

C3 had the highest curvature of the beams tested in the laboratory and is considered on the high end for tendon curvatures for NDOT bridges. The spacing remained the same between the ducts at midspan (0.7 inches) as in C1 and C2. The axes

for the figures associated with C3 are the same as used in the previous two beams. The results for the embedded concrete strain gauges at midspan are provided in Figure 3-19.

During testing of C3, a rock pocket ended up serving as the weakest link and air started leaking profusely through the hole during air pressure testing. To continue air pressure testing, the hole was filled with a concrete anchoring adhesive.



a) Concrete rock pocket.



b) Pocket with high strength adhesive.

Figure 3-18: Repair of concrete rock in the web of C3.

As can be seen in Figure 3-19, the strains being produced in C3 are 11,000 $\mu\epsilon$, 16,000 $\mu\epsilon$, and 22,000 $\mu\epsilon$ respectively for the top, middle and bottom concrete gauges while reaching the strain limit on the middle and bottom gauges. The top gauge located between the top and middle ducts, had a much larger impact from the air pressure testing compared to the stressing of the tendons. The largest contributor to the strain in the top gauge is from the air pressure testing after 0.75fpu stressing whereas the air pressure after 0.85fpu had an increase in strain but not as large. The middle gauge between the middle and bottom ducts attained higher strains than the top gauge. The middle gauge broke after 0.75fpu as 100 psi air pressure was applied. The strain gauge located below the bottom duct also had large strains generated during air pressure testing after the 0.75fpu stressing phase. The strains were large enough to reach the limit of 22,000 microstrain. Once again, the air pressure testing showed larger concrete tension strain than during post-tensioning.

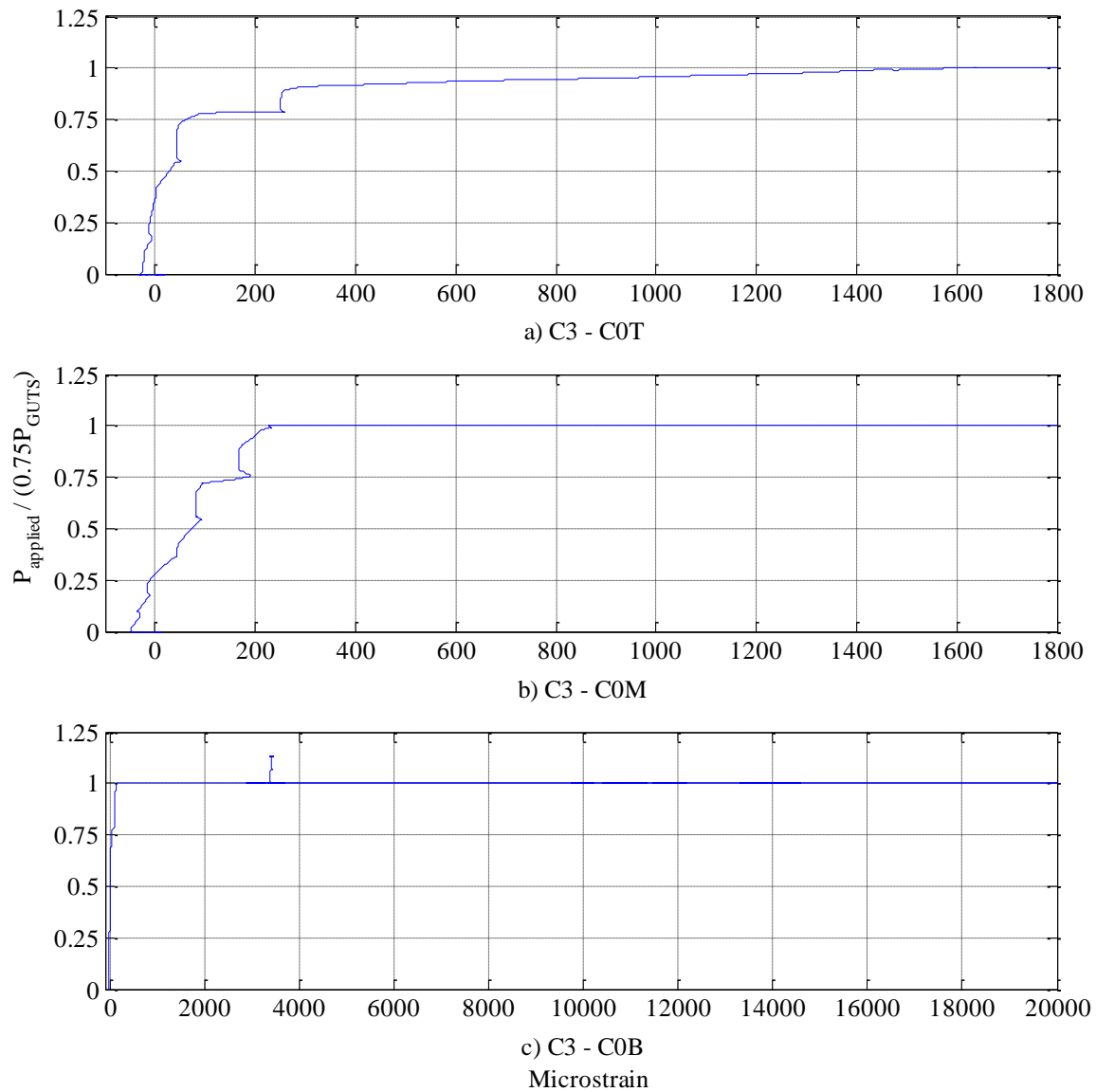


Figure 3-19: C3 embedded concrete strain at centerline.

Figure 3-20 shows the variations in strain for each loading stage. From inspection of the figure, it can be noticed that the initial 50 psi air pressure on the bottom duct delivers a substantial increase in strain to approximately 5,000 $\mu\epsilon$. 75 psi air pressure testing had a noticeable increase in strain in all three locations.

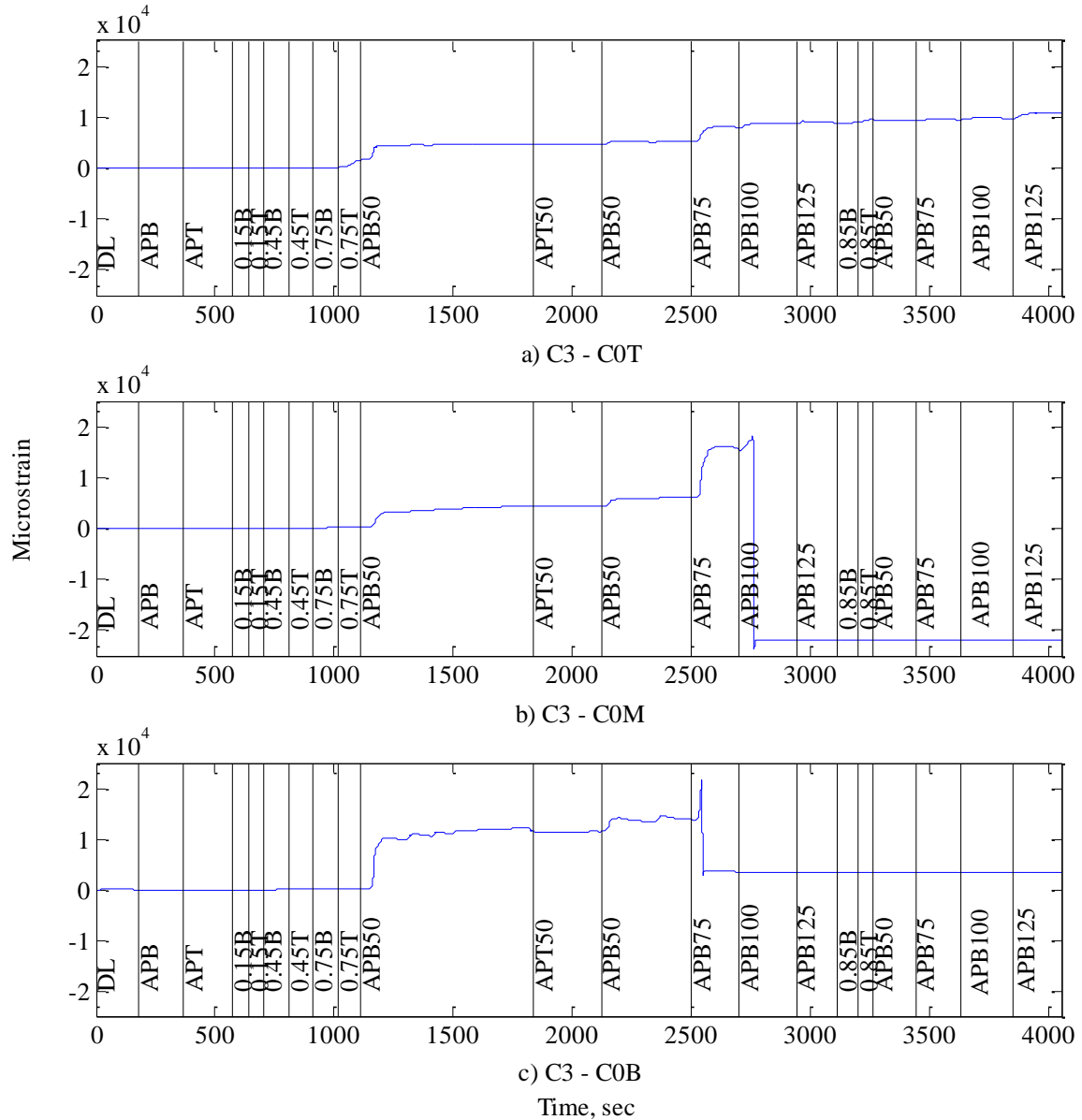


Figure 3-20: C3 embedded concrete strain versus time.

As shown in Figure 3-20, the air pressure did not follow the same loading sequence as outlined in Section 2.2.3. The air pressure was brought to 50 psi on both ducts and then only the middle duct was pressurized up to 125 psi, this was done because a larger strain occurred from air pressure on the middle duct as opposed to the top.

The strain associated with the strain gauges located at +30 inches from centerline (30 inches to the stressing side) are presented in Figure 3-21. The strain was exceptionally large in all gauges with each reaching $\pm 22,000 \mu\epsilon$. The strain in all three locations increased drastically during the air pressure testing after 0.75fpu.

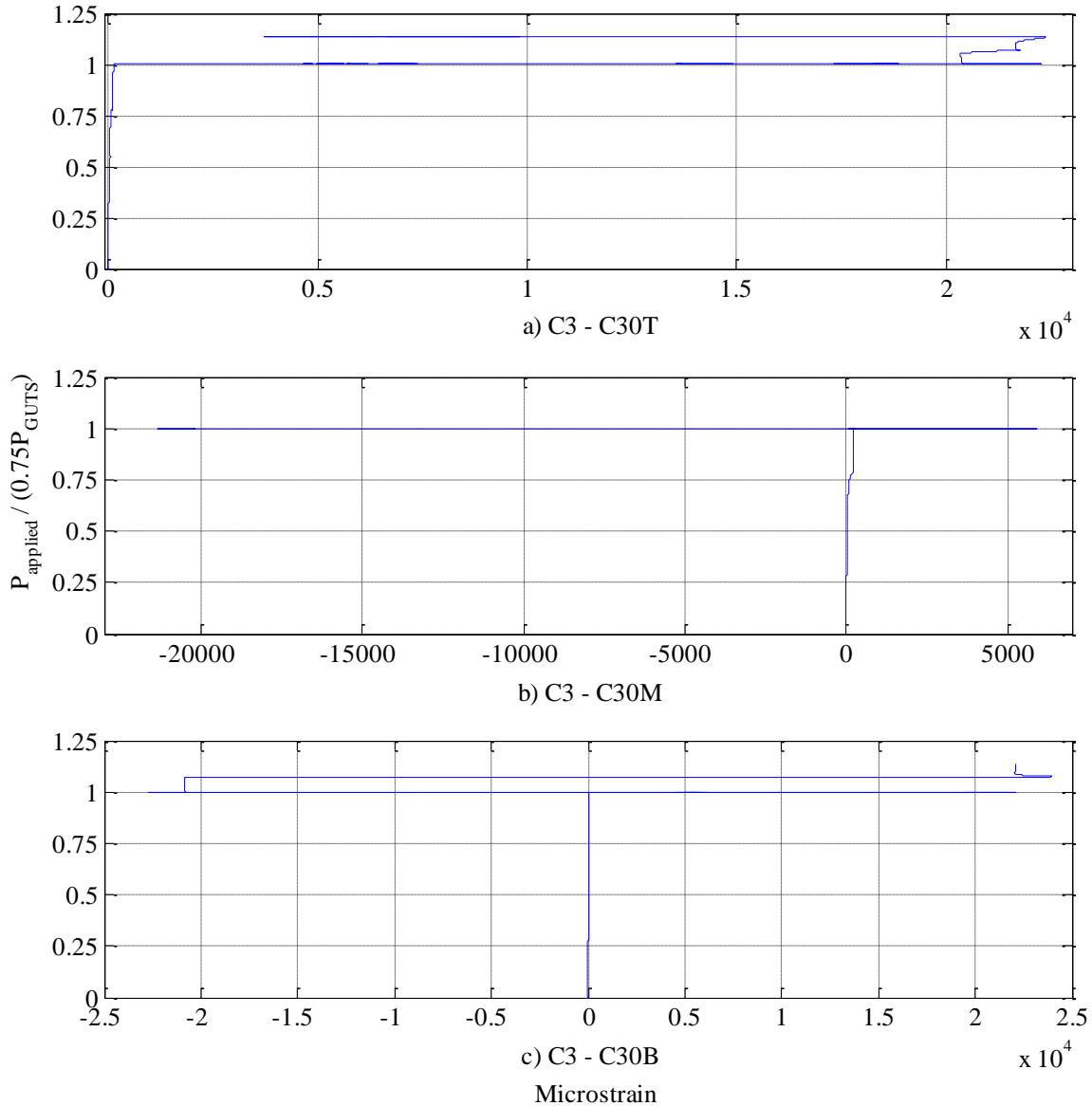


Figure 3-21: C3 embedded concrete strain at +30" from centerline.

The largest strain was in the middle gauge between the middle and bottom duct which is similar to all previous beams and locations along the beam. The strain limit for the embedded concrete gauges was met for the bottom gauge as the strain increased to the 22,000 microstrain limit and decreased to -22,000 microstrain. The strains at the end of each loading stage for the embedded concrete gauges are shown in Table 3-8. The loading stages with "CP" are for a constant air pressure being applied to the post-tensioning ducts for 1 minute. Air pressure testing was only conducted on the bottom duct after 0.85fpu as the pressurizing of the top duct was showing minimal damage.

Table 3-8: C3 embedded concrete gauges at each loading stage.

	C0T	C0M	C0B	C30T	C30M	C30B
	μϵ	μϵ	μϵ	μϵ	μϵ	μϵ
APB-50psi	3.3	1.3	0.0	-1.3	0.0	-0.7
APT-50psi	3.3	-0.7	-0.7	-2.0	0.7	-0.7
DL	-28.8	-49.8	-28.8	-15.1	-23.6	-18.3
0.15fpuB	-22.9	-34.7	-21.6	-11.1	-11.8	-13.8
0.15fpuT	-11.8	-14.4	-13.8	-2.0	-4.6	-8.5
0.45fpuB	2.0	43.9	7.9	10.5	32.1	11.1
0.45fpuT	42.6	84.5	20.3	38.0	49.8	24.9
0.75fpuB	110.0	161.8	87.2	82.5	201.7	41.3
0.75fpuT	1505	219.5	140.2	119.9	226.0	58.3
APB-50psi	4694	4345	11610	5713	122.5	5132
APT-50psi	4654	4412	11466	5713	116.6	5053
APB-50psi CP	5223	6005	13867	6695	86.5	5435
APB-75psi CP	7983	15624	3432	13656	0.0	19637
APB-100psi CP	8751	0.0	3378	17476	0.0	22079
APB-125psi CP	8829	0.0	3383	20622	0.0	-20862
0.85fpuB	8979	0.0	3415	21580	0.0	22079
0.85fpuT	9524	0.0	3427	22338	0.0	22079
APB-50psi	9425	0.0	3393	22376	0.0	22079
APB-75psi	9484	0.0	3377	22376	0.0	22079
APB-100psi	9737	0.0	3374	22376	0.0	22079
APB-125psi	10689	0.0	3389	6635	0.0	21465

3.2.3.2 Concrete Surface Strain Gauges

The number of strain gauges on the surface of the web was increased from three on the previous two beams to a total of seven for C3. The increase in gauges was to capture a broader range of data along the web surface. The locations of all seven gauges are noted in Chapter 2, Figure 2-34, with three gauges being in the center and two gauges 12 inches on either side of center at varying heights on both sides of the web.

The results for the concrete surface strain gauges are shown in Figure 3-22, Figure 3-23 and Figure 3-24. The non-stressing end of the beam, or dead end, is referred to as - 12 inches whereas the stressing side of the beam is +12 inches. The results for all of the 14 locations were similar in regards to having strains generally reaching around a maximum of +/-600 microstrain with exception of the bottom surface strain gauge on the east side of the beam which measured close to 2,000 microstrain in compression after all loading was complete. The slight variation in strain from the east and west sides are due to the fact that the post-tensioning ducts were tied to the west side of the shear reinforcement leading to the ducts being closer to that side of the face of concrete and thus increasing the strains on the west face of the web.

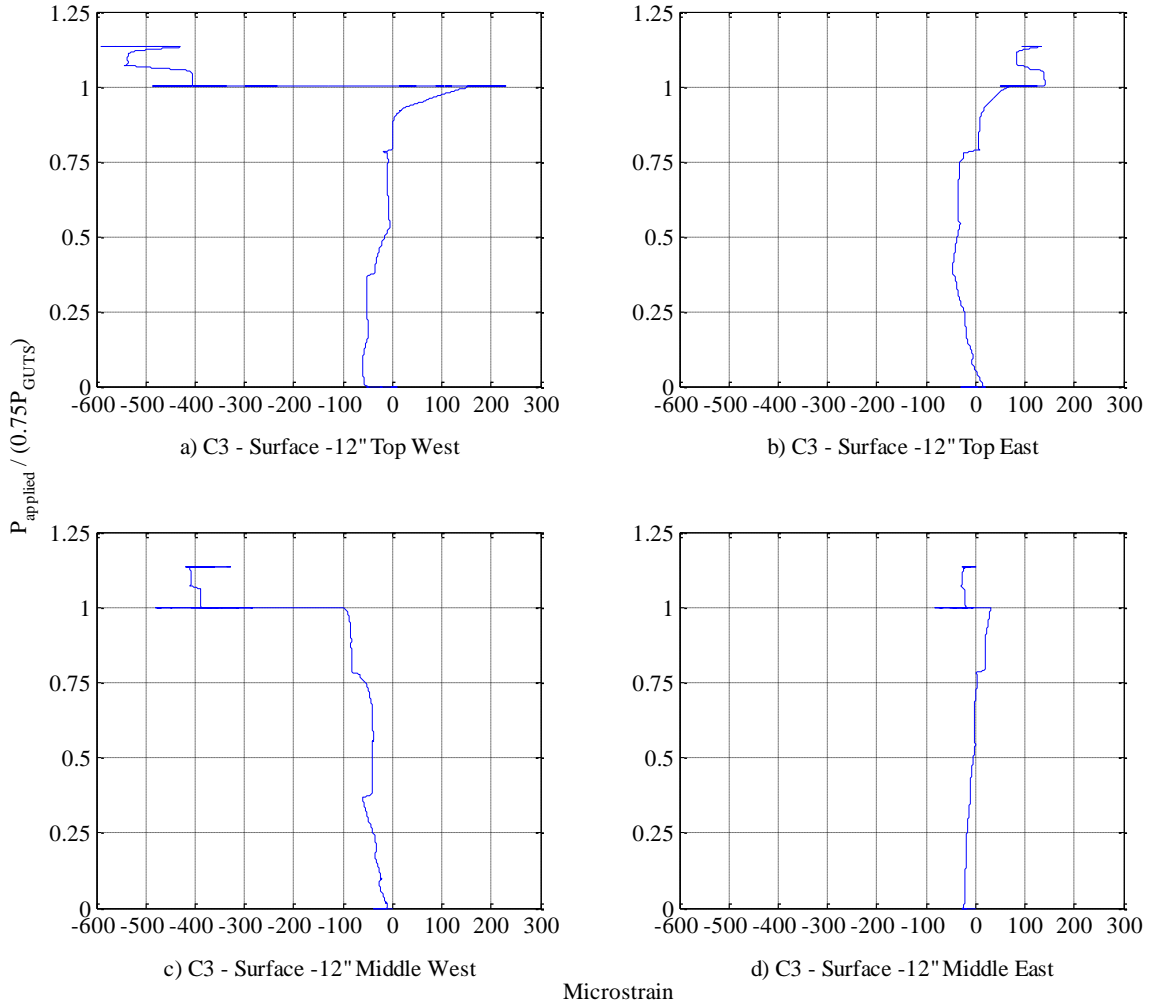


Figure 3-22: C3 concrete surface strain at -12 inches.

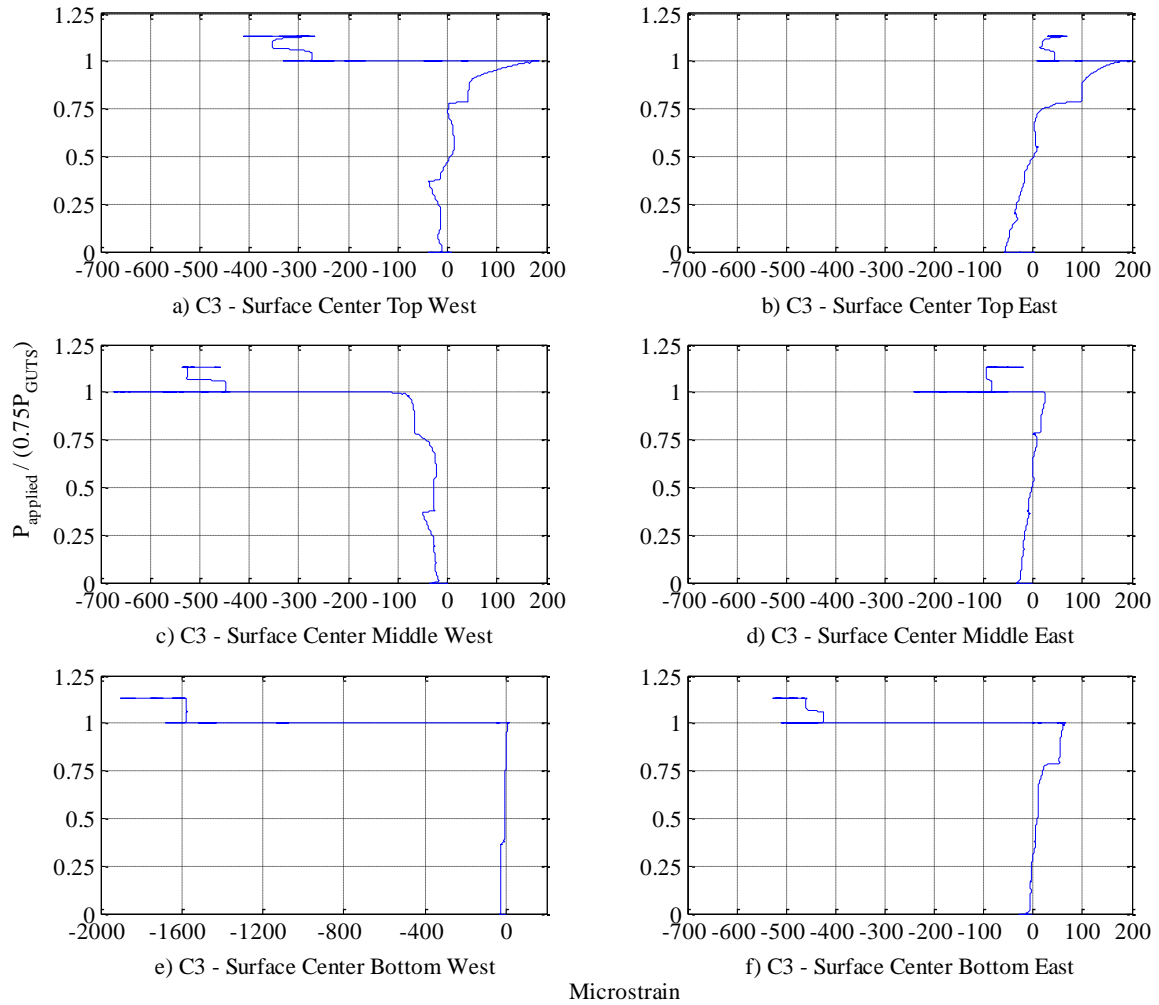


Figure 3-23: C3 concrete surface strain at centerline.

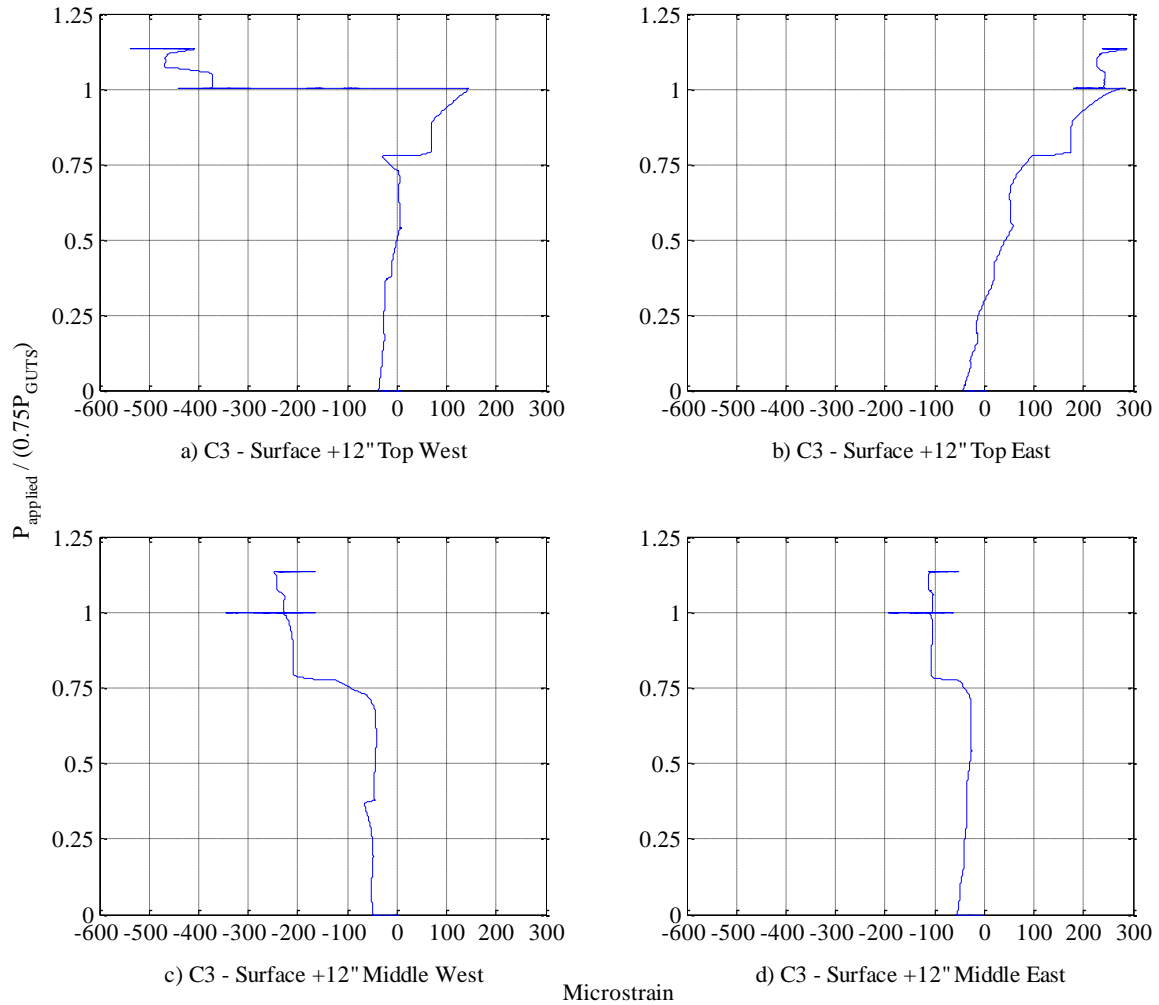


Figure 3-24: C3 concrete surface strain at +12 inches.

The final values for all the concrete surface strain gauges are shown in Table 3-9 for the west side of the web, and Table 3-10 shows the results for the east side of the web.

Table 3-9: C3 concrete west surface strain at each loading stage.

	CSLTW $\mu\epsilon$	CSLMW $\mu\epsilon$	CSCTW $\mu\epsilon$	CSCMW $\mu\epsilon$	CSCBW $\mu\epsilon$	CSRTW $\mu\epsilon$	CSRMW $\mu\epsilon$
APB-50psi	2.6	0.7	2.6	-0.7	0.0	0.7	-1.3
APT-50psi	2.6	-0.7	-0.7	-2.6	-2.0	1.3	-2.0
DL	-38.6	-48.5	-13.1	-24.9	-27.5	-51.7	-11.8
0.15B	-32.7	-50.5	-17.7	-22.9	-27.5	-59.6	-23.6
0.15T	-26.9	-49.8	-14.4	-25.6	-25.6	-50.4	-34.1
0.45B	-19.0	-58.3	-28.2	-41.9	-21.6	-45.8	-52.4
0.45T	4.6	-42.6	11.1	-24.9	-8.5	-9.2	-41.9
0.75B	63.5	-196.7	32.8	-65.5	-0.7	-7.9	-77.3
0.75T	139.5	-228.2	161.8	-100.9	4.6	140.8	-97.0
APB-50psi	-95.6	-263.6	36.0	-547.7	9.8	92.4	-369.6
APT-50psi	-91.7	-270.1	38.7	-553.0	13.1	96.3	-379.4
APB-50psi CP	-166.4	-345.5	-32.1	-668.9	-48.5	24.9	-478.4
APB-75psi CP	-299.3	-266.2	-171.7	-541.2	-1075.2	-247.6	-407.6
APB-100psi CP	-341.2	-242.6	-234.6	-496.0	-1436.8	-341.9	-387.9
APB-125psi CP	-377.2	-228.2	-277.8	-454.7	-1582.9	-410.0	-384.7
0.85B	-463.7	-242.6	-348.6	-525.5	-1577.7	-531.2	-411.5
0.85T	-419.8	-247.2	-285.0	-531.4	-1577.7	-452.6	-411.5
APB-50psi	-419.8	-242.6	-280.4	-532.0	-1584.9	-453.2	-412.2
APB-75psi	-422.4	-238.6	-279.1	-534.6	-1609.1	-455.9	-415.5
APB-100psi	-432.9	-235.4	-302.1	-516.3	-1693.0	-472.9	-416.1
APB-125psi	-471.6	-224.2	-354.5	-467.1	-1829.9	-529.9	-414.8

Table 3-10: C3 concrete east surface strain at each loading stage.

	CSLTE $\mu\epsilon$	CSLME $\mu\epsilon$	CSCTE $\mu\epsilon$	CSCME $\mu\epsilon$	CSCBE $\mu\epsilon$	CSRTE $\mu\epsilon$	CSRME $\mu\epsilon$
APB-50psi	-0.7	-0.7	1.3	-1.3	-0.7	0.7	0.0
APT-50psi	-2.0	0.7	-2.0	-2.0	-2.0	-1.3	-1.3
DL	15.1	-25.5	-57.0	-30.8	-13.8	-43.2	-55.0
0.15B	-6.6	-22.3	-51.1	-24.9	-7.2	-30.8	-48.5
0.15T	-21.6	-18.3	-34.7	-19.7	-5.2	-15.1	-40.0
0.45B	-45.9	-11.8	-17.0	-11.8	1.3	18.3	-36.7
0.45T	-35.4	-2.0	3.9	0.7	9.2	53.0	-27.5
0.75B	-13.8	-3.3	71.4	-8.5	21.0	151.9	-114.6
0.75T	59.6	26.9	165.2	17.7	59.0	257.4	-115.3
APB-50psi	111.4	-38.6	97.7	-180.2	52.4	239.7	-138.2
APT-50psi	106.1	-39.3	89.1	-183.5	53.1	237.7	-148.0
APB-50psi CP	74.0	-81.2	47.2	-237.2	2.6	216.1	-188.6
APB-75psi CP	85.2	-53.1	30.1	-133.7	-450.1	208.2	-137.5
APB-100psi CP	117.3	-34.1	38.0	-111.4	-457.3	221.3	-119.2
APB-125psi CP	136.9	-26.2	43.3	-91.1	-437.7	235.8	-108.7
0.85B	93.0	-26.9	24.2	-95.0	-460.0	229.2	-112.7
0.85T	119.9	-24.2	49.8	-94.4	-459.3	273.7	-110.0
APB-50psi	119.2	-24.2	51.8	-93.1	-463.2	271.8	-109.4
APB-75psi	127.1	-26.9	53.1	-91.1	-479.0	265.9	-109.4
APB-100psi	131.7	-24.9	60.3	-80.0	-508.4	273.7	-104.1
APB-125psi	127.7	-16.4	50.5	-52.4	-490.7	284.9	-90.4

As large strains were produced in this configuration, cracking was present on the surface of the webs. The first appearance of cracks on the web surface was during 0.75fpu post-tensioning with cracks shown in Figure 3-25 for both 0.75fpu of the top and middle ducts. Figure 3-26 shows the cracking pattern that was present on the face of the

east side of the web. Similar to C2, the crack followed the layout of the bottom duct, which is denoted by the red dashed lines. The maximum crack width along the outside of the web reached 0.04 inches located in the center of the beam, where the ducts were closest together. The crack is outlined in Figure 3-26 to highlight the location along the web face, it is not representative of the actual crack width. Cracking along the web face started during 0.75fpu post-tensioning of the middle duct and greatly extending once 50 psi air pressure was placed on the middle duct.



Figure 3-25: C3 crack appearance at 0.75fpuB.

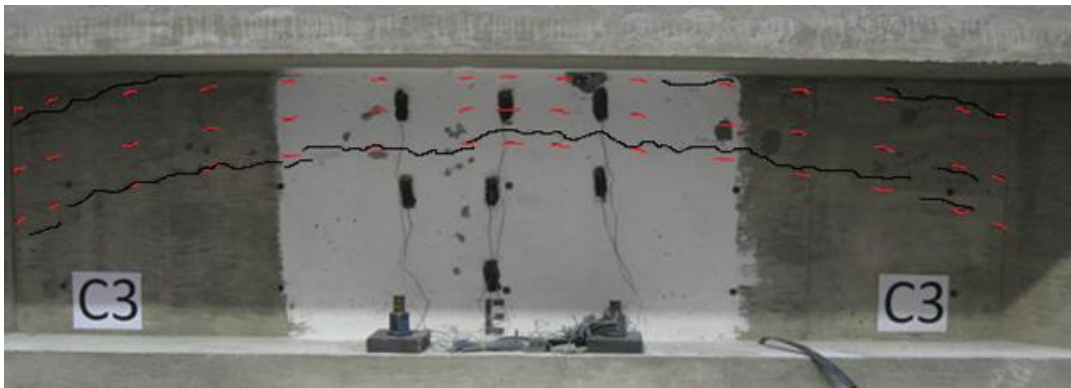


Figure 3-26: C3 web face after loading with cracks shown for clarity.

3.2.3.3 Cross Sectional Cracks

Upon completion of all the loading stages, the beam was cut in half to observe the crack layout within the cross section. Figure 3-27 shows the cross section of the beam once it is cut in half. The cracking pattern is similar to C2's cross sectional crack pattern with the exception that the middle and bottom ducts are not deformed. The crack widths were the same between all of the ducts (top-middle and middle-bottom) at 0.03 inches. Below the bottom duct, the crack width increased to 0.07 inches.



a) Cross section with cracks.



b) Cross section with cracks drawn.

Figure 3-27: C3 cut beam cross section.

The crack widths between the top-middle, middle-bottom and below bottom decreased compared to C2 even though the forces in C3 were higher. One explanation for this could be due to the fact that the tension capacity of C3 was 476.8 psi compared to C2 at 449.5 psi from the split-cylinder tests with C3 concrete coming from a different concrete truck.

3.2.3.4 Web Bulging

For C3, displacement transducers were included on the face of the web to measure the bulging of the web during post-tensioning and air pressure testing. With three transducers on each face of the web at varying heights as described in Section 2.6, the results are shown in Figure 3-28. The largest web bulge, 0.1 inch on the west face and 0.08 inch on the east face, is recorded at the transducer located at the quarter point from the top flange (7.875 inches below flange) with the centerline of the bottom ducts being at 8.975 inches below the top flange. This puts the location of the gauge between the centerline of the middle duct and the bottom duct, where the majority of cracking occurred. The web bulging diagram is broken up to each side of the web (east and west side) with each loading sequence being included and red lines being used for air pressure tests. The three numbers (10, 16 and 24) shown in Figure 3-28 are associated with particular loading runs. The three values were chosen as they show a large increase in web bulge from the previous step.

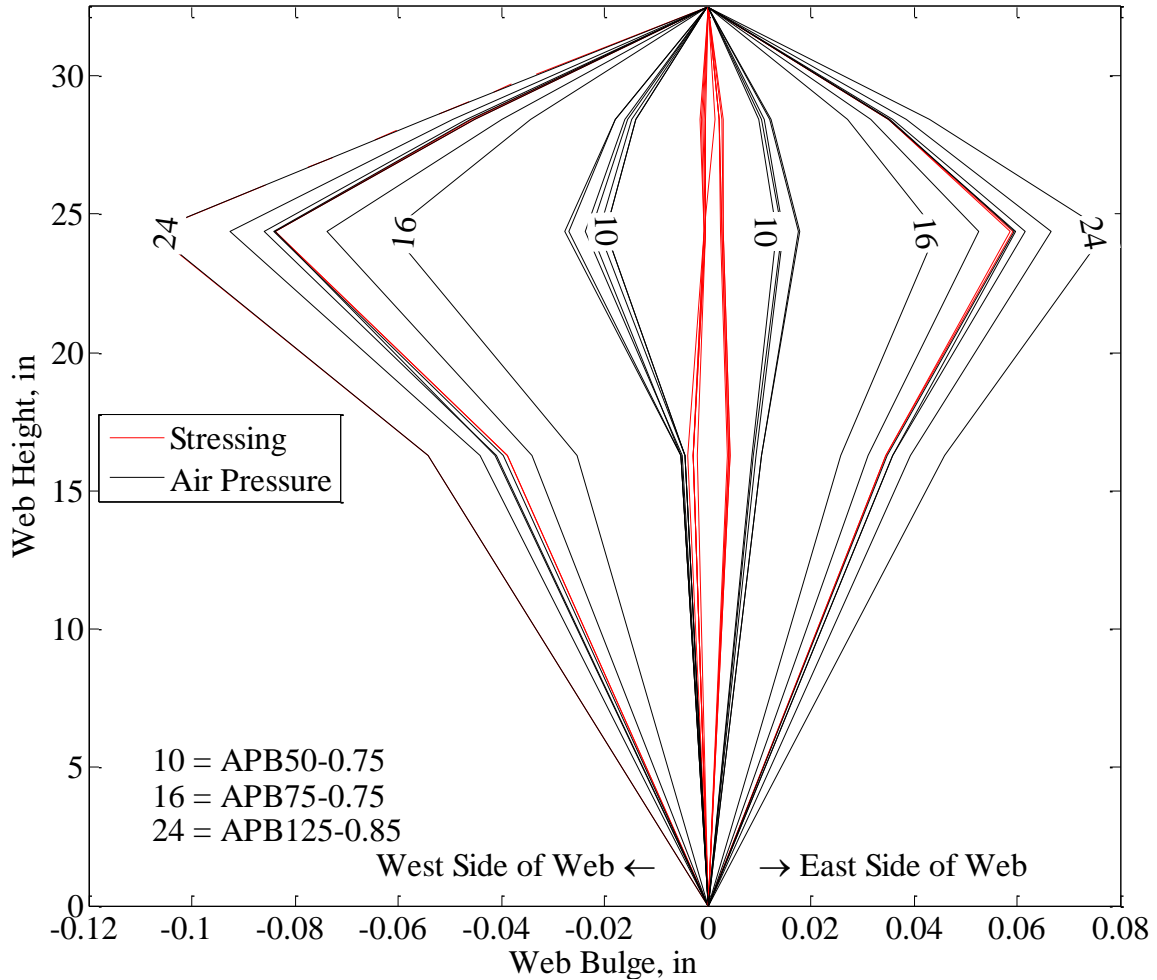


Figure 3-28: C3 web bulge.

The sizable increase of around 0.03 inches in web bulging is predominantly due to the air pressure testing instead of post-tensioning, with a substantial increase occurring at 75 psi air pressure testing of the middle duct after 0.75fpu. Table 3-11 shows the web bulging at the end of each loading. The total web bulge in Table 3-11 is the addition of the west and east face middle gauges. The labels are as follows: WBTE is web bulge top east face, WBME is middle east face, WBBE is bottom east face, WBTW is top west face, WBMW is middle west face and WBBW is the bottom west face gauge.

Table 3-11: C3 web bulge values at each loading stage.

	WBTW in.	WBMW in.	WBBW in.	WBTE in.	WBME in.	WBBE in.	M. Total in.
APIB	0.000	0.000	0.000	0.000	0.000	0.000	0.000
APIT	0.000	0.000	0.000	0.000	0.000	0.000	0.000
DL	-0.001	-0.001	-0.003	0.002	0.002	0.003	0.006
0.15fpuB	-0.001	-0.001	-0.003	0.002	0.002	0.004	0.006
0.15fpuT	-0.001	-0.001	-0.003	0.002	0.002	0.004	0.006
0.45fpuB	0.000	0.000	-0.003	0.002	0.003	0.004	0.007
0.45fpuT	0.000	0.000	-0.002	0.002	0.002	0.004	0.006
0.75fpuB	0.000	0.000	-0.002	0.003	0.003	0.004	0.005
0.75fpuT	-0.001	0.000	-0.004	0.003	0.003	0.004	0.008
APB-50psi	-0.015	-0.023	-0.005	0.010	0.014	0.009	0.037
APT-50psi	-0.015	-0.022	-0.005	0.010	0.014	0.009	0.037
APB-50psi Hold	-0.018	-0.026	-0.005	0.012	0.017	0.010	0.044
APB-75psi Hold	-0.034	-0.059	-0.024	0.027	0.043	0.025	0.102
APB-100psi Hold	-0.039	-0.072	-0.031	0.031	0.051	0.029	0.122
APB-125psi Hold	-0.044	-0.081	-0.038	0.034	0.057	0.034	0.138
0.85fpuB	-0.045	-0.084	-0.039	0.035	0.059	0.034	0.142
0.85fpuT	-0.045	-0.084	-0.039	0.035	0.058	0.034	0.142
APB-50psi	-0.046	-0.084	-0.039	0.035	0.059	0.035	0.143
APB-75psi	-0.047	-0.085	-0.039	0.036	0.061	0.035	0.145
APB-100psi	-0.049	-0.091	-0.042	0.038	0.065	0.038	0.155
APB-125psi	-0.053	-0.104	-0.051	0.042	0.074	0.044	0.179

3.2.3.5 Shear Reinforcement Gauges and Beam End Displacement

The strain gauge results from the shear reinforcement and the beam end displacement was not significant to this study. Therefore, refer to Appendices A and B for the results for the shear reinforcement strain gauges and the displacements on the ends of the beams.

3.2.3.6 C3 Results Overview

C3 had damage between the ducts, damage that extended vertically through the web and cracking that extended to the surface of the web. The air pressure testing proved to have the largest impact on strain compared to the post-tensioning with a number of gauges reaching their prescribed limit and breaking. The increase in number of concrete surface strain gauges provided a larger area to understand the effects; there was not a large variation between the gauges. The majority of web bulging can be associated to the

air pressure testing as opposed to the post-tensioning as the air pressure has higher forces being exerted in the horizontal direction compared with the post-tensioning.

3.2.4 Round A Results Overview

Overall the three beams with varying low, mild and high curvatures performed in general as expected. C2 did have more damage compared to C3 although the curvatures would suggest C3 should have the highest amount of damage. This presumably can be associated with the fact that C3 had higher tension concrete capacity. C2 also had a lot of damage between the ducts that could have been due to poor consolidation. Air pressure proved to have a much higher impact on strain within the web in comparison to the post-tensioning. It can be observed that with an increase in curvature there is an increase in damage within the beam. C3 had similar cracking along the bottom duct as C2 but with additional cracking along the top duct on the two sides of the webs.

3.3 Round B Experimental Beams

Round B experimental beam details were chosen based on improving the performance of the beams from Round A.

3.3.1 Configuration 4

C4 had the same design as C2 with only an increase in spacing between the ducts, (0.7 inches (1.0 inch full scale) to 1.05 inches (1.5 inch full scale)).

3.3.1.1 Embedded Concrete Strain Gauges

The embedded concrete strain gauges at the centerline of the beam, shown in Figure 3-29 with the top (between top and middle ducts) and middle gauge (between middle and bottom ducts), both broke during the air pressure after 0.75fpu. The locations of the embedded concrete strain gauges can be found in Figure 2-31.

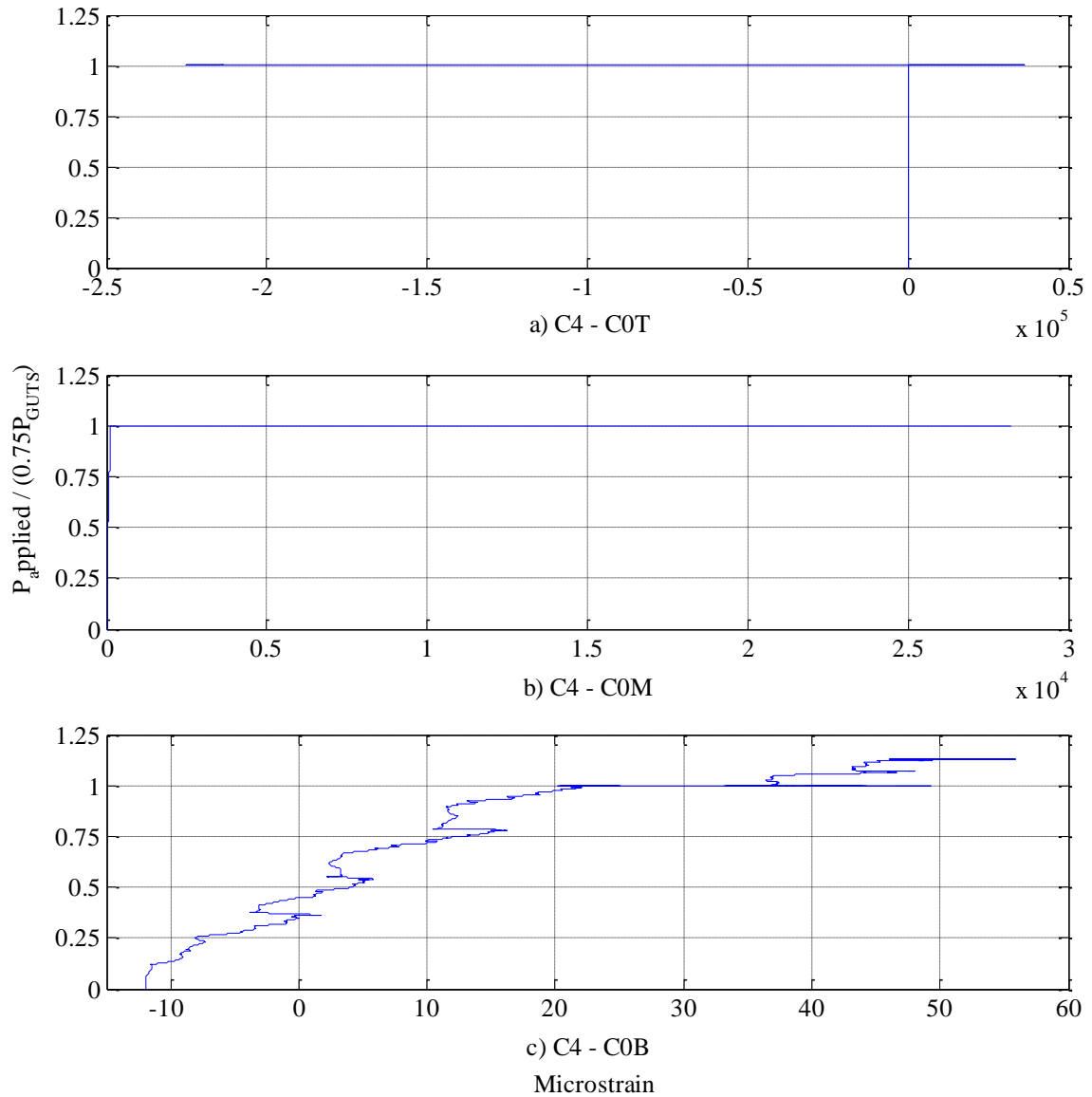


Figure 3-29: C4 embedded concrete strain at centerline.

As with the previous beams, the air pressure had the largest influence in the strain produced around the ducts with increasing from essentially $0 \mu\epsilon$ to $22,000 \mu\epsilon$ for the top and middle gauges. The bottom gauge did not have as large of an increase due to air pressure, $20 \mu\epsilon$ to $50 \mu\epsilon$, but air pressure still was a major contributing factor to the strain. To determine when the two gauges broke, a figure showing the loading sequences against the time is shown in Figure 3-30.

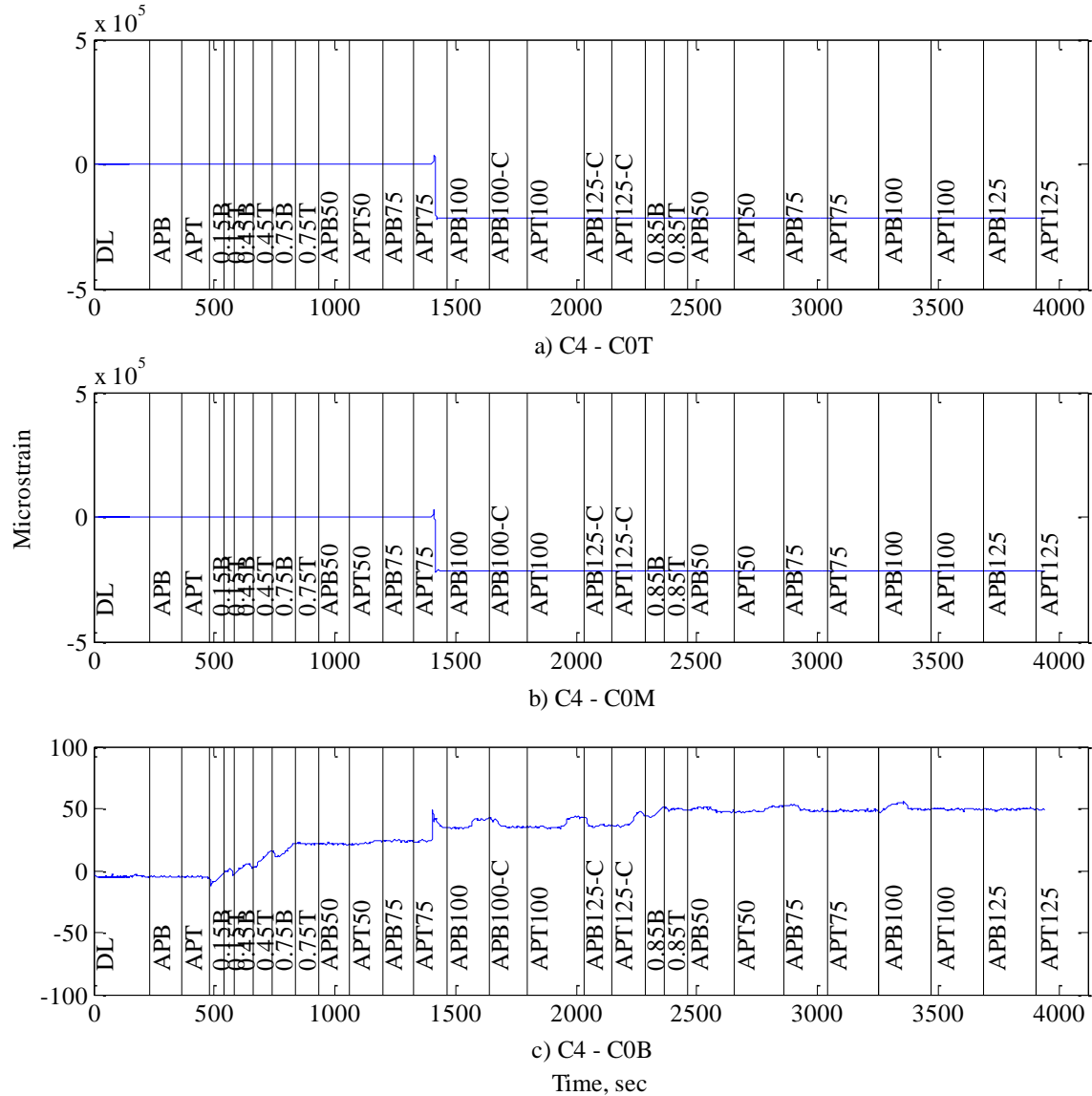


Figure 3-30: C4 embedded concrete strain versus time.

Upon review of the figure, there is a sudden increase in strain during 75 psi air pressure testing of the top duct for both the top and middle gauge increasing from 0 $\mu\epsilon$ to ~25,000 $\mu\epsilon$; this is when the two gauges broke. Looking at the bottom gauge (below bottom duct), there was also a noticeable strain increase during the 75 psi air pressure loading on the top duct but to a much lesser degree. Overall the strain below the bottom duct was not very large with reaching a peak of 55 microstrain. Comparing C4 to C2, there is a distinct difference in the strain during stressing with C4 stressing strain being much smaller in relation to the air pressure strain. Table 3-12 shows the embedded concrete strain at 0 inches from center for all loading stages.

Table 3-12: C4 embedded concrete strain at 0" O.C. for each loading stage.

	C0T, $\mu\epsilon$	C0M, $\mu\epsilon$	C0B, $\mu\epsilon$
APB-50psi	-26.2	6.5	-19.6
APT-50psi	-13.1	13.1	-6.5
DL	-6.5	13.1	-6.5
0.15fpuB	-19.6	13.1	-6.5
0.15fpuT	-6.5	6.5	-13.1
0.45fpuB	26.2	58.9	0.0
0.45fpuT	39.3	52.4	6.5
0.75fpuB	78.5	111.3	6.5
0.75fpuT	98.1	124.4	13.1
APB-50psi	104.7	117.8	19.6
APT-50psi	104.7	117.8	26.2
APB-75psi	143.9	104.7	19.6
APT-75psi	157.0	98.2	19.6
APB-100psi	-214238	-213550	32.7
APT-100psi	-214238	-213550	39.2
APB-125psi	-214238	-213550	26.2
APT-125psi	-214238	-213550	32.7
0.85fpuB	-214238	-213550	45.8
0.85fpuT	-214238	-213550	52.3
APB-50psi	-214238	-213550	39.2
APT-50psi	-214238	-213550	52.3
APB-75psi	-214238	-213550	58.9
APT-75psi	-214238	-213550	45.8
APB-100psi	-214238	-213550	52.3
APT-100psi	-214238	-213550	45.8
APT-125psi	-214238	-213550	52.3

The embedded concrete gauge 15 inches away from the center of the beam in both directions (-15 inches from centerline to the non-stressing end and +15 inches from centerline to the stressing end) are shown in the Figure 3-31 and Figure 3-32.

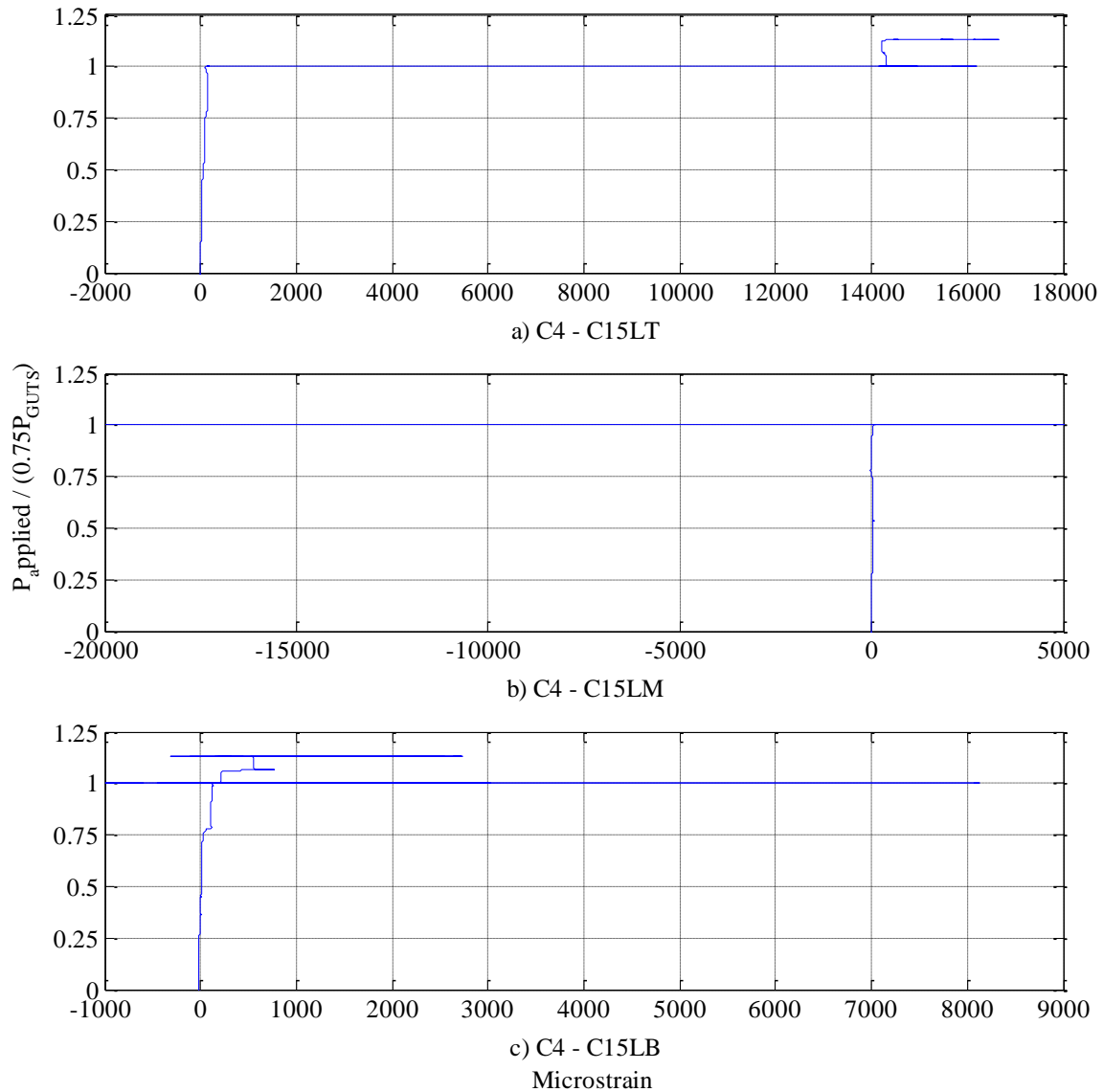


Figure 3-31: C4 embedded concrete strain at -15” from centerline.

The top and middle gauges acted very comparable to each other; each gauge increasing dramatically during the air pressure after 0.75fpu to around 20,000 $\mu\epsilon$ and the middle gauges breaking. The bottom strain gauge had larger strains when compared to the bottom strain gauge at the center of the beam.

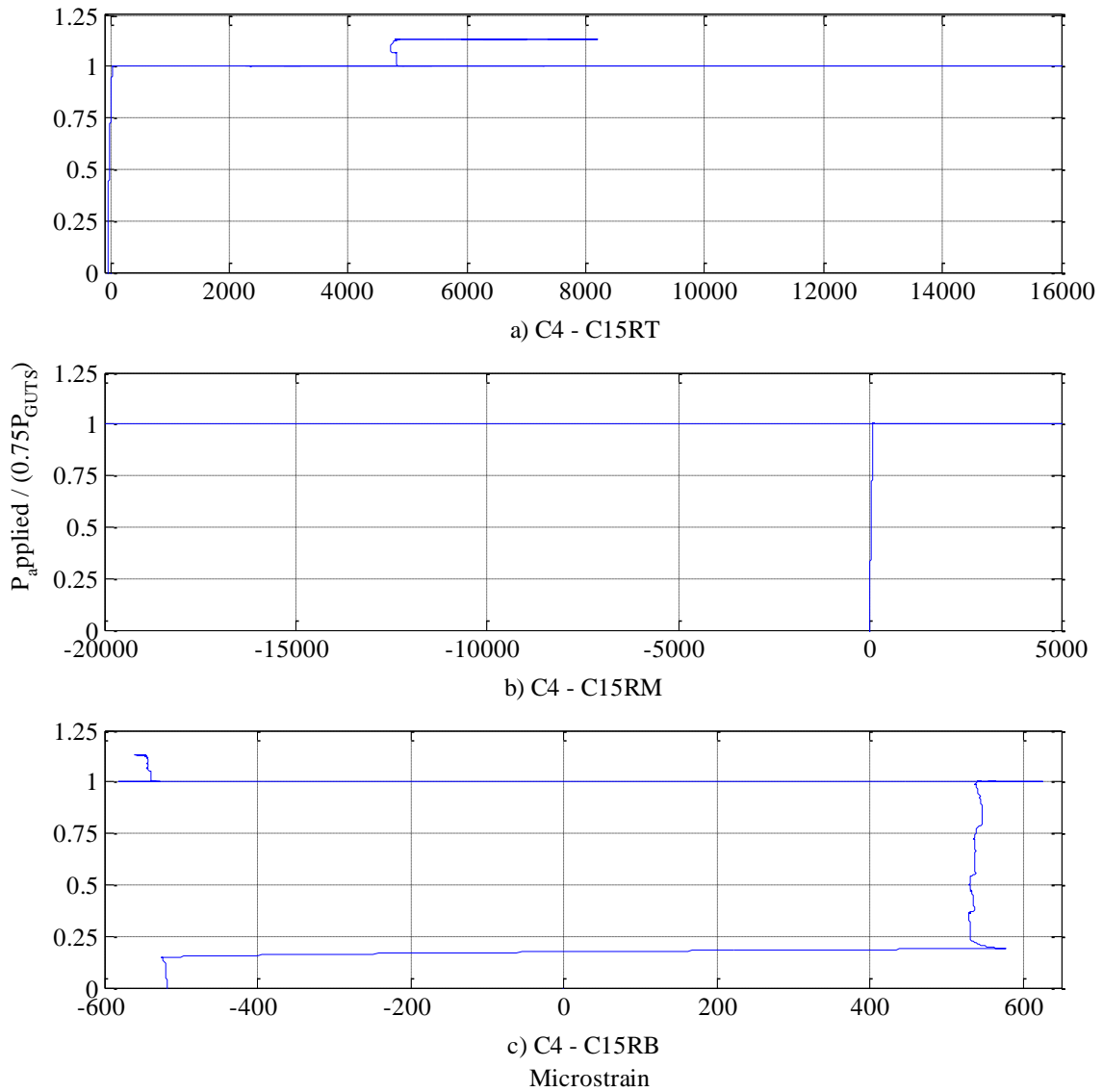


Figure 3-32: C4 embedded concrete strain at +15” from centerline.

The strain values at the end of each loading stage is presented in Table 3-13 for the embedded concrete strain at 15 inches from center to each side.

Table 3-13: C4 embedded concrete strain at 15" O.C. for each loading stage.

	C15TL	C15ML	C15BL	C15TL	C15ML	C15BL
	$\mu\epsilon$	$\mu\epsilon$	$\mu\epsilon$	$\mu\epsilon$	$\mu\epsilon$	$\mu\epsilon$
APB-50psi	19.6	0.0	-13.1	-26.2	-19.6	-497.4
APT-50psi	13.1	0.0	-6.5	-13.1	0.0	-517.0
DL	19.6	0.0	-13.1	-6.5	-6.5	-503.9
0.15fpuB	6.5	-13.1	-13.1	-52.3	0.0	-510.5
0.15fpuT	32.7	13.1	0.0	-32.7	6.5	-523.6
0.45fpuB	32.7	13.1	13.1	-26.2	32.7	536.7
0.45fpuT	71.9	52.4	6.5	-6.5	39.3	523.6
0.75fpuB	124.2	-6.5	130.8	19.6	72.0	549.7
0.75fpuT	111.2	45.8	130.8	39.2	91.6	549.7
APB-50psi	156.9	72.0	137.4	45.8	85.1	556.3
APT-50psi	150.4	72.0	137.4	52.3	98.2	543.2
APB-75psi	163.5	85.1	176.6	39.2	78.5	536.7
APT-75psi	176.6	91.6	170.1	52.3	78.5	536.7
APB-100psi	14379.6	-214029	150.5	4100.9	-212902	-530.1
APT-100psi	14203.1	-214029	294.4	2367.6	-212902	-536.7
APB-125psi	14523.5	-214029	-19.6	5088.5	-212902	-530.1
APT-125psi	14399.3	-214029	124.3	4905.3	-212902	-530.1
0.85fpuB	14261.9	-214029	765.5	4820.3	-212902	-536.7
0.85fpuT	14301.2	-214029	523.4	4866.1	-212902	-549.7
APB-50psi	14490.8	-214029	248.6	6429.2	-212902	-556.3
APT-50psi	14458.1	-214029	255.2	6305.0	-212902	-556.3
APB-75psi	15452.1	-214029	170.1	6069.5	-212902	-543.2
APT-75psi	15458.6	-214029	255.2	5925.6	-212902	-543.2
APB-100psi	16256.4	-214029	130.8	4905.3	-212902	-536.7
APT-100psi	16145.2	-214029	229.0	4794.1	-212902	-556.3
APT-125psi	16151.8	-214029	222.4	4800.7	-212902	-556.3

Strain gauges at -30 inches are shown in Figure 3-33 for the non-stressing end of the beam. The strain gauges at +30 inches are shown in Figure 3-34 for the stressing end of the beam. Just like the center of the beam and 15 inches from centerline, the middle strain gauges broke during the air pressure after 0.75fpu. The gauges located in the top are reaching higher strains, 7,500 $\mu\epsilon$, then the gauges on the bottom, 90 $\mu\epsilon$, but all the gauges are peaking at much smaller values compared to 15 inches from centerline (16,000 $\mu\epsilon$ and 8,000 $\mu\epsilon$, respectively). The stress in the top gauge compared to C2 decreased while the middle and bottom gauges remained relatively the same. Table 3-14 shows the strains at the end of each loading stage for embedded concrete gauges at 30 inches from centerline.

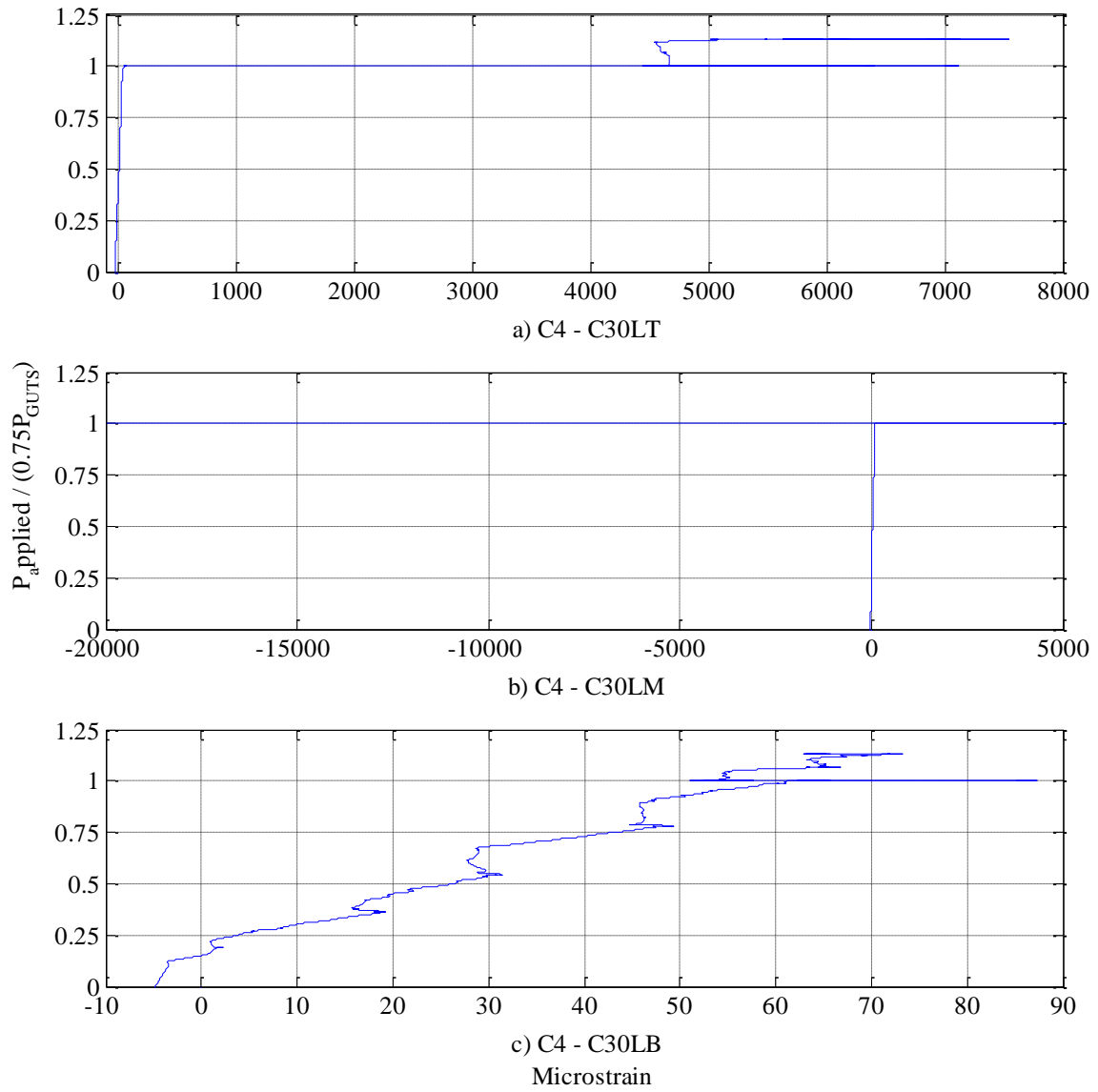


Figure 3-33: C4 embedded concrete strain at -30” from centerline.

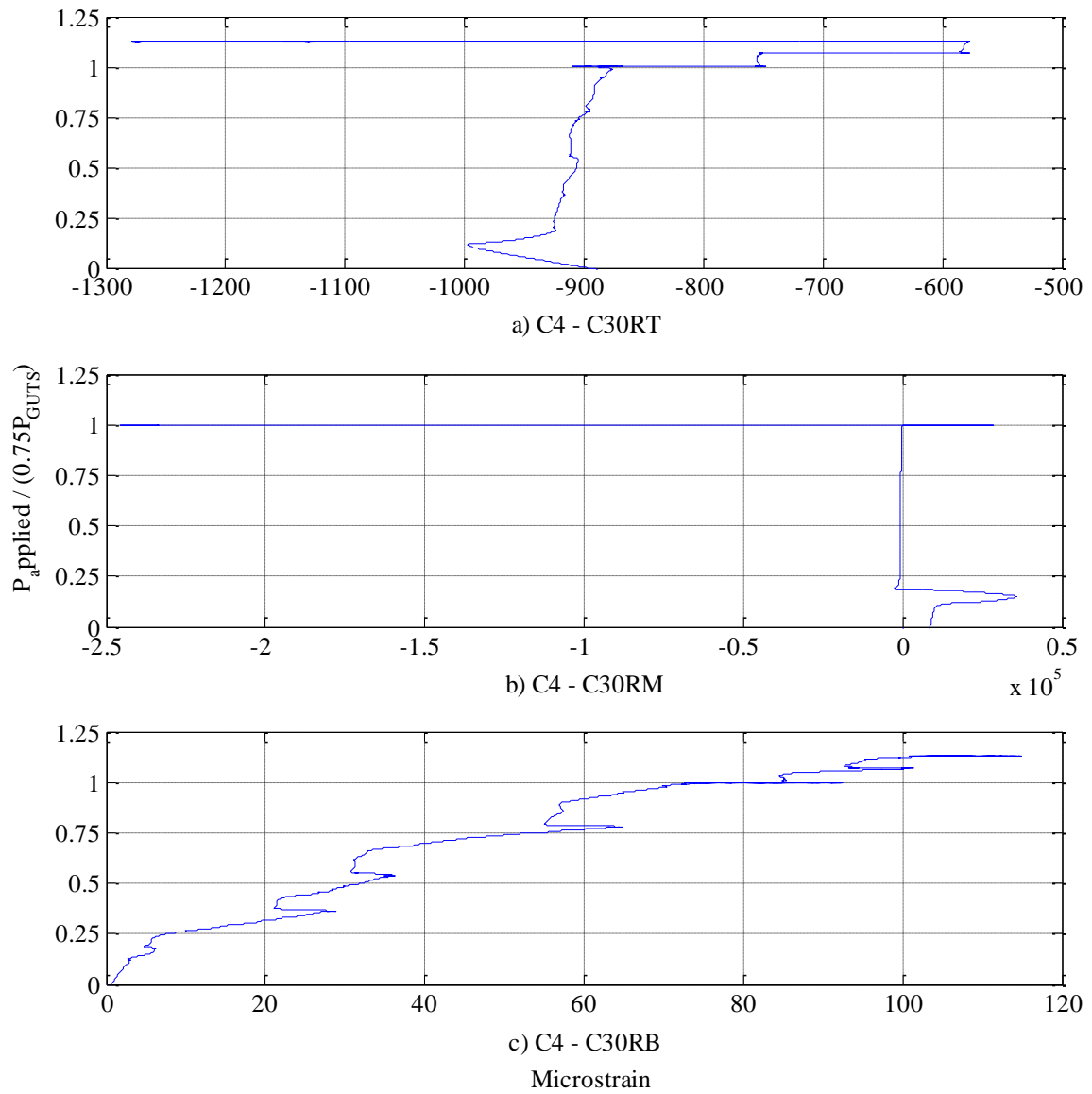


Figure 3-34: C4 embedded concrete strain at +30" from centerline.

Table 3-14: C4 embedded concrete strain at 30" O.C. for each loading stage.

	C30TL	C30ML	C30BL	C30TR	C30MR	C30BR
	μϵ	μϵ	μϵ	μϵ	μϵ	μϵ
APB-50psi	-6.5	0.0	0.0	268.3	-6.5	13.1
APT-50psi	-6.5	-6.5	6.5	261.7	-19.6	6.5
DL	-6.5	6.5	-13.1	268.3	-6.5	19.6
0.15fpuB	-19.6	-19.6	-13.1	-942.1	10187.9	6.5
0.15fpuT	6.5	-6.5	0.0	-935.6	37285.8	13.1
0.45fpuB	0.0	19.6	26.2	-916.0	-967.8	26.2
0.45fpuT	32.7	32.7	26.2	-909.4	-902.4	45.8
0.75fpuB	26.2	78.5	52.3	-883.3	-215.8	65.4
0.75fpuT	45.8	98.2	65.4	-889.8	-183.1	85.0
APB-50psi	52.3	111.3	65.4	-883.3	2635.2	78.5
APT-50psi	65.4	104.7	65.4	-876.7	2713.7	71.9
APB-75psi	52.3	98.2	72.0	-883.3	2883.7	71.9
APT-75psi	65.4	104.7	72.0	-896.4	3158.4	78.5
APB-100psi	4919.4	-214141	65.4	-765.5	-234034	85.0
APT-100psi	4455.0	-214141	58.9	-759.0	-234034	78.5
APB-125psi	4912.9	-214141	52.3	-745.9	-234034	78.5
APT-125psi	4723.2	-214141	52.3	-759.0	-234034	78.5
0.85fpuB	4631.6	-214141	65.4	-739.3	-234034	111.2
0.85fpuT	5017.6	-214141	78.5	-582.3	-234034	98.1
APB-50psi	5717.6	-214141	72.0	-1131.9	-234034	98.1
APT-50psi	5632.5	-214141	65.4	-1138.4	-234034	104.6
APB-75psi	6162.4	-214141	58.9	-1269.3	-234034	104.6
APT-75psi	6110.1	-214141	65.4	-1269.3	-234034	111.2
APB-100psi	6214.7	-214141	58.9	-1282.4	-234034	117.7
APT-100psi	6031.6	-214141	65.4	-1262.7	-234034	104.6
APT-125psi	6011.9	-214141	65.4	-1288.9	-234034	111.2

3.3.1.2 Concrete Surface Strain Gauges

The number of surface strain gauges was increased for C3 over C1 and C2, and maintained for C4, following the same location as Figure 2-34. The surface strain gauge results are presented in Figure 3-35, Figure 3-36 and Figure 3-37.

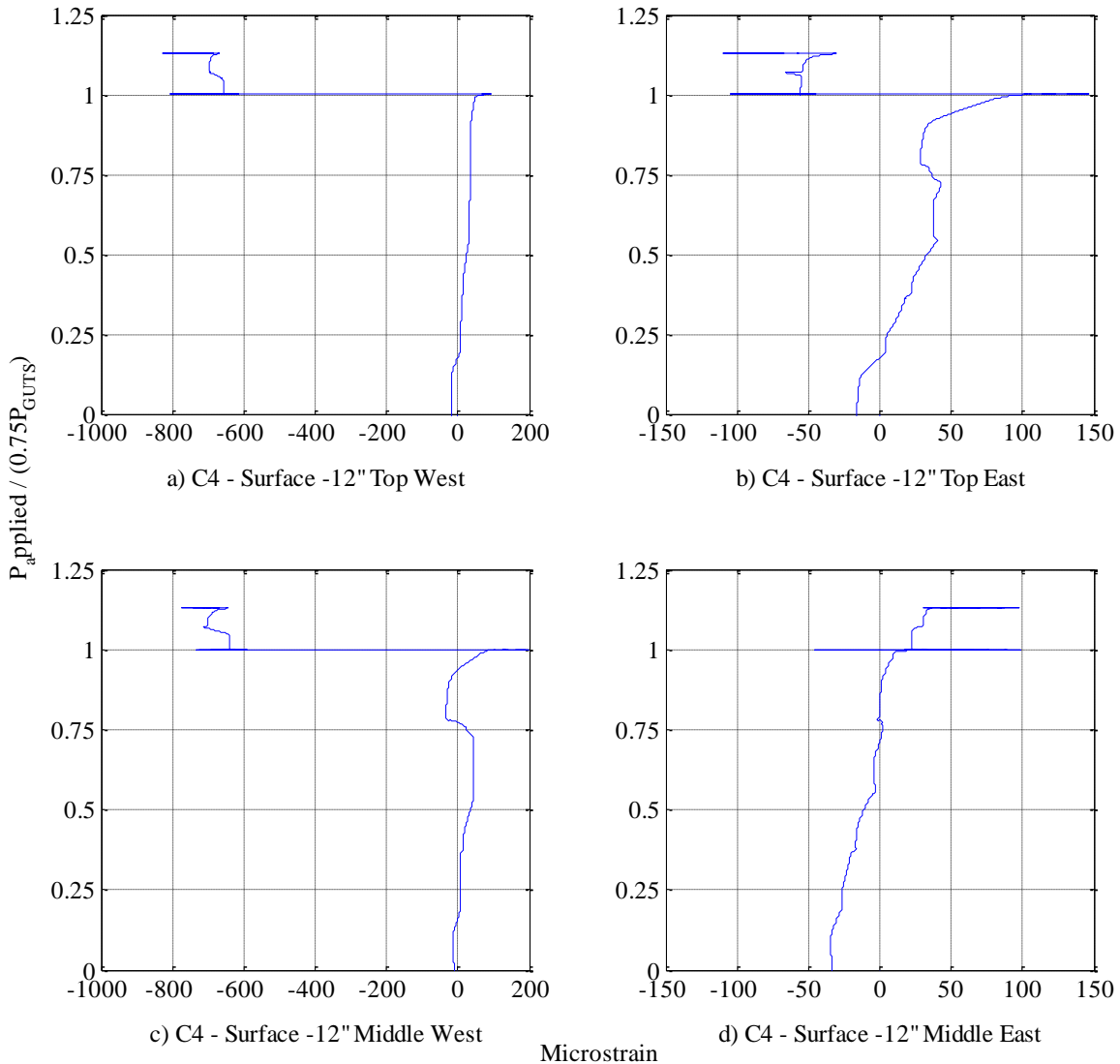


Figure 3-35: C4 concrete surface strain at -6" from centerline.

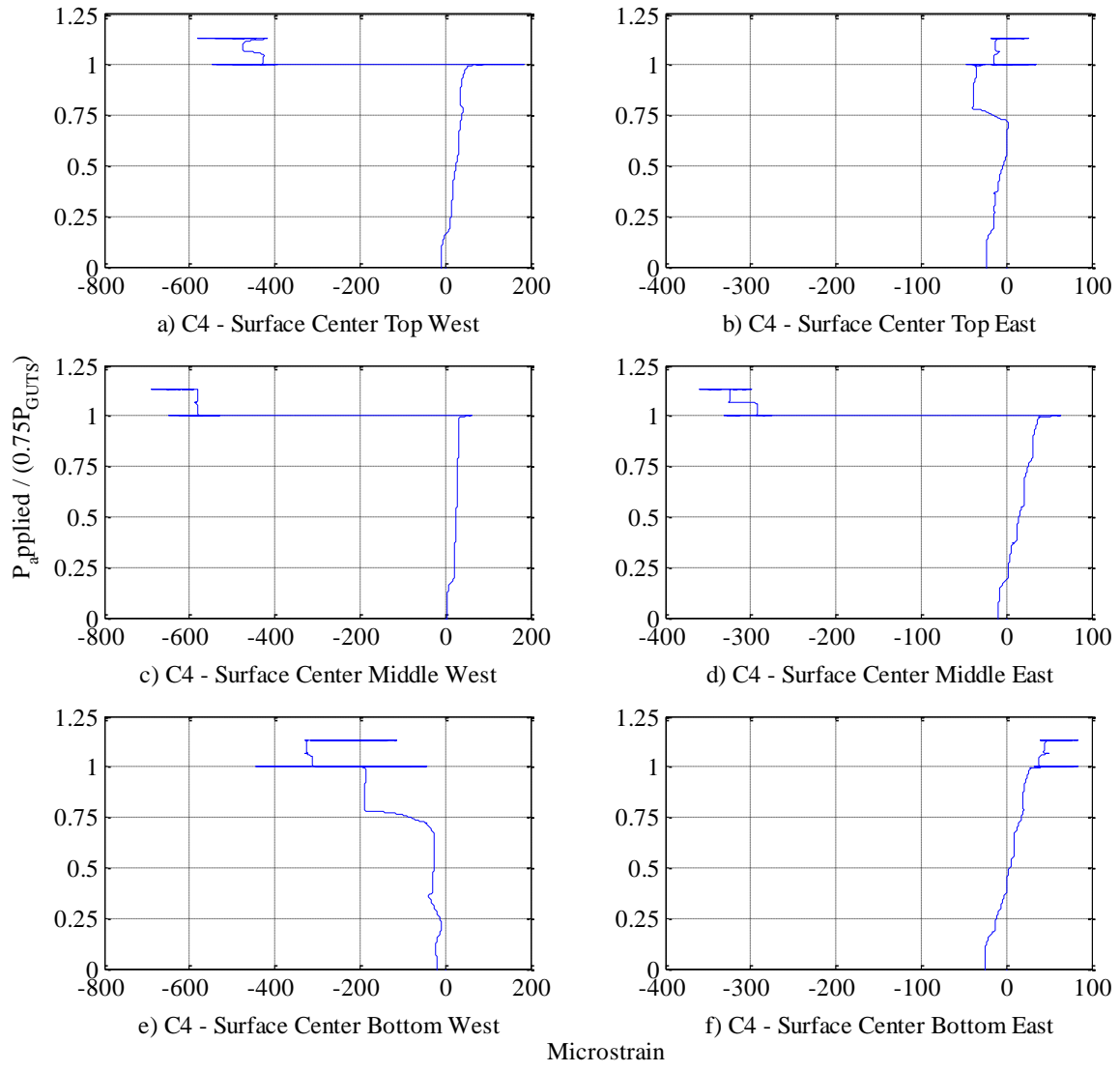


Figure 3-36: C4 concrete surface strain at centerline.

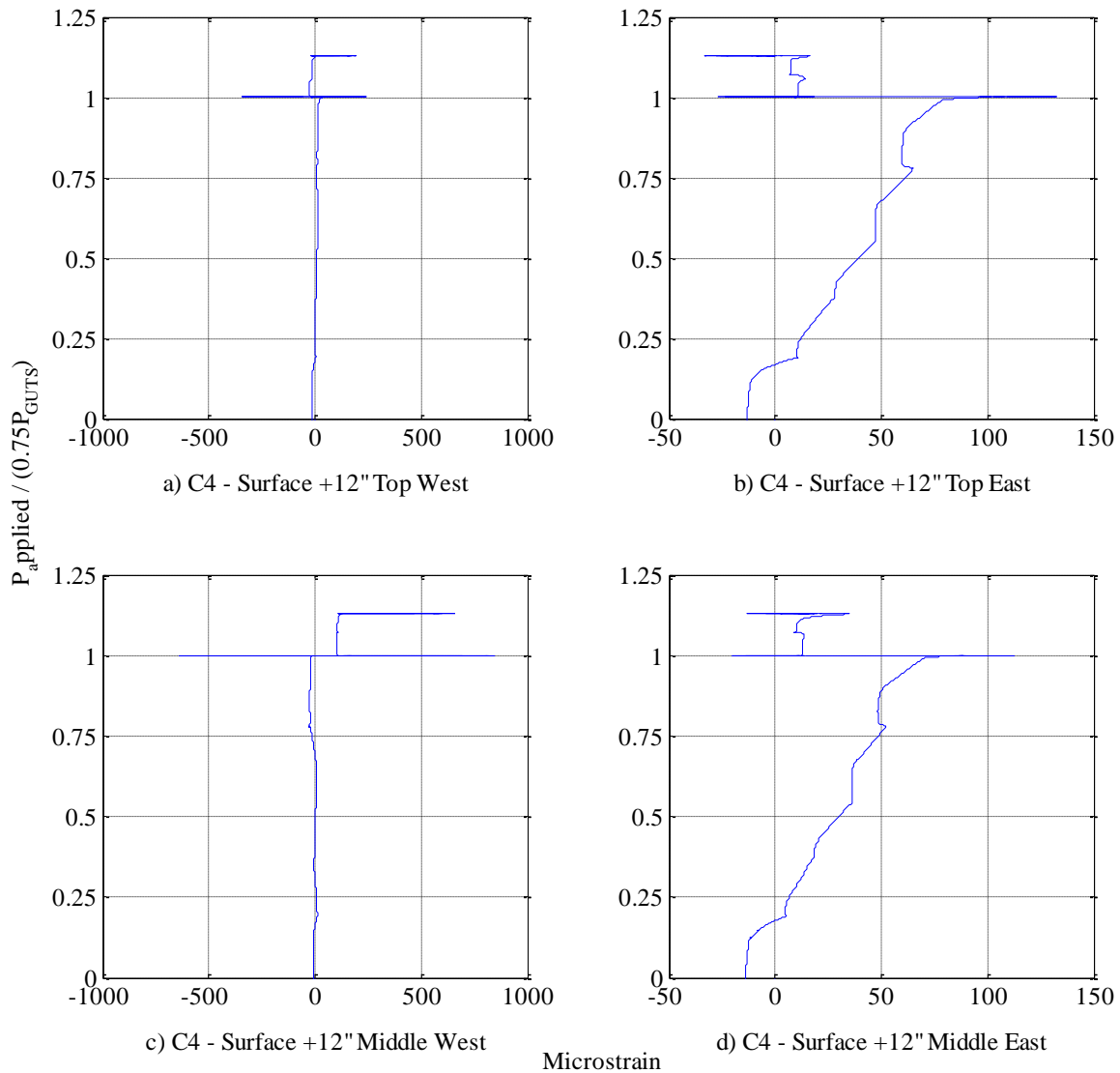


Figure 3-37: C4 concrete surface strain at +6" from centerline.

Overall the results from both sides of the web (east and west) for the concrete surface strain gauges acted comparable with larger strain on the side the ducts were tied (the west side). The performance for the surface concrete gauges are very close to the previous beams with air pressure providing the largest strains for the beam reaching a peak strain around $1,000 \mu\epsilon$. Table 3-15 and Table 3-16 show the strain for each loading stage for the concrete surface strain gauges.

Table 3-15: C4 concrete west surface strain at each loading stage.

	CSLTW $\mu\epsilon$	CSLMW $\mu\epsilon$	CSCTW $\mu\epsilon$	CSCMW $\mu\epsilon$	CSCBW $\mu\epsilon$	CSRTW $\mu\epsilon$	CSRMW $\mu\epsilon$
APB-50psi	-5.9	-3.3	-2.0	4.6	-9.2	-4.6	-8.5
APT-50psi	-5.2	-4.6	0.0	5.2	-9.2	-2.0	-6.5
DL	-2.0	0.0	0.7	5.2	-6.6	-1.3	-3.9
0.15B	-15.7	-7.9	-7.2	4.6	-23.6	-20.3	-13.1
0.15T	-6.6	0.0	0.7	8.5	-17.0	-7.2	0.7
0.45B	-1.3	-8.5	16.4	20.3	-41.3	9.8	9.8
0.45T	11.1	4.6	29.5	25.5	-26.2	31.4	46.5
0.75B	6.6	-32.8	41.9	30.1	-191.9	36.0	-33.4
0.75T	19.0	-18.3	51.1	34.1	-190.0	48.5	75.3
APB-50psi	36.7	-7.2	71.4	57.6	-216.8	78.6	100.2
APT-50psi	37.3	-3.9	73.4	58.3	-216.8	80.6	125.1
APB-75psi	35.4	-19.7	76.6	57.6	-266.6	68.8	122.5
APT-75psi	40.0	-17.7	80.6	61.6	-271.9	75.3	165.7
APB-100psi	-7.9	140.2	-408.1	-556.8	-294.8	-638.0	-607.8
APT-100psi	4.6	161.1	-398.9	-530.6	-288.9	-620.3	-597.3
APB-125psi	-3.3	144.1	-420.6	-569.9	-288.9	-653.7	-626.1
APT-125psi	-15.1	126.4	-430.4	-577.2	-300.0	-659.6	-637.2
0.85B	-6.6	103.5	-472.3	-585.7	-328.9	-698.3	-714.5
0.85T	0.7	122.5	-417.3	-580.4	-321.7	-668.1	-645.1
APB-50psi	-15.1	115.9	-446.8	-600.7	-314.4	-691.7	-672.6
APT-50psi	-11.1	118.6	-444.1	-593.5	-312.5	-685.2	-666.7
APB-75psi	-8.5	122.5	-470.4	-625.0	-310.5	-706.8	-692.2
APT-75psi	-11.1	115.9	-471.7	-621.7	-313.1	-709.4	-694.2
APB-100psi	-9.8	111.4	-493.3	-654.5	-311.8	-727.1	-713.2
APT-100psi	-11.8	108.1	-493.3	-649.9	-315.1	-728.4	-713.2
APT-125psi	-10.5	106.8	-493.3	-650.5	-313.8	-729.1	-715.8

Table 3-16: C4 concrete east surface strain at each loading stage.

	CSLTE	CSLME	CSCTE	CSCME	CSCBE	CSRTE	CSRME
	$\mu\epsilon$						
APB-50psi	-19.7	-28.8	-22.3	-19.0	-29.5	-17.7	-18.3
APT-50psi	-21.0	-28.2	-21.6	-20.3	-30.1	-17.7	-17.0
DL	-17.0	-26.2	-19.7	-15.7	-24.9	-13.1	-14.4
0.15B	-13.8	-34.1	-24.2	-8.5	-22.9	-11.8	-11.8
0.15T	-2.6	-28.2	-19.7	-6.6	-21.6	-3.9	-4.6
0.45B	19.0	-18.3	-12.4	7.2	-1.3	24.9	18.3
0.45T	40.6	-5.9	-0.7	17.7	7.2	45.9	36.7
0.75B	28.2	-1.3	-40.6	28.8	21.0	63.6	52.4
0.75T	85.2	11.1	-36.7	37.3	26.9	79.3	71.4
APB-50psi	104.2	32.1	-28.8	59.0	48.5	97.0	89.1
APT-50psi	116.0	31.4	-29.5	59.6	47.2	98.9	86.5
APB-75psi	114.7	20.3	-35.4	61.6	48.5	98.3	84.5
APT-75psi	132.4	22.3	-36.7	62.2	51.1	103.5	88.4
APB-100psi	-61.6	17.0	-16.4	-326.3	35.4	7.2	8.5
APT-100psi	-47.8	21.6	-13.8	-313.8	39.3	13.1	13.1
APB-125psi	-57.0	22.3	-14.4	-292.8	37.3	7.9	10.5
APT-125psi	-55.7	22.9	-15.1	-292.2	39.3	9.2	10.5
0.85B	-65.5	26.2	-9.2	-301.4	49.1	10.5	11.8
0.85T	-30.8	37.3	-10.5	-323.6	48.5	16.4	37.3
APB-50psi	-78.0	35.4	-16.4	-349.2	45.2	-10.5	16.4
APT-50psi	-72.1	35.4	-14.4	-347.2	42.6	-6.6	16.4
APB-75psi	-77.3	41.3	-15.7	-359.7	45.9	-8.5	11.8
APT-75psi	-71.4	45.2	-11.8	-307.9	50.4	-3.3	15.1
APB-100psi	-74.1	49.1	-13.8	-319.7	51.8	-3.9	11.8
APT-100psi	-72.1	50.4	-11.8	-319.0	52.4	-2.6	11.8
APT-125psi	-72.7	53.1	-10.5	-317.7	54.4	-3.9	12.4

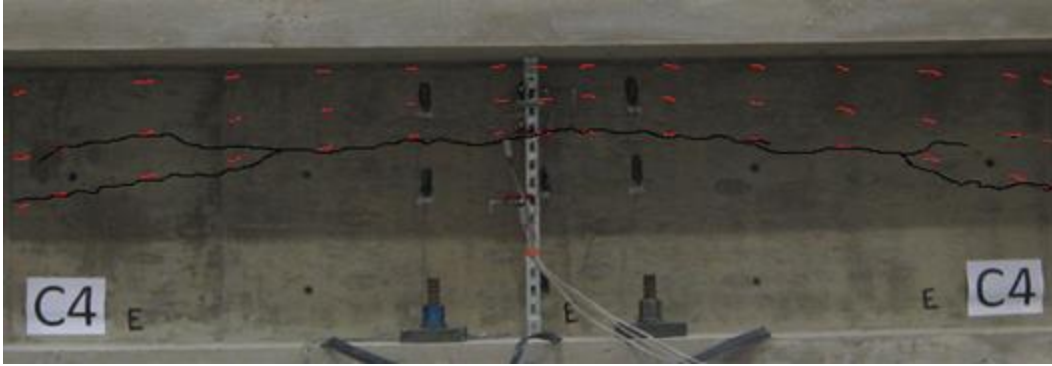


Figure 3-38: C4 crack appearance at 100psiB after 0.75fpu.

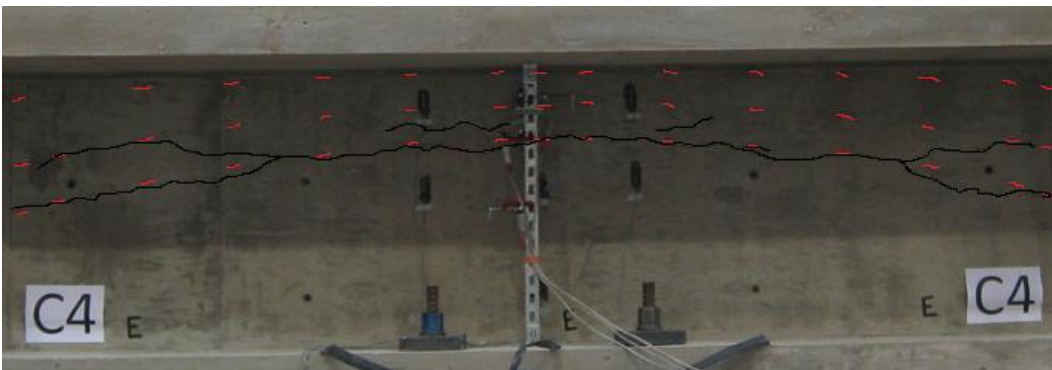


Figure 3-39: C4 web face after loading with cracks shown for clarity.

Cracking first appeared in C4 during 100 psi air pressure testing of the middle duct after 0.75fpu with the crack outline shown in Figure 3-38. The cracking on the surface follows the bottom ducts layout as seen in Figure 3-39. The cracks are highlighted in Figure 3-39 to be able to see the cracks as the cracks were only 0.04 inches on the web surface. There is a slight decrease in crack width compared to C2, which had 0.05 inch crack. The cracking became visible during 100 psi air pressure testing of the middle duct after 0.75fpu.

3.3.1.3 Cross Sectional Cracks

The crack width decreased around the ducts compared to C2 with 0.03 inch crack between top and middle ducts, 0.03 inches between middle and bottom ducts and 0.06 inch crack below the bottom duct. The cross section is shown in Figure 3-40 with cracks between all three ducts and a crack extending down through the web towards the base flange.



a) Cross section with cracks.



b) Cross section with cracks drawn.

Figure 3-40: C4 cut beam cross section.

3.3.1.4 Web Bulging

Similarly to C3, displacement transducers were placed on the face of the web to measure the bulging of the web. The results for C4 web bulging are provided in Figure 3-41. Similarly to C3, the air pressure had the greatest effect on the bulging of the web. Specifically the 100 psi air pressure test after 0.75fpu drastically increased the web bulging from 0 to 0.12 inches for the west side with the west side of the web having a more significant increase than the east side due to the ducts being secured to the shear reinforcement on the west side. The web bulging at the end of each loading stage is shown in Table 3-17. The total web bulge shown in Table 3-17 is the bulge from both faces in the middle gauge.

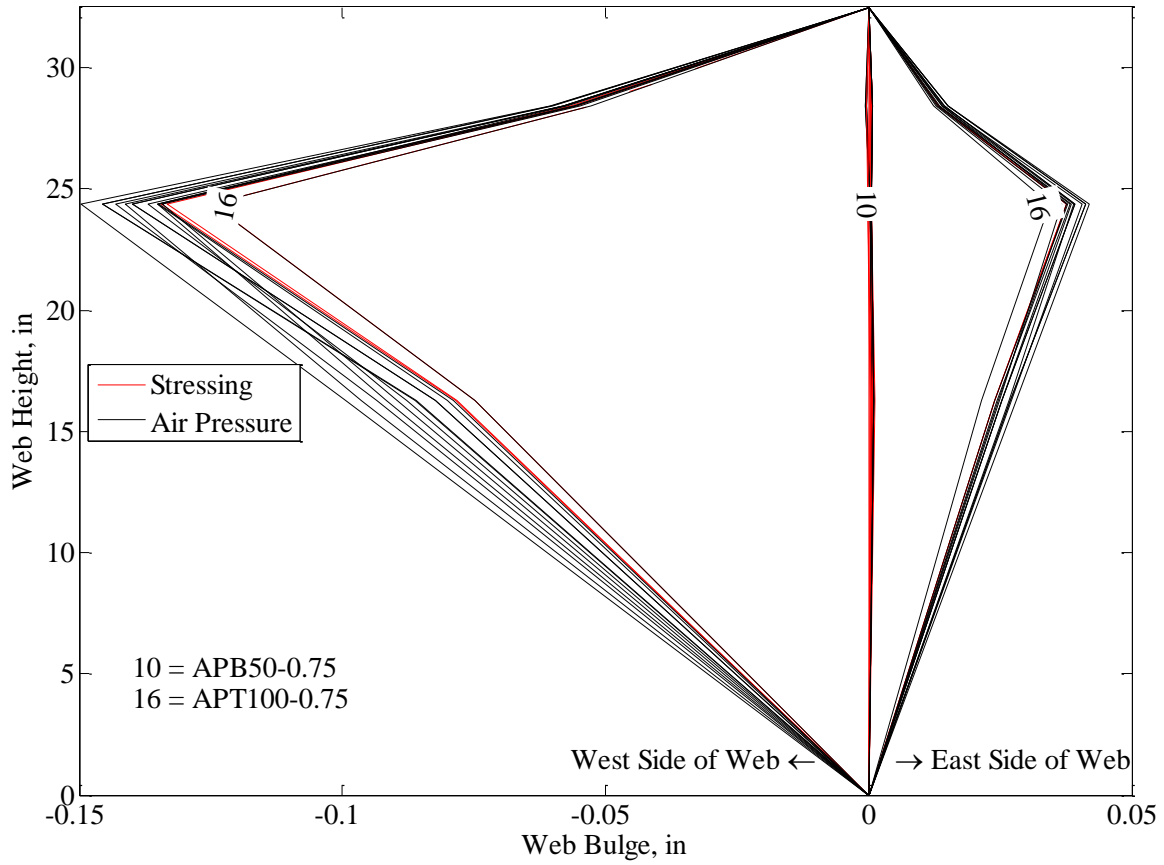


Figure 3-41: C4 web bulge.

Table 3-17: C4 web bulge values at each loading stage.

	WBTW in.	WBMW in.	WBMB in.	WBTE in.	WBME in.	WBBE in.	M. Total in.
APIB	-0.002	-0.002	-0.002	0.002	0.000	0.001	0.004
APIT	-0.002	-0.002	-0.002	0.002	0.000	0.002	0.005
DL	-0.002	-0.002	-0.003	0.002	0.000	0.002	0.005
0.15fpuB	0.000	0.000	0.000	0.000	0.000	0.000	0.000
0.15fpuT	0.000	0.000	0.000	0.000	0.000	0.000	0.000
0.45fpuB	0.000	0.000	0.000	0.000	0.000	0.001	0.001
0.45fpuT	0.000	0.000	0.000	0.000	0.000	0.001	0.001
0.75fpuB	0.000	0.000	0.001	0.000	0.000	0.001	0.001
0.75fpuT	0.000	0.000	0.001	0.000	0.000	0.001	0.001
APB-50psi	0.000	0.000	0.000	0.001	0.000	0.001	0.001
APT-50psi	0.000	0.000	0.001	0.001	0.000	0.001	0.001
APB-75psi	-0.001	0.000	0.001	0.001	0.000	0.001	0.002
APT-75psi	-0.001	0.000	0.001	0.001	0.000	0.001	0.002
APB-100psi	-0.054	-0.129	-0.076	0.013	0.035	0.023	0.165
APT-100psi	-0.052	-0.125	-0.075	0.012	0.034	0.021	0.159
APB-125psi	-0.057	-0.136	-0.080	0.014	0.038	0.024	0.173
APT-125psi	-0.057	-0.135	-0.080	0.014	0.038	0.024	0.173
0.85fpuB	-0.055	-0.134	-0.078	0.013	0.038	0.024	0.172
0.85fpuT	-0.055	-0.133	-0.078	0.013	0.037	0.024	0.170
APB-50psi	-0.056	-0.135	-0.079	0.013	0.038	0.024	0.173
APT-50psi	-0.056	-0.135	-0.079	0.013	0.038	0.024	0.173
APB-75psi	-0.058	-0.140	-0.082	0.014	0.039	0.025	0.179
APT-75psi	-0.058	-0.140	-0.082	0.014	0.039	0.025	0.179
APB-100psi	-0.060	-0.146	-0.086	0.015	0.041	0.027	0.187
APT-100psi	-0.060	-0.145	-0.085	0.015	0.041	0.027	0.186
APT-125psi	-0.060	-0.145	-0.085	0.015	0.041	0.027	0.186

3.3.1.5 Shear Reinforcement Gauges and Beam End Displacement

The strain gauge results from the shear reinforcement and the beam end displacement was not significant to this study. Therefore, refer to Appendices A and B for the results for the shear reinforcement strain gauges and the displacements on the ends of the beams.

3.3.1.6 C4 Results Overview

With a 50% increase in spacing between the ducts, the overall performance improved compared to C2. Air pressure still had a much larger impact on strain than the post-tensioning but the strains decreased with the increase in spacing. The increase in spacing allowed for more concrete between the ducts, thus increasing the tension capacity

of the concrete. Similar to C1, C2 and C3, the air pressure had the largest impact on the bulging of the web with the majority occurring during 100 psi air pressure after 0.75fpu; this was the same time cracks appeared on the web face.

3.3.2 Configuration 5

C5 design was based on C4. C4 and C5 had the same spacing between the ducts but C5 had the inclusion of steel reinforcement between the ducts at 17.5 inch spacing. The reinforcement was included to take the tension force produced between the ducts.

3.3.2.1 Embedded Concrete Strain Gauges

Figure 3-42 shows the embedded concrete strain gauges at centerline of the beam. The strain recorded in the middle and top strain gauge did not reach the limit of the strain gauge (22,000 microstrain) as seen in the C2 and C4. The strain associated with the air pressure after 0.75fpu still delivered the highest concrete strain increase compared to the stressing stages.

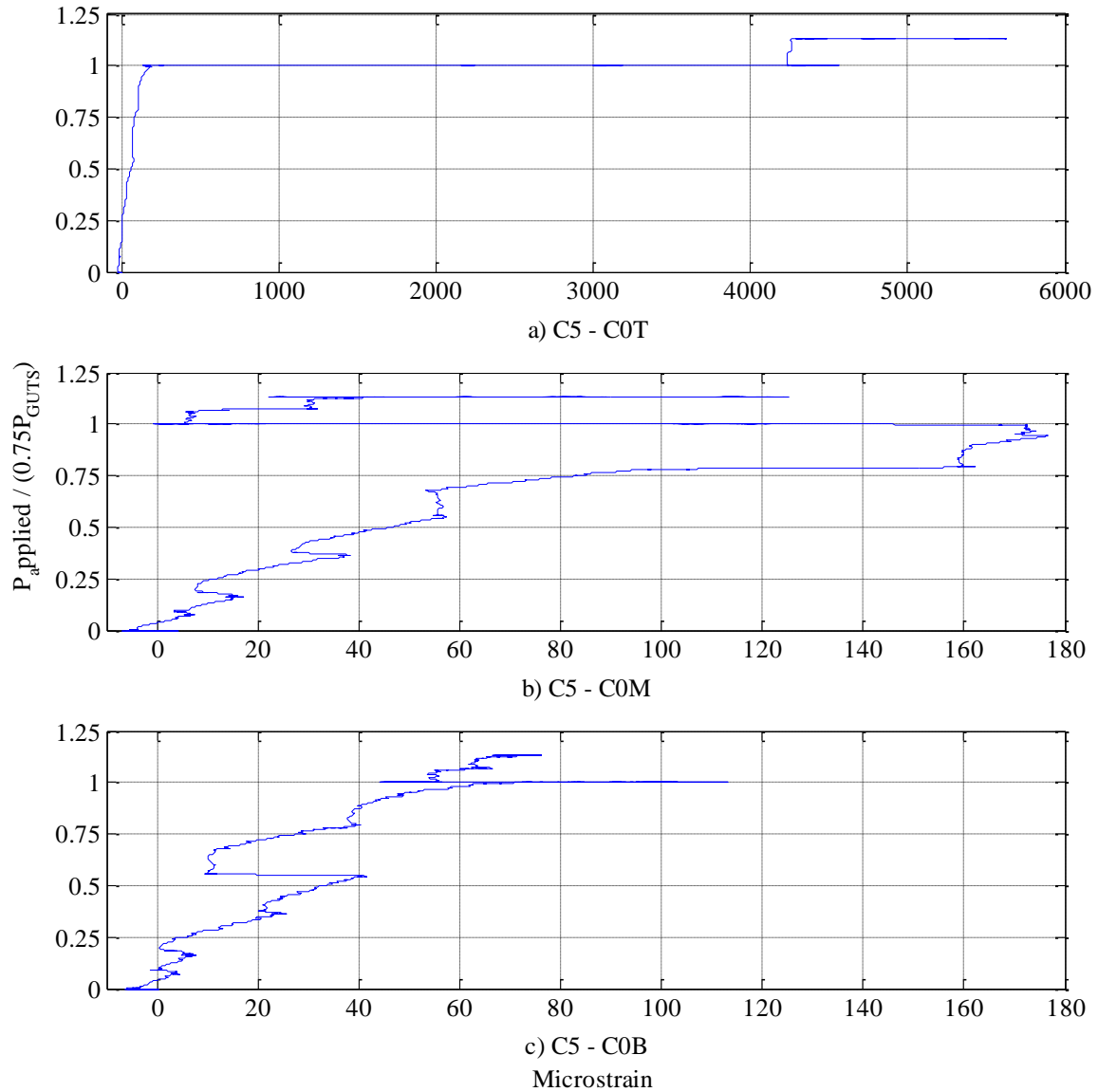


Figure 3-42: C5 embedded concrete strain at centerline

The strain associated with each loading step can be seen in Figure 3-43. It can be noted from the figure that post-tensioning had a larger impact on the strain in the middle gauge but the top gauge was still more affected from the air pressure. The post tensioning had a larger impact on the bottom gauge as well but the peak strain only reaching around 115 $\mu\epsilon$ compared to the middle gauge that reached 180 $\mu\epsilon$. The top gauge had the largest strain at 5,500 $\mu\epsilon$.

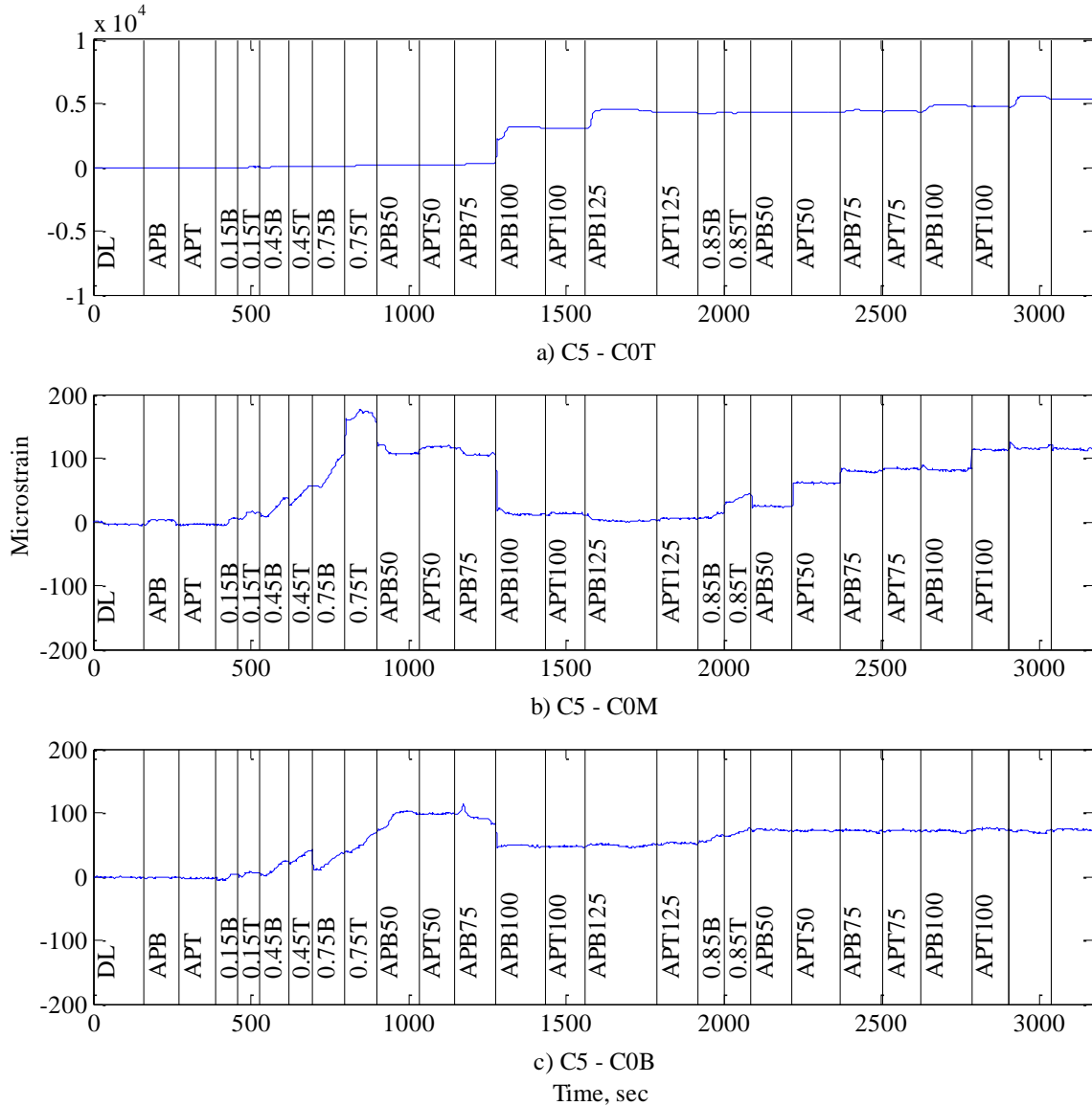


Figure 3-43: C5 embedded concrete strain versus time.

The strain for the embedded concrete strain gauge at -15 inches (from centerline to the non-stressing side) is shown in Figure 3-44 for the non-stressing side of the beam. The strain for the stressing side of the beam at +15 inches (from centerline to the stressing side) is shown in Figure 3-45.

Table 3-18: C5 embedded concrete strain at 0" O.C. at each loading stage.

	C0T	C0M	C0B
	μϵ	μϵ	μϵ
APB-50psi	-19.6	-6.5	0.0
APT-50psi	-32.7	6.5	0.0
DL	-26.2	0.0	0.0
0.15fpuB	-13.1	6.5	13.1
0.15fpuT	0.0	19.6	6.5
0.45fpuB	26.2	26.2	26.2
0.45fpuT	72.0	58.9	39.2
0.75fpuB	85.1	104.7	26.2
0.75fpuT	130.8	150.5	78.5
APB-50psi	163.6	124.4	91.5
APT-50psi	157.0	111.3	117.7
APB-75psi	215.9	104.7	78.5
APB-100psi	3042	0.0	45.8
APT-100psi	3003	6.5	52.3
APB-125psi	4298	0.0	52.3
APT-125psi	4266	0.0	52.3
0.85fpuB	4266	6.5	65.4
0.85fpuT	4272	52.4	65.4
APB-50psi	4311	13.1	71.9
APT-50psi	4292	58.9	71.9
APB-75psi	4364	72.0	65.4
APT-75psi	4364	85.1	71.9
APB-100psi	4737	85.1	71.9
APT-100psi	4711	104.7	78.5
APB-125psi	5365	124.4	85.0
APT-125psi	5312	111.3	85.0

Comparing 15 inches from centerline to midspan of the beam illustrates that the strain increases away from center as all three heights (top, middle and bottom) all have higher strains than at midspan. The strains between the two ends of the beam are all similar to each other with strains around 10,000 μϵ for both +/- 15 inches and at all three heights. The strains in the top and middle gauge are lower compared to C4. Whereas the bottom gauge reached a similar peak strain to C4 for the gauges at -15 inches (9,000 μϵ) but slightly higher for the gauges at +15 inches (7,250 μϵ). Table 3-19 shows the strain

values at the end of each loading stage for the embedded concrete gauges at 15 inches from center.

Table 3-19: C5 embedded concrete strain at 15" O.C. at each loading stage.

	C15TL	C15ML	C15BL	C15TR	C15MR	C15BR
	μϵ	μϵ	μϵ	μϵ	μϵ	μϵ
APB-50psi	-13.1	6.5	19.6	-19.6	-6.5	-6.5
APT-50psi	-6.5	-6.5	-13.1	-32.7	-6.5	6.5
DL	-6.5	0.0	-6.5	-26.2	-6.5	0.0
0.15fpuB	-6.5	26.2	0.0	-13.1	6.5	0.0
0.15fpuT	0.0	32.7	6.5	0.0	13.1	-6.5
0.45fpuB	39.2	91.6	13.1	32.7	19.6	19.6
0.45fpuT	98.1	333.8	6.5	58.9	45.8	39.3
0.75fpuB	78.5	916.2	-13.1	52.3	58.9	32.7
0.75fpuT	150.4	1446	0.0	163.5	91.6	39.3
APB-50psi	137.3	2565	-26.2	170.1	530.0	32.7
APT-50psi	143.9	3658	-13.1	228.9	536.6	39.3
APB-75psi	163.5	3652	-26.2	608.3	1446	52.4
APB-100psi	5016	10556	6104	3597	4921	3992
APT-100psi	4944	10465	5980	3597	4914	3894
APB-125psi	5630	12055	7013	3865	5163	4064
APT-125psi	5545	11983	6896	3878	5176	3992
0.85fpuB	5611	11617	6870	4160	6066	4261
0.85fpuT	5663	13299	6870	4474	5961	4162
APB-50psi	5885	18790	6935	4539	6341	4516
APT-50psi	5872	12572	6915	4533	6295	4477
APB-75psi	6068	14608	7079	4676	6478	4660
APT-75psi	6049	14608	7033	4644	6452	4614
APB-100psi	6356	10471	7556	4768	6419	4791
APT-100psi	6304	10910	7452	4729	6387	4725
APB-125psi	6506	11388	7635	4794	6419	4745
APT-125psi	6435	11427	7465	4775	6406	4660

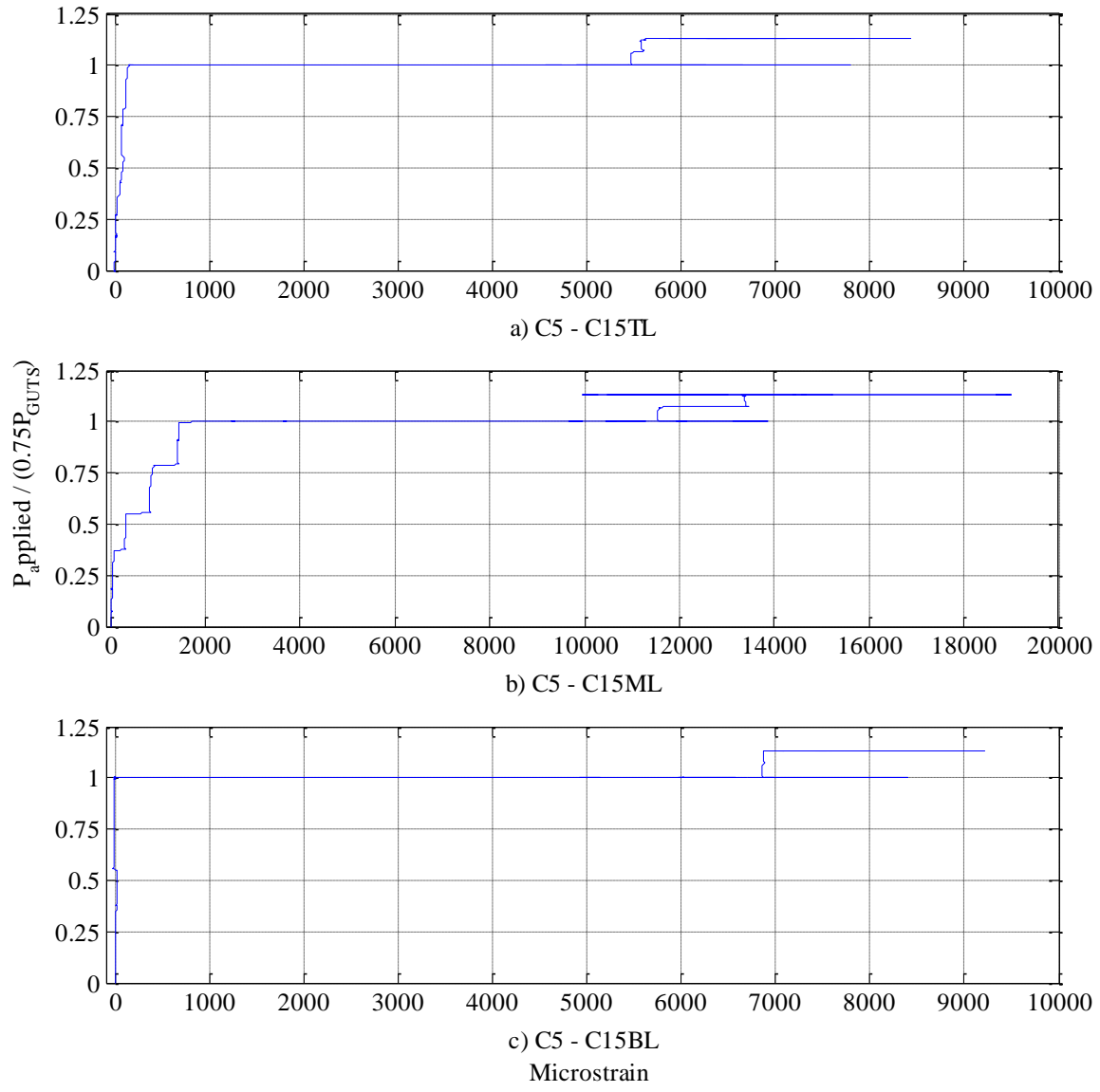


Figure 3-44: C5 embedded concrete strain at -15” from centerline.

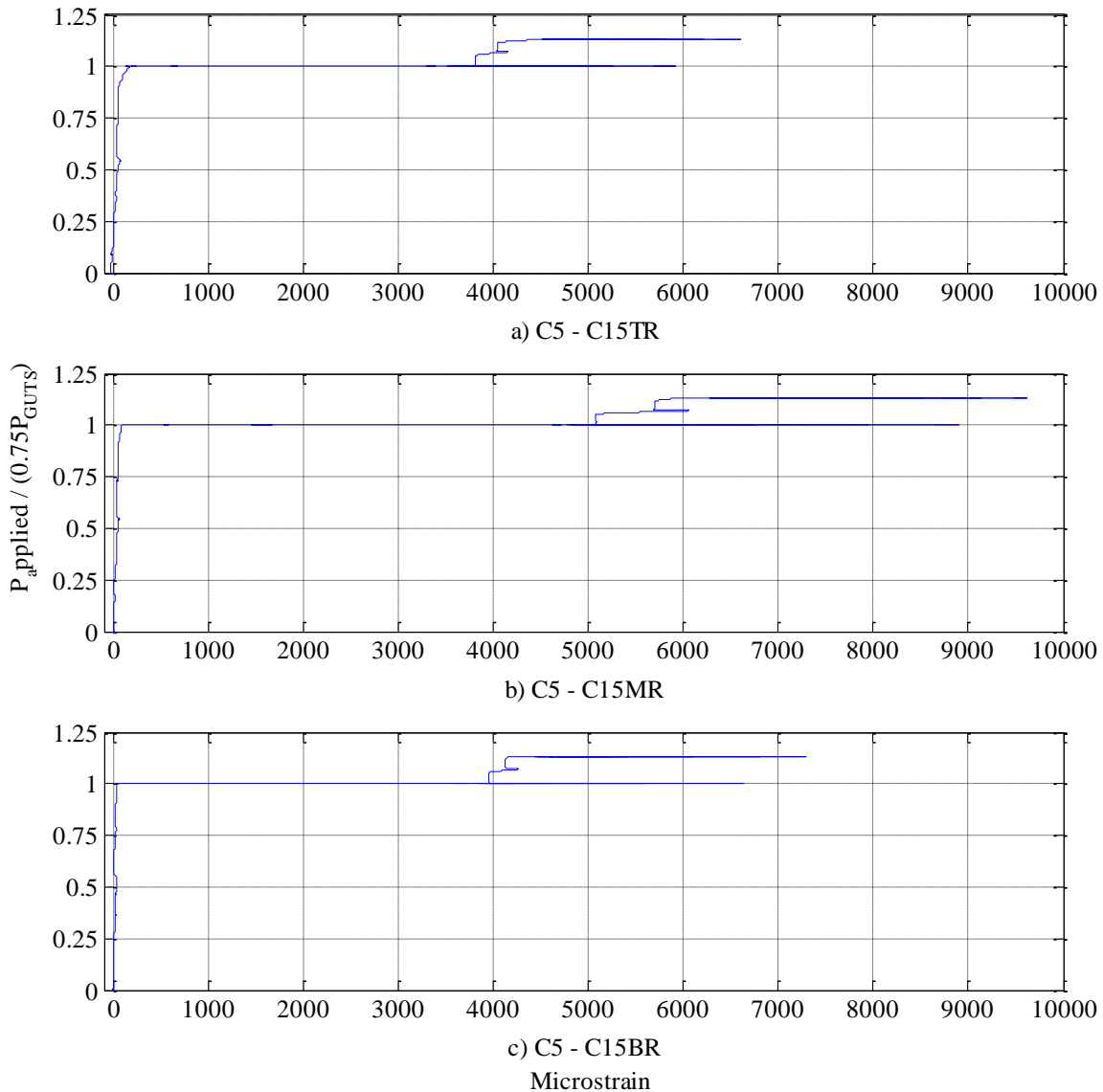


Figure 3-45: C5 embedded concrete strain at +15" from centerline.

The results for 30" from centerline are shown in Figure 3-46 and Figure 3-47. The gauges at 30 inches show a decrease in strain in the top and middle gauges for both ends compared to C4. The middle strain gauge reached its limit like previous configurations. As with all previous configurations, air pressure had a large impact on the strain around the ducts. Overall, the strains associated with the embedded concrete strain gauges were lower with the inclusion of the steel reinforcement between the ducts in C5 compared to C4 where no reinforcement was present. Table 3-20 shows the strain values for the embedded concrete strain gauges at 30 inches from center for all loading stages.

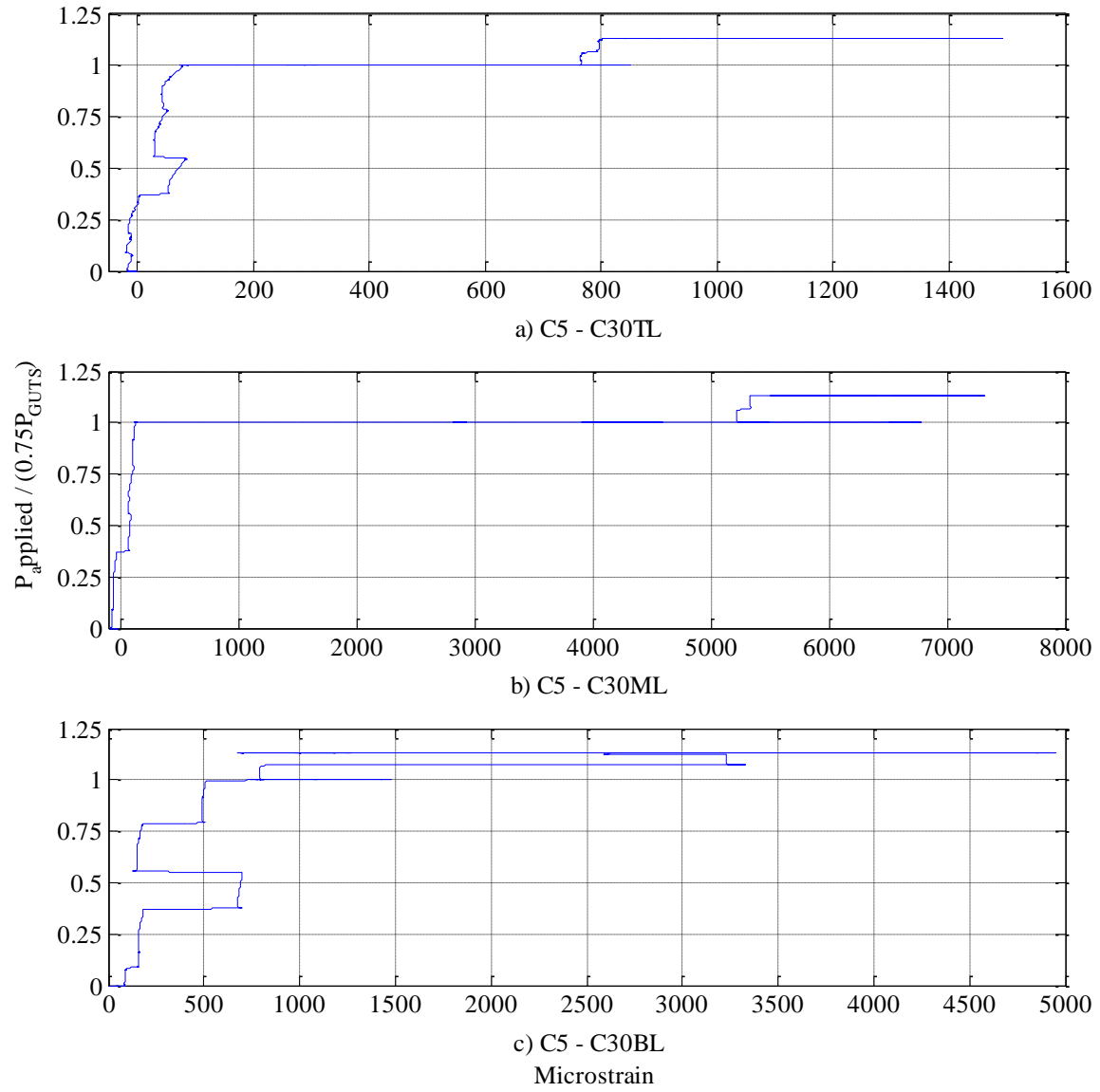
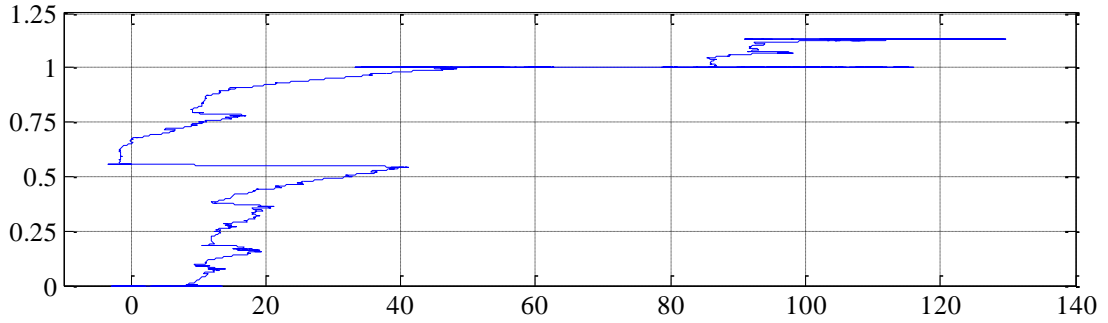
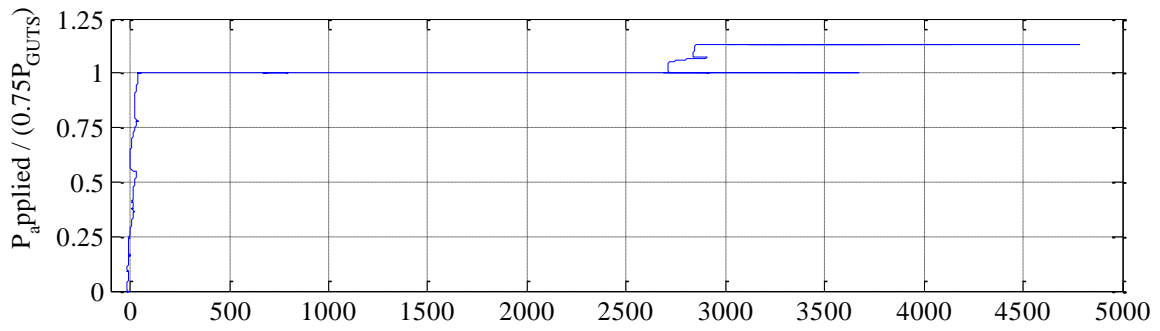


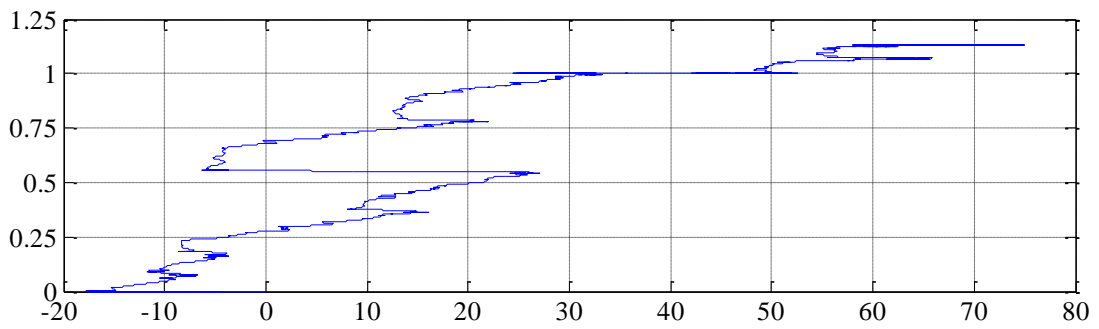
Figure 3-46: C5 embedded concrete strain at -30" from centerline.



a) C5 - C30TR



b) C5 - C30MR



c) C5 - C30BR

Microstrain

Figure 3-47: C5 embedded concrete strain at +30" from centerline.

Table 3-20: C5 embedded concrete strain at 30" O.C. at each loading stage.

	C30TL	C30ML	C30BL	C30TR	C30MR	C30BR
	με	με	με	με	με	με
APB-50psi	-26.2	-58.9	39.3	0.0	-19.6	-13.1
APT-50psi	-6.5	-45.8	45.8	6.5	-19.6	-26.2
DL	-13.1	-45.8	45.8	0.0	-26.2	-13.1
0.15fpuB	6.5	-65.4	91.6	6.5	-19.6	-6.5
0.15fpuT	-6.5	-72.0	150.5	19.6	-13.1	-6.5
0.45fpuB	6.5	-32.7	176.7	19.6	13.1	0.0
0.45fpuT	85.0	91.6	700.1	39.3	26.2	32.7
0.75fpuB	45.8	124.3	170.1	6.5	32.7	13.1
0.75fpuT	85.0	130.9	510.4	45.8	45.8	32.7
APB-50psi	72.0	137.4	1420	32.7	39.2	32.7
APT-50psi	58.9	130.9	1086	26.2	52.3	45.8
APB-75psi	78.5	124.3	1067	32.7	39.2	19.6
APB-100psi	255.1	3992	778.6	39.3	693.1	26.2
APT-100psi	268.2	3940	772.1	45.8	660.4	32.7
APB-125psi	765.4	5321	804.8	78.5	2746	39.2
APT-125psi	752.3	5255	791.7	72.0	2727	52.3
0.85fpuB	791.6	5347	817.9	111.2	2903	65.4
0.85fpuT	804.6	5340	2637	117.8	2851	58.9
APB-50psi	857.0	5510	4855	117.8	3028	58.9
APT-50psi	843.9	5504	1165	111.2	3015	71.9
APB-75psi	896.2	5707	680.5	98.1	3145	65.4
APT-75psi	896.2	5694	706.7	124.3	3132	58.9
APB-100psi	961.6	5811	988.0	104.7	3256	58.9
APT-100psi	961.6	5720	1001	117.8	3243	58.9
APB-125psi	1367	5877	1276	98.1	3466	65.4
APT-125psi	1354	5883	1250	85.1	3453	65.4

3.3.2.2 Concrete Surface Strain Gauges

The concrete surface strain gauges at locations noted in Figure 2-34 are shown in Figure 3-48, Figure 3-49 and Figure 3-50. Strains did not reach extreme levels on the surface of the web. Strains are highest at the cracks so the location of the gauge with respect to the crack can have a large impact on the strain values.

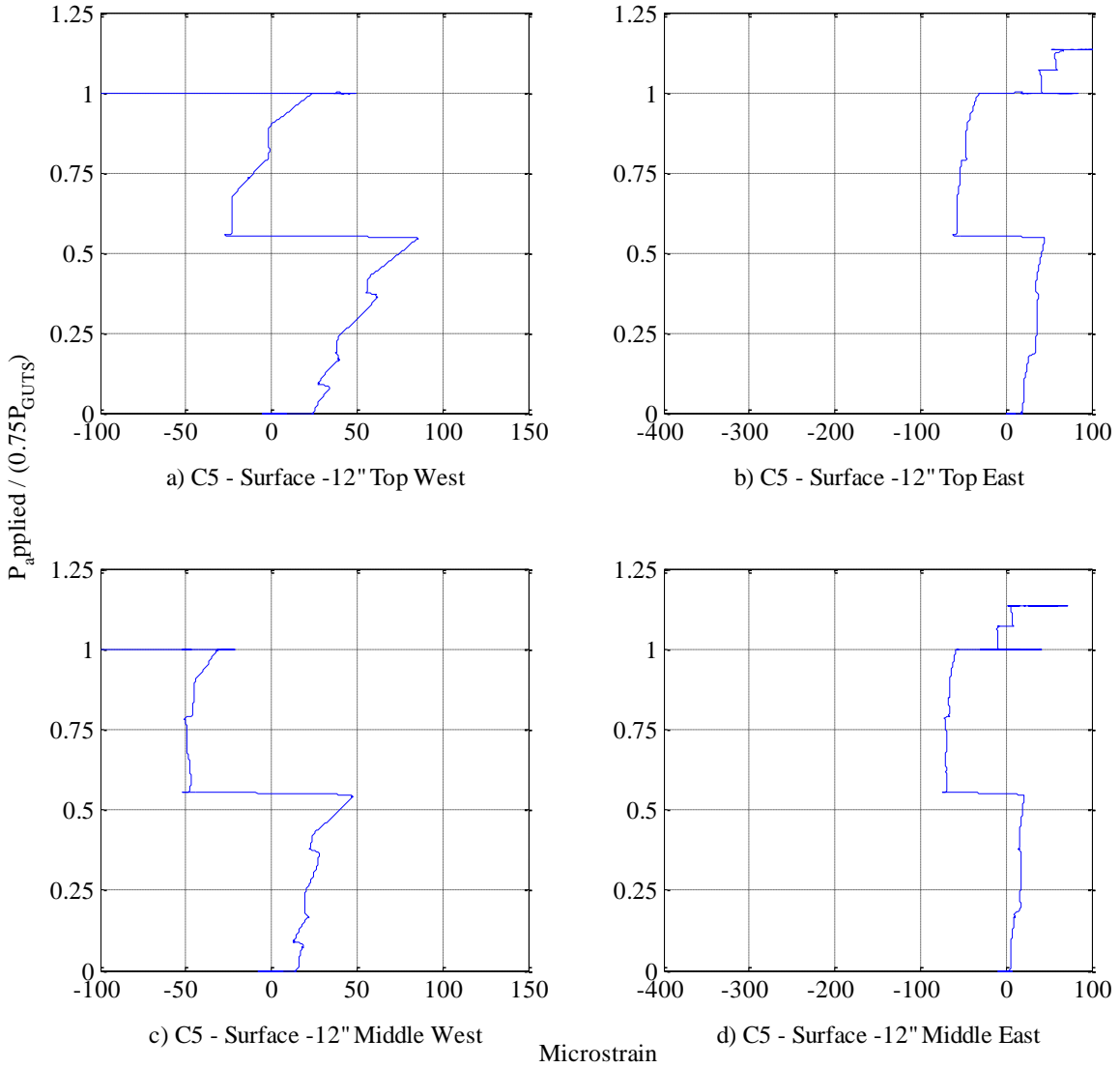


Figure 3-48: C5 concrete surface strain at -6" from centerline.

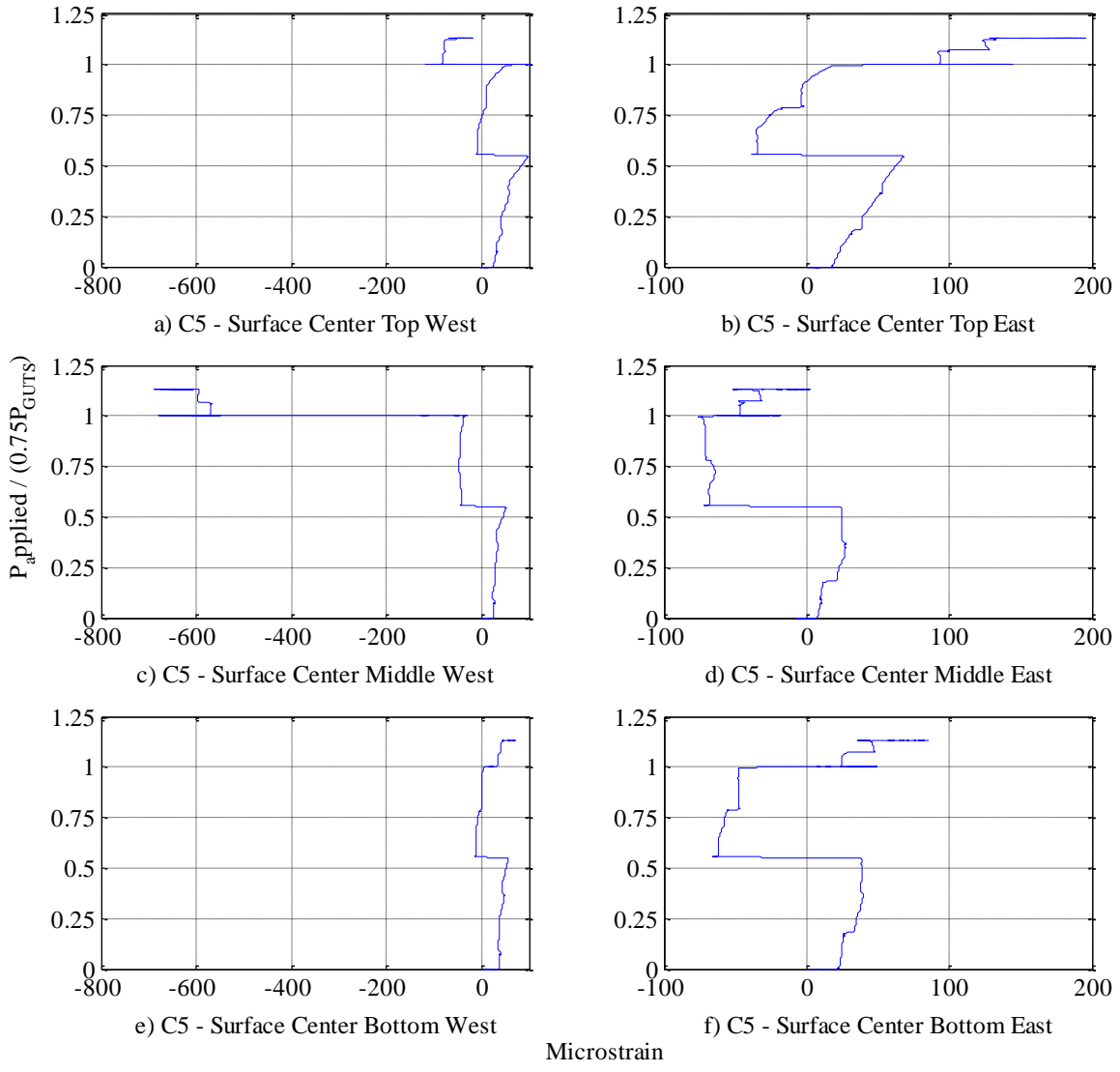


Figure 3-49: C5 concrete surface strain at centerline.

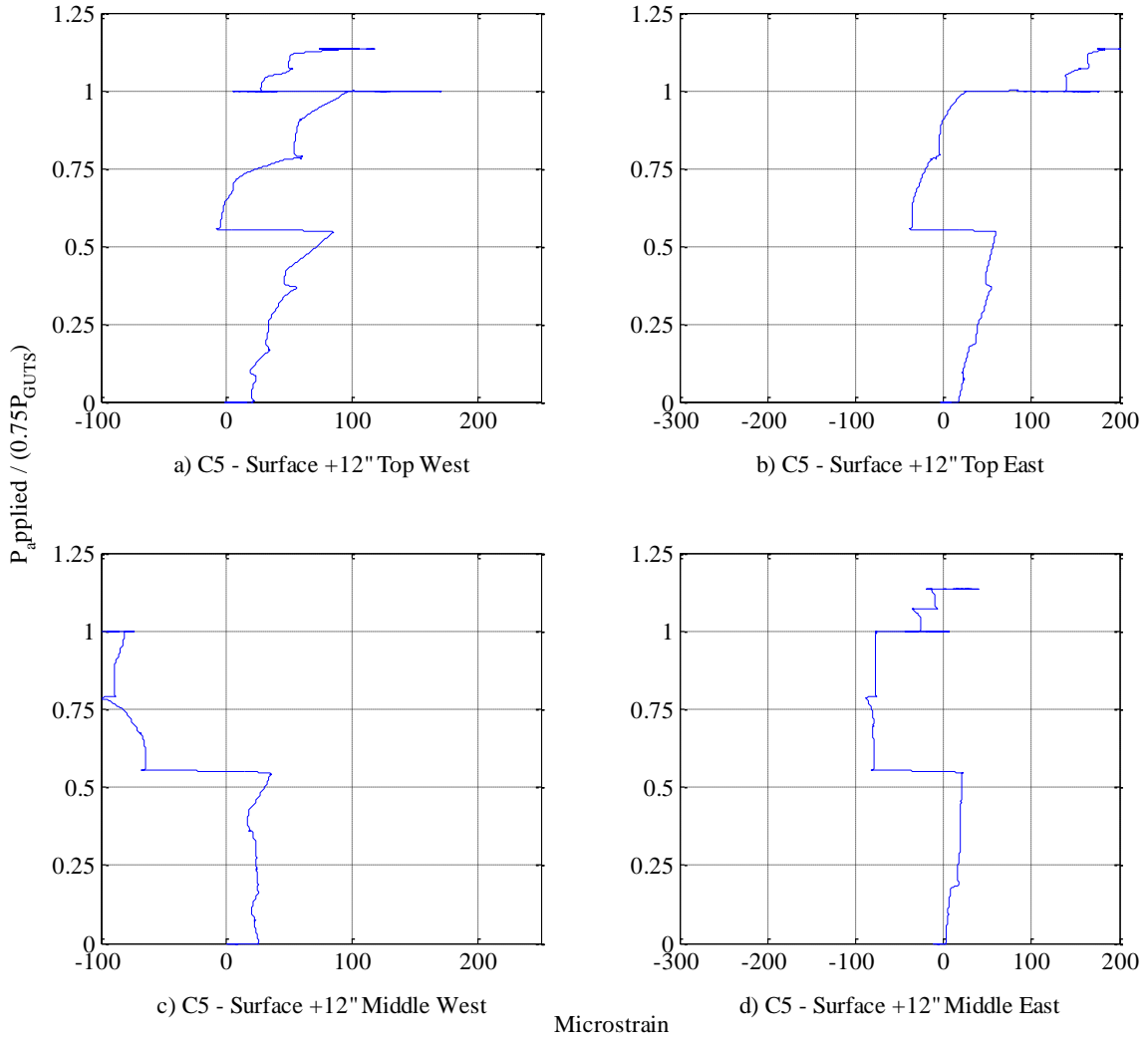


Figure 3-50: C5 concrete surface strain at +6" from centerline.

The concrete surface strain at the end of each loading stage is provided in Table 3-21 for the west side of the beam and Table 3-22 for the east side of the beam.

Table 3-21: C5 concrete west surface strain at each loading stage.

	CSLTW	CSLMW	CSCWTW	CSCMW	CSCBW	CSRTW	CSRMW
	$\mu\epsilon$						
APB-50psi	-2.0	0.0	-2.0	0.7	10.5	-4.6	-7.2
APT-50psi	3.9	7.2	5.9	8.5	17.0	2.6	-3.3
DL	4.6	7.2	5.9	8.5	17.7	3.9	-2.6
0.15B	24.2	22.9	32.1	26.9	39.3	33.4	18.3
0.15T	33.4	24.9	43.2	26.9	35.4	38.0	19.0
0.45B	55.0	17.0	58.3	32.1	47.2	61.6	27.5
0.45T	83.9	34.1	96.3	49.8	55.7	85.2	46.5
0.75B	60.9	-101.5	7.9	-49.8	-3.3	-4.6	-51.1
0.75T	95.0	-80.6	60.3	-38.7	4.6	24.9	-32.1
APB-50psi	117.3	-89.7	79.3	-51.8	15.7	37.3	-28.2
APT-50psi	120.6	-85.8	91.0	-48.5	19.7	42.6	-22.3
APB-75psi	148.7	-115.3	87.1	-110.7	21.0	17.0	-45.8
APB-100psi	22.3	-226.0	-71.4	-560.1	18.3	-189.3	-279.6
APT-100psi	25.6	-222.7	-64.8	-558.8	22.3	-182.8	-277.7
APB-125psi	22.9	-224.7	-81.9	-573.9	22.3	-231.2	-281.0
APT-125psi	26.2	-222.1	-77.3	-571.9	26.2	-225.3	-281.0
0.85B	51.8	-252.8	-77.9	-598.1	38.0	-245.0	-300.6
0.85T	88.5	-227.3	-36.7	-595.5	45.9	-203.7	-282.3
APB-50psi	83.2	-222.7	-45.9	-609.3	60.3	-210.3	-286.2
APT-50psi	83.9	-222.7	-41.3	-606.0	60.3	-207.0	-286.2
APB-75psi	87.8	-222.1	-37.3	-617.8	58.3	-212.9	-291.4
APT-75psi	89.8	-220.1	-33.4	-615.8	59.6	-209.0	-291.4
APB-100psi	94.4	-220.7	-34.1	-630.2	60.3	-216.2	-296.0
APT-100psi	100.3	-216.8	-29.5	-625.6	64.9	-209.0	-292.1
APB-125psi	104.8	-216.2	-32.1	-632.2	68.1	-229.3	-294.1
APT-125psi	110.7	-212.2	-24.9	-628.2	71.4	-222.7	-290.1

Table 3-22: C5 concrete east surface strain at each loading stage.

	CSLTE	CSLME	CSCTE	CSCME	CSCBE	CSRTE	CSRME
	με						
APB-50psi	1.3	-9.2	0.7	-6.6	5.9	-3.9	-11.1
APT-50psi	7.9	-4.6	6.6	-0.7	13.1	3.9	-5.2
DL	7.2	-4.6	6.6	-0.7	13.1	5.2	-4.6
0.15fpuB	21.0	7.2	22.9	9.8	26.2	22.3	5.9
0.15fpuT	26.2	9.8	32.1	11.1	26.2	28.2	6.6
0.45fpuB	38.7	17.7	53.1	26.2	39.3	55.0	20.3
0.45fpuT	45.2	21.0	68.1	24.9	38.7	59.6	22.3
0.75fpuB	-53.1	-72.7	-18.3	-71.4	-56.3	-7.9	-89.8
0.75fpuT	-30.8	-58.3	24.2	-76.7	-46.5	29.5	-76.6
APB-50psi	16.4	-17.0	100.9	-41.9	9.8	91.7	-34.7
APT-50psi	23.6	-12.4	110.1	-36.7	15.1	101.6	-30.1
APB-75psi	20.3	-26.9	116.0	-52.4	15.1	110.7	-38.7
APB-100psi	60.9	-9.8	116.0	-33.4	34.7	147.4	-16.4
APT-100psi	63.6	-7.9	121.2	-28.8	39.3	154.0	-12.4
APB-125psi	60.9	3.3	119.2	-24.9	44.5	155.3	-6.6
APT-125psi	64.9	5.9	121.9	-21.0	49.8	159.9	-3.3
0.85fpuB	37.4	-9.2	99.6	-47.2	28.8	154.0	-34.7
0.85fpuT	67.5	5.2	140.2	-41.9	42.6	182.1	-15.1
APB-50psi	52.4	2.6	130.4	-51.8	37.3	174.9	-20.3
APT-50psi	76.0	21.6	154.6	-26.2	61.6	199.8	3.3
APB-75psi	84.5	26.9	165.1	-19.7	67.5	209.0	10.5
APT-75psi	87.8	28.2	169.7	-17.0	71.4	212.9	14.4
APB-100psi	91.8	32.1	172.3	-15.7	75.3	220.1	17.0
APT-100psi	95.7	33.4	174.9	-11.1	77.3	222.8	20.3
APB-125psi	98.3	33.4	174.9	-6.6	81.2	230.6	24.9
APT-125psi	100.9	36.0	179.5	-2.6	85.8	235.2	28.8

Web cracking did occur in C5. There were very minor cracks that started at 75 psi on the middle duct after 0.75fpu, shown in Figure 3-51, with the majority of the cracks forming under 100 psi air pressure on the middle duct. The final crack pattern after completion of testing on the surface of the web can be seen in Figure 3-52. The cracks were outlined to better clarify the location of the cracks as they were very minor at 0.013 inches on the surface.

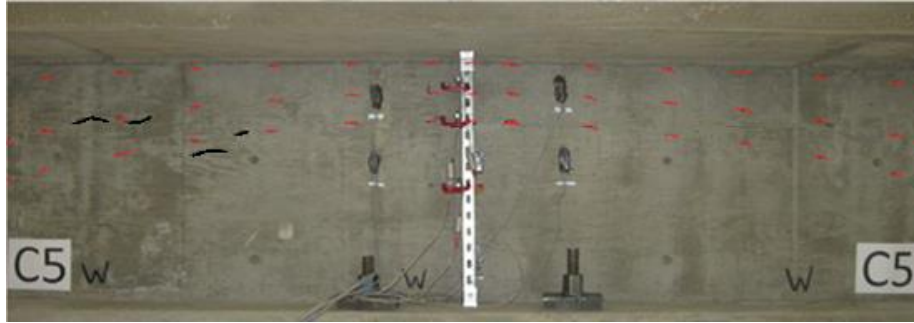


Figure 3-51: C5 appearance of cracks at 75psiB after 0.75fpu.

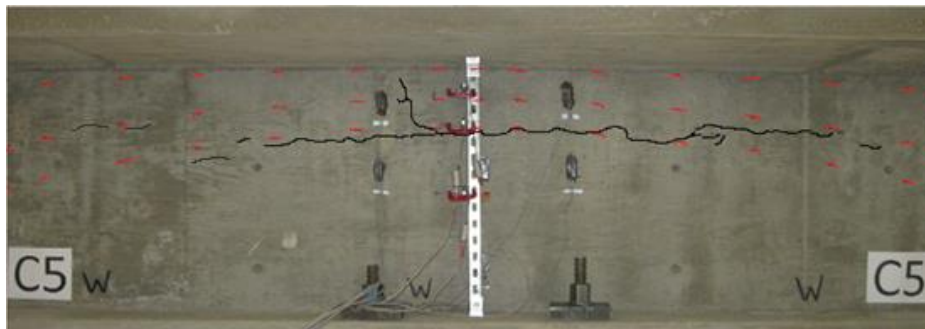


Figure 3-52: C5 cracking after loading with cracks highlighted for clarity.

3.3.2.3 Cross Sectional Cracks

Once the beams were cut in half, the crack layout in the cross section of the beam was able to be understood. The cracking in between the top and middle ducts was reduced as there were no cracks present. The cracking in between the middle and bottom ducts were 0.016 inches and below the bottom duct the crack width was 0.01 inches. Comparing C4 to C5, the amount of cracking in the cross section drastically decreased as there are minor cracks in C5 where C4 had much more apparent cracking (Figure 3-40).



a) Cross section with cracks.



b) Cross section with cracks drawn.

Figure 3-53: C5 cut beam cross section.

3.3.2.4 Duct Tie Reinforcement Gauges

Strain gauges were also included on the duct tie reinforcement bars in three different locations along the beam described in detail in Figure 2-19. The three sets of locations are shown in Figure 3-54, Figure 3-55 and Figure 3-56. The largest strain produced is in location “LM2”, which is in between the middle and bottom ducts in all three gauge locations. During the air pressure testing after 0.75fpu, the strain surpassed the yield strain of #3 reinforcement bar (2,250 microstrain, Table 2-12) towards the center of the beam. The strain in the duct ties decrease when moving to the next closest set of duct ties at 26.25 inches from center.

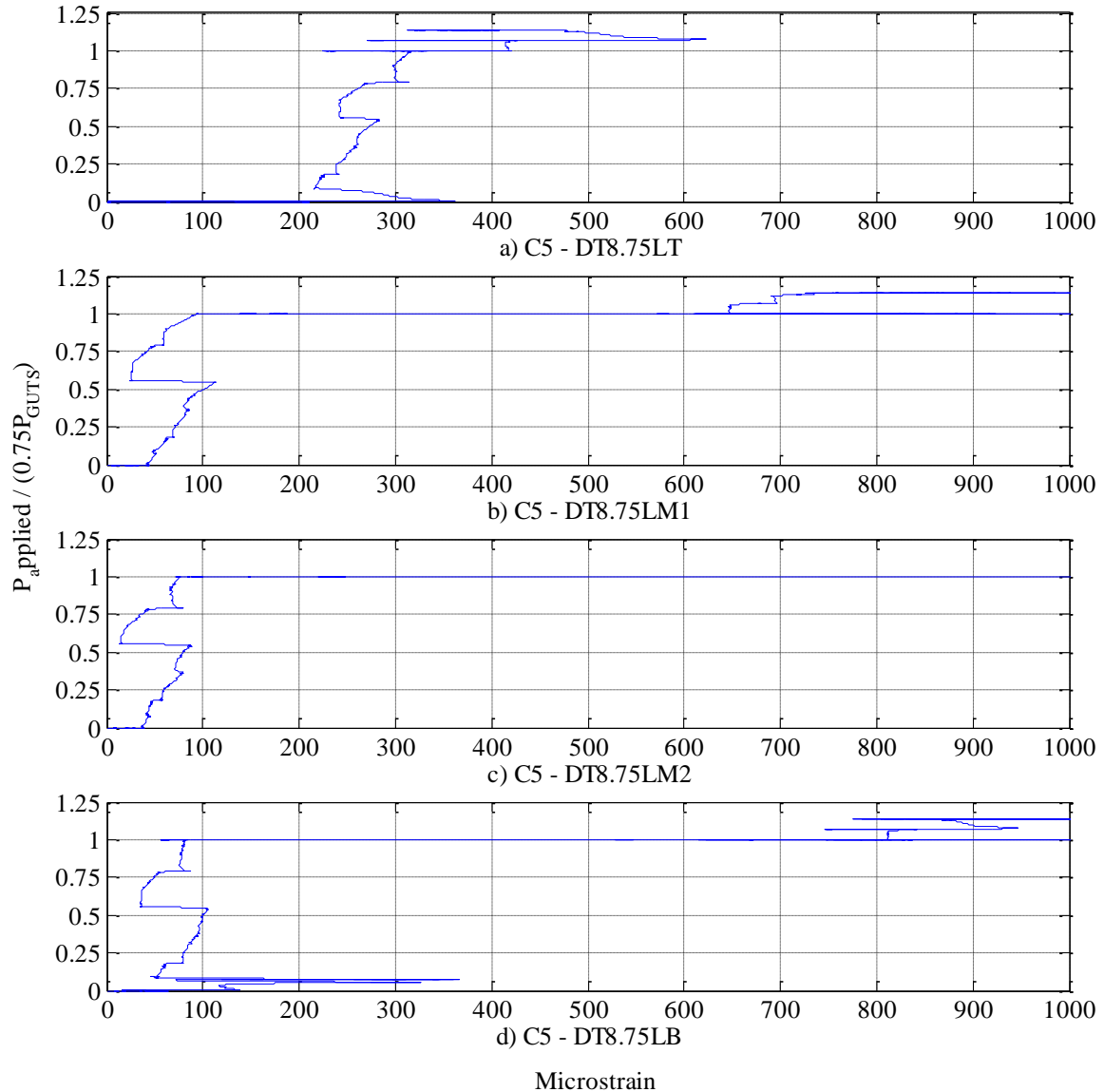


Figure 3-54: C5 duct tie reinforcement strain at -8.75" from centerline.

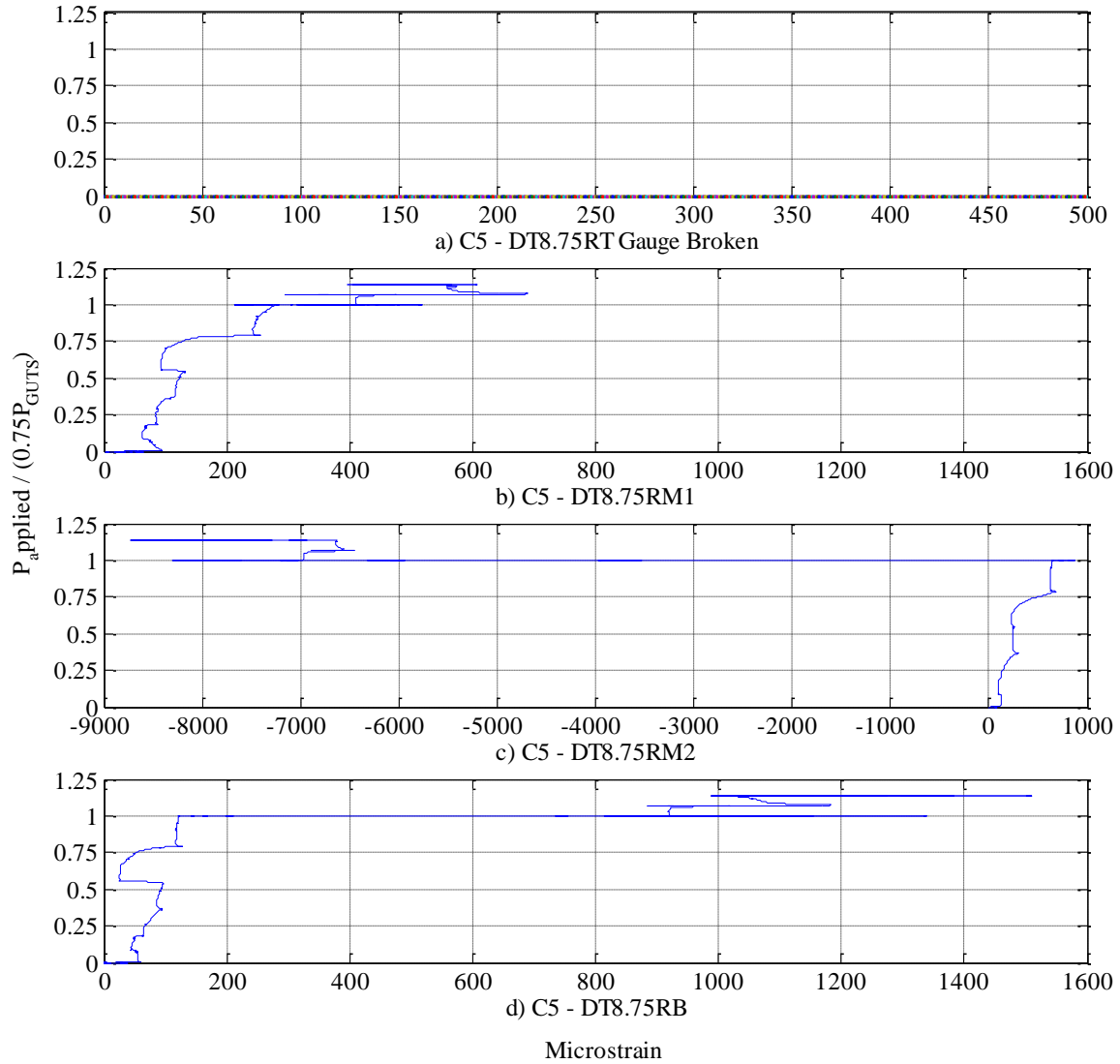


Figure 3-55: C5 duct tie reinforcement strain at +8.75" from centerline.

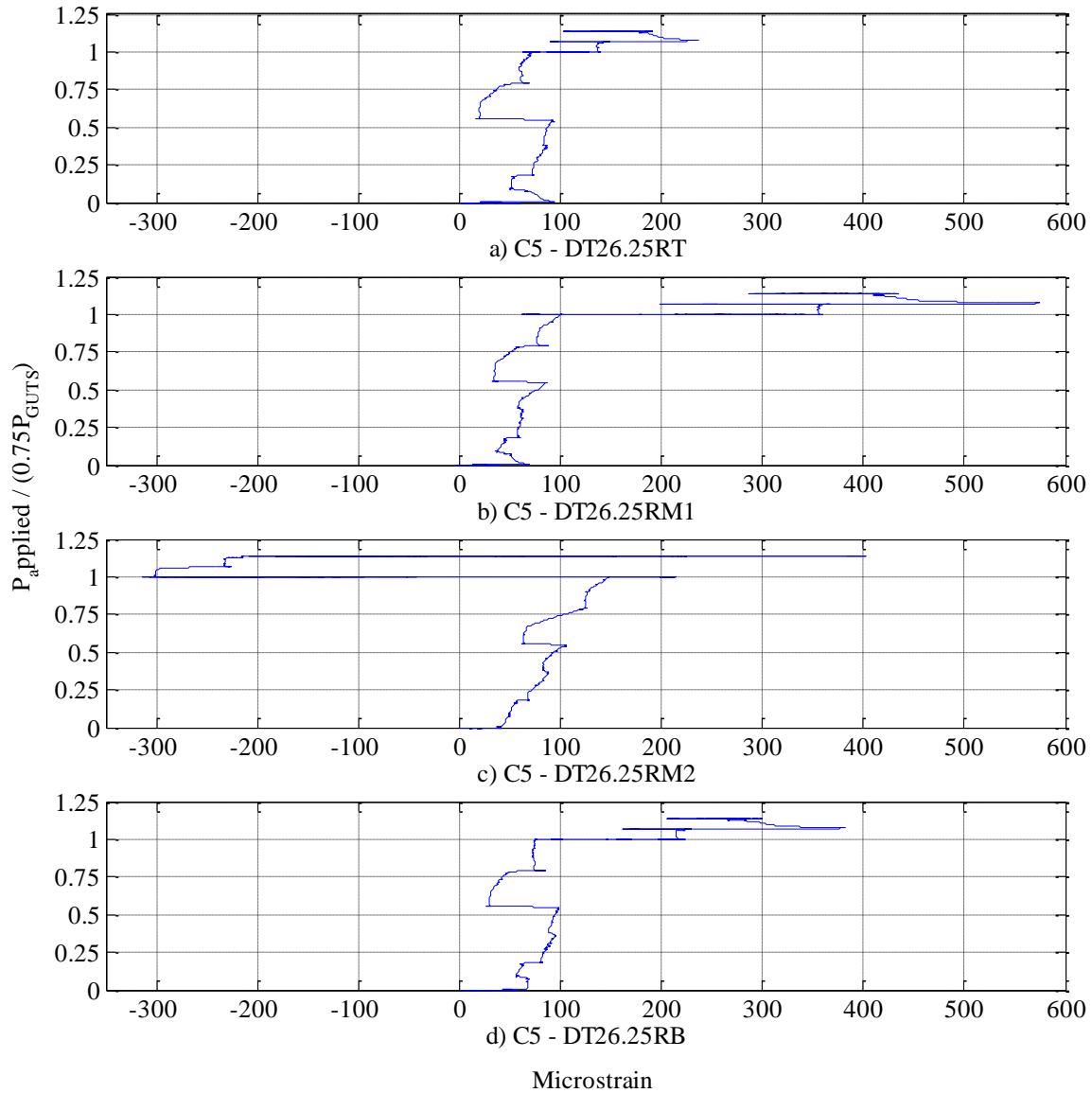


Figure 3-56: C5 duct tie reinforcement strain at +26.25" from centerline.

The strains for the duct tie reinforcement bars are shown in Table 3-23, Table 3-24 and Table 3-25 for the strain at the end of each loading stage on duct ties at -8.75 inches (on the non-stressing end), +8.75 inches (on the stressing end) and +26.25 inches (on the stressing side), respectively.

Table 3-23: C5 duct tie strain -8.75" at each loading stage.

	DT8.75LT	DT8.75LM1	DT8.75LM2	DT8.75LB
	με	με	με	με
APB-50psi	0.0	6.5	13.1	0.0
APT-50psi	-13.1	13.1	19.6	19.6
DL	0.0	13.1	6.5	26.2
0.15fpuB	248.5	58.9	45.8	130.8
0.15fpuT	222.4	58.9	52.3	65.4
0.45fpuB	261.6	98.1	78.5	91.6
0.45fpuT	287.8	111.2	91.6	98.1
0.75fpuB	268.2	52.3	39.3	39.3
0.75fpuT	313.9	98.1	72.0	72.0
APB-50psi	228.9	137.4	91.6	65.4
APT-50psi	222.4	143.9	85.1	72.0
APB-75psi	248.5	176.7	222.5	65.4
APB-100psi	287.8	615.0	2780.8	628.1
APT-100psi	294.3	615.0	2787.3	628.1
APB-125psi	307.4	693.6	3166.8	758.9
APT-125psi	313.9	687.0	3199.6	745.8
0.85fpuB	425.1	673.9	3337.0	844.0
0.85fpuT	484.0	745.9	3356.6	863.6
APB-50psi	333.6	732.8	3323.9	778.5
APT-50psi	340.1	765.5	3337.0	811.2
APB-75psi	353.2	778.6	3408.9	830.9
APT-75psi	353.2	785.2	3402.4	837.4
APB-100psi	366.3	824.4	3500.5	850.5
APT-100psi	366.3	811.3	3494.0	863.6
APB-125psi	385.9	876.8	3644.5	909.4
APT-125psi	385.9	876.8	3651.0	915.9

Table 3-24: C5 duct tie strain +8.75" at each loading stage.

	DT8.75RT	DT8.75RM1	DT8.75RM2	DT8.75RB
	μϵ	μϵ	μϵ	μϵ
APB-50psi	0.0	13.1	13.1	6.5
APT-50psi	0.0	13.1	26.2	13.1
DL	0.0	26.2	13.1	13.1
0.15fpuB	0.0	65.4	124.3	52.3
0.15fpuT	0.0	58.9	98.1	45.8
0.45fpuB	0.0	104.6	300.9	85.0
0.45fpuT	0.0	130.8	248.5	91.6
0.75fpuB	0.0	202.7	680.2	98.1
0.75fpuT	0.0	287.8	660.6	111.2
APB-50psi	0.0	235.5	726.0	163.6
APT-50psi	0.0	209.3	719.5	176.6
APB-75psi	0.0	228.9	791.4	196.3
APB-100psi	0.0	320.5	-6154.8	811.2
APT-100psi	0.0	313.9	-6082.8	824.3
APB-125psi	0.0	340.1	-7096.6	883.2
APT-125psi	0.0	346.6	-7083.6	902.8
0.85fpuB	0.0	484.0	-6442.6	1027.1
0.85fpuT	0.0	549.4	-6645.3	1033.7
APB-50psi	0.0	399.0	-7044.3	1001.0
APT-50psi	0.0	438.2	-7011.6	1027.1
APB-75psi	0.0	438.2	-7364.8	1033.7
APT-75psi	0.0	431.7	-7325.6	1053.3
APB-100psi	0.0	451.3	-7548.0	1059.8
APT-100psi	0.0	444.7	-7515.3	1066.4
APB-125psi	0.0	444.7	-7443.3	1092.6
APT-125psi	0.0	444.7	-7443.3	1112.2

Table 3-25: C5 duct tie strain +26.25" at each loading stage.

	DT26.25RT	DT26.25M1	DT26.25M2	DT26.25B
	μϵ	μϵ	μϵ	μϵ
APB-50psi	0.0	-6.5	19.6	19.6
APT-50psi	26.2	6.5	13.1	32.7
DL	13.1	6.5	19.6	26.2
0.15fpuB	65.4	52.3	58.9	58.9
0.15fpuT	45.8	39.2	52.3	58.9
0.45fpuB	91.6	65.4	85.0	104.7
0.45fpuT	98.1	91.6	111.2	98.2
0.75fpuB	32.7	52.3	130.8	45.8
0.75fpuT	58.9	111.2	143.9	72.0
APB-50psi	71.9	78.5	215.8	91.6
APT-50psi	65.4	65.4	196.2	98.2
APB-75psi	65.4	65.4	196.2	98.2
APB-100psi	85.0	215.8	-300.8	157.1
APT-100psi	78.5	222.4	-274.7	163.6
APB-125psi	104.6	268.2	-300.8	202.9
APT-125psi	104.6	268.2	-281.2	202.9
0.85fpuB	157.0	366.3	-228.9	229.1
0.85fpuT	176.6	412.0	-222.4	261.8
APB-50psi	98.1	287.8	-209.3	202.9
APT-50psi	130.8	320.5	-189.7	235.6
APB-75psi	143.9	327.0	-163.5	248.7
APT-75psi	143.9	327.0	-157.0	248.7
APB-100psi	150.4	320.5	-157.0	255.3
APT-100psi	157.0	333.6	-157.0	261.8
APB-125psi	163.5	366.3	39.2	281.4
APT-125psi	170.1	340.1	58.9	274.9

3.3.2.5 Web Bulging

Unlike the previous two beams where the post-tensioning did not have a large effect on the bulging of the web, it had a larger effect on C5 in relation to overall bulge. The overall web bulge decreased, compared to C4 (Figure 3-41), with the inclusion of duct ties and the effects due to air pressure were minimized to the level of post-tensioning compared to beams with no duct ties. The web bulging values at the end of each loading stage is provided in Table 3-26. The total web bulge shown in Table 3-26 is the total bulge from both the west and east face for the middle gauge.

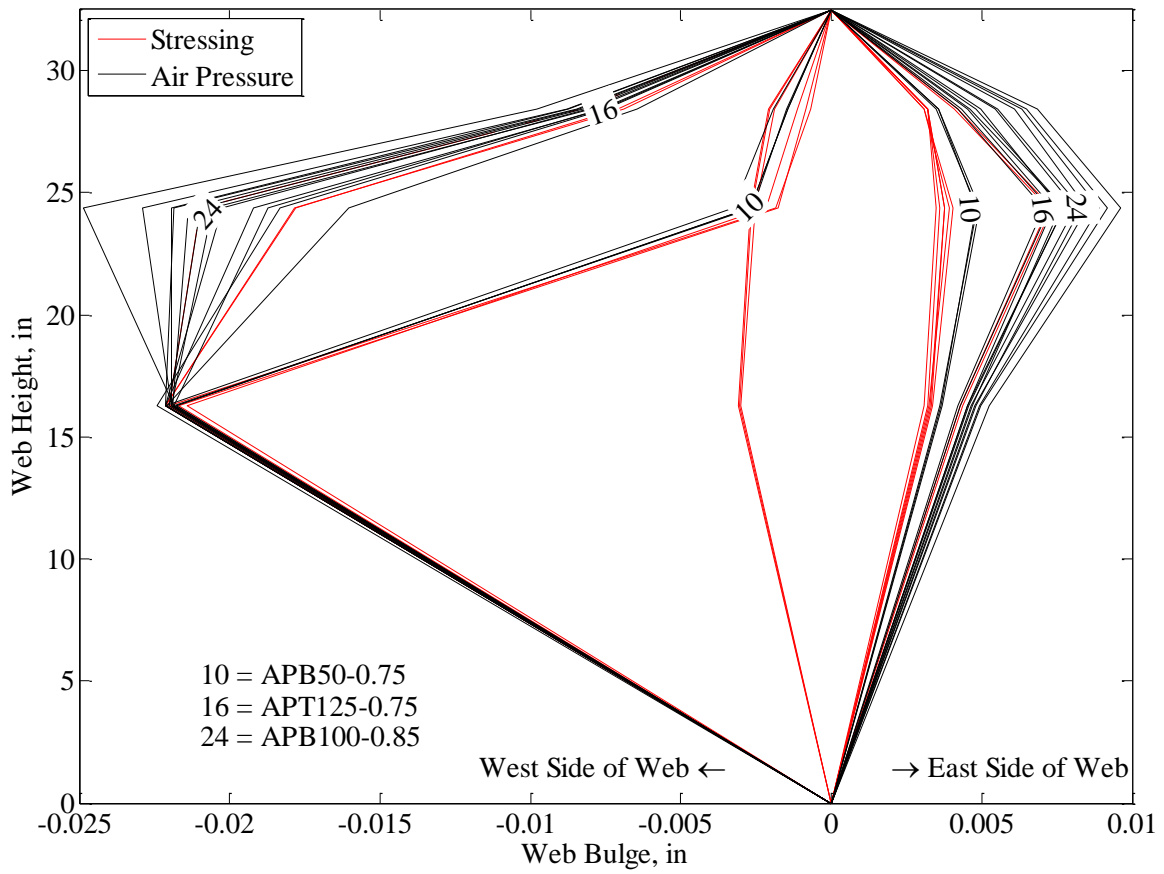


Figure 3-57: C5 web bulge.

Table 3-26: C5 web bulging at each loading stage.

	WBTW in.	WBMW in.	WBMB in.	WBTE in.	WBME in.	WBBE in.	M. Total in.
APIB	-0.002	-0.002	-0.003	0.003	0.003	0.003	0.006
APIT	-0.002	-0.002	-0.003	0.003	0.003	0.003	0.006
DL	-0.002	-0.002	-0.003	0.003	0.003	0.003	0.006
0.15fpuB	-0.002	-0.002	-0.003	0.003	0.003	0.003	0.006
0.15fpuT	-0.002	-0.002	-0.003	0.003	0.004	0.003	0.006
0.45fpuB	-0.002	-0.002	-0.003	0.003	0.004	0.003	0.006
0.45fpuT	-0.001	-0.002	-0.021	0.003	0.004	0.003	0.025
0.75fpuB	0.000	-0.001	-0.022	0.003	0.004	0.003	0.025
0.75fpuT	0.000	-0.001	-0.022	0.003	0.004	0.003	0.026
APB-50psi	-0.001	-0.002	-0.021	0.003	0.005	0.003	0.026
APT-50psi	-0.001	-0.002	-0.022	0.003	0.005	0.003	0.026
APB-75psi	-0.002	-0.003	-0.022	0.003	0.005	0.004	0.027
APB-100psi	-0.006	-0.015	-0.022	0.004	0.007	0.004	0.028
APT-100psi	-0.006	-0.014	-0.021	0.004	0.007	0.004	0.028
APB-125psi	-0.007	-0.017	-0.021	0.004	0.007	0.004	0.028
APT-125psi	-0.007	-0.017	-0.021	0.004	0.007	0.004	0.028
0.85fpuB	-0.006	-0.018	-0.022	0.004	0.007	0.004	0.029
0.85fpuT	-0.007	-0.018	-0.022	0.004	0.007	0.004	0.029
APB-50psi	-0.007	-0.018	-0.022	0.004	0.007	0.004	0.029
APT-50psi	-0.007	-0.018	-0.022	0.005	0.007	0.004	0.029
APB-75psi	-0.008	-0.019	-0.022	0.005	0.008	0.004	0.029
APT-75psi	-0.008	-0.019	-0.022	0.005	0.008	0.004	0.029
APB-100psi	-0.008	-0.020	-0.021	0.005	0.008	0.005	0.030
APT-100psi	-0.008	-0.020	-0.021	0.005	0.008	0.005	0.030
APB-125psi	-0.008	-0.021	-0.021	0.006	0.009	0.005	0.030
APT-125psi	-0.008	-0.021	-0.021	0.006	0.009	0.005	0.030

3.3.2.6 Shear Reinforcement Gauges and Beam End Displacement

The strain gauge results from the shear reinforcement and the beam end displacement was not significant to this study. Therefore, refer to Appendices A and B for the results for the shear reinforcement strain gauges and the displacements on the ends of the beams.

3.3.2.7 C5 Results Overview

C5 is the first beam to have reinforcement steel introduced in between the ducts. The spacing of the reinforcement is placed at 17.5 inches which is equivalent to 25 inches for full scale. The duct tie reinforcement had a positive impact on the overall performance of the beam. The strain around the ducts was generally lower for C5

compared to C4, with no duct tie reinforcement. The air pressure was still the major contributing factor to the increase in strain within the beam but not having as significant of an effect as the beams without reinforcement. With the inclusion of duct ties, the air pressure had a lesser effect on the associated web bulge.

3.3.3 Configuration 6

C6 is the final experimental beam with the design being based on C5 with the exception of the reinforcement spacing being at 7.0 inches instead of 17.5 inches. The design is outlined in Section 2.5.3.

3.3.3.1 Embedded Concrete Strain Gauges

The embedded concrete strain gauges in the center of the beam are shown in Figure 3-58. With the decrease in spacing between the duct tie reinforcement bars, the embedded concrete strain in the top and bottom locations were less in comparison to C5. The middle gauge saw an increase compared to C5 (Figure 3-42). The concrete strain in the bottom gauge had considerably lower strains around $100 \mu\epsilon$ whereas the top and middle gauges are reaching $4,000 \mu\epsilon$ and $3,000 \mu\epsilon$ respectively.

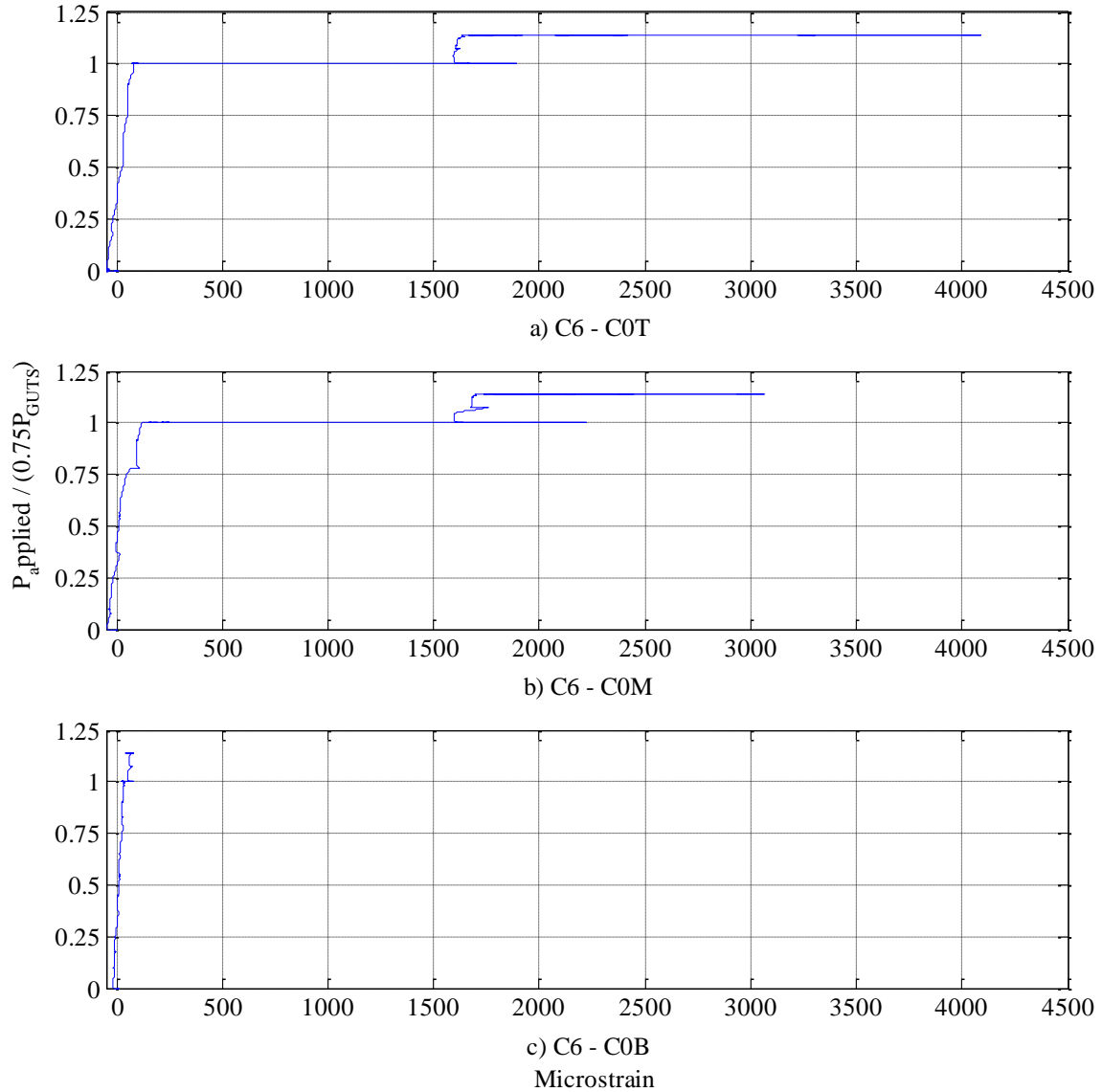


Figure 3-58: C6 embedded concrete strain at centerline.

The embedded concrete strain are plotted against time in Figure 3-59 to show the impact of air pressure values. Upon inspection of Figure 3-59, the 125 psi air pressure on the middle duct had a large impact on the strain. This is the same time that cracking became apparent on the surface of the web as well. Table 3-27 shows the embedded concrete strain gauges at the end of each loading step in the center of the beam at 0 inches from center.

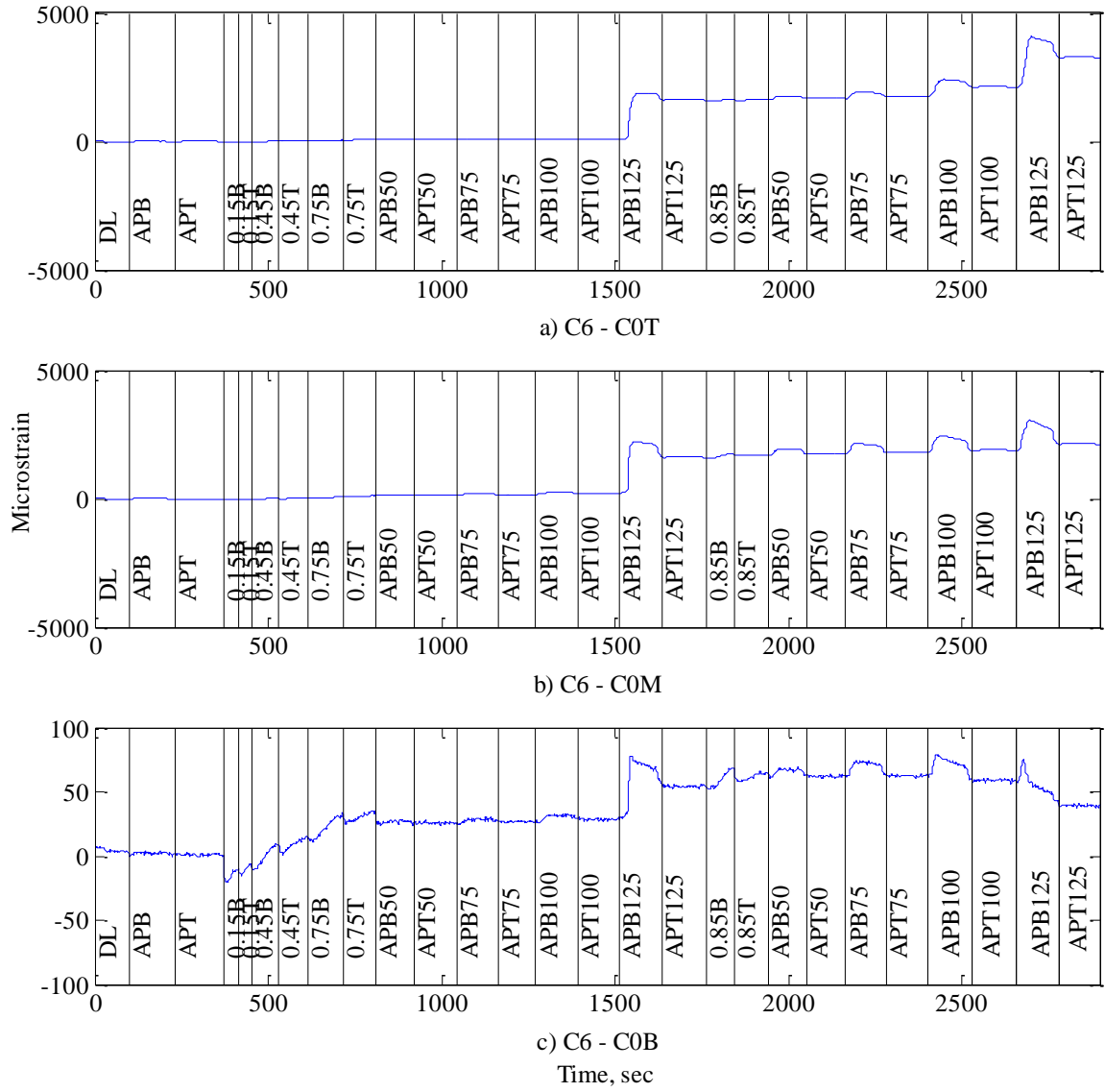


Figure 3-59: C6 embedded concrete strain versus time.

Table 3-27: C6 embedded concrete strain at 0" O.C. at each loading stage.

	C0T	C0M	C0B
	μϵ	μϵ	μϵ
APB-50psi	-13.1	-6.5	-6.5
APT-50psi	0.0	0.0	0.0
DL	-6.5	-6.5	0.0
0.15fpuB	-39.3	-32.7	-19.6
0.15fpuT	-13.1	-32.7	-6.5
0.45fpuB	6.5	26.2	6.5
0.45fpuT	39.3	13.1	13.1
0.75fpuB	58.9	104.7	32.7
0.75fpuT	91.6	111.3	32.7
APB-50psi	91.6	150.5	32.7
APT-50psi	78.5	144.0	19.6
APB-75psi	78.5	170.2	26.2
APT-75psi	78.5	170.2	26.2
APB-100psi	78.5	222.5	26.2
APT-100psi	78.5	222.5	32.7
APB-125psi	1649	1643	58.9
APT-125psi	1609	1603	45.8
0.85fpuB	1623	1754	71.9
0.85fpuT	1649	1695	65.4
APB-50psi	1668	1747	65.4
APT-50psi	1655	1747	65.4
APB-75psi	1747	1793	65.4
APT-75psi	1740	1793	52.3
APB-100psi	2120	1885	71.9
APT-100psi	2080	1872	58.9
APB-125psi	3304	2166	52.3
APT-125psi	3239	2114	52.3

The embedded concrete strain gauges at -15 inches are shown in Figure 3-60 for the non-stressing end of the beam and the embedded concrete strain gauges at +15 inches are shown in Figure 3-61 for the stressing end of the beam. Observing C6's gauges at 15 inches from centerline shows a substantial decrease in strain when compared to the same gauge locations in C5 (Figure 3-44 and Figure 3-45). The decrease in duct tie reinforcement spacing provides a shorter distance for the large tension force to travel, leading to an overall lower strain within the section. Table 3-28 shows the embedded concrete gauges at 15 inches from center at the end of each loading stage. Similarly for 30 inches from centerline, the strains are shown in Figure 3-62 and Figure 3-63.

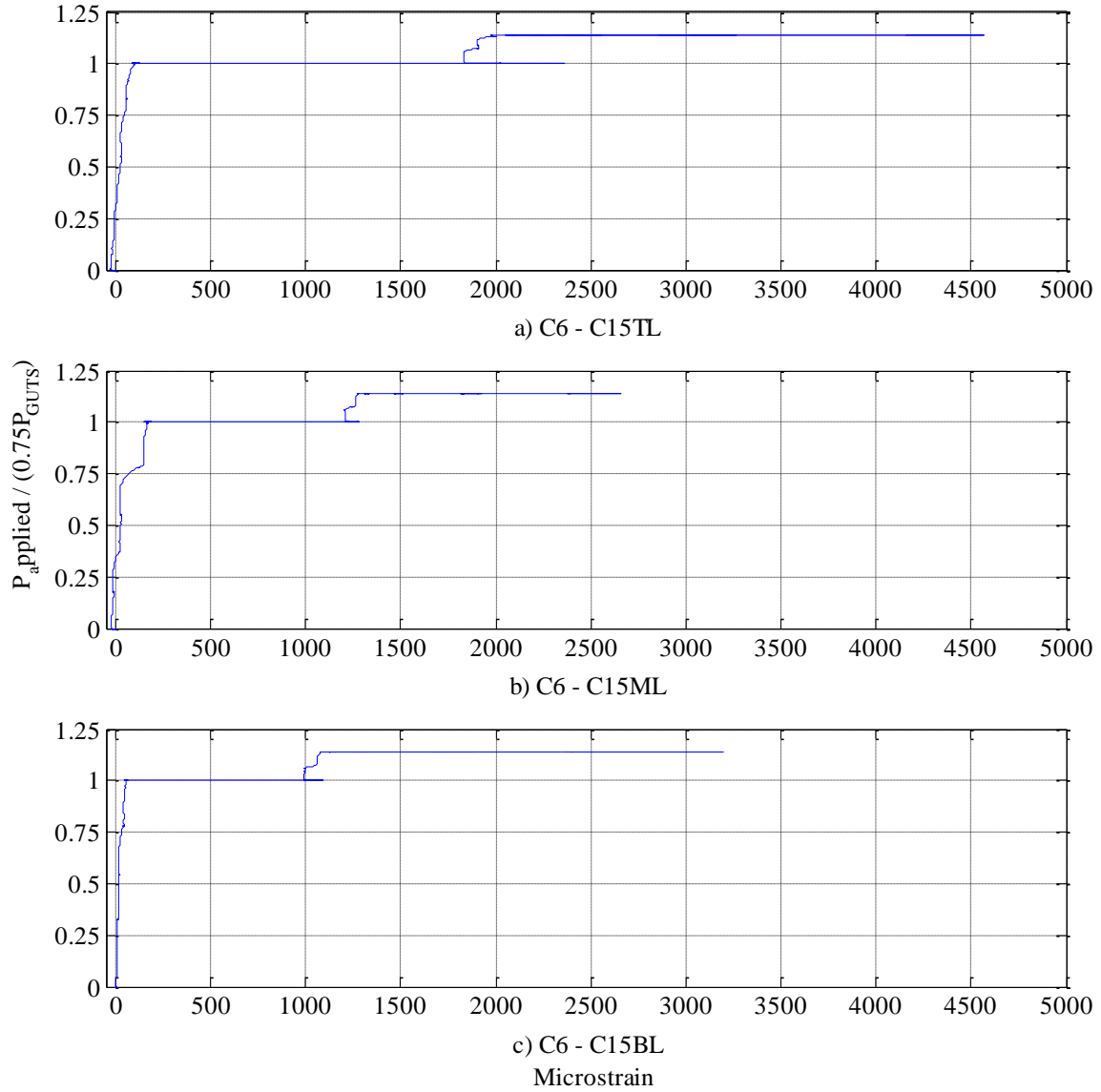


Figure 3-60: C6 embedded concrete strain at -15" from centerline.

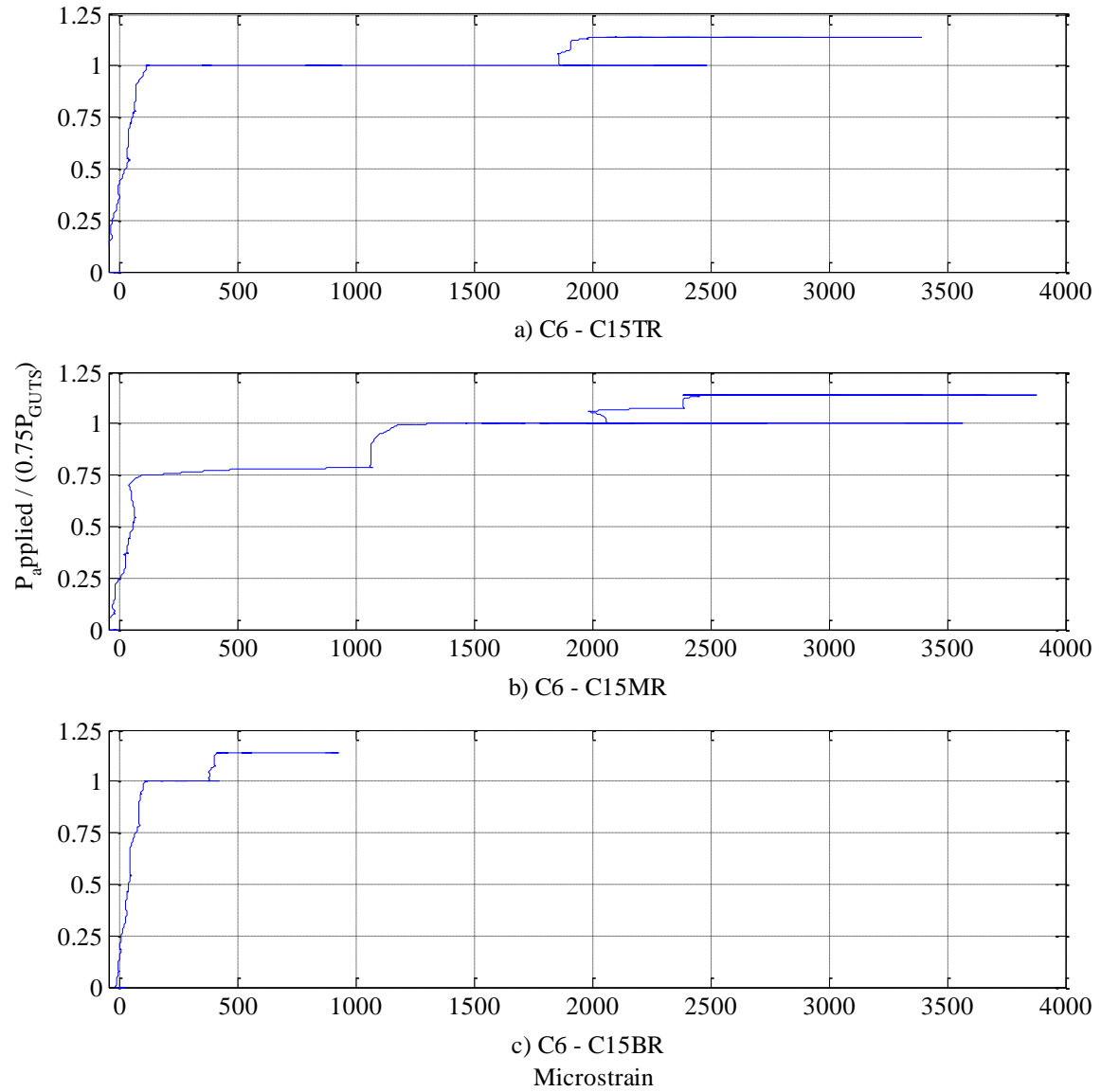


Figure 3-61: C6 embedded concrete strain at +15" from centerline.

Table 3-28: C6 embedded concrete strain at 15" O.C. at each loading stage.

	C15TL	C15ML	C15BL	C15TL	C15ML	C15BL
	με	με	με	με	με	με
APB-50psi	-6.5	-13.1	6.5	-26.2	-26.2	0.0
APT-50psi	-6.5	-26.2	0.0	-19.6	-19.6	0.0
DL	-13.1	-13.1	13.1	-19.6	-13.1	26.2
0.15fpuB	-32.7	-13.1	13.1	-58.9	-26.2	-13.1
0.15fpuT	-6.5	-13.1	19.6	-39.2	-13.1	6.5
0.45fpuB	19.6	19.6	13.1	0.0	19.6	26.2
0.45fpuT	39.2	26.2	19.6	45.8	72.0	39.3
0.75fpuB	45.8	124.3	45.8	58.9	778.7	78.5
0.75fpuT	91.5	163.6	45.8	124.3	1211	98.2
APB-50psi	91.5	157.1	45.8	111.2	1551	98.2
APT-50psi	91.5	157.1	45.8	98.1	1531	98.2
APB-75psi	85.0	157.1	45.8	353.2	1806	170.2
APT-75psi	91.5	157.1	58.9	366.3	1793	176.7
APB-100psi	85.0	137.4	58.9	804.5	2035	229.1
APT-100psi	98.1	157.1	58.9	804.5	2002	235.6
APB-125psi	1903	1224	1008	1943	2127	373.0
APT-125psi	1851	1217	981	1877	2074	386.1
0.85fpuB	1896	1243	1060	1897	2238	399.2
0.85fpuT	2021	1283	1073	1982	2454	412.3
APB-50psi	2073	1309	1125	2067	2539	412.3
APT-50psi	2060	1309	1132	2060	2513	412.3
APB-75psi	2217	1466	1263	2171	2552	418.9
APT-75psi	2191	1466	1243	2139	2519	431.9
APB-100psi	2452	1839	1694	2355	2500	523.6
APT-100psi	2393	1832	1662	2328	2467	523.6
APB-125psi	3139	2422	2427	2623	2408	870.4
APT-125psi	3028	2382	2388	2551	2375	863.9

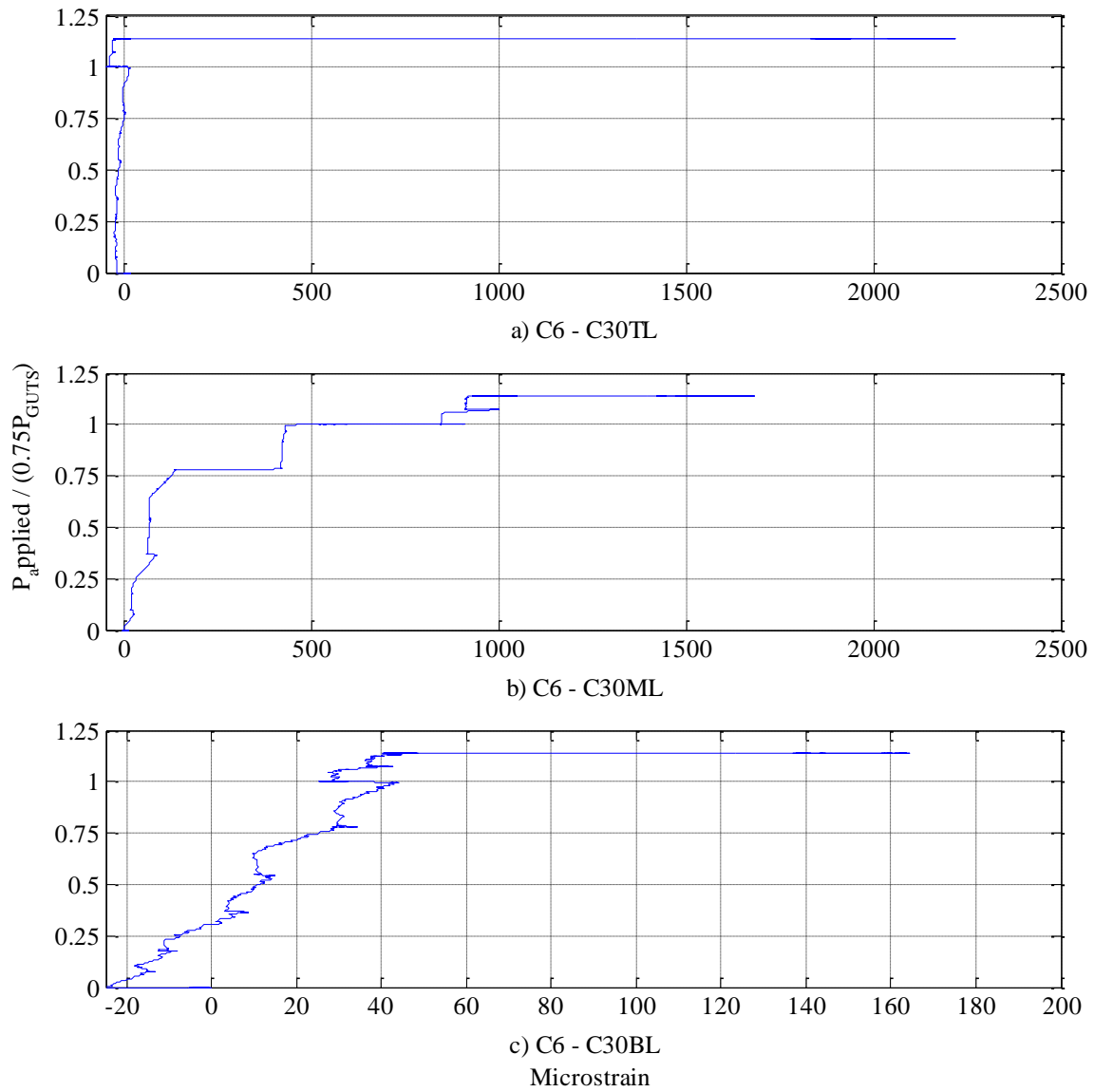


Figure 3-62: C6 embedded concrete strain at -30" from centerline.

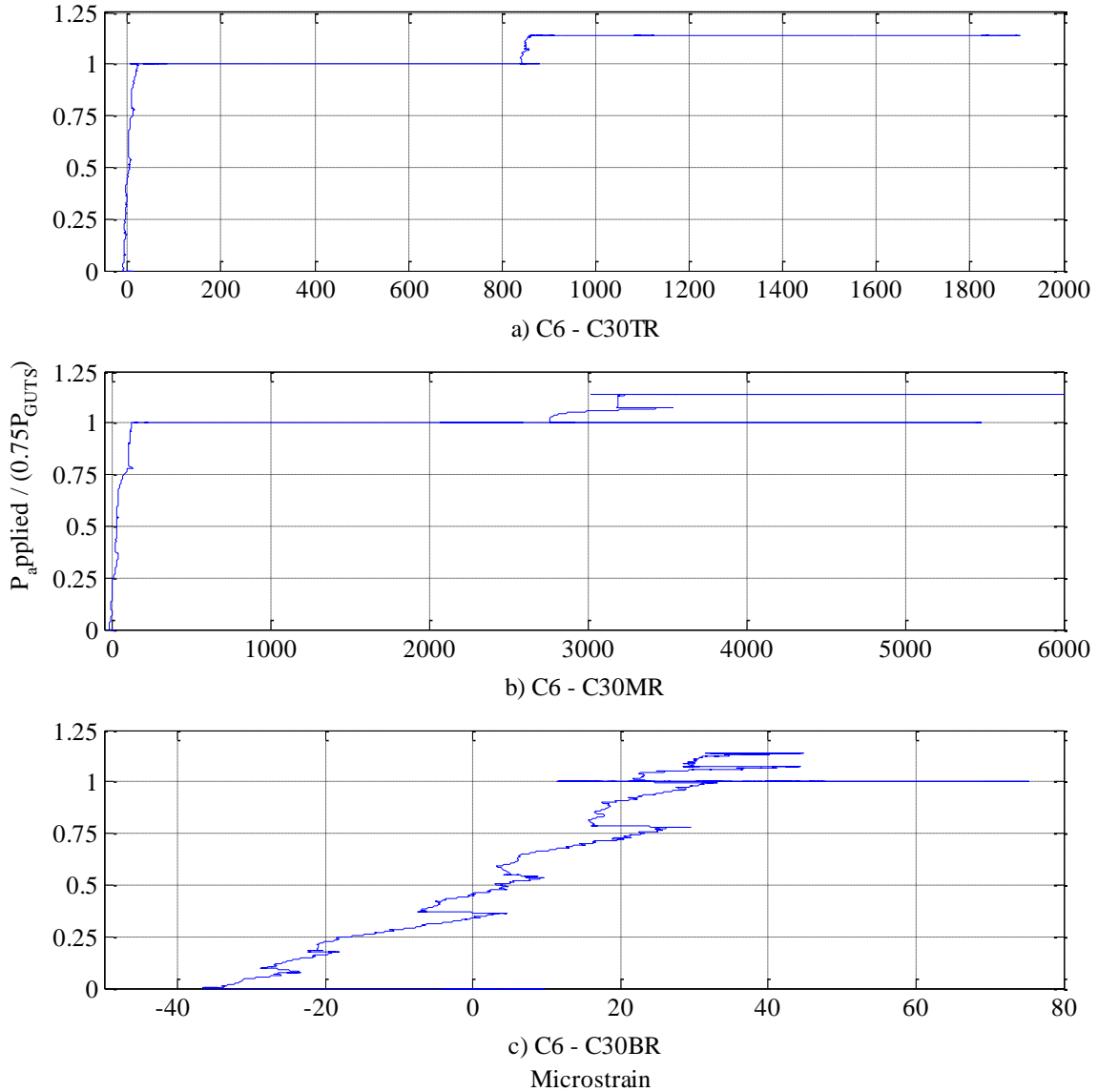


Figure 3-63: C6 embedded concrete strain at +30" from centerline.

The strain related to the gauges at 30 inches from centerline overall are showing that air pressure after 0.85fpu has a larger effect, compared to the post-tensioning and prior air pressuring, on the strain in C6 than all other configurations. From 15 inches to 30 inches from the centerline there is a decline in strain, particularly present in the bottom strain gauge. The strain at the end of each loading stage for the embedded concrete gauges at 30 inches off-center are shown in Table 3-29.

Table 3-29: C6 embedded concrete strain at 30" O.C. at each loading stage.

	C30TL	C30ML	C30BL	C30TR	C30MR	C30BR
	$\mu\epsilon$	$\mu\epsilon$	$\mu\epsilon$	$\mu\epsilon$	$\mu\epsilon$	$\mu\epsilon$
APB-50psi	13.1	0.0	6.5	-13.1	0.0	-6.5
APT-50psi	6.5	-6.5	-6.5	0.0	6.5	-6.5
DL	0.0	-6.5	-6.5	-13.1	0.0	-6.5
0.15fpuB	-26.2	19.6	-26.2	-6.5	0.0	-19.6
0.15fpuT	-19.6	19.6	-19.6	0.0	-13.1	-26.2
0.45fpuB	-19.6	85.1	6.5	-6.5	45.8	0.0
0.45fpuT	-6.5	65.4	13.1	6.5	26.2	0.0
0.75fpuB	0.0	386.1	45.8	6.5	124.2	26.2
0.75fpuT	6.5	431.9	45.8	19.6	124.2	19.6
APB-50psi	-13.1	523.6	32.7	13.1	137.3	13.1
APT-50psi	0.0	530.1	26.2	0.0	137.3	13.1
APB-75psi	6.5	530.1	26.2	6.5	202.7	13.1
APT-75psi	-32.7	523.6	26.2	6.5	209.3	13.1
APB-100psi	-52.3	556.3	26.2	45.8	2112	39.2
APT-100psi	-45.8	562.8	32.7	39.3	2093	32.7
APB-125psi	-39.3	857.3	32.7	844.0	2851	26.2
APT-125psi	-39.3	844.2	32.7	844.0	2766	19.6
0.85fpuB	-32.7	968.6	39.3	863.6	3531	32.7
0.85fpuT	-19.6	935.9	45.8	863.6	3198	39.2
APB-50psi	-26.2	935.9	45.8	863.6	3459	39.2
APT-50psi	-13.1	929.3	45.8	857.1	3420	45.8
APB-75psi	-32.7	942.4	45.8	876.7	3538	39.2
APT-75psi	-19.6	935.9	39.3	876.7	3466	45.8
APB-100psi	0.0	968.6	52.3	1086	3341	39.2
APT-100psi	0.0	981.7	45.8	1080	3289	45.8
APB-125psi	1871.0	1440	150.5	1838	3080	45.8
APT-125psi	1851.3	1420	150.5	1832	3015	26.2

3.3.3.2 Concrete Surface Strain Gauges

As C6 was designed with the smallest duct tie spacing, it was expected to have the least amount of damage. This was in fact the case, as the beam performed the best with minimal cracks reaching the web surface. The strain on the surface of the web along the beam are shown in the following figures: Figure 3-64 for -12 inches, Figure 3-65 for the center of the beam and Figure 3-66 for +12 inches. -12 inches from centerline is to the non-stressing side and +12 inches from centerline is to the stressing side. The air pressure after 0.75fpu is the highest contributing factor to the large strains along the surface of the web.

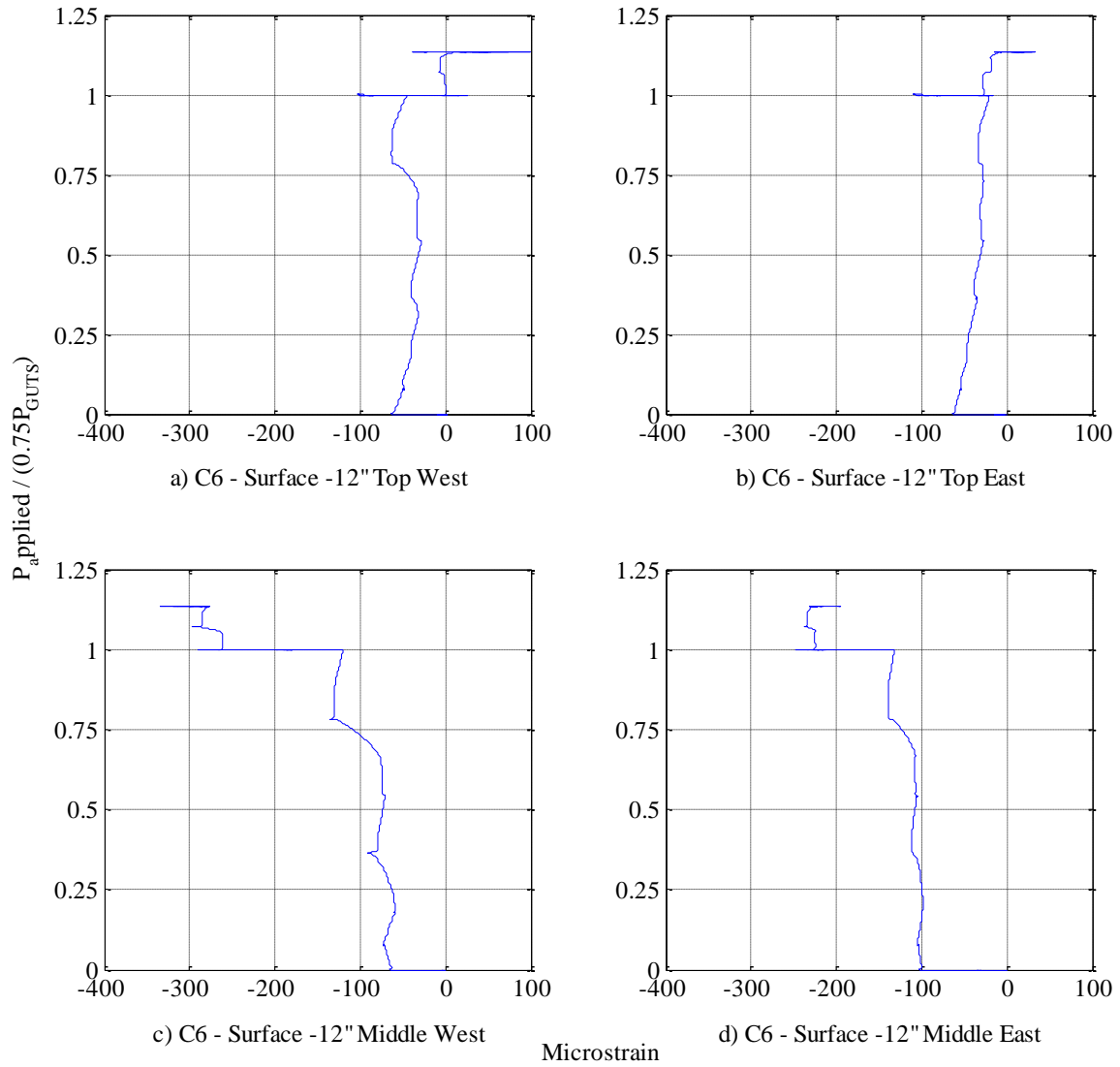


Figure 3-64: C6 concrete surface strain at -12" from centerline.

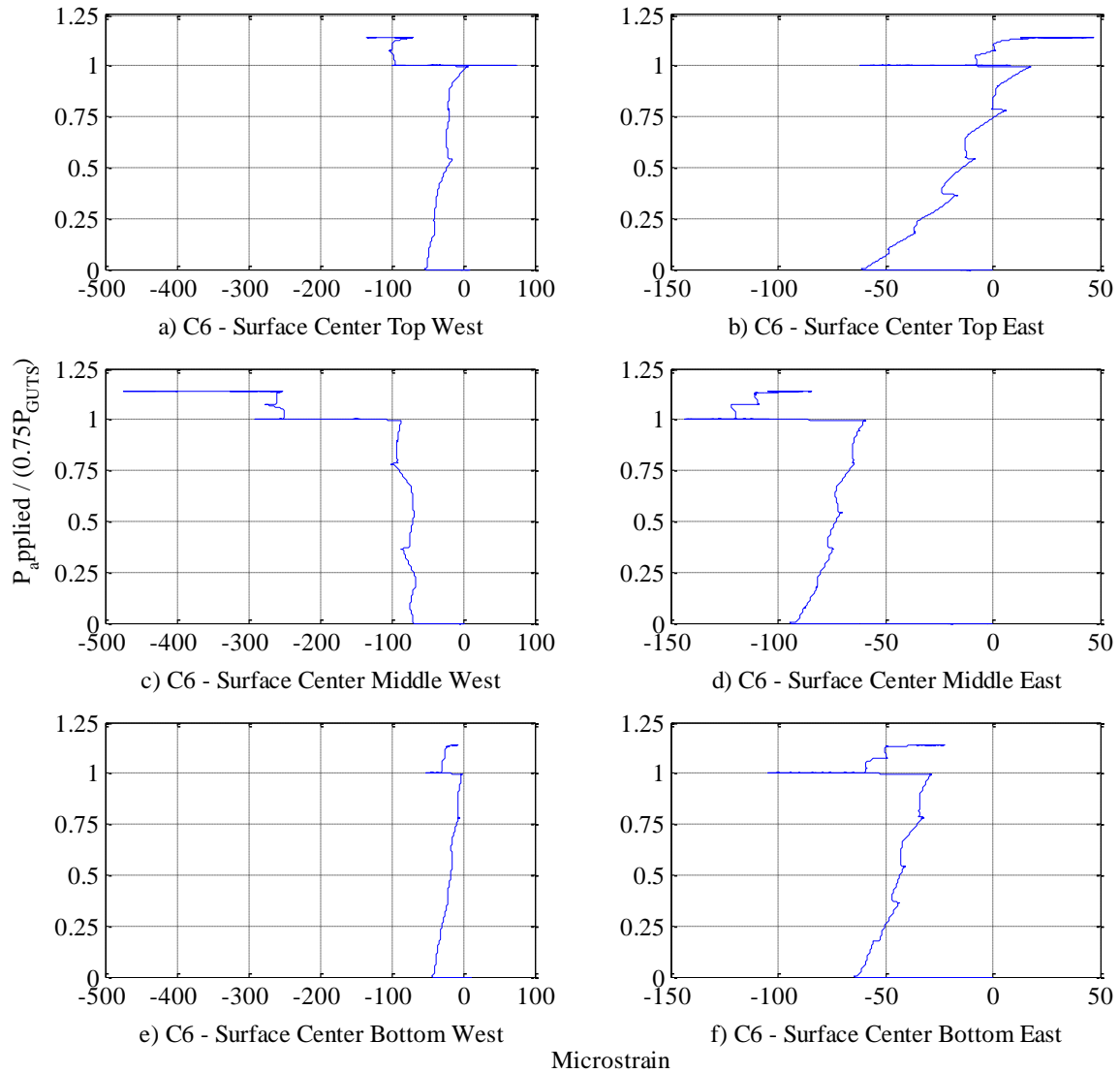


Figure 3-65: C6 concrete surface strain at centerline.

The strain gauges are starting at a negative values; this is due to the loading of the beam with the additional dead load towards the ends of the beams.

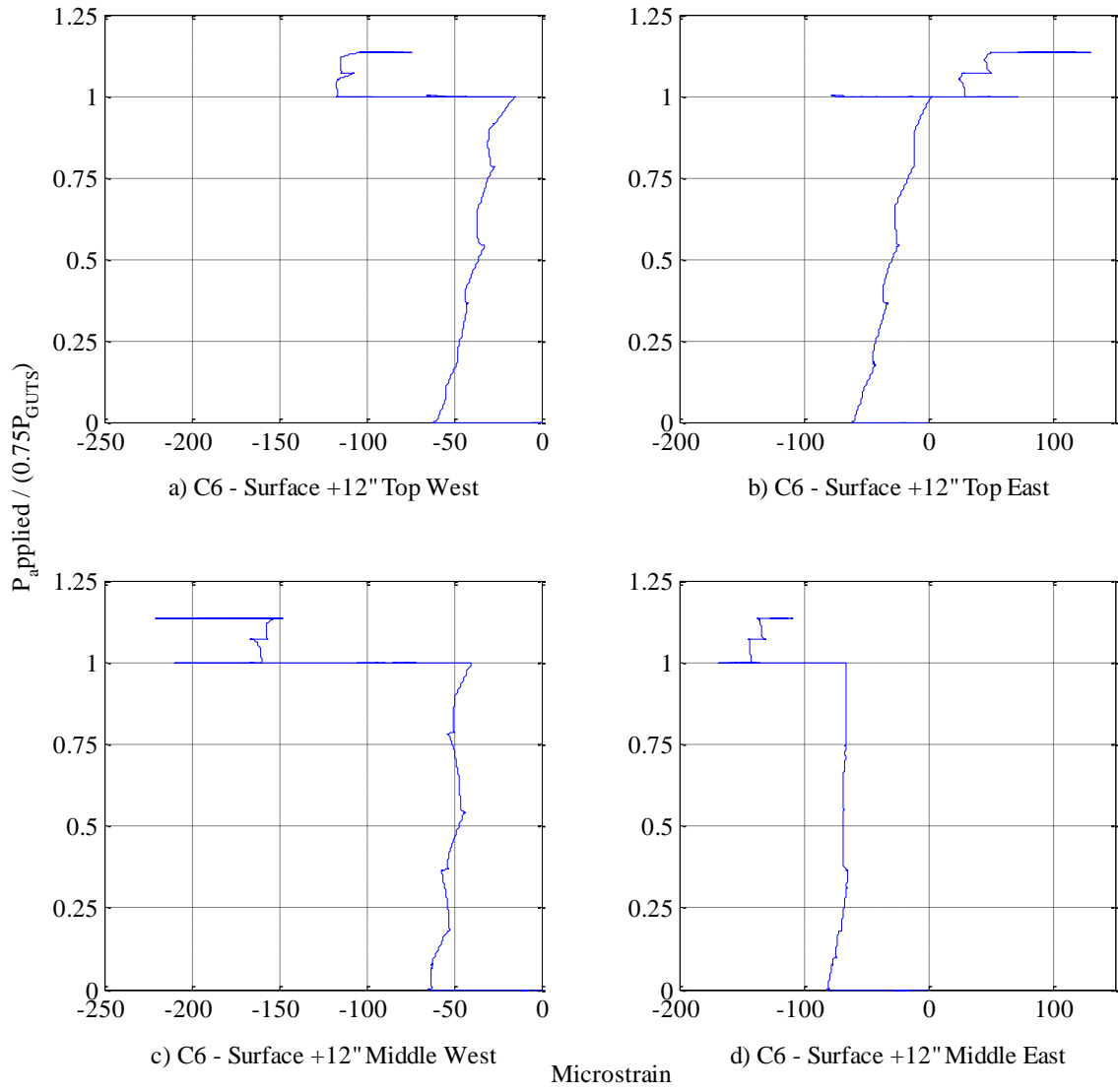


Figure 3-66: C6 concrete surface strain at +12" from centerline.

The concrete surface strain is minimal with the maximum strain on the surface attaining a maximum of 400-500 $\mu\epsilon$. The strain at the end of the loading stages for the concrete surface gauges are shown in Table 3-30 and Table 3-31 for each face of the beam.

Table 3-30: C6 concrete west surface strain at each loading stage.

	CSLTW	CSLMW	CSCTW	CSCMW	CSCBW	CSRTW	CSRMW
	$\mu\epsilon$						
APB-50psi	-3.9	-9.2	-2.0	-5.2	10.5	-7.9	-5.2
APT-50psi	-3.9	-8.5	2.6	-1.3	9.8	-2.6	-3.3
DL	-3.3	-9.2	2.6	-3.3	10.5	-2.6	-2.6
0.15fpuB	-54.4	-62.9	-47.2	-76.0	-37.3	-49.8	-70.7
0.15fpuT	-48.5	-54.4	-40.6	-66.2	-32.8	-41.3	-60.3
0.45fpuB	-41.3	-57.0	-36.0	-86.5	-21.0	-41.3	-91.0
0.45fpuT	-31.5	-45.2	-16.4	-67.5	-15.1	-28.2	-70.1
0.75fpuB	-26.2	-53.7	-21.6	-99.6	-5.9	-60.3	-134.9
0.75fpuT	-13.8	-40.6	5.9	-86.5	0.7	-45.2	-119.8
APB-50psi	-62.3	-74.7	-47.8	-150.7	-47.8	-101.5	-184.0
APT-50psi	-58.3	-72.7	-46.5	-145.4	-45.2	-98.9	-182.1
APB-75psi	-62.3	-79.9	-43.9	-148.7	-43.9	-98.9	-184.7
APT-75psi	-60.3	-77.3	-43.2	-146.1	-41.9	-89.1	-182.7
APB-100psi	-51.8	-93.7	-39.3	-147.4	-42.6	-90.4	-190.6
APT-100psi	-51.1	-93.7	-38.6	-149.4	-41.3	-92.4	-189.3
APB-125psi	-114.0	-168.3	-95.0	-258.1	-34.1	-2.6	-267.2
APT-125psi	-116.6	-164.4	-98.3	-254.2	-33.4	-2.6	-264.6
0.85fpuB	-108.1	-165.1	-101.5	-277.1	-25.5	-7.9	-297.3
0.85fpuT	-102.2	-150.7	-78.6	-256.8	-19.7	15.1	-275.7
APB-50psi	-101.6	-152.0	-83.8	-255.5	-16.4	17.7	-277.7
APT-50psi	-100.3	-150.0	-83.8	-254.2	-14.4	19.0	-276.4
APB-75psi	-100.3	-152.0	-86.5	-262.7	-13.8	30.8	-281.6
APT-75psi	-100.3	-152.0	-85.8	-260.7	-11.8	30.8	-282.9
APB-100psi	-102.2	-157.2	-92.4	-290.2	-10.5	44.5	-287.5
APT-100psi	-104.2	-155.9	-94.3	-288.2	-10.5	40.0	-286.2
APB-125psi	-101.6	-167.0	-133.0	-401.6	-8.5	-36.0	-298.0
APT-125psi	-105.5	-165.1	-136.2	-400.3	-11.1	-39.3	-297.3

Table 3-31: C6 concrete east surface strain at each loading stage.

	CSLTE	CSLME	CSCTE	CSCME	CSCBE	CSRTE	CSRME
	$\mu\epsilon$						
APB-50psi	-13.1	-34.1	-13.8	-21.6	-8.5	-24.2	-26.2
APT-50psi	-4.6	-30.1	-12.4	-18.3	-3.3	-20.3	-18.3
DL	-3.9	-30.1	-11.8	-17.7	-3.9	-20.3	-17.7
0.15fpuB	-53.7	-104.8	-47.8	-87.1	-58.3	-52.4	-76.6
0.15fpuT	-45.2	-98.9	-36.0	-82.5	-54.4	-43.2	-71.4
0.45fpuB	-36.0	-112.7	-15.7	-73.4	-43.9	-32.1	-65.5
0.45fpuT	-27.5	-106.8	-7.9	-70.1	-40.6	-24.2	-67.5
0.75fpuB	-30.8	-136.9	6.6	-64.2	-32.1	-10.5	-65.5
0.75fpuT	-18.4	-132.3	17.0	-59.6	-30.1	2.6	-66.2
APB-50psi	-103.5	-225.4	-57.7	-137.6	-100.2	-70.1	-154.0
APT-50psi	-96.3	-220.1	-51.8	-130.4	-93.7	-60.9	-147.4
APB-75psi	-93.7	-220.8	-51.1	-125.1	-89.1	-54.4	-146.7
APT-75psi	-87.8	-214.9	-43.2	-118.6	-83.2	-43.9	-141.5
APB-100psi	-81.9	-218.2	-41.9	-112.7	-78.0	-17.7	-145.4
APT-100psi	-80.6	-216.2	-41.3	-112.7	-76.0	-16.4	-143.5
APB-125psi	-34.1	-234.6	-11.8	-130.4	-66.2	40.6	-150.0
APT-125psi	-32.8	-231.9	-11.8	-125.8	-66.2	37.3	-148.1
0.85fpuB	-25.6	-239.1	-0.7	-122.5	-55.7	27.5	-144.8
0.85fpuT	-6.6	-229.3	13.8	-110.1	-49.1	50.4	-137.6
APB-50psi	5.2	-224.1	20.3	-95.6	-34.1	74.0	-120.5
APT-50psi	7.2	-222.1	23.6	-93.7	-30.8	83.2	-116.6
APB-75psi	7.9	-223.4	23.6	-91.7	-32.1	88.4	-116.6
APT-75psi	7.9	-223.4	23.6	-91.7	-29.5	87.1	-114.6
APB-100psi	12.5	-218.8	26.2	-93.0	-28.2	93.0	-115.3
APT-100psi	11.1	-219.5	26.2	-91.1	-27.5	93.0	-113.3
APB-125psi	-12.5	-197.9	14.4	-85.2	-24.2	89.1	-108.7
APT-125psi	-14.4	-197.9	11.1	-83.9	-23.6	85.8	-108.1

The first surface cracked occurred during 125 psi air pressure of the bottom after 0.75fpu post-tensioning as shown in Figure 3-67. The cracking on the surface of the concrete was very minor with the maximum crack width being 0.01 inches on the surface. The crack outline can be seen in Figure 3-68 with the cracks on the surface being traced to see them better.



Figure 3-69: C6 cut beam cross section with no cracks.

3.3.3.4 Duct Tie Reinforcement Gauges

Strain gauges were installed on the duct ties. As the spacing decreased between the duct ties, a similar approach was taken into account with gauges installed on both sets of duct ties located to either side of center and all subsequent duct ties out to the same previous location of +26.25 inches from centerline (on the stressing side). The details of the locations for the strain gauges can be seen in Chapter 2, Figure 2-21. The strain results are only shown for the duct ties to both sides of center and +26.25 inches from centerline for comparison purposes. The results for the remaining of the duct tie reinforcement bars are shown in Appendices A and B. The duct ties closest to the center of the beam did not reach the yield point of the reinforcement (in C5, the gauges did reach yield). The duct tie reinforcement bars are reaching a maximum of approximately 1,000 $\mu\epsilon$ along the beam, a stress of 29 ksi.

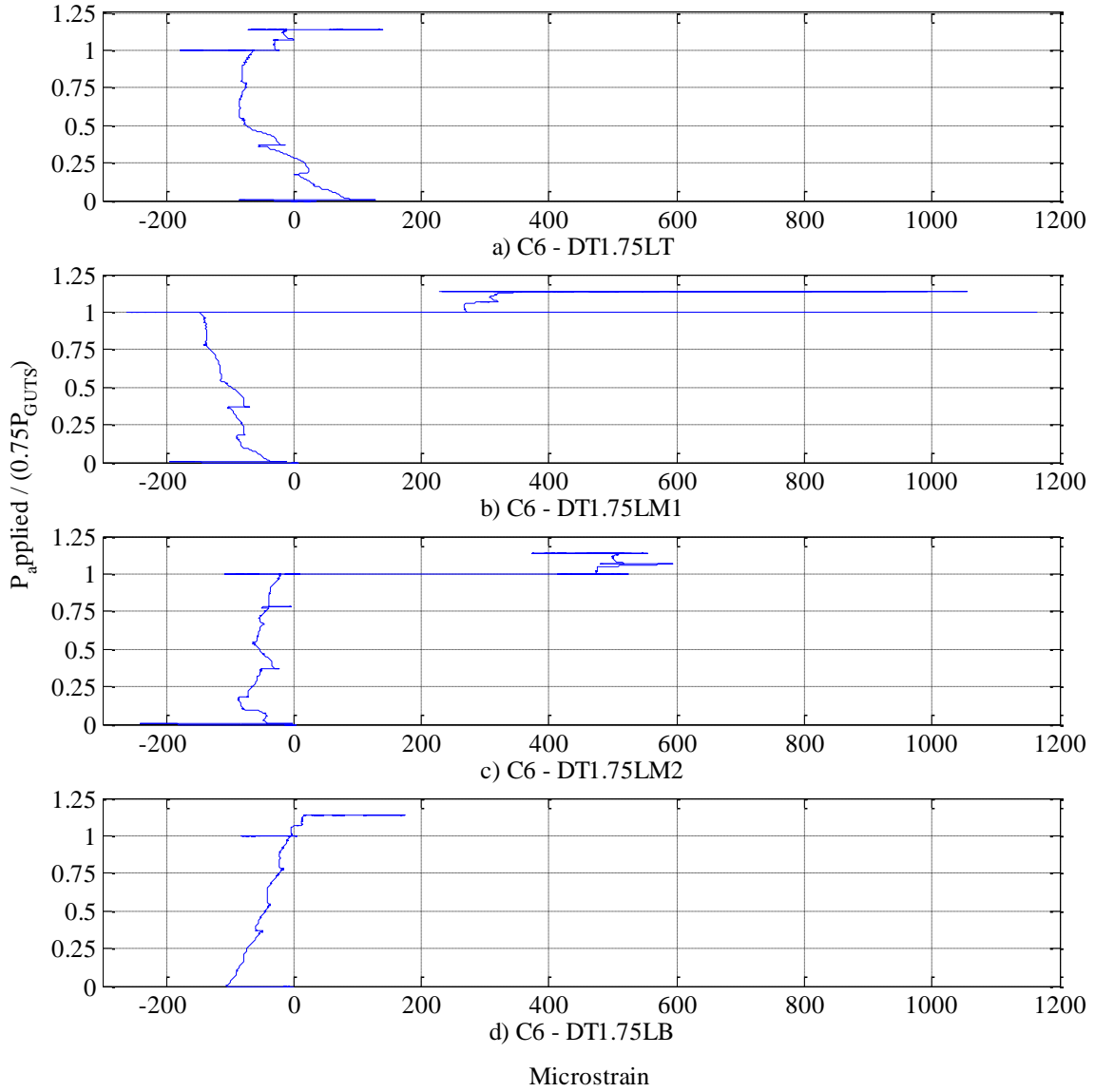


Figure 3-70: C6 duct tie reinforcement strain at -1.75" from centerline.

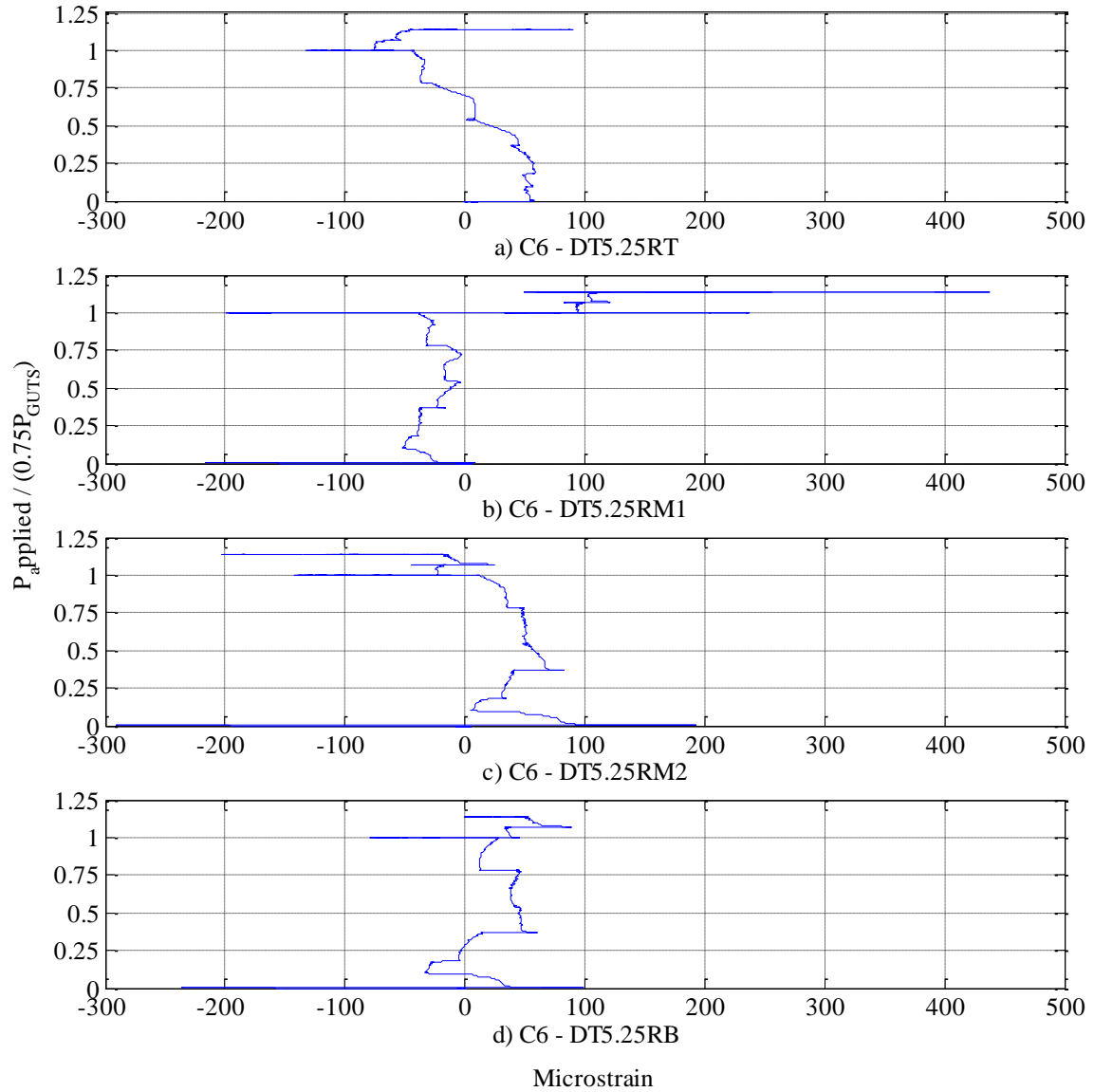


Figure 3-71: C6 duct tie reinforcement strain at +5.25" from centerline.

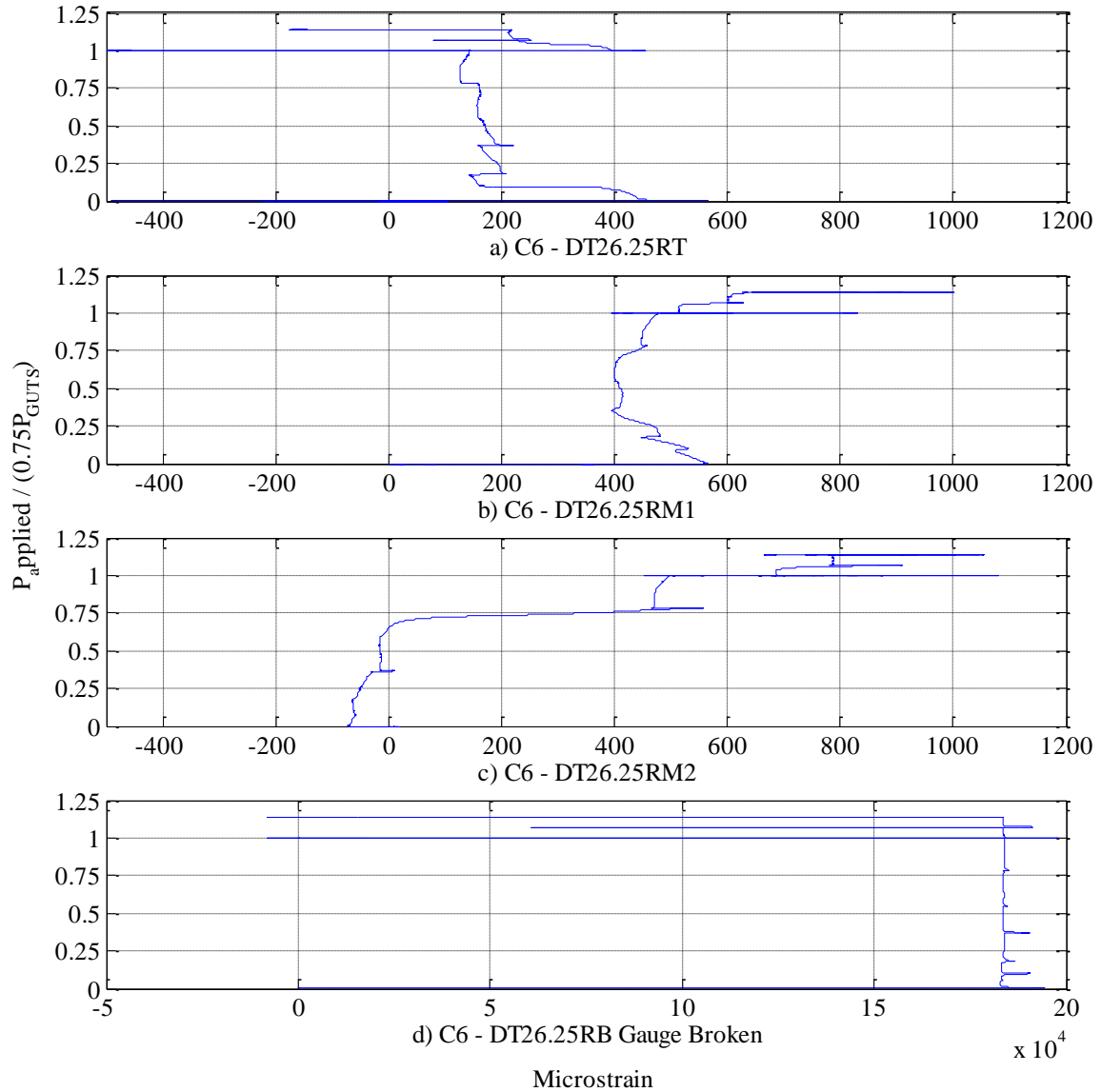


Figure 3-72: C6 duct tie reinforcement strain at +26.25" from centerline.

With duct ties being located in the same position along the beam at +26.25 inches from center for both C5 and C6, comparing the beams, Figure 3-56 for C5, shows slightly larger strains in C6 which has the shorter spacing between duct tie reinforcement bars. Only one duct tie yielded with the location being at +19.25 inches from centerline between the middle and bottom ducts (shown in Appendices A and B). Both +12.25 inches and +19.25 inches from center duct tie reinforcement strain gauge results are shown in Appendices A and B. The strain values for the duct ties on each side of center (-1.75 inches and 5.25 inches) and at +26.25 inches are shown in Table 3-32, Table 3-33 and Table 3-34 at the end of each loading stage.

Table 3-32: C6 duct ties at -1.75" at each loading stage.

	DT1.75LT	DT1.75LM1	DT1.75LM2	DT1.75LB
	με	με	με	με
APB-50psi	6.5	13.1	0.0	-13.1
APT-50psi	26.2	-13.1	-26.2	-13.1
DL	13.1	0.0	0.0	-13.1
0.15fpuB	32.7	-72.0	-45.8	-78.5
0.15fpuT	0.0	-91.6	-78.5	-65.4
0.45fpuB	-52.3	-104.7	-45.8	-52.3
0.45fpuT	-85.0	-124.3	-58.9	-39.2
0.75fpuB	-72.0	-124.3	-6.5	-19.6
0.75fpuT	-65.4	-143.9	-32.7	-13.1
APB-50psi	-170.1	-242.1	-91.6	-85.0
APT-50psi	-157.0	-255.2	-85.1	-72.0
APB-75psi	-176.6	-248.6	-58.9	-58.9
APT-75psi	-157.0	-248.6	-58.9	-65.4
APB-100psi	-157.0	-222.5	-13.1	-65.4
APT-100psi	-163.5	-209.4	-6.5	-72.0
APB-125psi	-104.7	235.5	405.7	-6.5
APT-125psi	-91.6	209.4	412.2	-6.5
0.85fpuB	-32.7	301.0	595.4	0.0
0.85fpuT	-26.2	353.3	510.4	19.6
APB-50psi	-72.0	418.7	464.6	19.6
APT-50psi	-65.4	418.7	477.6	39.2
APB-75psi	-58.9	477.6	438.4	45.8
APT-75psi	-52.3	471.1	464.6	45.8
APB-100psi	-39.2	359.9	399.1	58.9
APT-100psi	-26.2	346.8	418.8	65.4
APB-125psi	65.4	242.1	379.5	117.7
APT-125psi	45.8	222.5	392.6	104.7

Table 3-33: C6 duct ties at +5.25" at each loading stage.

	DT5.25RT	DT5.25RM1	DT5.25RM2	DT5.25RB
	με	με	με	με
APB-50psi	6.5	6.5	6.5	-6.5
APT-50psi	13.1	-6.5	-6.5	-6.5
DL	13.1	0.0	0.0	-6.5
0.15fpuB	52.3	-39.2	52.3	6.5
0.15fpuT	58.9	-52.3	19.6	-19.6
0.45fpuB	39.2	-39.2	45.8	13.1
0.45fpuT	13.1	-6.5	52.3	32.7
0.75fpuB	-32.7	-19.6	45.8	45.8
0.75fpuT	-52.3	-45.8	19.6	26.2
APB-50psi	-111.2	-202.7	-124.3	-52.3
APT-50psi	-137.3	-196.2	-117.7	-72.0
APB-75psi	-104.6	-196.2	-111.2	-72.0
APT-75psi	-104.6	-183.1	-98.1	-65.4
APB-100psi	-104.6	-176.6	-78.5	-65.4
APT-100psi	-104.6	-183.1	-71.9	-58.9
APB-125psi	-78.5	52.3	-137.3	-32.7
APT-125psi	-71.9	32.7	-143.9	-26.2
0.85fpuB	-52.3	85.0	-19.6	32.7
0.85fpuT	-39.2	104.6	-19.6	39.3
APB-50psi	-32.7	52.3	-98.1	-13.1
APT-50psi	-32.7	52.3	-98.1	0.0
APB-75psi	-26.2	71.9	-91.6	6.5
APT-75psi	-39.2	71.9	-98.1	13.1
APB-100psi	-26.2	78.5	-117.7	13.1
APT-100psi	-19.6	85.0	-117.7	13.1
APB-125psi	58.9	157.0	-183.1	26.2
APT-125psi	45.8	150.4	-202.7	19.6

Table 3-34: C6 duct ties at +26.25" at each loading stage.

	DT26.25RT	DT26.25RM1	DT26.25RM2	DT26.25RB
	με	με	με	με
APB-50psi	6.5	26.1	0.0	0.0
APT-50psi	58.9	339.9	13.1	0.0
DL	52.3	366.1	19.6	0.0
0.15fpuB	385.8	503.3	-58.9	183390
0.15fpuT	143.9	451.0	-58.9	183489
0.45fpuB	157.0	405.3	13.1	183855
0.45fpuT	163.5	405.3	-6.5	183678
0.75fpuB	143.9	457.6	549.5	183986
0.75fpuT	137.3	490.3	503.7	184058
APB-50psi	-562.4	418.4	510.2	0.0
APT-50psi	-555.9	418.4	503.7	0.0
APB-75psi	-523.2	483.7	654.2	0.0
APT-75psi	-536.3	483.7	641.1	0.0
APB-100psi	-497.0	509.9	686.9	0.0
APT-100psi	-503.6	503.3	680.3	0.0
APB-125psi	-490.5	536.0	706.5	0.0
APT-125psi	-477.4	522.9	680.3	0.0
0.85fpuB	215.8	634.1	896.2	183672
0.85fpuT	215.8	634.1	791.5	183318
APB-50psi	-163.5	640.6	798.1	0.0
APT-50psi	-150.4	640.6	791.5	0.0
APB-75psi	-170.0	653.7	791.5	0.0
APT-75psi	-157.0	660.2	785.0	0.0
APB-100psi	-170.0	660.2	758.8	0.0
APT-100psi	-163.5	653.7	739.2	0.0
APB-125psi	-176.6	679.8	680.3	0.0
APT-125psi	-176.6	666.7	667.2	0.0

3.3.3.5 Web Bulging

The web bulge for C6 is shown in Figure 3-73. The overall web bulge drastically decreased to approximately one-fifth of C5 (Figure 3-57). Similarly to C5, the duct ties provided extra reinforcement to limit the web expansion due to the air pressure and reduce it to the same level as the post-tensioning web bulge. The web bulging at the end of each loading stage is shown in Table 3-35. The total web bulge shown in Table 3-35 is the total bulge from both the west and east face for the middle gauge.

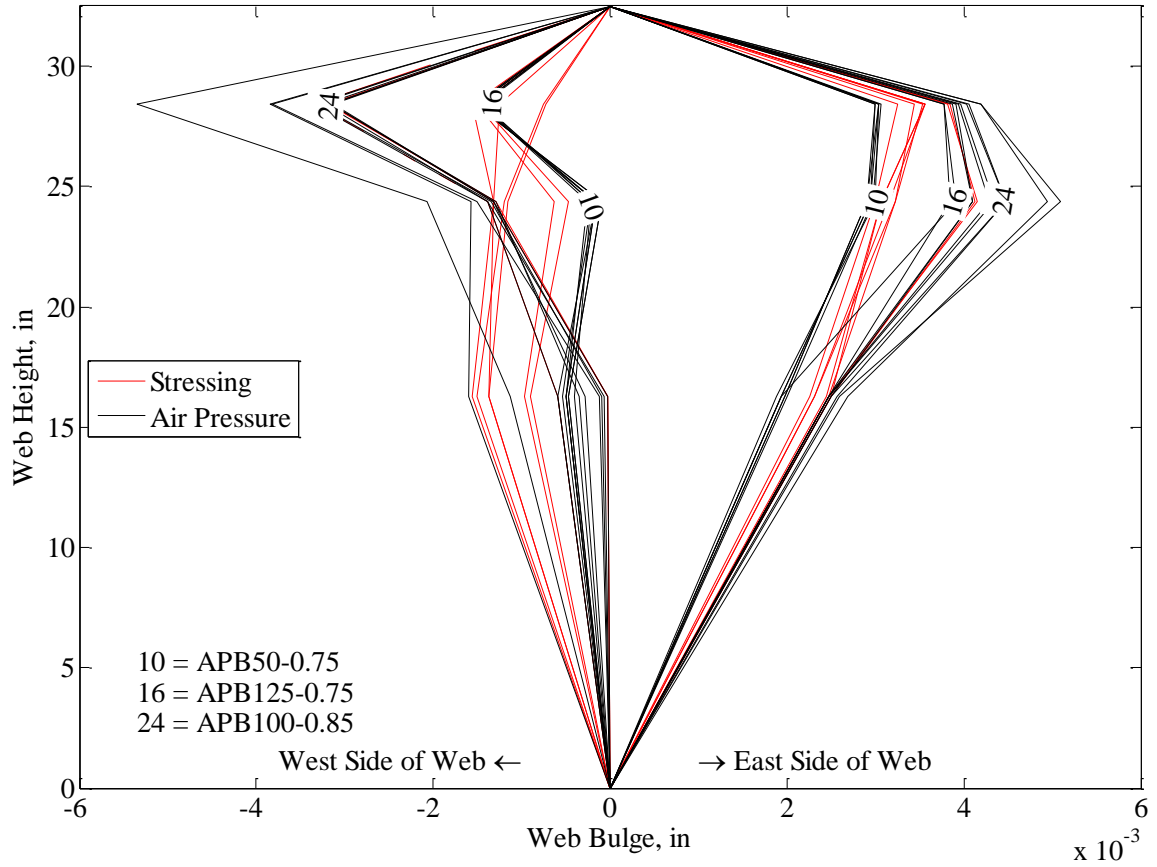


Figure 3-73: C6 web bulge.

Table 3-35: C6 web bulging at each loading stage.

	WBTW in.	WBMW in.	WBMB in.	WBTE in.	WBME in.	WBBE in.	M. Total in.
APIB	-0.0003	-0.0012	-0.0013	0.0021	0.0019	0.0017	0.0034
APIT	-0.0003	-0.0012	-0.0015	0.0025	0.0019	0.0018	0.0040
DL	-0.0002	-0.0012	-0.0015	0.0024	0.0020	0.0019	0.0039
0.15fpuB	-0.0009	-0.0013	-0.0017	0.0034	0.0029	0.0027	0.0051
0.15fpuT	-0.0009	-0.0014	-0.0018	0.0034	0.0030	0.0025	0.0052
0.45fpuB	-0.0014	-0.0014	-0.0017	0.0033	0.0031	0.0026	0.0050
0.45fpuT	-0.0017	-0.0015	-0.0018	0.0034	0.0030	0.0025	0.0052
0.75fpuB	-0.0016	-0.0009	-0.0011	0.0032	0.0031	0.0026	0.0048
0.75fpuT	-0.0016	-0.0006	-0.0011	0.0032	0.0028	0.0023	0.0048
APB-50psi	-0.0017	-0.0003	-0.0008	0.0028	0.0028	0.0021	0.0045
APT-50psi	-0.0017	-0.0003	-0.0008	0.0029	0.0028	0.0022	0.0046
APB-75psi	-0.0016	-0.0003	-0.0008	0.0029	0.0028	0.0021	0.0045
APT-75psi	-0.0016	-0.0003	-0.0008	0.0028	0.0028	0.0021	0.0045
APB-100psi	-0.0016	-0.0005	-0.0008	0.0029	0.0028	0.0020	0.0045
APT-100psi	-0.0016	-0.0004	-0.0008	0.0029	0.0029	0.0021	0.0045
APB-125psi	-0.0033	-0.0015	-0.0003	0.0036	0.0038	0.0026	0.0071
APT-125psi	-0.0033	-0.0015	-0.0003	0.0037	0.0037	0.0026	0.0071
0.85fpuB	-0.0033	-0.0015	-0.0001	0.0036	0.0041	0.0028	0.0074
0.85fpuT	-0.0033	-0.0014	-0.0002	0.0037	0.0040	0.0027	0.0073
APB-50psi	-0.0033	-0.0014	-0.0001	0.0038	0.0040	0.0026	0.0073
APT-50psi	-0.0033	-0.0015	-0.0002	0.0038	0.0040	0.0026	0.0073
APB-75psi	-0.0035	-0.0014	-0.0001	0.0038	0.0042	0.0026	0.0077
APT-75psi	-0.0034	-0.0014	-0.0001	0.0038	0.0042	0.0026	0.0076
APB-100psi	-0.0039	-0.0017	-0.0001	0.0040	0.0044	0.0028	0.0083
APT-100psi	-0.0040	-0.0017	-0.0001	0.0039	0.0043	0.0027	0.0083
APB-125psi	-0.0055	-0.0023	0.0005	0.0041	0.0048	0.0028	0.0103
APT-125psi	-0.0055	-0.0023	0.0005	0.0042	0.0048	0.0028	0.0103

3.3.3.6 Shear Reinforcement Gauges and Beam End Displacement

The strain gauge results from the shear reinforcement and the beam end displacement was not significant to this study. Therefore, refer to Appendices A and B for the results for the shear reinforcement strain gauges and the displacements on the ends of the beams.

3.3.3.7 C6 Results Overview

Reducing the duct tie reinforcement spacing from C5's 17.5 inches to the specified 7.0 inches in C6 resulted in a decrease in overall strain around the post-tensioning ducts. With the reduced strain values present, it in turn led to cracking being

delayed with a minor crack appearing at 125 psi air pressure of bottom duct after 0.75fpu testing of the middle duct. Web bulging decreased with the decrease in spacing between the duct ties compared to C5 while preventing the air pressure from exerting a significant effect on the web bulging.

3.3.4 Round B Results Overview

Round B beams focused on varying design details to accomplish a better performance over Round A beams. The design details that were altered were the spacing between the ducts at midspan of the beam, the inclusion of duct tie reinforcement between the duct and the spacing of the duct ties. The increase in spacing of the ducts was chosen based on the weak tension capacity of concrete and minimal concrete between the ducts. With additional concrete between the ducts, the tension capacity would be higher. The increased spacing between the ducts improved the overall performance of the beam with recorded strains being lower and the amount/width of cracking shrinking compared to the beam with smaller spacing.

The addition of reinforcement around the ducts provides extra tension capacity around the areas with high tension forces present. The reinforcement added the extra tension capacity and the strains produced within the beam were much lower comparatively while the cracks that transferred to the surface of the web were in turn reduced. As expected with the spacing of the duct tie reinforcement, lessening the distance between the bars helped transfer the transverse forces. With the spacing being at closer intervals, the strains were lowered around the ducts with minimal crack widths reaching the surface of the web. Additionally, the duct ties controlled the effect the air pressure had on the bulging of the web and the less spacing between duct ties delivering less web bulging.

3.4 Beam Comparisons

3.4.1 Curvature Parameter

3.4.1.1 Embedded Concrete Strain Gauges at Centerline

Round A experimental testing beams consisted of varying the tendon curvatures to understand the effect curvatures had on cracking within the web. The larger the curvature, the larger the distributed force being exerted on the beam and therefore an increase in the cracking potential. Figure 3-74 shows the comparisons of the embedded strain gauges of each beam in Round A. It should be kept in mind that C1 and C2 used the same concrete mixture whereas C3 had a slight difference due to the use of a second concrete delivery truck. Overall comparing the beams, C1 with the lower curvature forces performed better than C2 for the top (between top and middle ducts) and middle (between middle and bottom ducts) gauges. Upon inspection it can be noticed that C3 performed better than C1 and C2 in most cases; this can be due to the fact that the tensile strength of concrete in C3 was higher (C1: 448.8 psi, C2: 449.5 psi, C3: 476.8 psi). It should also be noted that after cutting C2 in half after the conclusion of the experiment, there was evidence of poor consolidation between the ducts. This could have influenced the comparisons between C2 and C3. With the slightly larger tensile strength for C3, it led to less cracking around the ducts and a noticeable decrease in concrete strain during the

0.75fpu stressing phase of both ducts. Looking at the strains at the end of 50 psi air pressure testing after 0.75fpu, the strains are larger between the top-middle ducts and middle-bottom ducts in C2 compared with C1 and C3 as shown in Table 3-36.

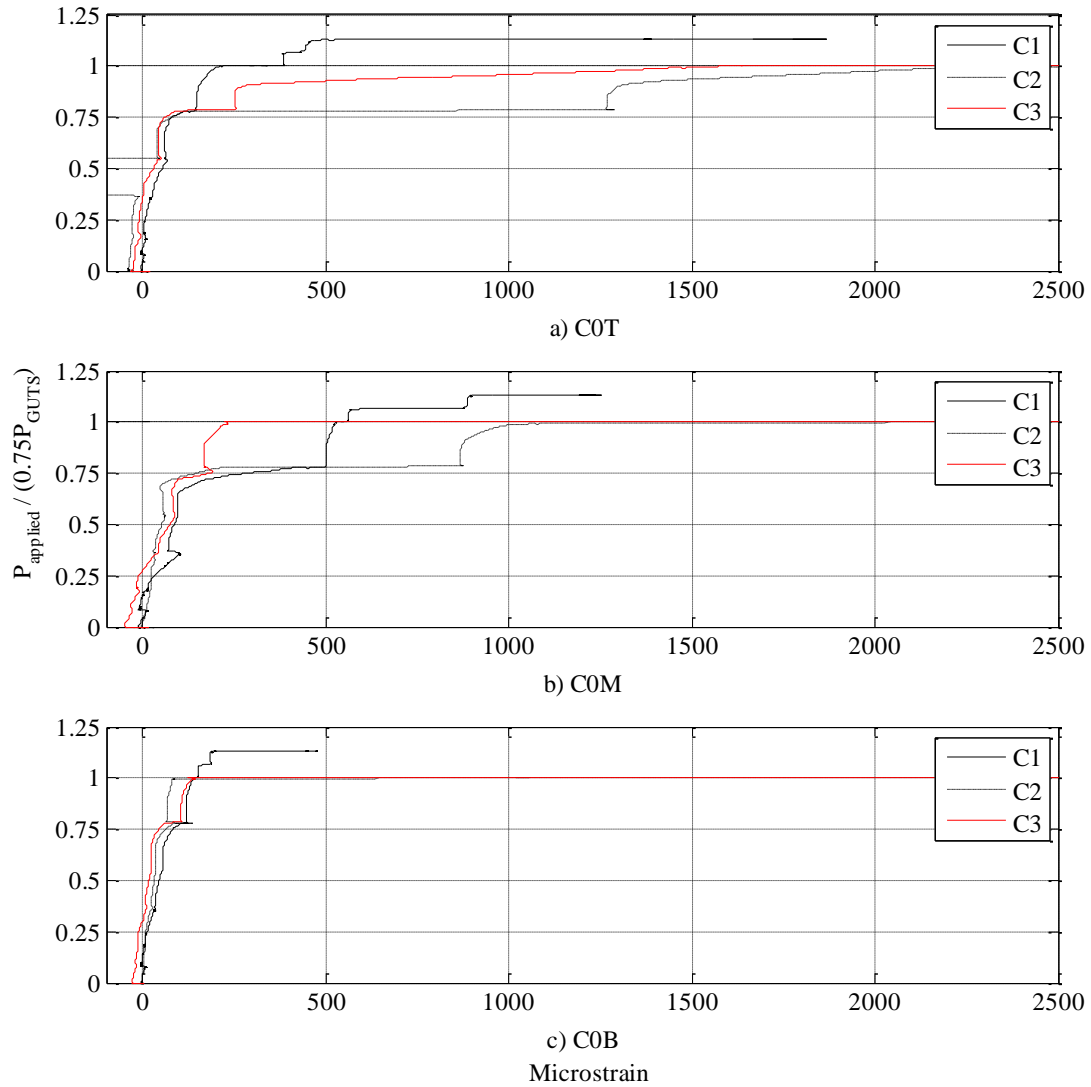


Figure 3-74: Round A embedded concrete strain at centerline.

Table 3-36: Embedded concrete strain 0” O.C. at 50 psi after 0.75fpu.

	C1	C2	C3
C0T, $\mu\epsilon$	323.5	5690.5	4654.3
C0M, $\mu\epsilon$	545.3	6399.7	4411.9
C0B, $\mu\epsilon$	142.0	8027.8	11465.7

3.4.1.2 Embedded Concrete Strain Gauges at 30 inches from Centerline

At thirty inches from center, the performance of the beams are similar, as seen in Figure 3-75. C1 achieved the least amount of strain around the ducts with air pressure having a minor effect. The air pressure had a larger role for C2 and C3 with having a long

horizontal line at 1.0 on the y-axis, which represents air pressure testing after 0.75fpu.

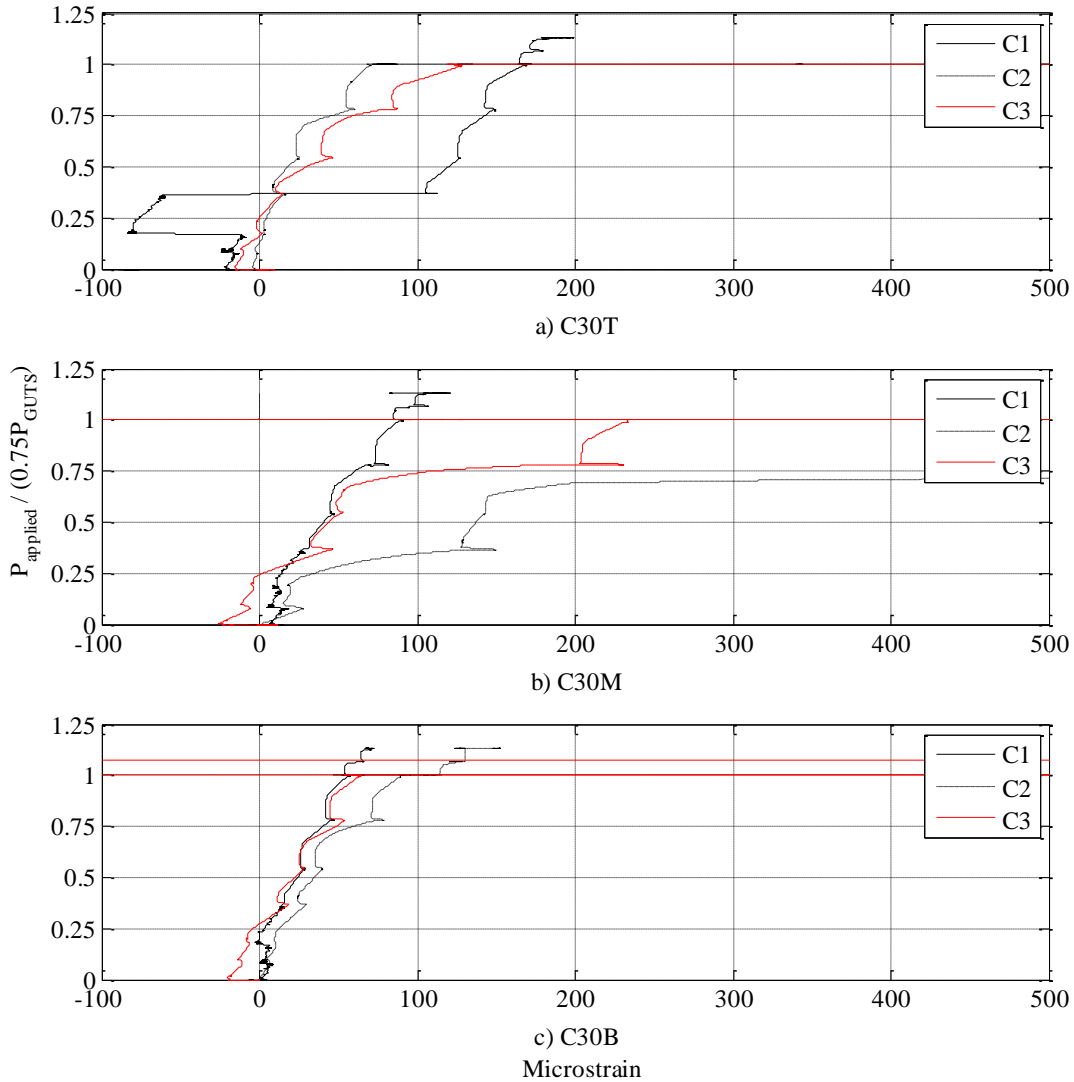


Figure 3-75: Round A embedded concrete strain at +30" from centerline.

At +30 inches, C3 had lower concrete strain compared to C1 and C2. During stressing up to 0.75fpu, the strain between the middle and bottom ducts (C30M) increased dramatically for both C2 and C3 compared to C1. Overall, the larger the post-tension curvatures in a design caused larger concrete strains around the ducts. C3 results in higher strain values except for between the middle and bottom ducts at +30 inches from centerline as seen in Table 3-37.

Table 3-37: Embedded concrete strain 30" O.C. at 50 psi after 0.75fpu.

	C1	C2	C3
C30T, $\mu\epsilon$	165.4	76.0	5713.0
C30M, $\mu\epsilon$	87.3	4603.7	116.6
C30B, $\mu\epsilon$	57.2	91.7	5053.3

3.4.2 Duct Spacing and Duct Tie Reinforcement

3.4.2.1 Embedded Concrete Strain Gauges at Centerline

Round B experimental beams were developed to improve the design and performance of Round A beams. All of Round B beams were based on the same curvature as C2 with design specifications outlined in Section 2.5. The results of comparing Round B beams to C2 are shown in Figure 3-76. C4, C5 and C6 all had an increased duct spacing over C2 (1.05" vs. 0.7"). C5 and C6 also had duct tie reinforcement added with C5 having #3 bar at 17.5 inches and C6 having #3 bar at 7.0 inches. C4, C5 and C6 all had smaller embedded concrete strains throughout the stressing phases. The best performing beam was C6 which had the increased spacing between ducts and the duct tie with the smaller spacing. Examining the strains at 50 psi after 0.75fpu (Table 3-38), it is noticed that the strains at centerline significantly reduced with the increase in spacing between the ducts.

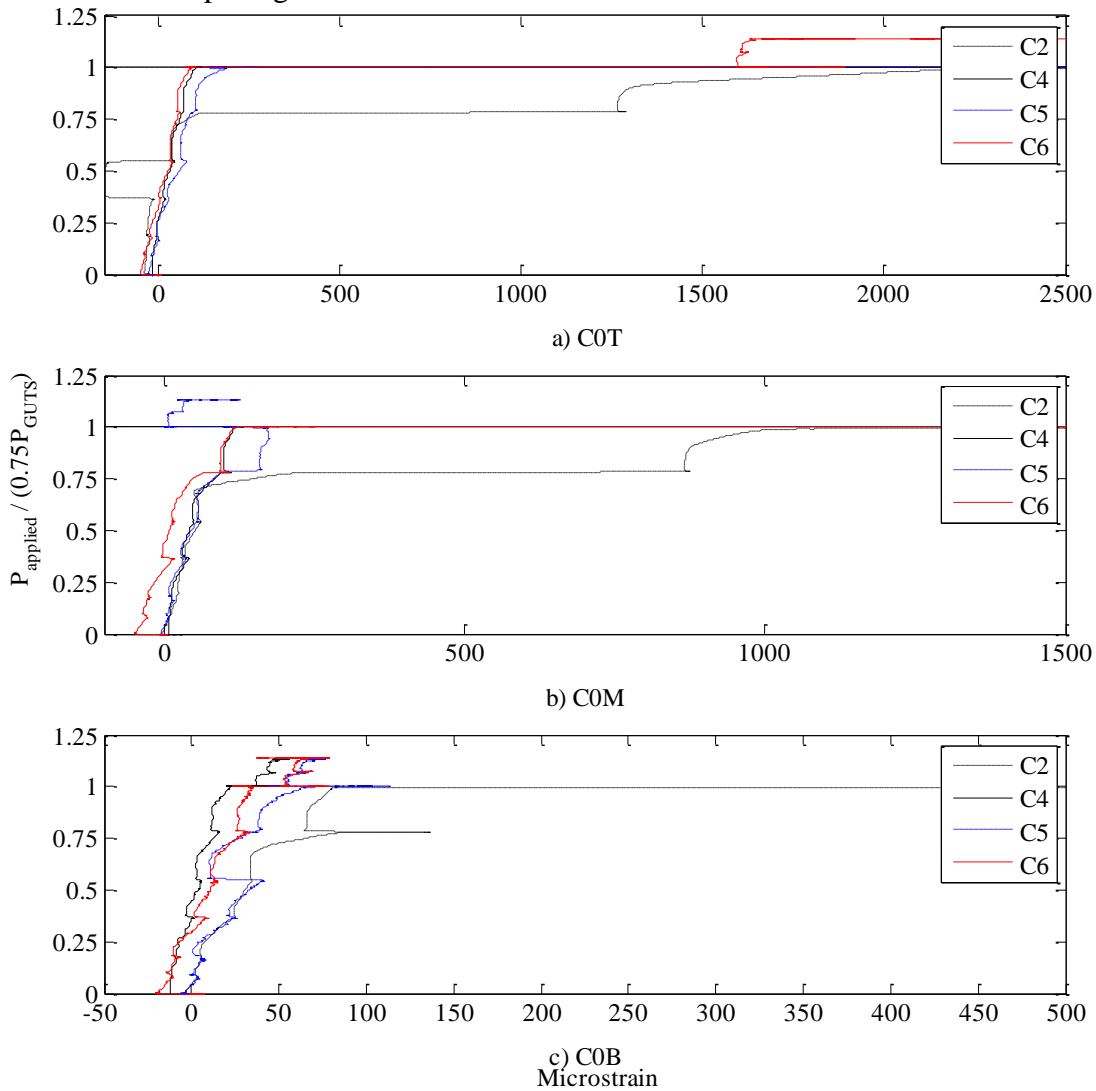


Figure 3-76: Embedded concrete comparisons at centerline.

Table 3-38: Embedded concrete strain 0” O.C. at 50 psi after 0.75fpu.

	C2	C4	C5	C6
C0T, $\mu\epsilon$	5690.5	104.7	157.0	78.5
C0M, $\mu\epsilon$	6399.7	117.8	111.3	144.0
C0B, $\mu\epsilon$	8027.8	26.2	117.7	19.6

With the duct tie reinforcement bars added to the beams for C5 and C6, the concrete strains do not decrease compared to C4 as expected. As mentioned in Section 2.6.2, the embedded strain gauges were attached with steel wire to the shear steel before the concrete was poured. During the concrete pour it is possible that the gauges were altered leading to each gauge reading a different combination of x, y and z strain within the beam. C4, C5 and C6 strains were all relatively similar to each other and all performed better than C2.

3.4.2.2 Embedded Concrete Strain Gauges at 30 inches from Centerline

The embedded concrete strain gauges at +30 inches from center are shown in Figure 3-77 to compare the increase in duct spacing and duct tie reinforcement spacing. The strains associated at +30 inches from center better represent the expectations with the increase in duct spacing and spacing of duct tie reinforcement. C4 with the larger spacing between the ducts had lower strains compared to the smaller duct spacing of C2. The added duct tie reinforcement in C5 and C6 further decreased the concrete strain in comparison to C4. The one exception for C5 is when the strain experienced an unexpected decrease around 0.6 on the y-axis which is when 0.45fpu stressing is completed. Comparing the strains at 50 psi after 0.75fpu, going from C2, C4, C5 to C6, each beam has less strain than the previous beam with only the strain between the middle and bottom ducts on C6 showing a slightly larger strain. This could be from the strain gauge being altered during the concrete casting process leading to the strain reading a different direction than the intended transverse direction. The strains for C2, C4, C5 and C6 are shown for 30 inches from centerline upon completion of 50 psi after 0.75fpu in Table 3-39.

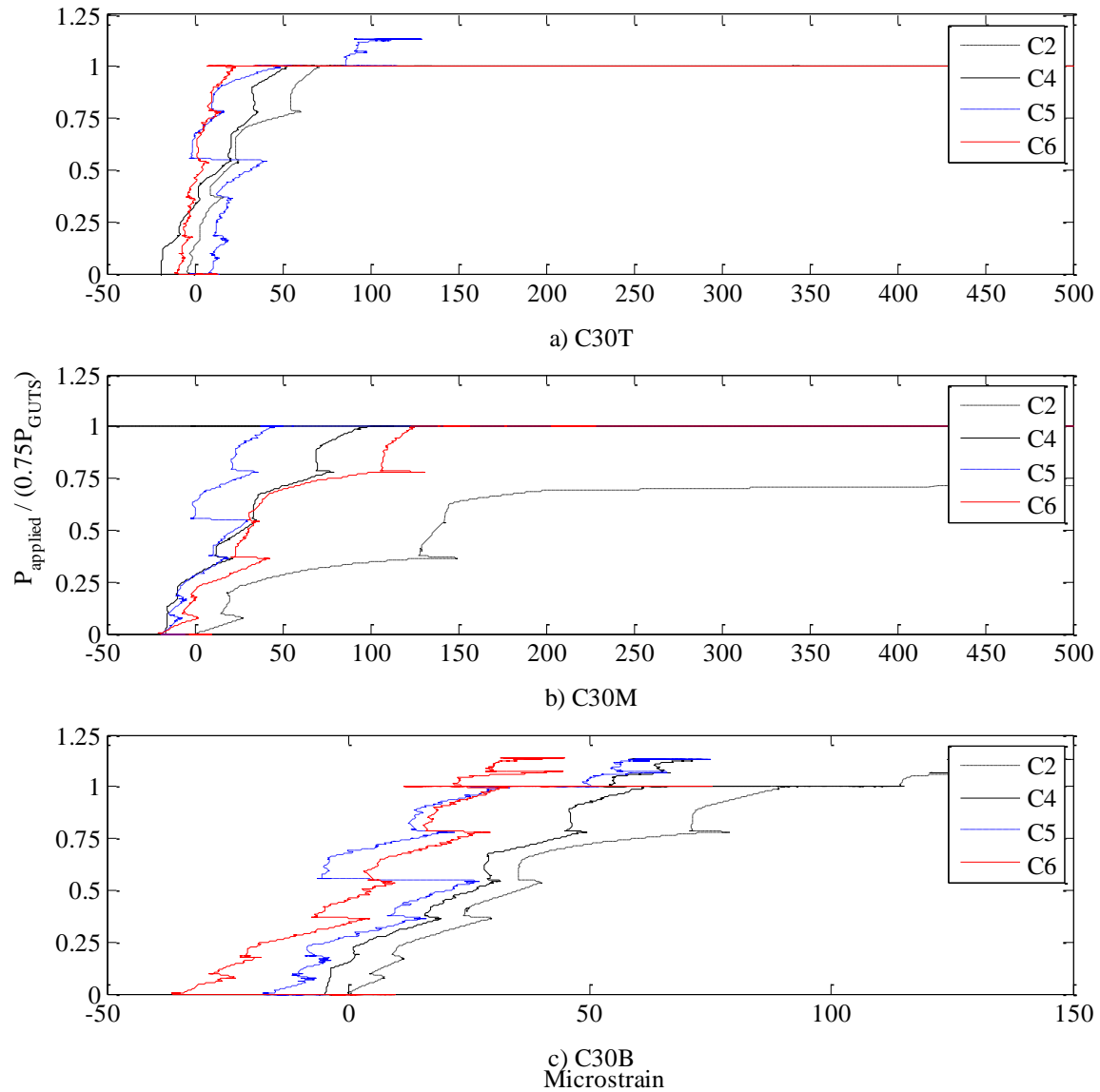


Figure 3-77: Embedded concrete comparisons at +30” from centerline.

Table 3-39: Embedded concrete strain 30” O.C. at 50 psi after 0.75fpu.

	C2	C4	C5	C6
C30T, $\mu\epsilon$	76.0	65.4	26.2	0
C30M, $\mu\epsilon$	4603.7	104.7	52.3	137.3
C30B, $\mu\epsilon$	91.7	65.4	45.8	13.1

3.4.2.3 Web Bulging

Web bulging was recorded in C3, C4, C5 and C6. The results are shown in Figure 3-78 for 50 psi after 0.75fpu. C3 was included even though the curvature is higher compared to the succeeding beams which have curvatures equal to C2’s.

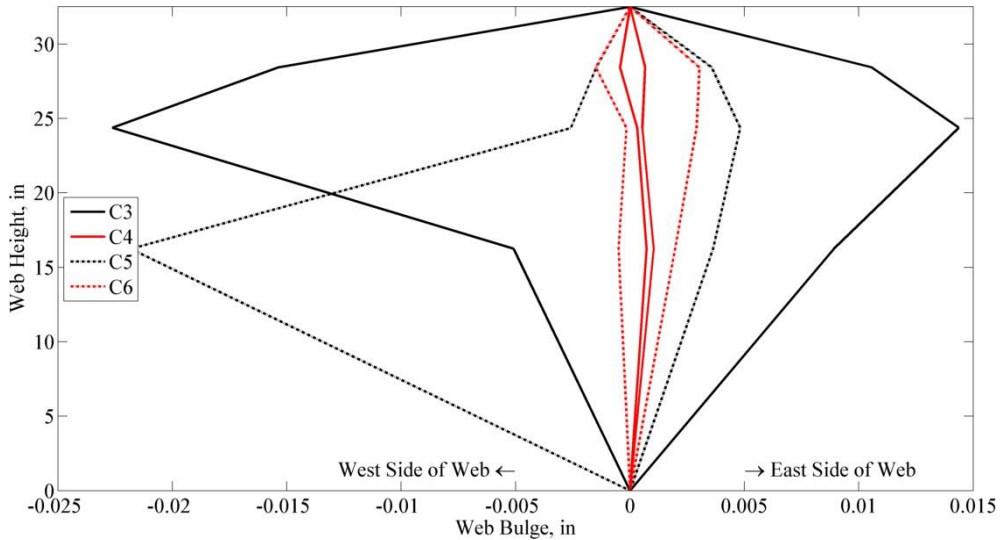


Figure 3-78: Web bulge comparisons at 50psi after 0.75fpu.

When increasing the spacing between the ducts and adding duct tie reinforcement bars, the web bulge decreased. C4 had the least web bulge at the end of NDOT loading sequence. It should be noted that during the testing of C4, at 100 psi air pressure of the middle duct after 0.75fpu (following NDOT loading sequence), the beam suddenly cracked along the entire surface of the web. The web bulging halfway down the west side of the web on C5 shows a large increase in web bulging; this is most likely due to an error in the transducer reading. Similarly comparing the results of the web bulging at the end of all the experimental loading is provided in Figure 3-79.

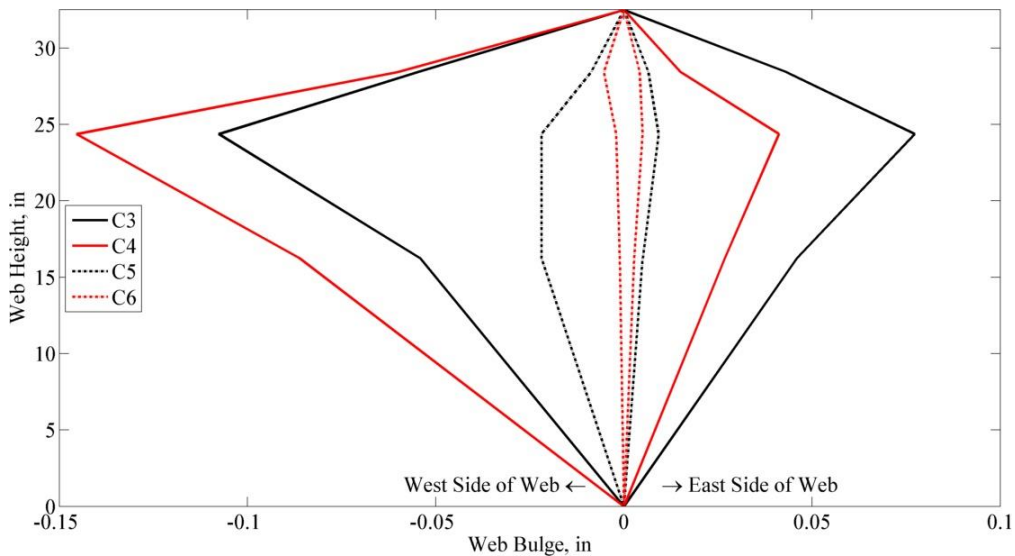


Figure 3-79: Web bulge comparisons at 125psi after 0.85fpu.

The web bulging at the end of all the loading provides a comparison between the various configurations. The two beams that do not have any duct tie reinforcement included have the largest web bulging. The web bulging is approximately ten times larger in Figure 3-79 than the end of the web bulging after NDOT loading sequence in Figure

3-78. The web bulging in C4 exceeded that of C3 on the west facing web only which could be from the fact that the ducts in C4 were closer to that face than C3 leading to the higher web bulge. Table 3-40 shows the total web bulging in the middle gauge at the end of 50 psi after 0.75fpu and at the end of loading at 125 psi after 0.85fpu.

Table 3-40: Total middle web bulge values for C3, C4, C5 and C6.

	C3	C4	C5	C6
50psi-0.75fpu, in.	0.037	0.001	0.026	0.0046
125psi-0.85fpu, in.	0.179	0.186	0.03	0.0103

3.4.3 Web Cracking

Appearance of concrete cracks on the surface of the web are shown in Table 3-41. Cracks first appeared in C5 during 75 psi air pressure testing after 0.75fpu but were hairline cracks and became more apparent during 100 psi air pressure testing after 0.75fpu. Overall the beams performed as anticipated with an increase in curvature leading to an increase in cracking, shown in Table 3-42, and strains. Once the spacing was increased between the ducts, the concrete strains decreased, and once again decreased upon the insertion of the duct tie reinforcement bars around the post-tensioning ducts. When the duct tie reinforcement bar spacing was reduced, the performance increased providing less concrete strain around the ducts as the reinforcement bars attracted the tension forces.

Table 3-41: Appearance of cracks on web face.

C1: No Cracks
C2: 0.75fpu-Bottom
C3: 0.75fpu-Bottom; 50psi greatly increased cracks
C4: 100psi Bottom (0.75fpu)
C5: 75psi Bottom (0.75fpu): Very minor cracks; 100psi Bottom (0.75fpu)
C6: 125psi Bottom (0.75fpu)

Table 3-42 shows the maximum crack size with TM representing between top and middle ducts; MB is between middle and bottom ducts; BB is below the bottom duct. C1 and C6 performed the best for prolonging the appearance of surface cracks and minimizing crack sizes.

Table 3-42: Maximum crack widths throughout the beam.

	On surface, in	TM, in	MB, in	BB, in
C1	0	0.005	0	0
C2	0.05	0.03	0.15	0.2
C3	0.04	0.03	0.03	0.07
C4	0.04	0.03	0.03	0.06
C5	0.013	0	0.016	0.01
C6	0.01	0	0	0

4.0 Analytical Parametric Study

4.1 Introduction

The experimental program studied the effects of curvature, increased duct spacing and the introduction of duct tie reinforcement bars in laboratory conditions. The purpose of the analytical modeling is to:

1. Study the effects of additional variables.
2. Determine the most influential design detail in reducing web cracking.
3. Understand the flow of forces throughout the web.
4. Develop a design equation for improved web performance.

The parametric study was designed to look at the number of ducts, duct location within the web, the post-tensioning duct curvatures and the duct tie reinforcement spacing. Table 4-1 shows the parametric study in full detail. The experimental beams accounted for various curvatures and duct tie reinforcement spacings where the analytical models furthered study the effects of a larger variety of curvatures and duct tie spacings. The amount of ducts within the web were based on NDOT practice. NDOT typically uses 2, 3 and 4 ducts in their post-tensioned bridges. The location of the ducts in the web varied from the top of the web over columns and towards the bottom at midspan.

Initial loading of the analytical models were patterned after the loading protocol used in the experimental program (see Section 2.2.3). For the purpose of the analytical program, the loading was simplified to a single tendon loading stress of 0.80fpu and air pressure of 100 psi. This is slightly higher than the NDOT's standard of 0.75fpu and 50 psi to account for possible over loadings of the tendon/duct during construction.

Table 4-1: Parametric Study at 0.7 scale and duct spacing at 1.05"

# of Ducts	Equivalent Curvature Loads, kip/ft	Reinforcement Spacing, in	Duct Location on Web	Loading
2	19.12 (C2)	N, 17.5, 3.5	Top	0.80fpu + 100psi
3	19.12 (C2)	N, 17.5, 3.5	Top	0.80fpu + 100psi
4	19.12 (C2)	N, 17.5, 3.5	Top	0.80fpu + 100psi
3	19.12 (C2)	N	Top	0.80fpu + 100psi
	19.12 (C2)	N	Middle	0.80fpu + 100psi
	19.12 (C2)	N	Bottom	0.80fpu + 100psi
3	11.75 (C1)	N, 17.5, 10.5, 3.5	Top	0.80fpu + 100psi
	19.12 (C2)	N, 17.5, 10.5, 3.5	Top	0.80fpu + 100psi
	22.6	N, 17.5, 10.5, 3.5	Top	0.80fpu + 100psi
	26.1 (C3)	N, 17.5, 10.5, 3.5	Top	0.80fpu + 100psi
	29.7	N, 17.5, 10.5, 3.5	Top	0.80fpu + 100psi

Some configurations in Table 4-1 were further modeled to include an artificial crack between the ducts (see Table 4-2). C1 and C3 equivalent loads were determined based on

NDOT's extreme curvature cases, with C2 being the average of the extremes and C3+ being a slight increase from C3 configuration to capture higher loads. The equivalent curvatures were calculated based on the average amplitude heights, a_{avg} , for both tendons and substituting into equation 2-12 for a single amplitude, "a".

Table 4-2: Atena models with the artificial crack between the ducts.

# of Ducts	Equivalent Curvature Loads, kip/ft.	Reinforcement Spacing, in	Duct Location on Web	Loading
3	11.75 (C1)	17.5, 14.0, 10.5, 7.0, 3.5	Top	0.80fpu + 100psi
	19.12 (C2)	17.5, 14.0, 10.5, 7.0, 3.5	Top	0.80fpu + 100psi
	26.1 (C3)	17.5, 14.0, 10.5, 7.0, 3.5	Top	0.80fpu + 100psi
	29.7 (C3+)	17.5, 14.0, 10.5, 7.0, 3.5	Top	0.80fpu + 100psi

The pressure in the ducts was modeled with area loads around the duct instead of actual pressure. Therefore, when the cracks form in the model, air pressure does not flow into the crack as would be the case in the experiment or in the field. Through introducing the crack, pressure is placed on either side of the crack to allow for loading in the transverse direction of the beam (Section 4.5).

4.2 Parametric Model

The parametric study used the Atena 3D finite element (FE) analysis software. In order to be able to make comparisons with the experimental results and models, the analytical models were based on the experimental beams and the experimental setup. Since the beams are symmetrical in geometry and loading, the models in Atena were cut in half to decrease the processing time. As the beams were cut in half, the proper boundary conditions were applied to appropriately model the beam as the full beam. Boundary conditions consist of applying supports to the cut face, which is at midspan of the beam, to prevent the cut face from being able to rotate about the longitudinal direction, as seen in Figure 4-1. With the proper boundary conditions and loading, the half model would react the same as the full beam model.

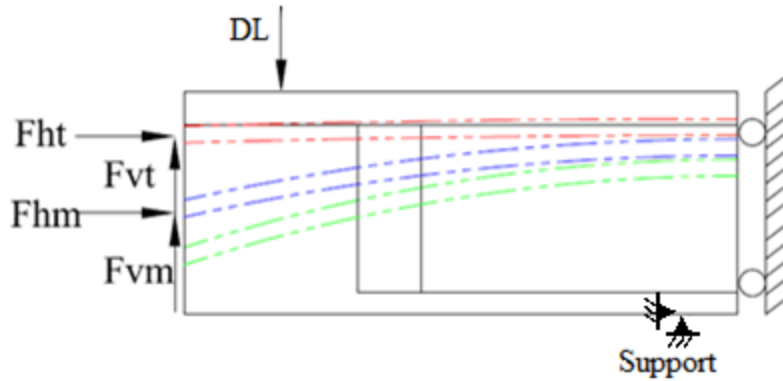
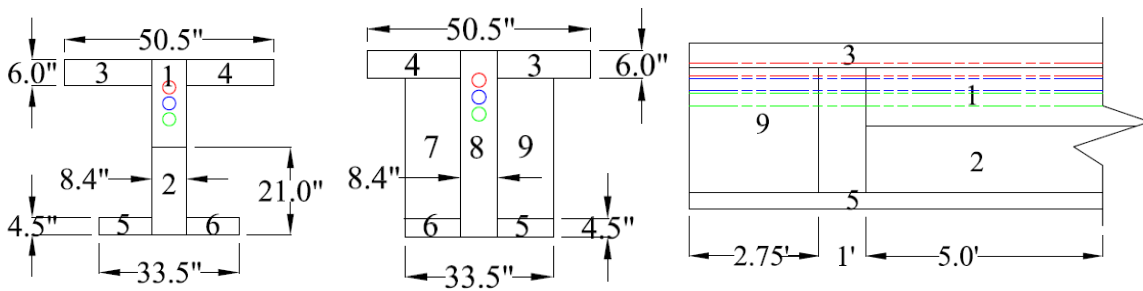


Figure 4-1: Atena boundary conditions.

The half beam was divided into macroelements in Atena. There are a total of 9 macroelements for each beam. The macroelement properties consist of 3D elastic isotropic and user defined properties of the as-built concrete of C2. The macroelements consisted of dividing the web from the flanges with the web macroelement extending the full height, from 0-42 inches. Each flange was its own macroelement extending the full 105 inches (half length of the beam), #3, #4, #5 and #6 in Figure 4-2. The anchorage zone, where the web flares out to the width of the bottom flanges was divided into two macroelements, #7 and #9 in Figure 4-2. The web was divided into three different areas, one for the anchorage zone area (full 42 inch height #8) and two areas towards the center of the beam (#1 and #2). The web was divided into two areas to have a finer FE mesh size for macroelement #1 having a mesh of 1.36 inches and being refined around the ducts to 0.136 inches to have two layers of mesh between the ducts. Whereas macroelement #2 has a larger mesh size of 3.2 inches.



a) Center cross section. b) End cross section. c) Longitudinal area assignments.

Figure 4-2: Atena model macroelement assignments.

The full list of Atena mesh details for each macroelement is shown in Table 4-3 with the refinements for each macroelement listed and the associated material properties. The refinements were accounted for with surface mesh refinements offered by Atena. The larger mesh was used in areas of least interest with an improved mesh for the areas of interest. In addition to having a larger mesh in certain macroelements, keeping the material elastic (3D Elastic Isotropic) was also used to shorten the run time of the models. Both material properties, As-Built and 3D Elastic Isotropic, are based on C2 properties with As-Built being non-linear and 3D Elastic Isotropic being linear elastic. The As-Built Concrete material properties in Table 4-3 were based on C2 concrete cylinder tests for the

compressive strength (5,957 psi), tensile strength (449.5 psi) and elastic modulus (4,399,153 psi) shown in Table 2-11. The 3D Elastic Isotropic material available in Atena was set to have the same elastic modulus as the C2.

Table 4-3: Macroelement Atena mesh detail, refinements and material properties.

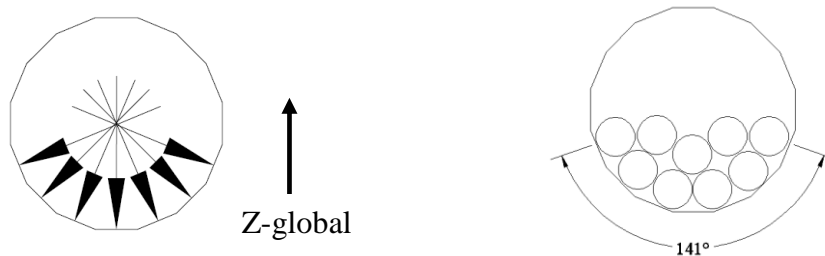
Macroelement	Mesh Size, in.	Refinements & Locations	Material Property
1	1.36	0.136" around ducts	As-built Concrete
2	3.2	1.36" on surface meeting #1	As-built Concrete
3	4		3D Elastic Isotropic
4	4		3D Elastic Isotropic
5	3.2		3D Elastic Isotropic
6	3.2		3D Elastic Isotropic
7	8		3D Elastic Isotropic
8	6	1.5" around ducts, 1.2" on surface meeting #1 and #2	3D Elastic Isotropic
9	8		3D Elastic Isotropic

Another simplification of the analytical models was making the ducts straight instead of curved as seen in the experimental beams. The straight ducts were placed so they would be at the same location as the ducts in the center of the beam as seen in Figure 4-2. With the straight ducts, it drastically decreased the modeling and run time of the parametric studies. In Atena curved lines are not available. To model a curved line, it was necessary to use a series of small segments of straight lines to produce a line similar to a curve. With the small line segments and three ducts per beam with sixteen sides per duct, modeling the duct as being curved was possible but difficult and the run times were lengthy. In addition, with each curvature, the duct profile changes. Even though the ducts were modeled as being straight throughout the beam, the point loads on the end of the beams and the magnitude of the distributed duct load were modeled as if the ducts were curved. Models detailed after the experiments utilized the straight ducts and provided results that were similar to the experiment. This will be described in detail in Section 4.3.

The loading and supports on the analytical beam are comparable to the experimental beam with a support in the center of the beam, the dead load applied at the ends of the beams, and the loads from the post-tensioning cable within the duct. The ducts were modeled as a simple void within the beam with the steel duct not included as it is thin steel. To properly model the duct as a circular shape, the duct was produced with sixteen sides as opposed to a perfect circle. As the duct is a sixteen sided polygon, the duct was able to be loaded with the post-tensioning tendons and the applied air pressure using distributed loads, shown in Figure 4-3.

With a total of nine strands within each post-tensioning duct, the distribution of strands and therefore the associated tendon force on the ducts is complex. The strands are in a random order throughout the duct with each duct having the possibility of being different. With the wide array of strand layouts available inside the ducts, the applied forces to the ducts can vary. To simplify the equivalent curvature loads applied to the ducts, the same force was used on all associated faces of the duct for the post-tensioning. The faces being loaded for the post-tensioning consists of the bottom seven faces of the

sixteen sided duct as seen in Figure 4-3. The seven sides were established based on the symmetric layout of the tendons inside of the duct as noticed in Figure 4-3, although symmetry is highly unlikely (VSL International LTD., 1991). With the seven sides of the duct being loaded, that is equivalent to 157 degrees of the duct having load. If 9 strands are placed in the duct graphically, an equivalent 141 degrees of the duct face is being loaded as shown in Figure 4-3b. Given the approximation of the strand locations, this analytical approximation was sufficient. All seven faces have the same area and the same magnitude of force in the global Z-axis of the beam. The magnitude of force varied in the local axis Z-direction to bring the beam in equilibrium and maintain the same global Z-axis forces. The local Z-axis is represented by the arrows in Figure 4-3a.



a) Distributed load on faces due to PT. b) Duct cross-section with 9 strands.

Figure 4-3: Duct loading configuration.

For the air pressure testing of the ducts, all sixteen sides of the duct were loaded with the appropriate air pressure value and all loads are in the local Z-axis of each duct face. As mentioned previously, the equivalent tendon point loads at the end of the beams are in the same location as if the duct was curved. The tendon point loads at the beam ends are from the post-tensioning anchorages assumed to be at the location as if the tendons were curved, as seen in Figure 4-1. Therefore, there is both a horizontal and vertical force for each anchorage.

The loading on the ducts and the point loads on the ends of the beam are provided in Table 4-4. The loading on the duct faces (w) are prescribed as an area load in units of ksi as per Atena. The point load “ P_x ” is in the longitudinal direction and “ P_y ” in the vertical direction with the locations of the point loads noted as “ y ” measured from the base.

Table 4-4: Atena loads and locations.

		C1	C2	C2,C3 avg.	C3	C3+
w, ksi	Top	0.0515	0.1434	0.1859	0.2283	0.2725
	Mid	0.2631	0.4023	0.4365	0.4706	0.5224
P_x, kip	Top	355.5	353.2	350.7	348.2	346.3
	Mid	345.6	334.8	329.0	323.2	317.7
P_y, kip	Top	16.9	44.0	59.0	74.0	88.3
	Mid	85.1	120.8	134.9	149.0	165.0
y, in.	Top	32.5	28.5	26.25	24	21.875
	Mid	18.5	13	10.75	8.5	6

As with the experimental test setup, a dead load was applied near the end of the beam of 22.5 kips. This load models the dead load that comes from the rest of the beam that is not modeled or constructed in the case of the experiments. In the case of the analytical model, the dead load was applied as an area load on the cross sectional area, shown in Figure 4-4. This method of the dead load is more accurate of an actual bridge as the bridge beam is cut at the inflection points and would continue on from the ends of the beam and therefore, the dead load would be applied to the cross sectional area and not just a line load. Figure 4-4 shows the dead load on the end of the beam as an area load as opposed to the point load on top of the beam, shown in red. The weight of the beam was included in the model.

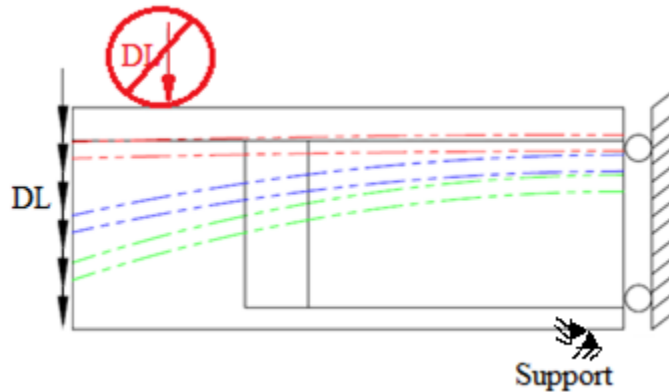


Figure 4-4: Analytical model dead loading.

The reinforcement modeled within the beam is the same as what was used in the experimental beams with exception of the anchorage spirals. The longitudinal reinforcement, transverse reinforcement and shear reinforcement, Section 2.2.1, were all included in the Atena models at the specified locations of the experimental beams. The reinforcement was modeled as a perfect bonded condition. The supports and boundary conditions are user defined and specified. The anchorage spirals were not included because the concrete in that area was take as elastic.

The loading protocol was similar for all beams with the dead load being applied, followed by the post-tensioning of each tendon and then the air pressure to each duct. The full loading protocol is outlined as follows for all analytical models:

1. Apply support and boundary conditions (applied over 1 step)
2. Dead load applied on ends of beam (applied over 5 steps)
3. Post-tensioning middle duct to 0.80fpu (applied over 25 steps)
4. Post-tensioning top duct to 0.80fpu (applied over 25 steps)
5. Air pressurizing middle duct to 100 psi (applied over 20 steps)
6. Take air pressure off middle duct (applied over 1 step)
7. Air pressurizing top duct to 100 psi (applied over 20 steps)
8. Take air pressure off top duct (applied over 1 step)

Total: 98 steps

Various monitors were used to track the progression of the different values throughout the beam. Monitors being used included capturing the stress, strain and crack width in the transverse direction of the beam above the top duct, between the top and middle ducts, between the middle and bottom ducts, and below the bottom duct. In

addition, the maximum web bulge was recorded for both sides of the web. With the beams that had duct tie reinforcement bars, the stress along the length of the bar (transverse direction of the beam) was recorded for most of the included bars except for the 3.5 inch duct tie spacing, where every second bar was monitored.

4.3 Model Verification

Verification of the models against the experimental results and the performance of the actual bridges is important to ensure the models were accurate. The Atena models were verified with the dead load being modeled as a line load across the transverse direction of the beam, as in the experimental beams, and once verified, the dead load was updated to the area load as described in Figure 4-4. The area load provided similar results as the line load for the dead load application. Comparison to the experimental beams show the Atena models received comparable damage to the experimental beams with cracks between the ducts and cracking along the web surface. Stresses around the ducts and along the web face are difficult to match between experimental and Atena models. Table 4-5 shows the concrete strain results comparing the Atena models to the experimental results for COM (between middle and bottom ducts) after 0.75fpu post-tensioning and before air pressure. The experimental strains are higher for C1 and C2 than Atena and can be attributed to Atena reading the strain only in the horizontal (transverse) direction whereas the experimental strain gauges have the possibility of capturing strain from the vertical direction.

Table 4-5: COM between Atena and experimental results (0.75fpu-top duct).

	C1	C2	C3
Atena, $\mu\epsilon$	95	140	230
Experiment, $\mu\epsilon$	529.6	1087.9	219.5
% Error	82.1	87.1	-4.8

Table 4-6 compares the COM stresses of the Atena models to the experimental results after 125 psi air pressure testing after 0.85fpu. C1 has the largest percent error at 56% whereas C2 and C3 provide similar results between the experimental and Atena results with each having less than 25% error.

Table 4-6: COM between Atena and experimental results (125psi AP - 0.85fpu).

	C1	C2	C3
Atena, $\mu\epsilon$	536	15300	22400
Experiment, $\mu\epsilon$	1229	14000	18000
% Error	56.4	-9.3	-24.4

The error is because the Atena models do not apply an air pressure to the crack once it is formed whereas in the experimental beams, once a crack formed, the air pressure leaked into the crack and applied a pressure in the horizontal direction of the crack. For similar loading scenarios, an artificial crack between the ducts needs to be modeled. The parametric study with artificial cracks between the ducts is discussed in Section 4.5. Table 4-7 shows the results for the extreme fiber stresses comparing the

Atena FE models to NDOT bridges. The stress values were provided by NDOT bridge engineers as typical for NDOT bridges such as to the Steamboat Hills Bridge and the Rancho Drive Bridge. Stress from NDOT bridges are calculated values upon completion of 0.75fpu post-tensioning without air pressure. According to NDOT, it is typical that the top stress is approximately three times larger than the bottom stress.

Table 4-7: Extreme fiber stress between NDOT estimates and Atena.

		NDOT 0.7 Scaled		0.7 Scaled UNR Model		
		Rancho	S.S.	C1	C2	C3
Stress over pier	Top, psi	-819	-1299	-1205	-1120	-1074
	Bottom, psi	-615	-437	-402	-378	-358

The experimental duct tie reinforcement bars are compared to the Atena models that have the artificial cracks included (Section 4.5) at 100 psi Top after 0.75fpu, shown in Table 4-8. The duct ties at 8.75 inches from centerline for C5 are approximately three times larger for the experimental beam compared to Atena whereas at 26.25 inches from centerline, the experimental beam is three times smaller compared to Atena. C6 stresses are closer between experimental and analytical results. At 12.25 inches from centerline for C6, the experimental duct ties have a stress of 10 ksi compared to Atena with a stress of 16.5 ksi. The duct tie stresses at 26.25 inches from centerline are 20 ksi for experimental and 18 ksi for Atena. The locations of the shear reinforcement and duct ties for the Atena models were shifted 1.75 inches to properly mirror the reinforcement about the cut face (longitudinal centerline) as only half of the beam was modeled. The shift of reinforcement is further discussed in Section 4.5. While the comparison of values between the analytical model and the experimental model are not exact, the values are of a similar order of magnitude.

Table 4-8: Experimental vs. Atena duct tie results (100psi Top - 0.75fpu).

Bar	Experimental, ksi	Bar	Atena, ksi
C5-8.75L-MB	81	C5-8.75-MB	27.5
C5-26.25R-MB	8	C5-26.25-MB	23
C6-12.25R-MB	10	C6-10.5-MB	16.5
C6-26.25R-MB	20	C6-24.5-MB	18

In the experimental beams, the length of the cracks are unknown between the ducts and is possible the cracks did not extend the full length of the beam whereas in Atena, the artificial cracks were modeled as the full length of the beams. The experimental beams have the possibility of no cracking at the location of the monitored duct ties, so the difference in duct tie stresses can be associated to this. The artificial crack models are deemed adequate in properly modeling the air pressure application to the cracks between the ducts.

4.4 Duct Curvatures and Duct Tie Reinforcement Models

As the experimental program was limited to six beams, there was a need to have a greater understanding of the effects of curvature and duct tie reinforcement. A number of

Atena models were designed according to Table 4-9 to determine the effects that curvature and duct ties have on the performance; this is a subset of what is shown in Table 4-1.

Table 4-9: Duct curvatures and duct tie reinforcement Atena model outline.

# of Ducts	Equivalent Curvature Loads, kip/ft	Reinforcement Spacing, in.	Duct Location on Web	Loading
3	11.75 (C1)	N, 17.5, 10.5, 3.5	Top	0.80fpu + 100psi
	19.12 (C2)	N, 17.5, 10.5, 3.5	Top	0.80fpu + 100psi
	22.6	N, 17.5, 10.5, 3.5	Top	0.80fpu + 100psi
	26.1 (C3)	N, 17.5, 10.5, 3.5	Top	0.80fpu + 100psi
	29.7	N, 17.5, 10.5, 3.5	Top	0.80fpu + 100psi

Additional equivalent loads/tendon curvatures were chosen between C2 and C3 as seen in Table 4-9 at 22.6 kip/ft. and 29.7 kip/ft. to expand the amount of data at higher loads. The locations of the ducts and the spacing between the ducts were kept the same for each model: ducts at the top of the web as in the experiments and the spacing between the ducts of 1.05 inches (1.50 inches for NDOT full scale bridges). Each curvature had four different duct tie reinforcement spacings. The duct tie reinforcement spacing was chosen to be at 17.5 inch, 10.5 inch and 3.5 inch (NDOT full scale: 25 inch, 15 inch, 5 inch) and each curvature also had the case with no duct ties included. The spacing between the duct tie bars was chosen to correspond with the shear reinforcement.

Figure 4-5 provides the cross section principal stresses at centerline at the end of 100 psi after 0.80fpu for C2 with no duct tie reinforcement. The dark black lines represent concrete cracks present from the loading.

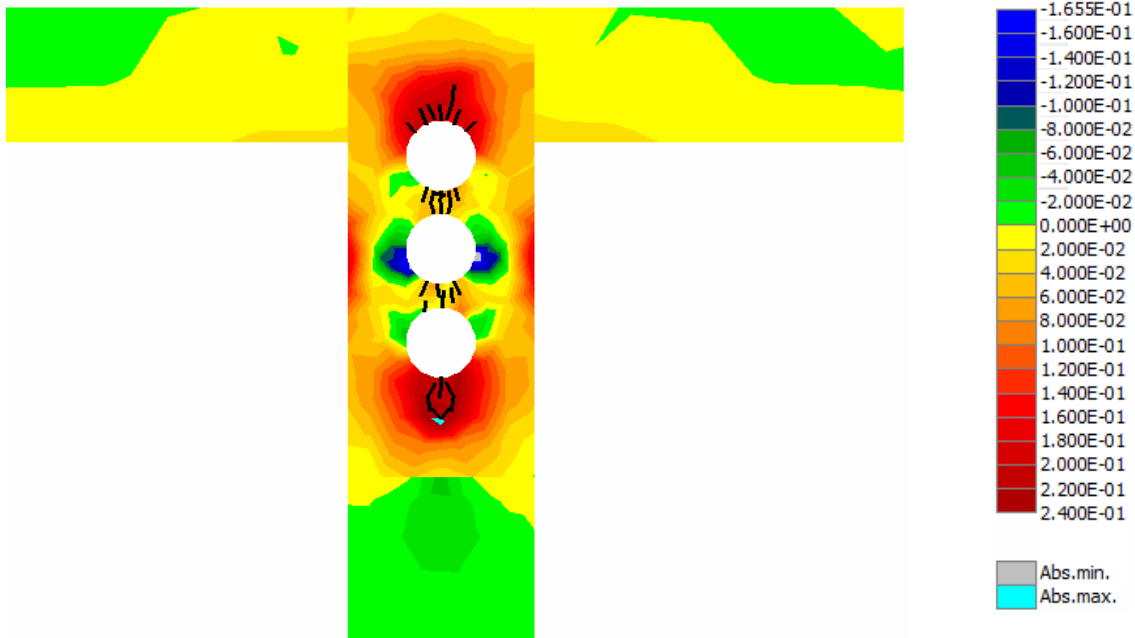


Figure 4-5: Principal stresses at centerline for C2 with no reinforcement.

Figure 4-6 shows the principal stresses in the cross section at centerline of the beam at the end of 100 psi air pressure after 0.80fpu for C2 with duct tie reinforcement bars at 10.5 inches. Comparing Figure 4-5 to Figure 4-6, the maximum and minimum stresses did not vary greatly but the stress flow changed. With no duct tie reinforcement bars included, a tensile stress is present on the surface of the web near the middle duct however once duct ties are included, the web surface stress near the middle duct is compressive. Concrete principal stresses between the ducts increase from approximately 0.03 ksi to 0.19 ksi once duct ties are included.

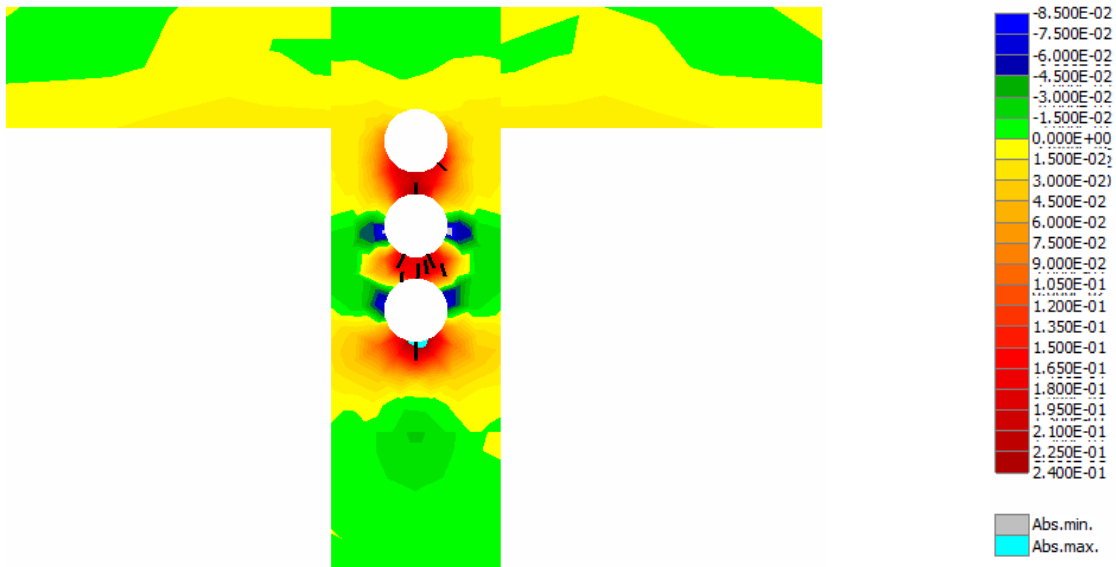


Figure 4-6: Principal stresses at centerline for C2 with reinforcement at 10.5".

Based on the various monitors placed within the beams, the stress in the duct ties, the web bulge and crack width between ducts were recorded. With the same areas being monitored, the results of each beam are able to be compared. The results for the stress in the duct ties are for the duct ties closest to the center of the beam and between the middle and bottom ducts as they had the highest stresses in the model. Similarly for the crack width, the area between the middle and bottom ducts provided the largest crack width. The web bulge is the total bulge taken from both sides of the web. The results for the stress in the duct tie reinforcement bars are shown in Figure 4-7 and Figure 4-8. The equivalent curvature load against bar stress is shown in Figure 4-7, and Figure 4-8 shows the tie spacing versus stress in the bars. Figures showing the crack width and web bulge are provided in Appendix C, Figures C-1 to C-20. It is important to note that tendons were loaded to 0.8fpu, both top and bottom by loading step 56. The air pressure was then applied as shown in Table C-1.

Figure 4-7 shows that with an increase in the equivalent curvature loads, there is an increase in the stresses associated in the duct tie reinforcement bars. The post-tensioned ducts have air pressure applied and no artificial cracks between the ducts are present. Additionally, as the spacing between the duct ties increase, the stresses in the duct ties increase.

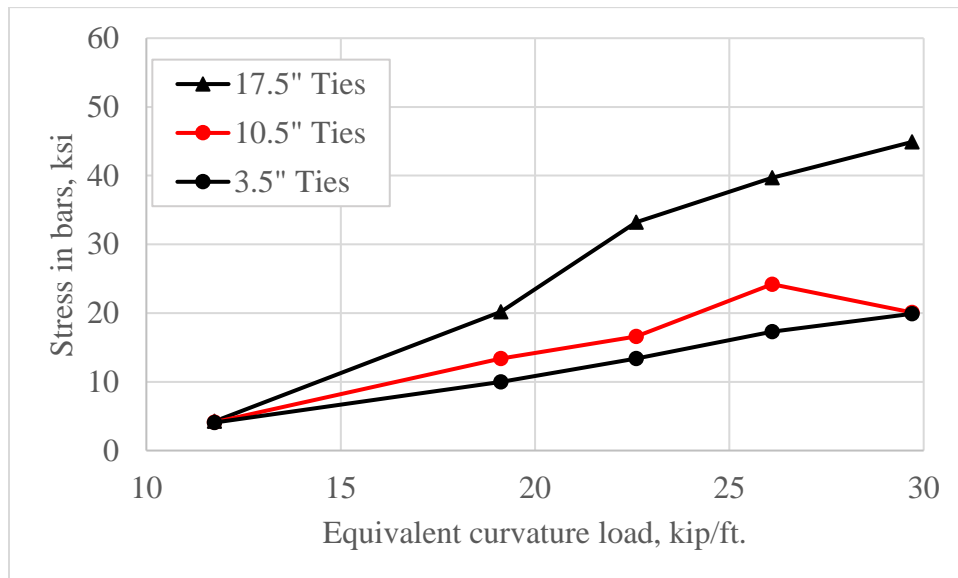


Figure 4-7: Duct tie stress vs. curvature (No artificial crack).

Figure 4-8 provides the impact of difference in curvatures for various duct tie spacings. The general trend is that with the increase in duct tie spacing, there is an increase in stress in the duct tie reinforcement bars. The stresses in the bars increase with the increase of post-tension curvature.

The results from the maximum web bulge are shown in both Figure 4-9 and Figure 4-10. The web bulge is the total bulge from both faces of the web. The web bulge against various curvatures is shown in Figure 4-9, and Figure 4-10 shows the web bulge versus duct tie spacing.

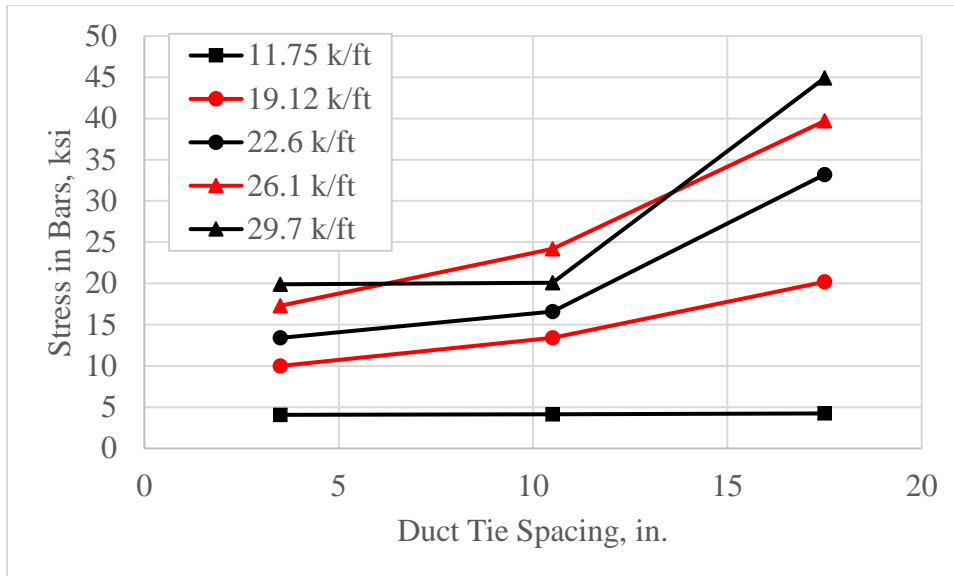


Figure 4-8: Duct tie stress vs. duct tie spacing (No artificial crack).

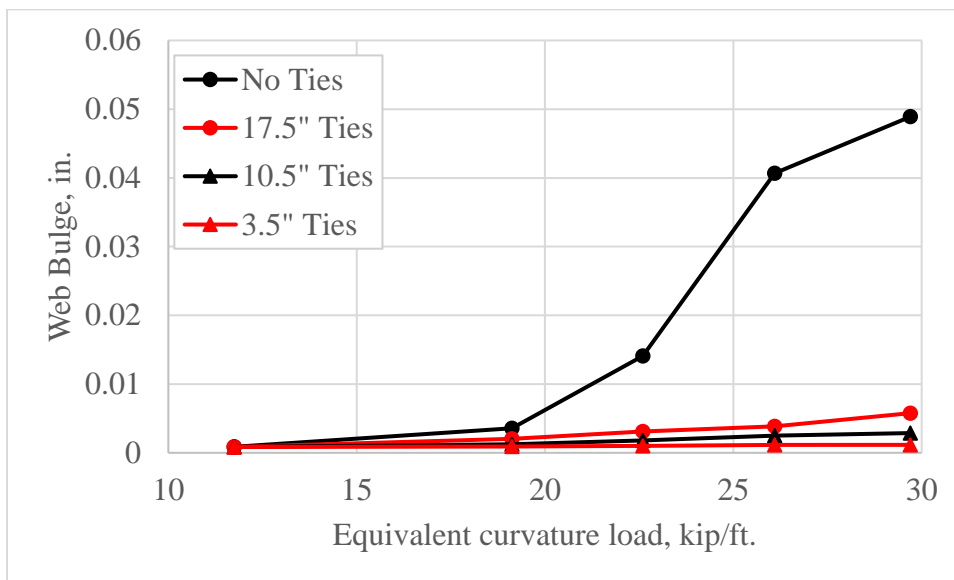


Figure 4-9: Total web bulge vs. curvatures (No artificial crack).

Figure 4-9 shows that with the simple inclusion of duct ties at any spacing, the web bulging drastically decreases. Between the various duct tie spacings, the overall web bulge is not affected. With no duct ties included, the web bulge significantly increases around 19 kip/ft. With the presence of duct ties, there is no clear point with an unfavorable increase in web bulge. At lower curvatures, the duct ties have the least effect on the web bulge. It is important to remember that figures are for the 0.7 scale specimens.

Figure 4-10 shows that an increase in duct tie spacing increases the web bulging. Additionally, as noted in the previous figure, the higher the curvature, the greater the web bulge. At smaller duct tie spacings, the curvature doesn't have as large of an effect on the web bulge as for all curvatures the web bulge is around 0.001 inch.

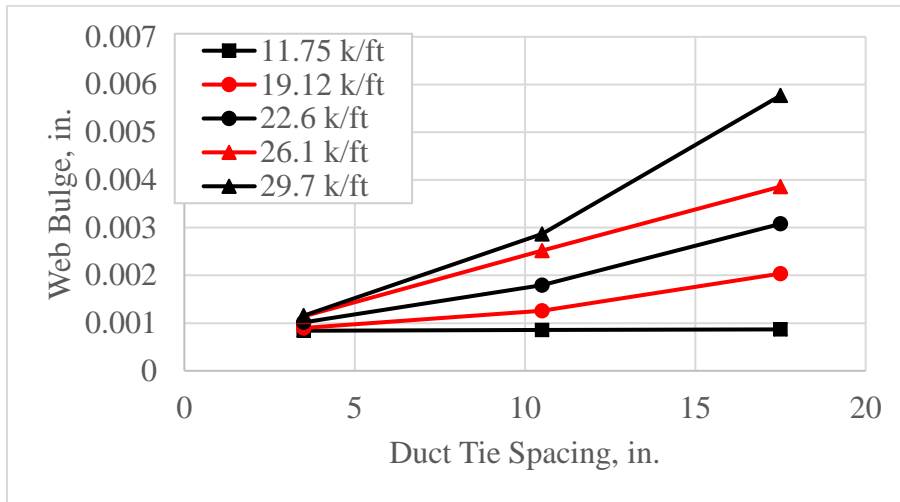


Figure 4-10: Total web bulge vs. duct tie spacings (No artificial crack).

Recording the crack width in between the middle and bottom ducts provides the opportunity to understand how the curvature and duct tie reinforcement affect the cracking. Figure 4-11 shows the results of the crack width size versus the equivalent curvature loads at various duct tie spacing. The figure shows that with no duct ties included, the crack width is significantly larger than models with the included reinforcement. The overall crack width does not change much between changing the spacing between the duct tie reinforcement bars. As noticed with the web bulge, with the simple addition of duct tie reinforcement bars, the crack width decreases drastically to around 10% compared to no ties.

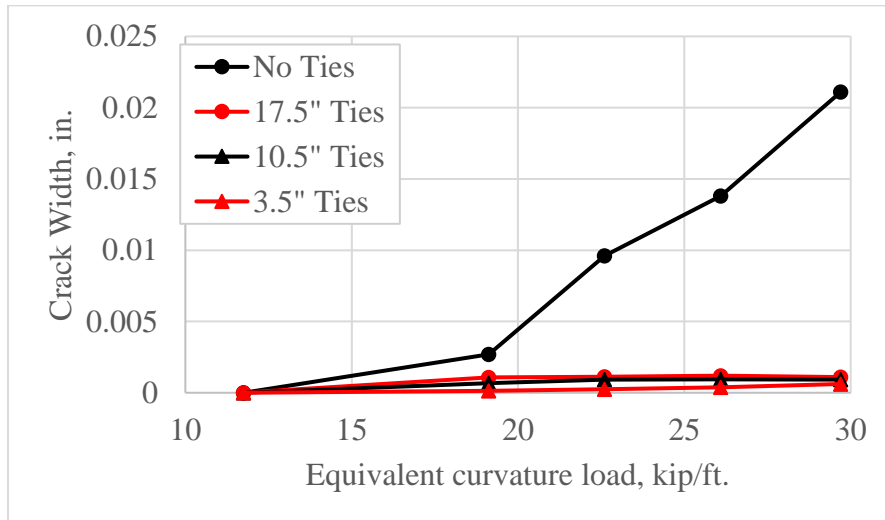


Figure 4-11: Crack width (MB) vs. curvatures (No artificial crack).

The crack widths against different duct tie spacings with equivalent curvature loads are shown in Figure 4-12. It can be noticed that at the lowest curvature that there are no cracks for any of the tie spacing. With an increase in curvature and duct tie spacing, the crack width inherently increases. At the large tie spacing, the crack width for

the four largest curvatures have little difference between them. The model with no duct ties is not included in Figure 4-12. Comparing the bar stress against the crack width is shown in Figure 4-13 for the several curvatures. In general the stress in the bars increased with an increase in crack width. The stress and crack width both are larger with each increase in equivalent curvature load as previously mentioned.

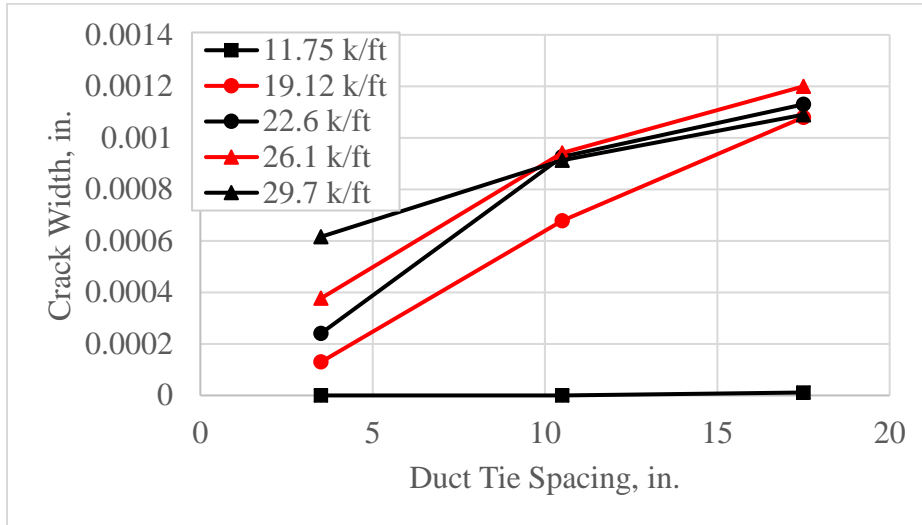


Figure 4-12: Crack width (MB) vs. duct tie spacing (No artificial crack).

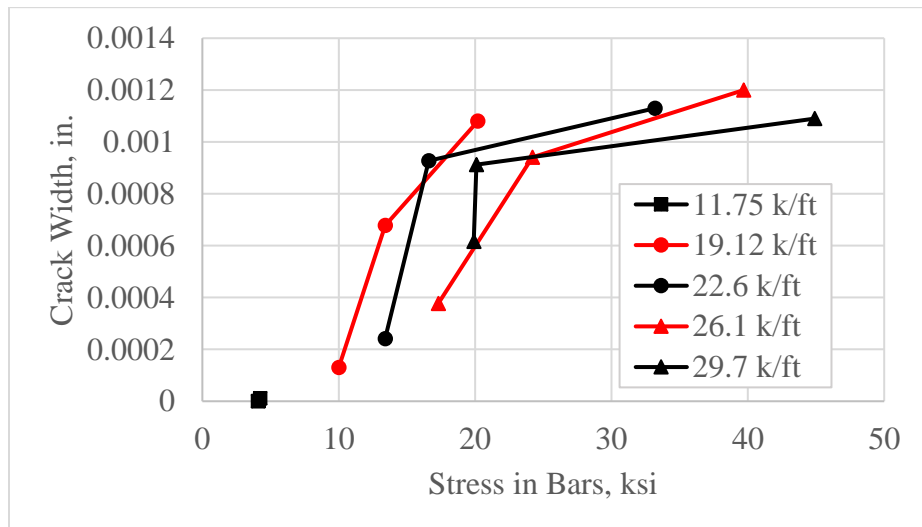


Figure 4-13: Crack width vs. duct tie stress (No artificial crack).

The maximum web bulge along each web face at each loading step for C2 with no duct tie reinforcement included is shown in Figure 4-14.

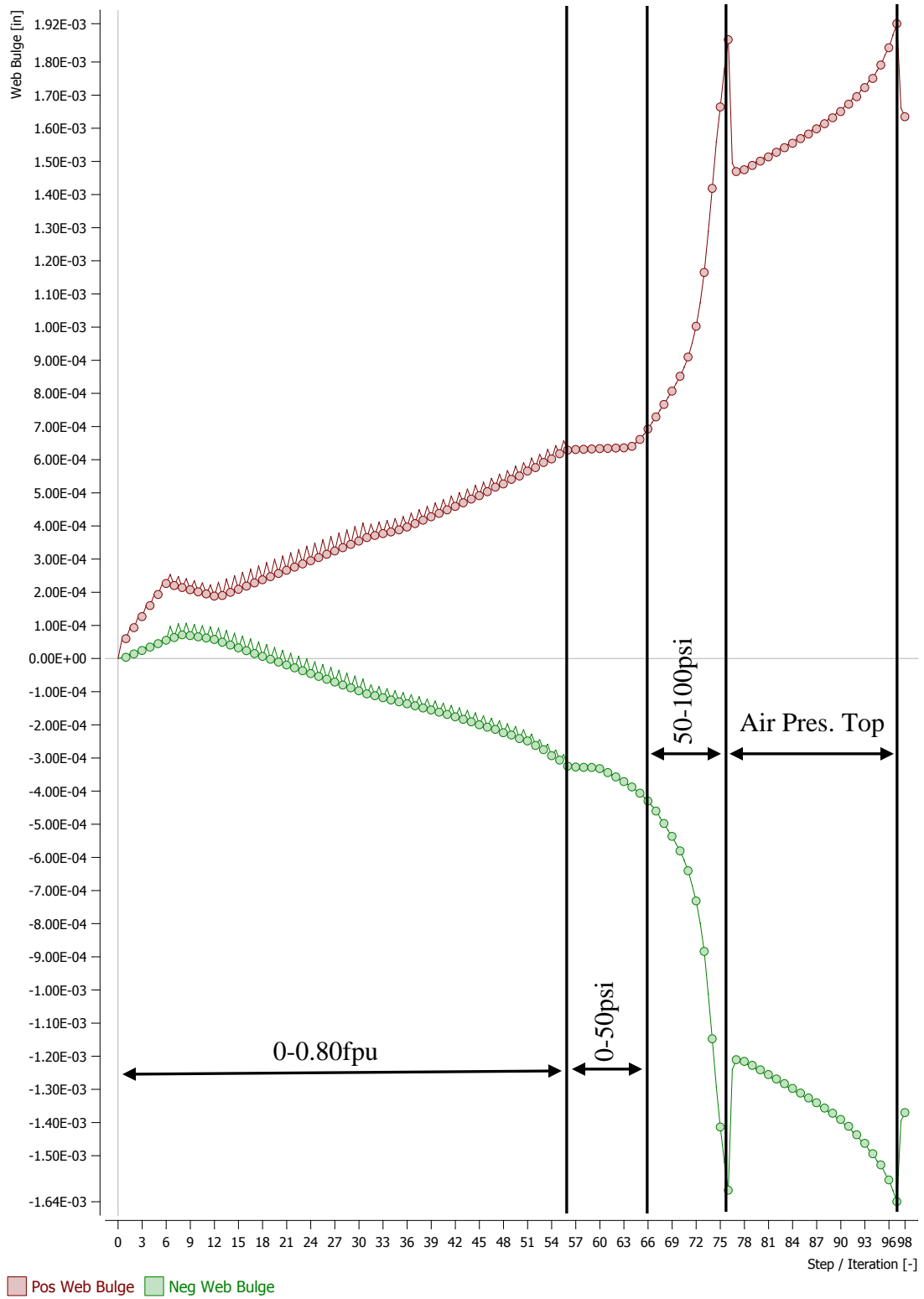


Figure 4-14: Web bulging at each loading step for C2 with no reinforcement.

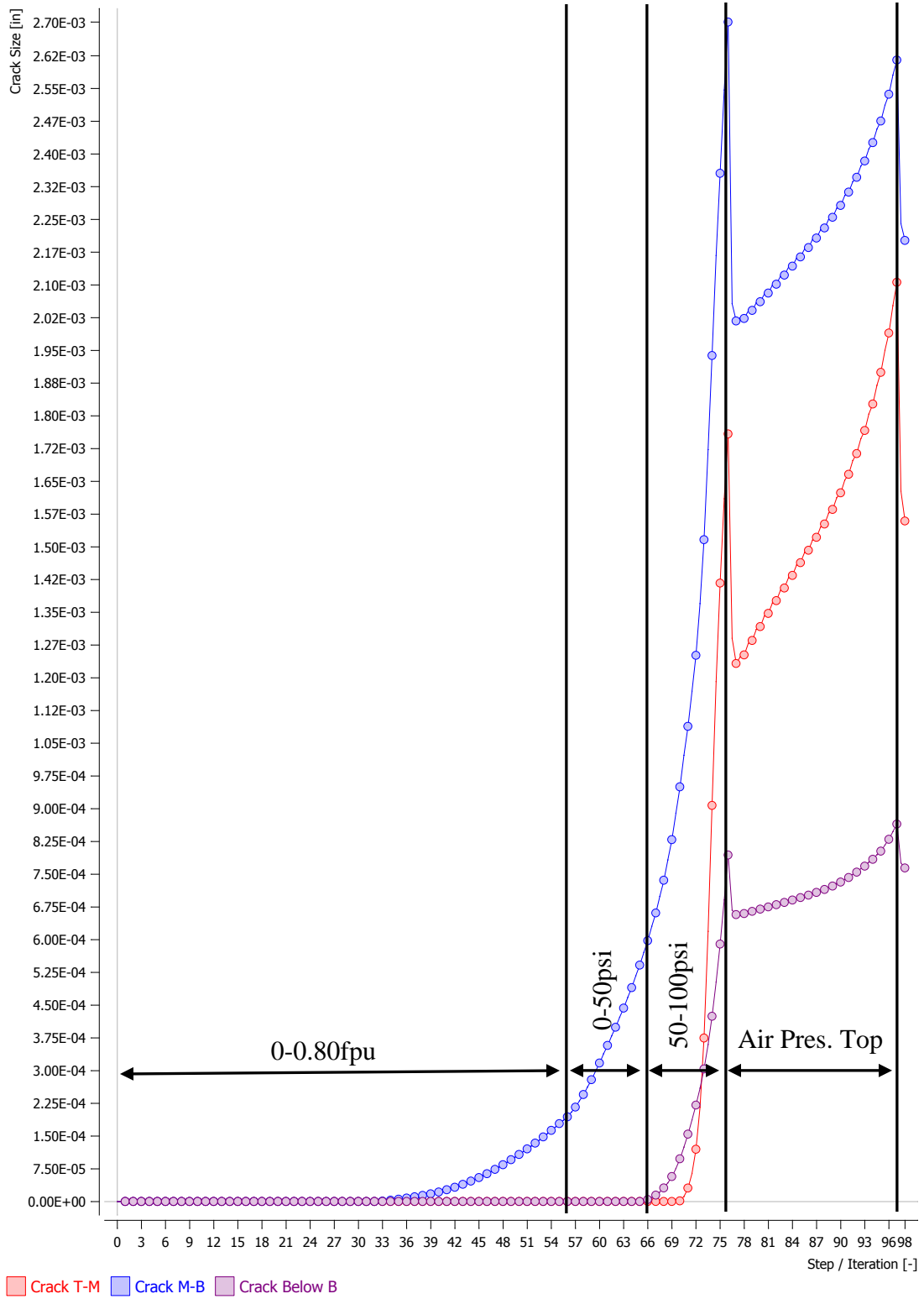


Figure 4-15: Crack size at each loading step for C2 with no reinforcement.

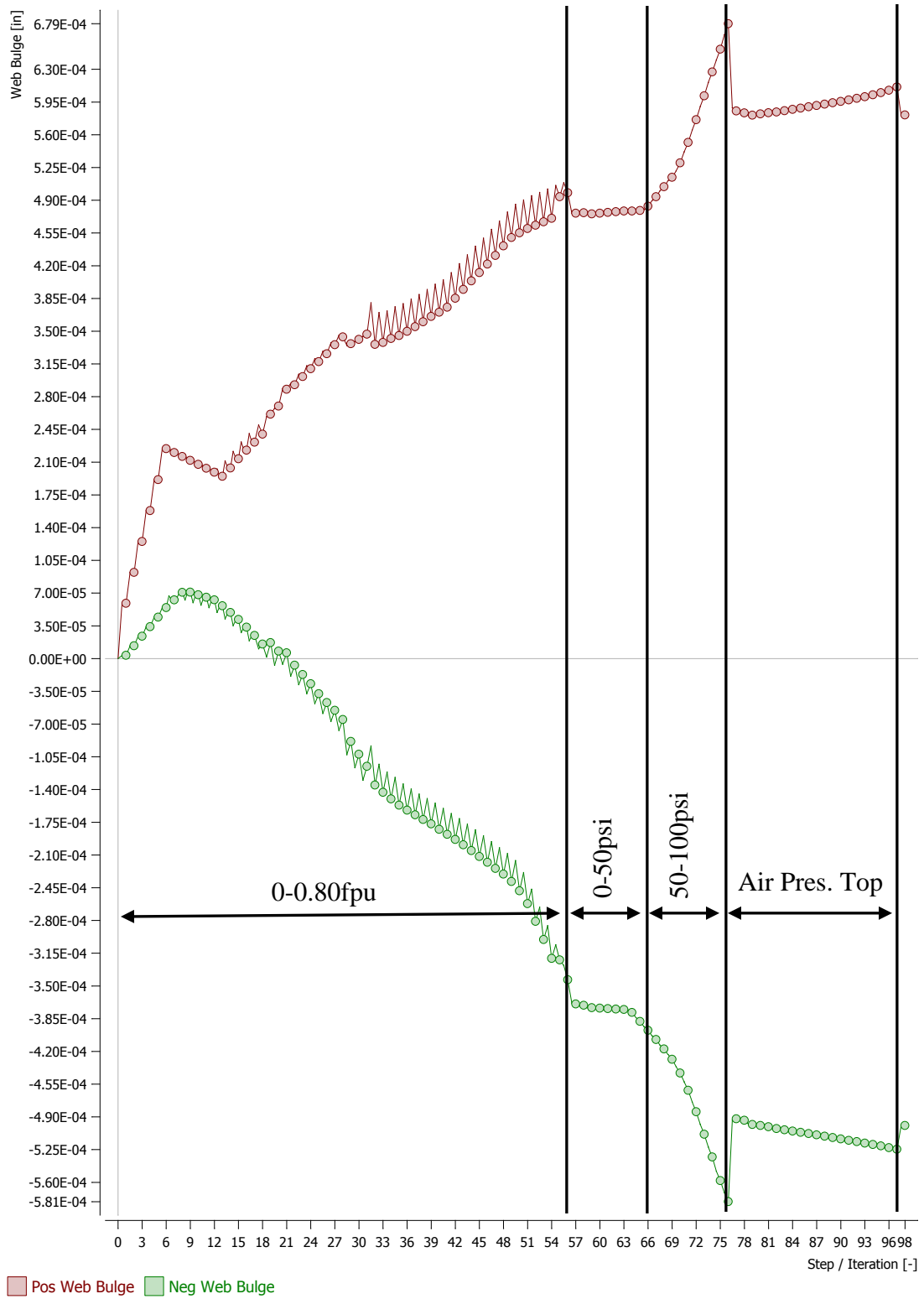


Figure 4-16: Web bulging at each loading step (C2 – duct tie 10.5" spacing).

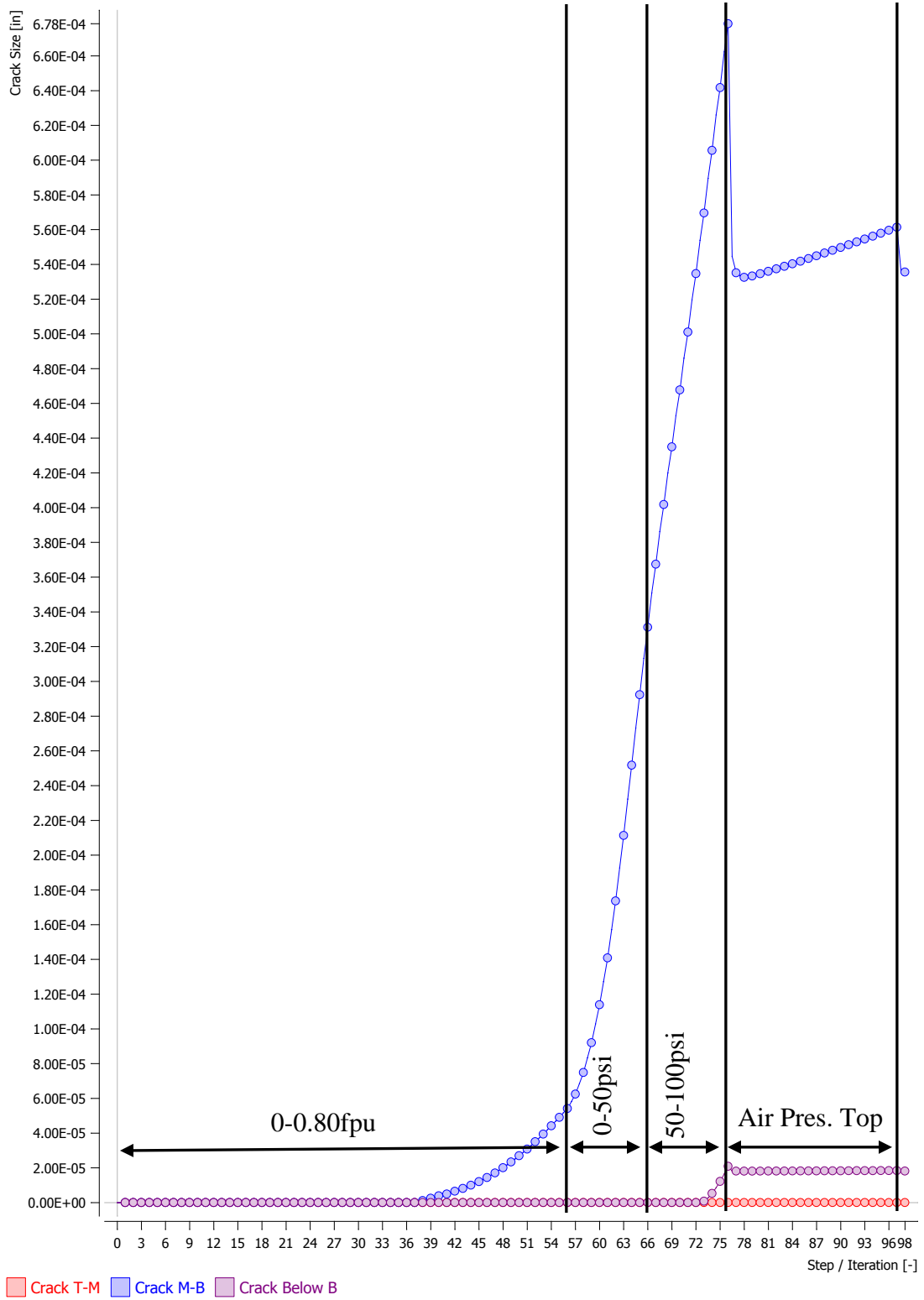


Figure 4-17: Crack size at each loading step (C2 – duct tie 10.5" spacing).

Figure 4-15 provides the crack size at each loading step at the centerline of the beam. For both Figure 4-14 and Figure 4-15, show a significant increase in web bulging and crack size between 50 psi and 100 psi compared to post-tensioning and 0 psi to 50 psi air pressuring. Figure 4-16 shows the maximum web bulging on each face for each loading step. The crack size at centerline of the beam between the ducts is shown in Figure 4-17. With the addition of reinforcement (Figure 4-17), the air pressure testing had less of an effect on the web bulging and crack sizes between ducts. The damage between 0 psi to 50 psi was noticeably less compared to the damage between 50 psi and 100 psi air pressure testing.

4.5 Artificial Crack Models

4.5.1 Scaled Version (0.7 scale)

Models described to this point included air pressure but only in the ducts. In the specimens and in an actual bridge, air pressure in the ducts would spread into a crack that is formed by the ducts. With a corrugated metal duct, air can escape through the duct and into cracks. If the ducts were plastic, this would not be the case, as long as the duct did not crack. The increase in damage was seen in the experiments with no surface web cracking occurring until after the air pressure was applied.

To accurately model the movement of the air pressure into the cracks, an artificial crack was introduced between the ducts with pressure applied along the surface of the crack. The artificial crack models assumed a worst case scenario with a crack already formed between the ducts from the beginning of loading. It is unknown when the crack starts to form during post-tensioning and air pressure testing, so a conservative approach of saying the crack is present before prestressing and air pressure testing was assumed. The artificial crack between the ducts allowed for an air pressure force to be applied in the transverse direction of the beam whereas if the artificial crack was not included, there would be no air pressure force on the crack between the ducts as the air pressure is modeled via an area pressure.



a) Air pressure from middle duct.

b) Air pressure from top duct.

Figure 4-18: Artificial cracks with applied air pressures from ducts.

Figure 4-18 shows the artificial crack between the ducts and the air pressure force being applied; this substantially increases the transverse/splitting forces in the beam. With the increase in transverse forces, the associated stresses in the duct tie reinforcement

bars increases. The artificial crack models were mainly used to determine the stresses in the duct tie reinforcement bars throughout the testing process to help determine the proper spacing needed to keep the reinforcement stresses at a reasonable level. Figures are provided in Appendix C that show the bar stress for various equivalent curvature loads and duct tie spacing, see Figures C-21 to C-28. It is important to note that tendons were loaded to 0.8fpu, both top and bottom by loading step 56. The air pressure was then applied as shown in Table C-1. The figures are for cases where an artificial crack (AC) is utilized. The data is taken midway between the middle and bottom duct (MB).

The parametric study is similar to the models without the artificial crack included as seen in Table 4-2. One notable difference is the addition of two reinforcement spacings of 14.0 inches and 7.0 inches. To achieve the 14.0 and 7.0 inch spacing, the shear reinforcement and duct ties were shifted in the longitudinal direction of the beam by 1.75 inches to allow symmetry about the midspan of the beam while keeping the duct ties located at the shear reinforcement. With the shift of the shear reinforcement, this places a shear reinforcement bar right at midspan and duct ties at every other bar for the 7.0 inch spacing and every fourth bar for the 14.0 inch spacing based on the shear reinforcement spacing of 3.5 inches.

The models used the same loading sequence as stated in Section 4.1. During the air pressure testing stages, the air pressure was also applied to the associated artificial cracks between the ducts. For the air pressure applied to the top duct, the same air pressure was applied to the artificial crack between the top and middle ducts. When air pressure was applied to the middle duct, the crack between the middle and bottom ducts had the same air pressure applied. The applied loading on the ducts can be seen in Figure 4-18. Air pressure was not applied to the artificial crack above the middle duct during air pressure testing of the middle duct because in the experimental testing, concrete cracks were larger on the bottom side of the ducts, where the tendons are located, compared to the top of the ducts, where the crack was minimal, leading to the air pressure traveling to the bottom of the duct that is being pressurized as opposed to the top of the duct.

The results for the bar stress at various duct tie reinforcement spacings and curvatures are shown in Figure 4-19 and Figure 4-20. The bar stresses are recorded as the stress in the x-direction of the beam (transverse direction) or along the length of the duct tie reinforcement bars. Figure 4-19 shows that with an increase in spacing between duct ties, the bar stress increases as well. In addition, with an increase in the equivalent curvature loads there is an increase in bar stress. At the lowest curvature force (11.75 kip/ft.), the relationship is similar to a third degree polynomial whereas with each subsequent increase in curvature force, the relationship becomes more linear.

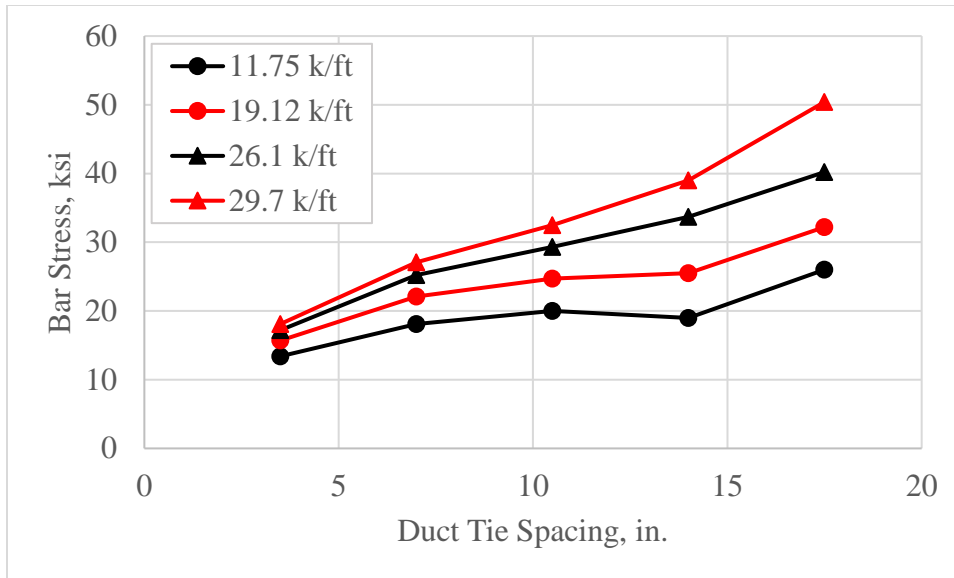


Figure 4-19: Bar stress vs. duct tie spacing (with artificial crack).

Figure 4-20 provides a similar result showing an increase in bar stress as the equivalent curvature load increases. The bar stress also increases with the increase in spacing between the duct ties. From the two figures, it can be observed that with the increase in duct tie reinforcement spacing and the increase in equivalent curvature load, there is an increase in the duct tie reinforcement bar stress.

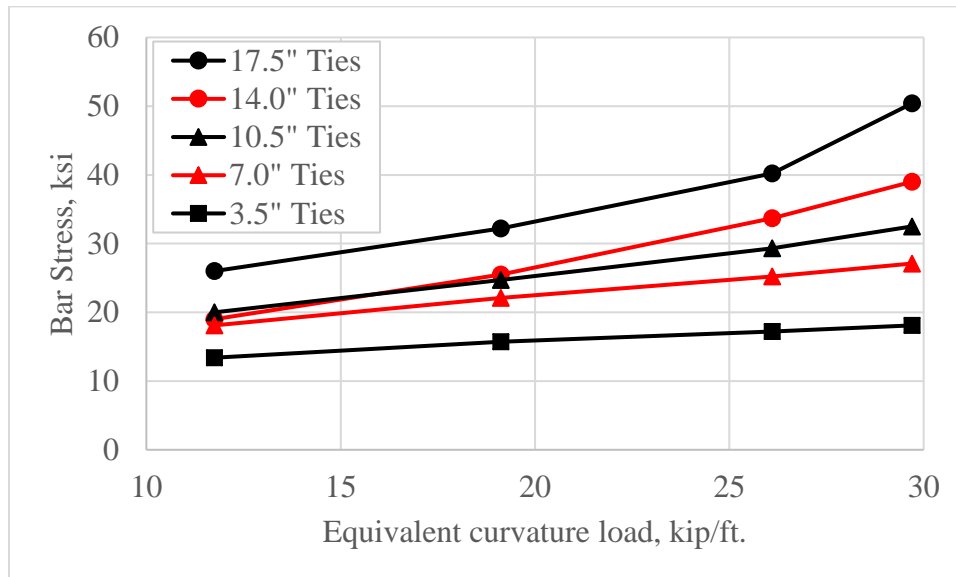


Figure 4-20: Bar stress vs. equivalent curvature loads (with artificial crack).

The comparison between models with no artificial crack and an artificial crack are shown in Figure 4-21. The stresses for the artificial crack models are higher compared to no crack included. The air pressure on the cracks between the ducts has an effect with increasing the bar stresses for all curvatures. Figure 4-22 shows the comparison between including an artificial crack between the ducts to no crack between the ducts for the bar

stress versus curvatures. The artificial crack proves to have an impact on the duct tie stresses with an increase in stresses compared to no artificial crack included.

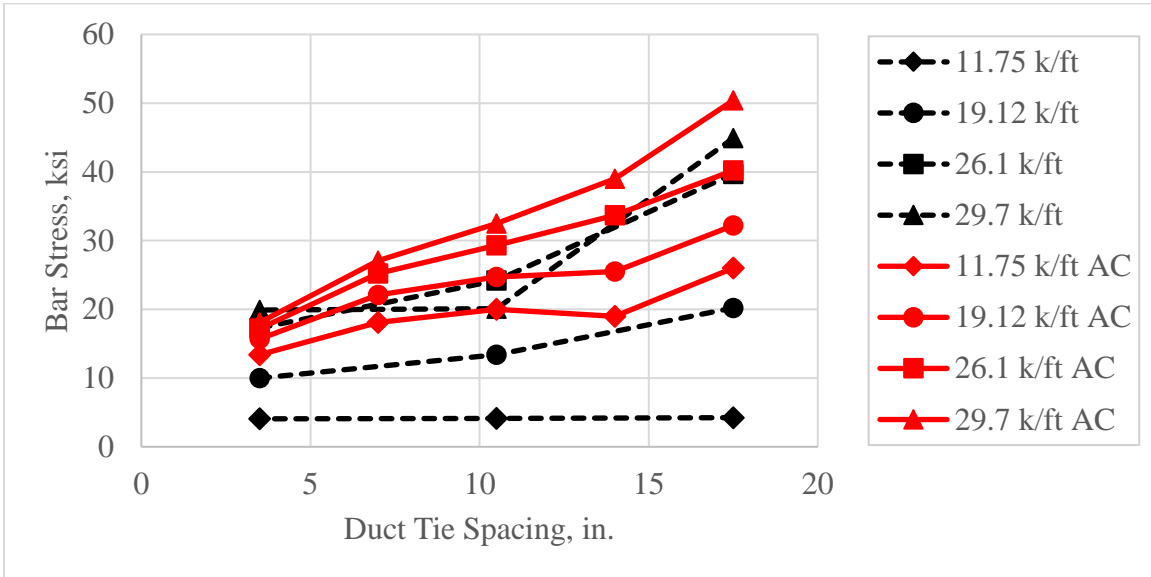


Figure 4-21: Bar stress vs. tie spacing for no AC and AC (Artificial Crack).

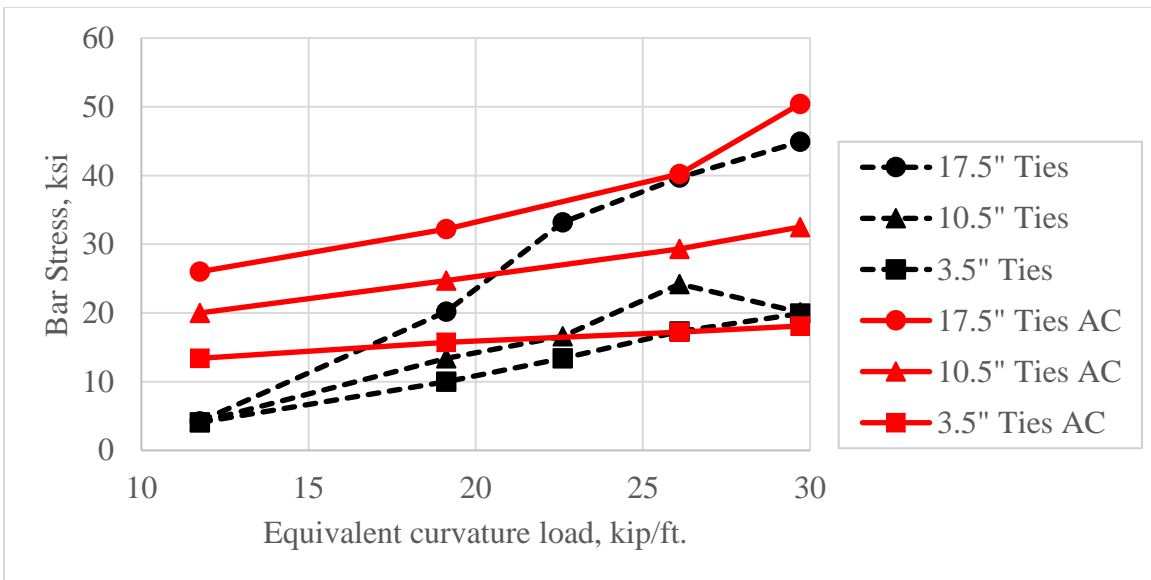


Figure 4-22: No AC and AC for bar stress vs. curvatures (Artificial Crack).

Calculating the stresses in the duct tie reinforcement bars allows the determination of a proper duct tie spacing in accordance to various equivalent curvature load. The allowable tensile stress for Grade 60 reinforcement bars per ACI 318-99 Appendix A is 24 ksi. The allowable stress limit of 24 ksi is comparable to the stress in the duct ties in C6, shown in Chapter 3 experimental results: Figure 3-70, Figure 3-71 and Figure 3-72. Beam C6 performed the best with minimal cracks forming after overstressing and over air pressurizing. Limiting the stress in the duct ties to 24 ksi provides the opportunity to determine the duct tie spacing that achieves 24 ksi stress in the bars. Using Figure 4-20, a

line was placed at 24 ksi to determine the spacing of the duct ties for each of the equivalent curvature load that would produce a duct tie stress of 24 ksi. For an equivalent curvature load that did not intersect the appropriate line on the graph, the lines were extended until an intersection was achieved. These values are shown in Figure 4-24 as a ratio of duct tie reinforcement for various equivalent curvature loads. The ρ values were determined as provided in Equation 4-1.

$$\rho = \frac{A_s}{A_c} \quad (4-1)$$

Where:

A_s = area of reinforcement, in.²

$$A_c = sh_d \quad (4-2)$$

A_c = area of concrete, in.²

s = spacing of duct tie reinforcement bars, in.

h_d = clear height between ducts = 1.05 inches

This allows a designer with an equivalent curvature load from the prestressing radii's to effectively choose a percentage of reinforcement needed for an area of concrete. The equivalent curvature load (w) is the total of all curvature forces from all post-tensioning radii's in the beam.

$$w = \sum_{i=1}^n \frac{2P_i a_i}{L_i^2} \quad (4-3)$$

With:

w = equivalent curvature load, kip/ft.

n = total number of ducts

P_i = post-tensioning force, kip

a_i = height of post-tensioning tendons, ft., shown in Figure 4-23.

L_i = half-length of post-tensioning tendons, ft., shown in Figure 4-23.

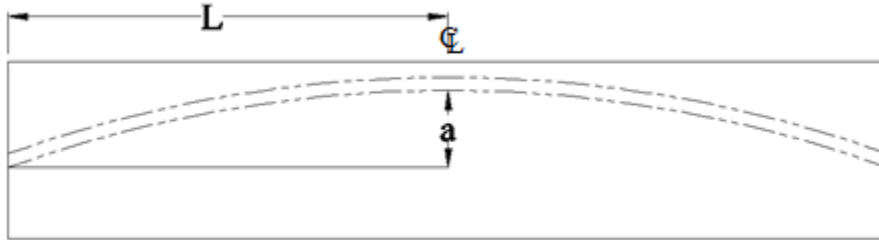


Figure 4-23: Post-tensioning equation descriptions.

A trendline was added to the **Error! Reference source not found.** to provide a simplification the relationship between duct tie reinforcement ratio and the equivalent curvature load. From the trendline, an equation can be formed to calculate the ρ from the equivalent curvature loads shown:

$$\rho = \frac{6w - 9}{10000} \quad (4-4)$$

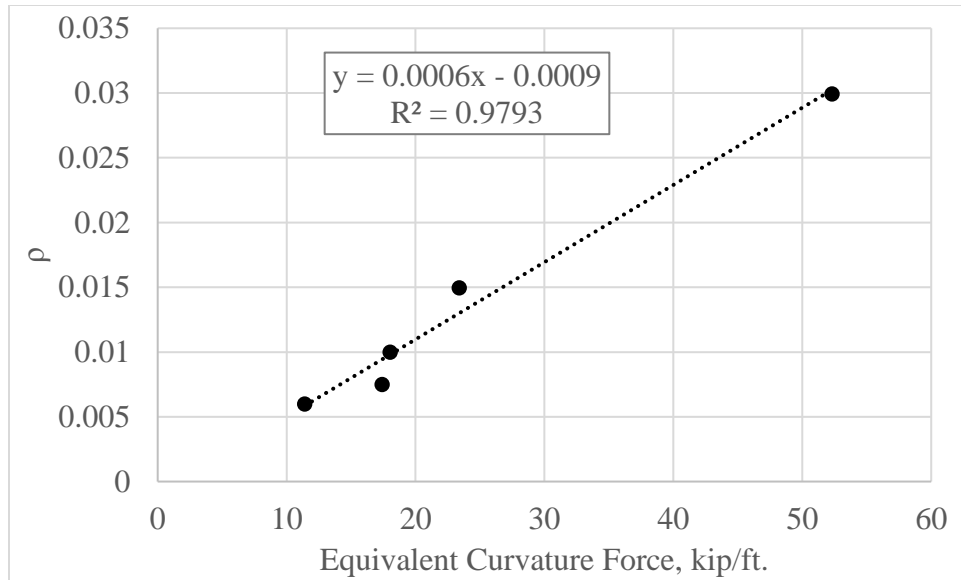


Figure 4-24: Reinforcement ratio vs. equivalent curvature force (0.7 scale).

The equation can be checked against the #3 duct tie reinforcement bar as that was the reinforcement bar used in the Atena models. In addition, if the #3 duct tie bar spacing is transformed into an equivalent #4 duct tie reinforcement spacing, the equation can be used for #4 duct ties as well. Rearranging equation (4-1) and knowing the ρ -value, the spacing of duct tie reinforcement bars can be calculated.

$$s = \frac{A_s}{\rho(1.05'')} \quad (4-5)$$

With:

s = duct tie reinforcement spacing, in.

A_s = area of one duct tie reinforcement, in.²

The comparison of the Atena model comparisons of the #3 and #4 bar against using the ρ -equation for the calculated spacing for various equivalent curvature loads are shown in Figure 4-25 for the scaled models.

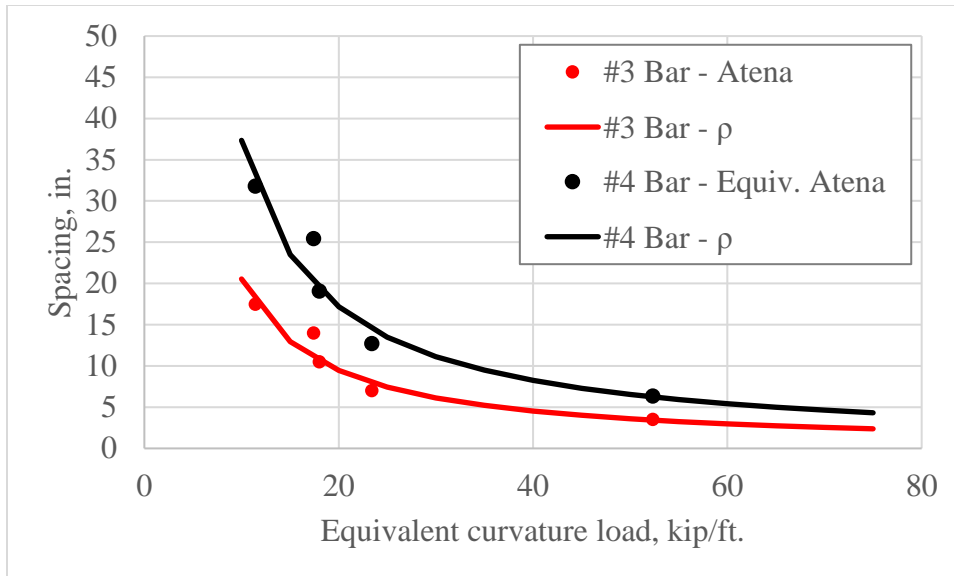


Figure 4-25: Atena spacing vs. equivalent curvature (0.7 scale).

The ρ -equation provides a good fit when compared against the Atena bar values for both the #3 and the #4 bar as seen in Figure 4-25. There is a small variance in the spacing values at lower curvature forces around 15-25 kip/ft. for both #3 and #4 bars. Combining equation (4-4) and equation (4-5) provides an equation to calculate a required spacing for various equivalent curvature loads and duct tie reinforcement bar sizes (using a scaled spacing between the ducts of 1.05 inches).

$$s = \frac{100,000A_s}{63w - 94.5} \quad (4-6)$$

With:

s = required duct tie reinforcement spacing, in.

A_s = area of one reinforcement bar, in.²

w = equivalent curvature load, kip/ft.

When examining Figures C-21 to C-28, a comparison can be made between what Equation 4-6 is recommending and what the Atena results show. The figures were used to determine if the duct ties provided for the given equivalent curvature load was enough to prevent a duct tie stress of 24 ksi. Table 4-10 shows for each value of the equivalent curvature load whether the duct tie spacing caused a duct tie stress of less than 24 ksi. The table also provide the recommended spacing for that equivalent load. While the spacing range used in the Atena models is quite large, the recommend spacing values fall within the range. This table uses a duct spacing of 1.05 inches for the 0.7 scale model.

Table 4-10 along **Error! Reference source not found.** and Figure 4-25 provides input into what equivalent curvature load that will no longer require any duct ties. If a 24-inch spacing is assumed for full-scale, this would be equivalent to 16.8 inches in the 0.7 scale. If a #3 bar is spaced every 16.8 inches with a clear duct spacing of 1.05 inches, Equation 4-6 produces a w of 11.9 kips/ft. This is consistent with Specimen C1. Specimen C1 performed extremely well. It had equivalent curvature load of 11.5 kips/ft and no duct ties, plus it only had a duct spacing of 0.7 inches, and a web thickness of 8.4

inches. For the Atena model with duct ties at 17.5 inches and an equivalent curvature load of 11.5, Table 4-10 indicates that the stress limit was exceeded. Upon further examination, the peak duct tie stress was 26 ksi, so very close to the limit of 24 ksi. In addition, the Atena model that was identical to Specimen C1, except it had a duct spacing of 1.05 inches, showed no cracking, see Figure C-3.

Table 4-10 Duct tie spacing versus duct tie stress

Equivalent Curvature Load (k/ft)	Duct Tie Spacing (inches)	Duct Stress Greater than 24 ksi	Duct Tie	
			Eq. 4-4 ρ	Eq. 4-6 s (inches)
11.5	7	No	0.0060	17.5
11.5	17.5	Yes		
19.12	3.5	No	0.0106	9.9
19.12	17.5	Yes		
26.1	3.5	No	0.0148	7.1
26.1	17.5	Yes		
29.7	3.5	No	0.0169	6.2
29.7	17.5	Yes		

The concrete tensile strength influence the cracking results. Since the results are dominated by cracking, a rough approximation could be to take the equivalent force (kips/ft) divided by the gap between the ducts and then divided that by the tensile strength; this would be 11.5 kips/ft (1/12 in/ft)/(1.05 inches /0.45 ksi) which equals 2. This has not been systematically proven but could be a starting point for a relationship where no duct ties are needed.

$$\frac{\frac{w}{12}}{s_{clear\ spacing} \times f_t} < 2 \quad (4-7)$$

With:

w = equivalent curvature load, kip/ft.

$s_{clear\ spacing}$ = clear spacing between the ducts, in.

f_t = tensile capacity of the concrete, ksi, may be taken as $0.19 \sqrt{f'c}$ were $f'c$ is in ksi

4.5.2 Full scale version (1.0 scale)

To apply the design equations developed for the scaled specimens, the equations and figures were transformed to full scale versions for design purposes. Various ρ -values plotted against the equivalent curvature loads are shown in **Figure 4-26** to provide an approximate equation. An equation can be formed from the trendline to calculate ρ at various curvatures.

$$\rho = \frac{4.2w - 9}{10000} \quad (4-8)$$

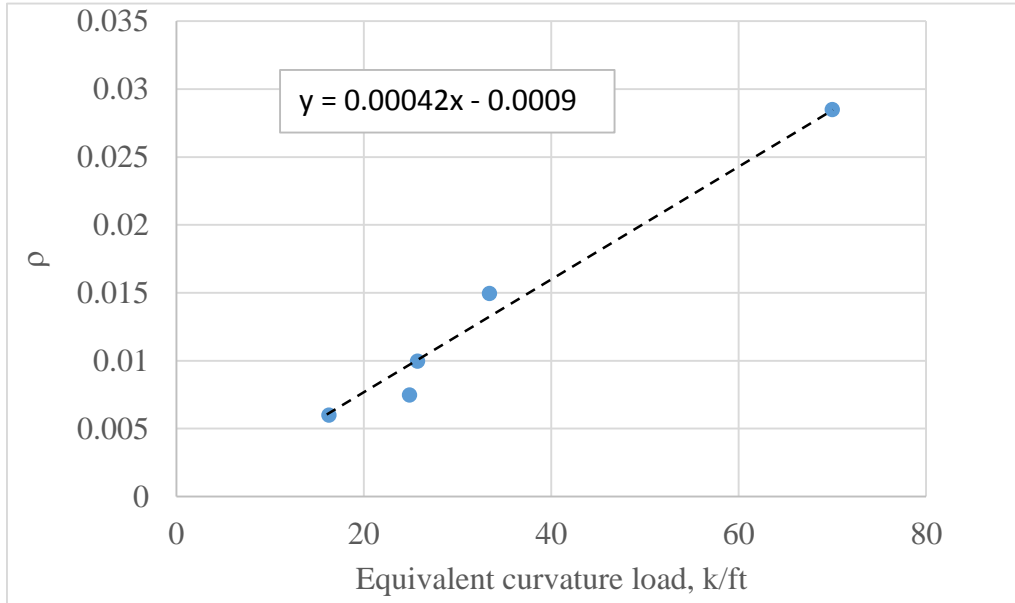


Figure 4-26: Reinforcement ratio vs. equivalent curvature load (1.0 scale).

Similar to the 0.7 scaled equations, the ρ equation (equation 4-7) can be used for #3 and #4 duct ties bars, shown in Figure 4-27.

$$s = \frac{A_s}{\rho(1.5'')} \quad (4-9)$$

With:

s = duct tie reinforcement spacing, in.

A_s = area of duct tie reinforcement, in.²

The height between the ducts is set as 1.5 inches. Equation (4-8) allows the opportunity to calculate the spacing for both #3 and #4 bars. Figure 4-27 shows the relationship between the Atena models using equation 4-8.

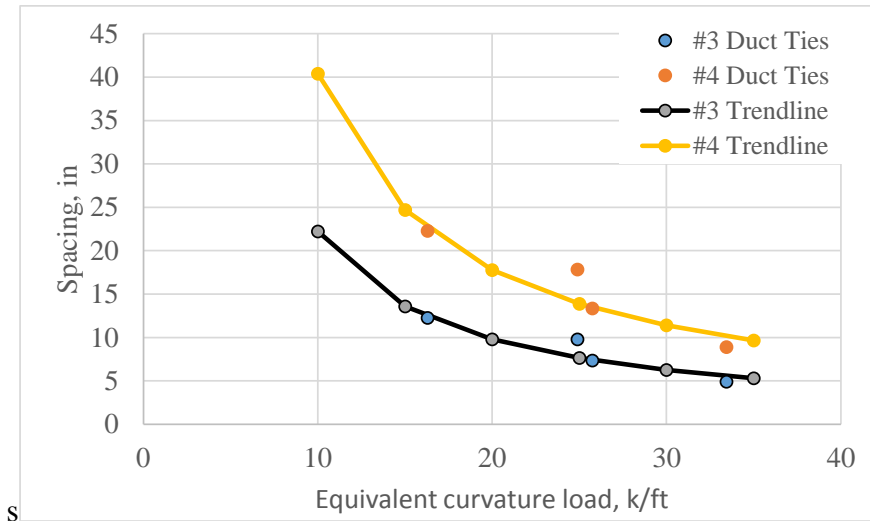


Figure 4-27: Atena spacing vs. equivalent curvature (1.0 scale).

The equation provides a good fit when compared against the Atena values for both the #3 and the #4 bar as seen in Figure 4-27. There is a small variance in the spacing values around 25 kip/ft. for both #3 and #4. Combining equation (4-8) and equation (4-9) gives an equation to calculate a required spacing for various equivalent curvature loads and duct tie reinforcement bar size for full-scale design.

$$s = \frac{10,000A_s}{6.3w - 13.5} \quad (4-10)$$

With:

s = required duct tie reinforcement spacing, in.

A_s = area of one reinforcement bar, in.²

w = equivalent curvature load, kip/ft.

When studying the experimental results and Atena results for the 0.7 scale, it was determined to limit the stress in the duct tie stress to 24 ksi. It was also determined that if the equivalent curvature load was 11.5 kips/ft or lower that duct ties would not be needed with a duct clear spacing of 1.05 inches. At full scale this is approximately equivalent to 16 kips/ft with a clear duct spacing of 1.5 inches.

The equation for full scale is the same for full scale as for the 0.7 scale since the equation is non-dimensional. This equation is based on the principle that the spacing between the ducts and the tension capacity of the concrete are the primary influences.

$$\frac{\frac{w}{12}}{s_{clear\ spacing} \times f_t} < 2 \quad (4-7)$$

With:

w = equivalent curvature load, kip/ft.

$s_{clear\ spacing}$ = clear spacing between the ducts, in.

f_t = tensile capacity of the concrete, ksi, may be taken as $0.19 \sqrt{f'c}$ where $f'c$ is in ksi

4.6 Number of Ducts Models

NDOT generally uses two, three or four ducts within the web of a bridge beam so determining if the number of ducts in the web affects the flow of forces and the overall performance of the bridge was vital. The number of ducts (2, 3 and 4) within the web are shown in Figure 4-28. As seen in Table 4-1, the equivalent curvature loads used in all three beams are the same for comparison purposes with 1.05 inch (1.50 inch NDOT/full scale) spacing between the ducts. The equivalent curvature loads were distributed over the same two top ducts within the web for all three setups. This leaves the bottom duct in the three duct beam empty and the bottom two ducts in the four duct beam empty.

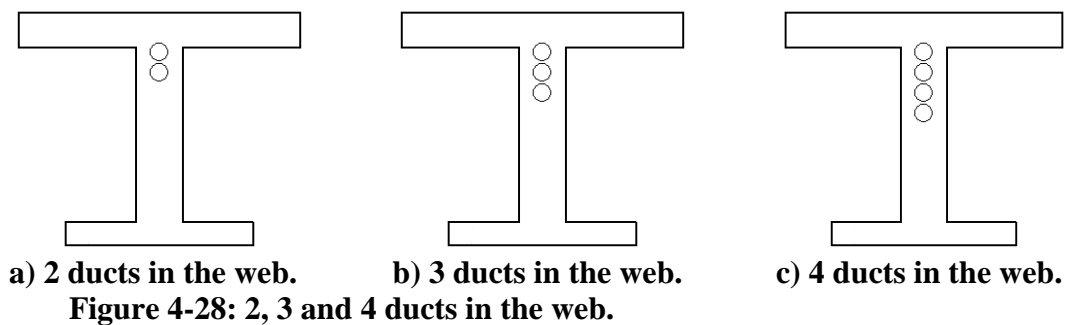
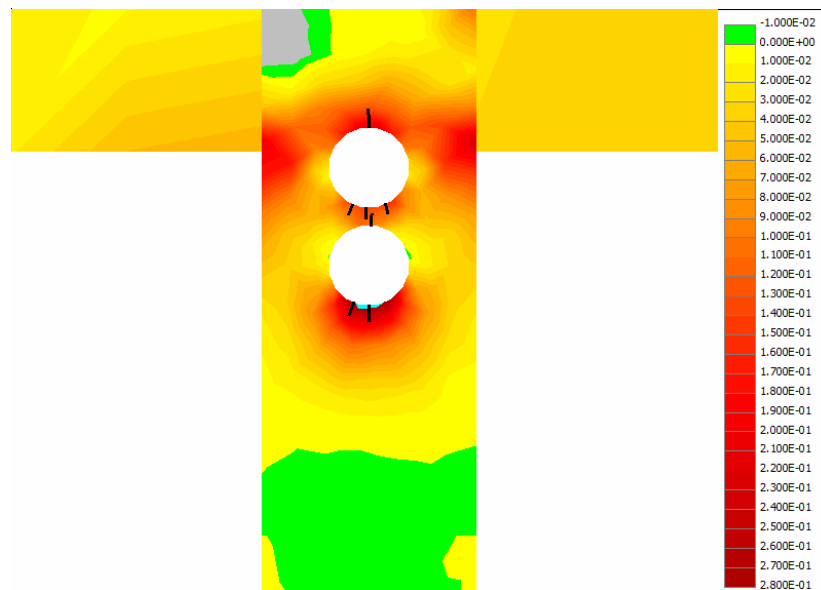


Figure 4-29, Figure 4-30 and Figure 4-31 shows the principal stresses at centerline of the beams in a view to accentuate the stresses around the ducts. The dark black lines represent any cracks in the concrete. Figure 4-29, Figure 4-30 and Figure 4-31 are taken after 100 psi air pressure of both ducts testing of only the ducts after 0.85fpu. No artificial cracks are included.



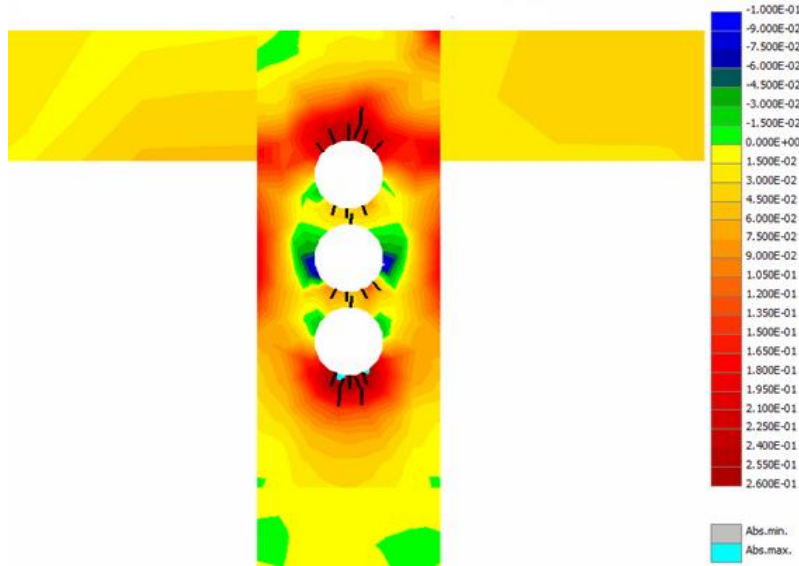


Figure 4-30: Parametric study with 3 ducts in the web at midspan of the beam.

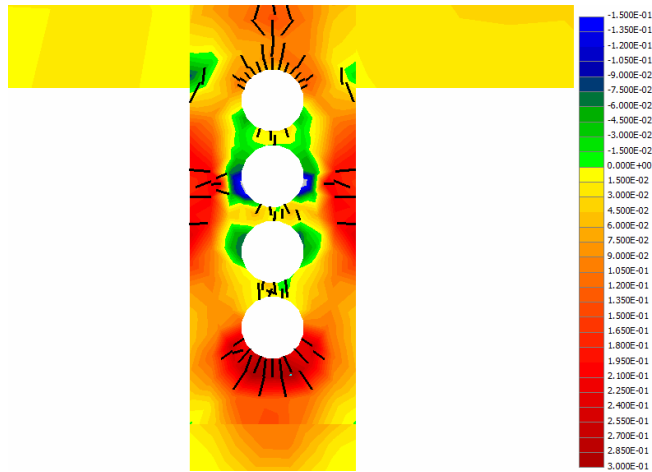


Figure 4-31: Parametric study with 4 ducts in the web at midspan of the beam.

The principal stresses in Figure 4-29, Figure 4-30 and Figure 4-31, were highest with 4 ducts (-0.15 ksi and 0.30 ksi) as opposed to 2 ducts (-0.01 ksi and 0.28 ksi). The maximum tensile and compressive stresses can be seen in Table 4-11. Additionally, the amount of cracks increased when the number of ducts increased.

Table 4-11: Maximum stresses for 2, 3 and 4 duct beams.

	2 Ducts	3 Ducts	4 Ducts
Tensile, ksi	0.28	0.26	0.30
Compressive, ksi	-0.01	-0.10	-0.15

To understand if including duct tie reinforcement would mitigate the difference between the 2, 3 and 4 duct models, these models were run again with #3 duct ties at 3.5 and 17.5 inch spacing. Duct ties are described in detail in Section 4.4. The duct tie

spacing's were chosen as they both are on the extremes of spacing being studied. The Atena models were designed similarly to Section 4.1. The results comparing the number of ducts with duct tie reinforcement included is shown in Table 4-12.

Table 4-12: Number of ducts with and without duct tie reinforcement.

	Equivalent Curvatures, kip/ft.	Rein. Spacing, in.	Concrete Stress, ksi	Total Web Bulge, in.	Crack Width, in.
C2 - #2	19.12	-	0.448	0.001573	0.000404
C2 - 17.5R #2	19.12	17.5	0.448	0.001542	0.000135
C2 - 3.5R #2	19.12	3.5	0.333	0.001489	0
C2 - #3	19.12	-	0.45	0.00273	0.00204
C2 - 17.5R #3	19.12	17.5	0.446	0.002038	0.000361
C2 - 3.5R #3	19.12	3.5	0.45	0.000898	0.00013
C2 - #4	19.12	-	0.447	0.00942	0.00961
C2 - 17.5R #4	19.12	17.5	0.447	0.00287	0.00242
C2 - 3.5R #4	19.12	3.5	0.349	0.00221	0

The crack widths decreased with the inclusion of duct ties and further decreased with the decrease spacing. The web bulge didn't fluctuate much with the inclusion of duct ties in the 2 duct models but decreased with duct ties for both 3 and 4 duct models. The web bulge is the total bulge from all bulging measurements from both faces of the web. Concrete stress between the ducts stayed essentially the same with exceptions of models with 2 and 4 ducts and 3.5 inch spacing, where the stress were less with the increased tie spacing. The number of ducts in a web effects the performance of the beam with an increase in crack size and web bulge as the number of ducts increase. Including duct tie reinforcement delivers a better performing beam by decreasing the crack width and the web bulging. The number of ducts does not significantly change the performance of the beams with the inclusion of duct ties, therefore equation (4-9) works for designs up to 4 ducts in a web.

4.7 Duct Locations Models

In most typical bridge layouts with post-tensioning, the post-tensioning tendons change location within the web based on the position along the bridge as discussed in Chapter 2. Usually above the column the post-tensioning tendons are located at the top of the web, whereas in the middle of span, the tendons are located at the bottom of the web. Generally the curvature is largest above columns and less in the midspan and abutments. With the duct locations varying from the top of the web towards the bottom of the web, it is important to determine if the duct location alters the outcome of the beam's performance.

Even with the curvatures generally being lower in the midspan of the bridge, the same equivalent curvature loads were applied to the ducts. The Atena models are providing a worst case scenario with high curvature forces. With moving along the beam into the midspan of the column and abutment, the support conditions for the Atena models will change as there is no column located below the beam as in the previous Atena models. For the Atena models where the ducts are located in the bottom of the web

and the middle of the web, the support conditions were modified to a simply supported beam condition, shown in Figure 4-32. The dead load is applied as an area load, shown in Figure 4-4.

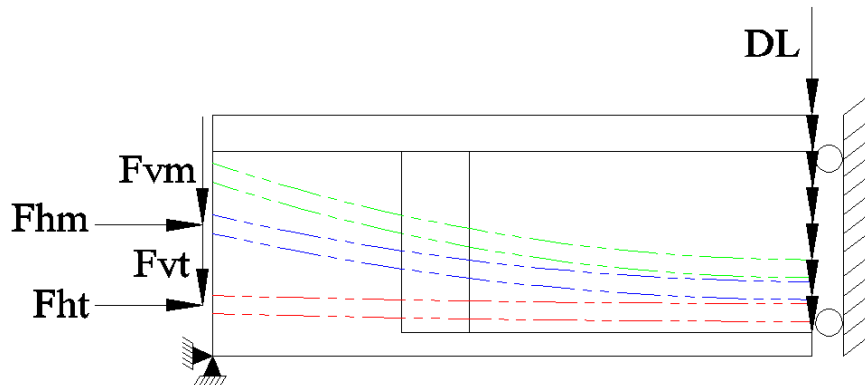


Figure 4-32: Support conditions for ducts in the middle and bottom of the web.

In addition to changing the support conditions, the location of the forces were also revised to account for the typical location for anchorages at the end of a beam. For instance, when the ducts are in the bottom of the web, the post-tensioning tendons will be exerting forces on the upper part of the ducts as opposed to the bottom side. When the ducts are in the middle of the web, the post-tensioning tendons were assumed to be on the bottom side of the duct, as with all previous Atena models. All duct location models were post tensioned to $0.80f_{pu}$ and air pressure to 100 psi. Artificial cracks were not included in the models. The principal stresses at the center of the beam are shown for both the ducts being in the middle of the web (Figure 4-33) and bottom of the web (Figure 4-34).

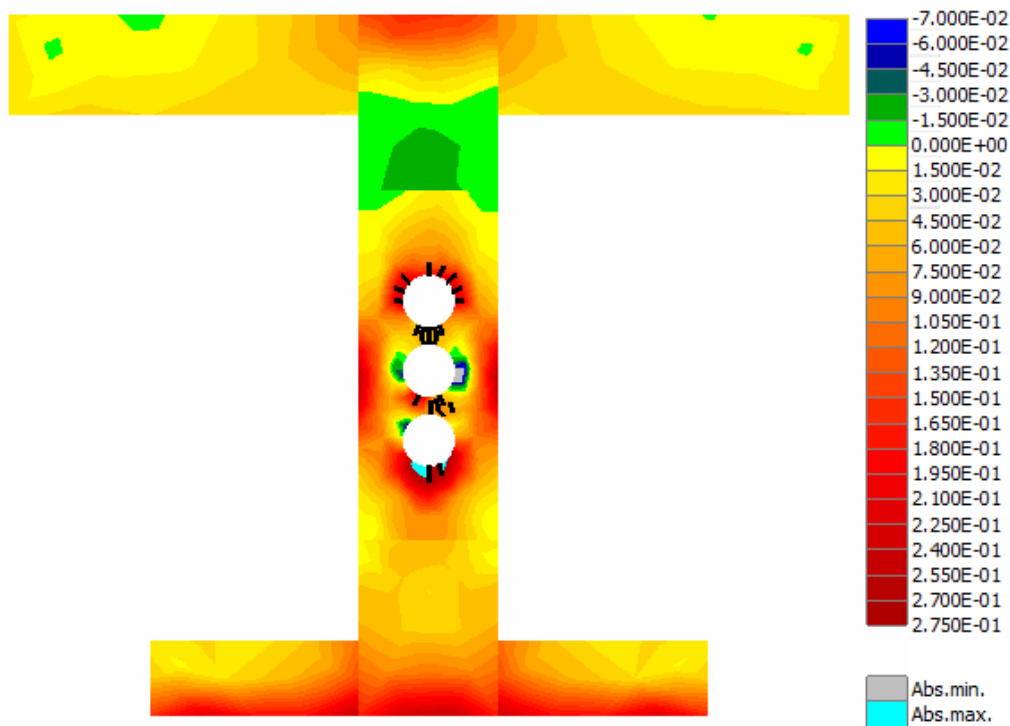


Figure 4-33: Principal stresses at centerline (ducts in the middle of the web).

From inspecting the figures, it can be noticed that the maximum principal stresses are not much different between the beams, shown in Table 4-13. In addition, the cracking is minor around the ducts on both Atena models. Overall the stresses and cracking are similar to when the ducts are in the top of the web so the location of the ducts within the web does not have a large effect on the beams performance as seen in Table 4-13. Therefore the equations developed in Section 4.5.2 are valid for tendon locations in the top, middle or bottom of the section.

Table 4-13: Cross section stresses - ducts in the top, middle and bottom.

	Top	Middle	Bottom
Tensile, ksi	0.260	0.260	0.250
Compressive, ksi	-0.100	-0.125	-0.125

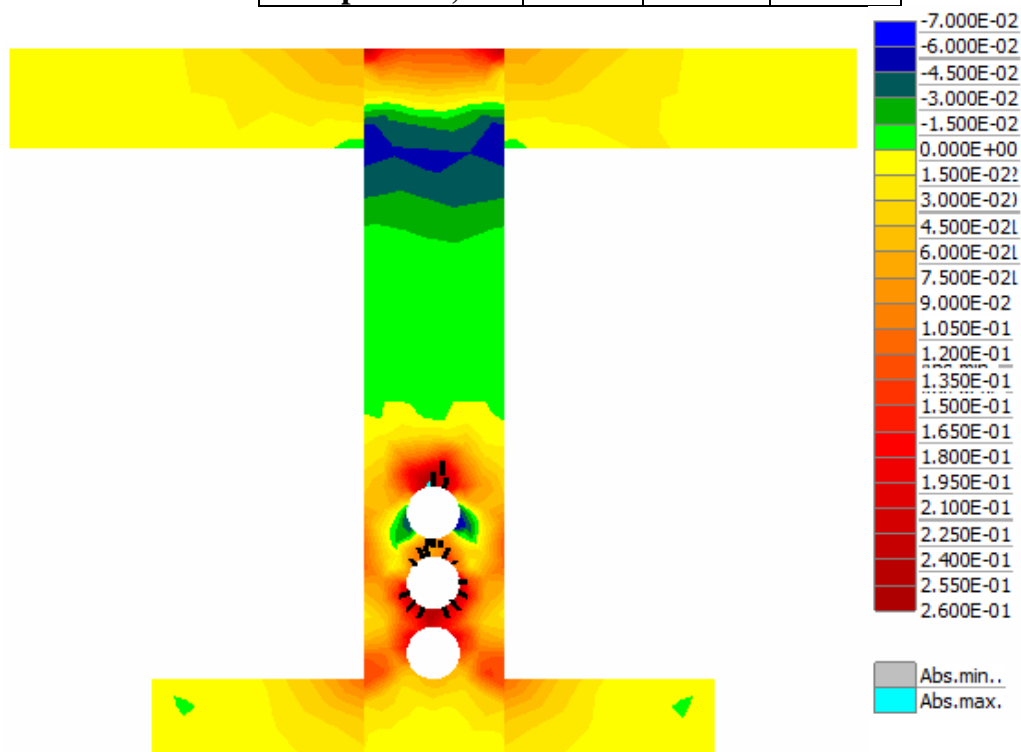


Figure 4-34: Principal stress at centerline (ducts at the bottom of the web).

4.8 Results Overview

An Atena parametric study was completed to understand the effects of the curvatures of the ducts and various duct tie reinforcement spacings, number of ducts in the web and the location of the ducts within the web. In all models the air pressure testing had the largest effect on the performance of the beams. The Atena models were loaded to 100 psi air pressure testing as a safety factor for unknown loading events that may occur in the field. Between 50 psi and 100 psi, the damage of the beams increased considerably for the crack size in between the ducts, the maximum web bulge and the stress in the duct ties reinforcement. Limiting the air pressure to a strict 50 psi would assure the beams are performing effectively with controlling the damage.

Not knowing when the cracks between the ducts form during the post-tensioning and air pressurizing, it was assumed that the crack formed from the beginning of loading. An equation was developed to calculate the required spacing and size of duct ties for different equivalent curvature loads as shown in equation (4-6) with the assumed crack. The inclusion of duct tie reinforcement around the ducts reduces the damage from the post-tensioning and air pressure testing with shorter distances between duct ties even further lowering the damage. The duct curvatures has a large effect on the performance of the beam with larger equivalent curvature loads delivering higher amounts of damage to the beam and lower equivalent curvature loads having lower damage.

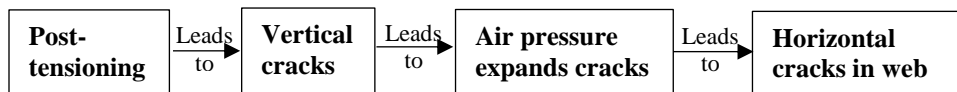
The number of ducts included in a web has an effect on the performance of the beam with crack sizes and web bulging increasing with an increase in ducts. The addition of duct tie reinforcement reduces damage for 2, 3 and 4 ducts within a web. The design procedure can be used for up to 4 ducts within a web. The location of the ducts being in the top, middle and bottom of the web does not have an effect on the beam performance.

5.0 Conclusions and Recommendations

5.1 Experimental Conclusions

The experimental research consisted of six 0.7-scale beams patterned after existing NDOT bridges including the Rancho Drive and Steamboat Hills Bridges. The experimental beam setup (Figure 2-7) was designed to recreate the load condition of an actual bridge in the area above a column (Figure 2-1). The experimental beams were designed to study the effects of post-tensioning curvature, spacing between post-tensioning ducts and inclusion of reinforcement around the post-tension ducts. Each beam was loaded with the same protocol that included a post-tensioning force corresponding to a tendon stress of 0.85fpu and 125 psi air pressure in the ducts. The primary results from the experimental program are as follows:

- Reducing tendon curvature decreases the likelihood of web cracking.
- Increasing spacing between ducts reduces web cracking.
- Inclusion of duct tie reinforcement bars between post-tensioning ducts decreases web cracking and is more effective than increasing spacing between ducts at reducing web cracks.
- Combined increase spacing between ducts and small spacing between duct tie reinforcement bars leads to minimal web surface cracks.
- Vertical internal web cracking started between the ducts during post-tensioning and expanded significantly during air pressure testing.
- Air pressure testing was the primary cause of web surface cracking.



5.2 Parametric Study Conclusions

To further study various parameters for minimizing the concrete web cracking, a parametric study was conducted. The parametric study focused on looking at the following parameters:

- Curvatures
- Location of ducts within the web (top, middle and bottom)
- Number of ducts (2, 3 or 4 ducts)
- Spacing between post-tensioning ducts
- Spacing of duct tie reinforcement bars
- Web width

All of the finite element models were run using the Atena 3D finite element program with the beams being designed similarly to the experimental beams. The loading protocol consisted of a tendon stress of 0.80fpu and duct air pressure of 100 psi to account for any unexpected overloading of the beam. The results are as follows for the parametric study:

- Increasing the equivalent curvature loads (tendon curvature), increases the web cracking damage.
- Duct location within the web does not greatly affect the web cracking.
- Number of ducts did not greatly impact the web cracking, revised design detail will provide better performance and less cracking for 2, 3 or 4 ducts within the web.

- Increasing the spacing between the ducts decreases the amount of cracking damage.
- Inclusion of duct tie reinforcement at any spacing decreases the web bulge and cracking between the ducts.
- Decreasing the spacing between the duct tie reinforcement bars decreased the stresses in the duct ties and cracking between the ducts.
- Increasing the web width by 25% had minor performance increases, not enough to consider web width a factor in beam performance.
- Air pressure testing caused the majority of the damage, similar to the experimental testing.

5.3 Recommendations

Bridge design recommendations to increase the performance and decrease the cracking within vertical or inclined webs were developed:

- Duct tie reinforcement shall be included in bridges with a total equivalent curvature load larger than 16 kip/ft. with a duct clear spacing of 1.5 inches.
- Equation 5-1 is proposed for when duct tie reinforcement is no longer needed. It is important to note that there was limited data for this equation.

$$\frac{\frac{w}{12}}{s_{clear\ spacing} \times f_t} < 2 \quad (5-1)$$

With:

w = total equivalent curvature load for all tendons, kip/ft.

$$w = \sum \frac{2P_i a_i}{L_i^2} \quad (5-2)$$

$s_{clear\ spacing}$ = clear spacing between the ducts, in.

P = post-tensioning force of each tendon, kip

a = height of each post-tensioning tendon, ft.

L = half-length of each post-tensioning tendon parabola, ft.

f_t = tensile capacity of the concrete, ksi, may be taken as $0.19 \sqrt{f'c}$ where $f'c$ is in ksi

- Duct ties when provided should be as shown in Figure 5-1 with one 90 degree hook and one 135 degree hook for the ties.

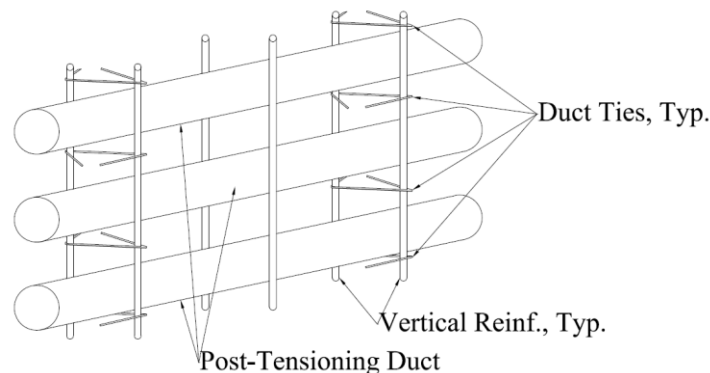


Figure 5-1: Duct tie reinforcement design detail.

- To calculate the size and spacing of duct tie reinforcement, the following equation is recommended:

$$s = \frac{10,000A_s}{6.3w - 13.5} \quad (5-3)$$

With:

s = duct tie reinforcement spacing, in.

A_s = one duct tie reinforcement nominal area, in²

- Enforce an upper limit of 50 psi on the air pressure testing of post-tensioning ducts. It was clear that the air pressure is what was causing the trouble.
- It is important to provide proper quality control during concrete casting to ensure good concrete consolidation around tendon ducts.

6.0 References

- AASHTO, American Association of State Highway and Transportation Officials. (2012). *AASHTO LRFD Bridge Design Specifications*. Washington, DC.
- ASTM International. (2011). *ASTM C496/C496M - 11 Standard Test Method for Splitting Tensile Strength of Cylindrical Concrete Specimens*. West Conshohocken, PA.
- ASTM International. (2012). *ASTM C143/C143M - 12 Standard Test Method for Slump of Hydraulic-Cement Concrete*. West Conshohocken, PA.
- ASTM International. (2014). *ASTM A370 - 14 Standard Test Methods and Definitions for Mechanical Testing of Steel Products*. West Conshohocken, PA.
- ASTM International. (2014a). *ASTM C39/C39M - 14a Standard Test Method for Compressive Strength of Cylindrical Concrete Specimens*. West Conshohocken, PA.
- Cervenka, V., Jendele, L., & Cervenka, J. (2014). *Atena Program Documentation Part I Theory*. Prague.
- NDOT, Nevada Department of Transportation. (2014). *Standard Specifications for Road and Bridge Construction*. Carson City, NV.
- Podolny, Jr., W. (1985). The Cause of Cracking in Post-Tensioned Concrete Box Girder Bridges and Retrofit Procedures. *PCI Journal*, 60.
- Stone, W. C., & Breen, J. E. (1981). *Design of Post-Tensioned Girder Anchorage Zones*. Austin, TX: The University of Texas at Austin.
- VSL International LTD. (1991). *Detailing for Post-Tensioning*. Bern, Switzerland.

Appendix A: Experimental Tables

Table A-1: C2 shear reinforcement strain values.

	S6LT, $\mu\epsilon$	S6LM, $\mu\epsilon$	S6LB, $\mu\epsilon$	S6RT, $\mu\epsilon$	S6RM, $\mu\epsilon$	S6RB, $\mu\epsilon$
APIB	-5.9	-13.8	0.0	0.0	0.0	2.6
APIT	4.6	-9.8	0.0	0.0	0.0	12.4
DL	-3.3	-3.3	-4.6	-30.8	-6.5	-6.6
0.15fpuB	478.1	-0.7	-3.9	11.1	-2.6	-13.8
0.15fpuT	476.8	-0.7	-0.7	14.4	-1.3	-7.2
0.45fpuB	503.6	21.0	10.5	55.7	27.5	-7.2
0.45fpuT	95.6	50.4	44.5	-4750.9	62.2	41.3
0.75fpuB	220.7	64.2	43.2	-3793.3	74.7	11.1
0.75fpuT	277.7	70.7	59.0	-3989.8	77.9	36.7
APB-50psi	301.9	103.5	123.1	-3700.2	174.9	15.7
APT-50psi	302.6	106.1	125.1	-3700.9	176.8	19.0
APB-50, 75, 100psi	1116.7	515.5	1866.9	-3057.7	633.9	1346.7
APB-125psi	1132.4	531.2	2056.9	-2926.0	640.5	1548.5
0.85fpuB	2451.4	545.6	1997.9	1483.0	641.1	1493.4
0.85fpuT	2448.8	547.6	1987.4	1589.8	646.4	1497.4
APB	2679.3	620.9	2506.2	-122.5	716.4	1947.4

Table A-2: C2 beam end displacements.

	Disp. Stress, in.	Disp. Non-Stress, in.
APIB	-0.002	-0.003
APIT	-0.004	-0.106
DL	0.022	0.047
0.15fpuB	-0.008	0.047
0.15fpuT	-0.014	0.043
0.45fpuB	-0.022	0.023
0.45fpuT	-0.039	0.014
0.75fpuB	-0.050	0.007
0.75fpuT	-0.067	-0.009
APB-50psi	-0.070	-0.036
APT-50psi	-0.071	-0.036
APB-50, 75, 100psi	-0.079	-0.042
APB-125psi	-0.080	-0.043
0.85fpuB	-0.087	-0.050
0.85fpuT	-0.099	-0.052
APB	-0.097	-0.057

Table A-3: C3 shear reinforcement strain values.

	S6LT, $\mu\epsilon$	S6LM, $\mu\epsilon$	S6LB, $\mu\epsilon$	S6RT, $\mu\epsilon$	S6RM, $\mu\epsilon$	S6RB, $\mu\epsilon$
APIB	0.7	0.0	1.3	-0.7	0.7	-0.7
APIT	0.7	-0.7	0.0	0.0	0.0	-0.7
DL	104.2	4.6	0.7	-100.2	-48.5	-56.4
0.15fpuB	115.3	2.0	0.0	-85.8	-40.6	6335.5
0.15fpuT	97.0	-9.2	-11.1	-71.4	-33.4	7294.4
0.45fpuB	81.3	-21.6	-35.4	-37.3	-22.3	-34.1
0.45fpuT	86.5	-24.9	-38.0	-22.3	-21.0	6715.6
0.75fpuB	92.4	-15.1	-66.8	-9.8	-7.9	6389.9
0.75fpuT	126.5	-3.3	-56.4	29.5	6.5	6460.0
APB-50psi	287.7	81.2	70.8	250.8	201.7	77.3
APT-50psi	287.7	81.8	67.5	244.3	204.4	77.3
APB-50psi Hold	304.7	78.6	70.1	281.6	224.0	83.2
APB-75psi Hold	479.0	257.3	338.8	503.0	383.2	523.7
APB-100psi Hold	538.0	314.3	431.8	575.7	428.4	690.8
APB-125psi Hold	600.2	369.3	514.4	630.7	466.4	844.2
0.85fpuB	631.7	398.7	522.3	661.5	495.8	6147.4
0.85fpuT	634.3	393.5	509.2	651.6	491.2	6753.0
APB-50psi	640.8	395.5	513.1	653.6	493.2	832.4
APB-75psi	659.8	403.3	528.8	670.0	498.5	850.8
APB-100psi	704.4	428.9	578.6	697.5	525.3	919.6
APB-125psi	789.6	505.5	717.6	761.7	573.1	1156.2

Table A-4: C3 beam end displacements.

	Disp. Stress, in	Disp. Non-Stress, in
APIB	0.000	0.000
APIT	0.000	0.000
DL	0.021	0.066
0.15fpuB	0.025	0.062
0.15fpuT	0.022	0.052
0.45fpuB	0.011	0.041
0.45fpuT	0.001	0.024
0.75fpuB	-0.012	0.012
0.75fpuT	-0.025	-0.008
APB-50psi	-0.028	-0.008
APT-50psi	-0.030	-0.009
APB-50psi Hold	-0.038	-0.011
APB-75psi Hold	-0.041	-0.014
APB-100psi Hold	-0.042	-0.015
APB-125psi Hold	-0.043	-0.016
0.85fpuB	-0.045	-0.025
0.85fpuT	-0.049	-0.035
APB-50psi	-0.053	-0.034
APB-75psi	-0.053	-0.034
APB-100psi	-0.054	-0.034
APB-125psi	-0.056	-0.035

Table A-5: C4 shear reinforcement strain values.

	S6LT, με	S6LM, με	S6LB, με	S6RT, με	S6RM, με	S6RB, με
APIB	-26.2	0.0	-21.6	-16.4	80.6	-22.3
APIT	-19.6	0.0	-22.3	-17.0	84.5	-22.3
DL	-6.5	0.0	-16.4	-11.8	100.3	-17.0
0.15fpuB	-6.5	0.0	7.2	0.0	0.0	2.6
0.15fpuT	0.0	0.0	8.5	1091.4	0.0	5.2
0.45fpuB	85.0	0.0	67.5	2471.1	0.0	64.2
0.45fpuT	98.1	0.0	89.1	8500.8	0.0	87.1
0.75fpuB	130.8	0.0	95.0	11065.6	0.0	91.7
0.75fpuT	150.4	0.0	107.5	10214.6	0.0	104.1
APB-50psi	176.5	0.0	110.8	0.0	0.0	112.0
APT-50psi	170.0	0.0	110.1	0.0	0.0	112.7
APB-75psi	176.5	0.0	109.4	0.0	0.0	109.4
APT-75psi	176.5	0.0	111.4	0.0	0.0	112.0
APB-100psi	523.1	0.0	1139.0	23379.2	-3802.3	1050.6
APT-100psi	496.9	0.0	1104.9	21605.2	-3791.8	1009.9
APB-125psi	542.7	0.0	1177.0	24648.8	-3797.7	1095.1
APT-125psi	549.2	0.0	1173.7	24790.4	-3799.0	1093.8
0.85fpuB	575.4	0.0	1213.1	8137.9	0.0	1136.4
0.85fpuT	562.3	0.0	1210.4	18927.0	0.0	1127.2
APB-50psi	555.8	0.0	1182.9	442.9	-3514.7	1095.1
APT-50psi	568.9	0.0	1188.8	1224.4	-3506.8	1103.6
APB-75psi	601.6	0.0	1231.4	1567.0	-3488.5	1144.9
APT-75psi	601.6	0.0	1230.1	1834.3	-3486.5	1144.9
APB-100psi	614.6	0.0	1270.7	2139.6	-3478.0	1187.4
APT-100psi	627.7	0.0	1265.5	2328.3	-3479.9	1185.5
APT-125psi	608.1	0.0	1263.5	2361.0	-3481.9	1184.2

Table A-6: C4 beam end displacements.

	Disp. Stress, in.	Disp. Non-Stress, in.
APIB	0.029	0.033
APIT	0.030	0.034
DL	0.030	0.035
0.15fpuB	-0.007	-0.001
0.15fpuT	-0.014	-0.005
0.45fpuB	-0.025	-0.013
0.45fpuT	-0.041	-0.025
0.75fpuB	-0.046	-0.037
0.75fpuT	-0.063	-0.050
APB-50psi	-0.058	-0.074
APT-50psi	-0.059	-0.074
APB-75psi	-0.059	-0.074
APT-75psi	-0.058	-0.074
APB-100psi	-0.064	0.097
APT-100psi	-0.063	0.099
APB-125psi	-0.064	0.096
APT-125psi	-0.064	0.096
0.85fpuB	-0.073	0.057
0.85fpuT	-0.081	0.052
APB-50psi	-0.076	-0.016
APT-50psi	-0.076	-0.016
APB-75psi	-0.076	-0.017
APT-75psi	-0.076	-0.016
APB-100psi	-0.078	-0.017
APT-100psi	-0.078	-0.017
APT-125psi	-0.078	-0.017

Table A-7: C5 shear reinforcement strain values.

	S6LT, με	S6LM, με	S6LB, με	S6RT, με	S6RM, με	S6RB, με
APIB	6.5	-3.9	0.0	-2.6	30.8	-13.1
APIT	13.1	5.9	0.0	5.2	38.7	-8.5
DL	13.1	7.2	0.0	4.6	47.2	-7.2
0.15fpuB	39.2	41.3	0.0	44.5	13423.1	17810.9
0.15fpuT	32.7	40.0	0.0	42.6	13423.1	15826.4
0.45fpuB	58.8	62.9	0.0	83.9	13423.1	11025.6
0.45fpuT	65.4	70.8	0.0	85.2	13423.1	13480.4
0.75fpuB	-32.7	-23.6	0.0	12.4	13423.1	7810.4
0.75fpuT	0.0	-2.0	0.0	34.7	13423.1	8351.4
APB-50psi	52.3	47.8	0.0	85.8	601.5	-88.4
APT-50psi	52.3	53.1	0.0	92.4	608.1	-87.1
APB-75psi	65.4	59.6	0.0	90.4	621.2	-86.5
APB-100psi	71.9	96.3	0.0	128.4	678.2	-60.3
APT-100psi	91.5	104.2	0.0	135.0	686.7	-60.9
APB-125psi	91.5	117.9	0.0	141.5	719.4	-57.6
APT-125psi	98.1	121.9	0.0	144.8	724.0	-56.3
0.85fpuB	78.5	102.9	0.0	128.4	13423.1	14459.5
0.85fpuT	98.1	128.4	0.0	150.7	13423.1	13033.7
APB-50psi	104.6	116.0	0.0	142.2	735.8	-11.8
APT-50psi	117.7	144.8	0.0	169.0	768.6	17.0
APB-75psi	130.8	154.6	0.0	179.5	784.3	27.5
APT-75psi	137.3	159.9	0.0	182.8	791.5	31.4
APB-100psi	143.9	165.8	0.0	188.0	799.4	33.4
APT-100psi	137.3	169.0	0.0	192.6	806.6	36.7
APB-125psi	156.9	185.4	0.0	199.2	820.4	42.6
APT-125psi	163.5	190.0	0.0	205.1	830.2	45.8

Table A-8: C5 beam end displacements.

	Disp. Stress, in.	Disp. Non-Stress, in.
APIB	0.024	0.036
APIT	0.028	0.038
DL	0.028	0.038
0.15fpuB	0.278	0.031
0.15fpuT	0.271	0.027
0.45fpuB	0.262	0.019
0.45fpuT	-0.970	0.010
0.75fpuB	-0.985	0.005
0.75fpuT	-1.003	-0.009
APB-50psi	-0.997	-0.014
APT-50psi	-0.997	-0.014
APB-75psi	-0.997	-0.014
APB-100psi	-0.997	-0.014
APT-100psi	-0.997	-0.014
APB-125psi	-0.997	-0.014
APT-125psi	-0.998	-0.014
0.85fpuB	-1.004	-0.028
0.85fpuT	-1.011	-0.033
APB-50psi	-1.006	-0.037
APT-50psi	-1.006	-0.037
APB-75psi	-1.006	-0.037
APT-75psi	-1.006	-0.037
APB-100psi	-1.006	-0.037
APT-100psi	-1.006	-0.037
APB-125psi	-1.006	-0.037
APT-125psi	-1.006	-0.037

Table A-9: C6 shear reinforcement strain values.

	S6LT, με	S6LM, με	S6LB, με	S6RT, με	S6RM, με	S6RB, με
APIB	-6.5	-22.3	-26.9	-20.3	-27.5	-33.4
APIT	-26.2	-22.9	-28.2	-18.3	-28.2	-43.2
DL	-19.6	-22.9	-28.8	-19.7	-27.5	-42.6
0.15fpuB	-65.4	-86.5	-98.3	-91.7	4370	7050
0.15fpuT	-58.8	-85.8	-92.4	-79.9	4347	7050
0.45fpuB	-39.2	-63.6	-26280	-56.3	4336	7050
0.45fpuT	-32.7	-63.6	-26280	-44.5	4294	7050
0.75fpuB	-6.5	-38.7	-26280	-25.5	4249	7050
0.75fpuT	0.0	-40.0	-26280	-15.1	4226	7050
APB-50psi	-71.9	-100.9	-26280	-77.3	-121.9	-83.8
APT-50psi	-65.4	-97.0	-26280	-72.7	-117.3	-73.4
APB-75psi	-58.8	-91.1	-26280	-69.4	-114.0	-62.9
APT-75psi	-58.8	-86.5	-26280	-64.2	-107.5	-53.1
APB-100psi	-65.4	-84.5	-26280	-64.9	-105.5	-47.8
APT-100psi	-58.8	-81.9	-26280	-62.2	-102.9	-41.3
APB-125psi	-52.3	-76.7	-26280	-57.7	-85.2	-87.1
APT-125psi	-58.8	-78.6	-26280	-57.0	-85.8	-85.8
0.85fpuB	-39.2	-56.4	-26280	-45.2	3943	7050
0.85fpuT	-13.1	-53.1	-26280	-36.0	3962	7050
APB-50psi	-19.6	-43.2	-26280	-26.9	-101.6	328.8
APT-50psi	-6.5	-40.0	-26280	-23.6	-96.3	337.3
APB-75psi	-13.1	-38.0	-26280	-22.9	-97.6	334.0
APT-75psi	0.0	-37.3	-26280	-21.6	-95.7	339.3
APB-100psi	0.0	-36.0	-26280	-21.0	-91.7	336.0
APT-100psi	0.0	-36.0	-26280	-21.6	-90.4	338.0
APB-125psi	0.0	-30.8	-26280	-26.9	-89.1	439.5
APT-125psi	0.0	-33.4	-26280	-30.1	-93.7	432.3

Table A-10: C6 beam end displacements.

	Disp. Stress, in.	Disp. Non-Stress, in.
APIB	-1.688	-0.391
APIT	-1.688	-0.385
DL	-1.688	-0.385
0.15fpuB	-1.769	-0.377
0.15fpuT	-1.781	-0.384
0.45fpuB	-1.796	-0.394
0.45fpuT	-1.812	-0.407
0.75fpuB	-1.821	-0.418
0.75fpuT	-1.837	-0.433
APB-50psi	-1.853	-0.463
APT-50psi	-1.853	-0.463
APB-75psi	-1.853	-0.463
APT-75psi	-1.853	-0.463
APB-100psi	-1.853	-0.463
APT-100psi	-1.853	-0.463
APB-125psi	-1.853	-0.464
APT-125psi	-1.853	-0.464
0.85fpuB	-1.861	-0.466
0.85fpuT	-1.870	-0.470
APB-50psi	-1.864	-0.469
APT-50psi	-1.864	-0.469
APB-75psi	-1.864	-0.469
APT-75psi	-1.864	-0.469
APB-100psi	-1.864	-0.469
APT-100psi	-1.864	-0.469
APB-125psi	-1.865	-0.470
APT-125psi	-1.864	-0.470

Table A-11: C6 duct tie reinforcement at 12.25" right of centerline.

	DT12.25RT, με	DT12.25RM1, με	DT12.25RM2, με	DT12.25RB, με
APIB	-6.5	13.1	-13.1	6.5
APIT	-13.1	13.1	-26.2	13.1
DL	0.0	19.6	-19.6	13.1
0.15fpuB	-71.9	71.9	-137.3	-13.1
0.15fpuT	-85.0	32.7	-98.1	-19.6
0.45fpuB	-91.6	32.7	-85.0	0.0
0.45fpuT	-98.1	45.8	-65.4	13.1
0.75fpuB	-45.8	45.8	-52.3	26.2
0.75fpuT	-6.5	39.2	-39.2	26.2
APB-50psi	-85.0	-98.1	-19.6	-45.8
APT-50psi	-85.0	-78.5	-6.5	-39.3
APB-75psi	-65.4	-26.2	150.4	-32.7
APT-75psi	-71.9	-39.2	150.4	-32.7
APB-100psi	-45.8	52.3	359.7	-19.6
APT-100psi	-45.8	65.4	346.6	-13.1
APB-125psi	-6.5	143.9	582.0	124.4
APT-125psi	-6.5	124.3	582.0	124.4
0.85fpuB	45.8	215.8	627.8	144.0
0.85fpuT	52.3	255.1	640.9	163.7
APB-50psi	19.6	196.2	660.5	189.8
APT-50psi	19.6	189.7	667.1	189.8
APB-75psi	26.2	215.8	693.2	196.4
APT-75psi	32.7	209.3	693.2	209.5
APB-100psi	39.2	235.5	791.3	229.1
APT-100psi	32.7	209.3	797.9	235.7
APB-125psi	65.4	242.0	1118.3	261.8
APT-125psi	71.9	235.5	1098.7	255.3

Table A-12: C6 duct tie reinforcement at 19.25" right of centerline.

	DT19.25RT, με	DT19.25M1, με	DT19.25M2, με	DT19.25RB, με
APIB	6.5	13.1	-6.5	0.0
APIT	0.0	26.2	-6.5	13.1
DL	0.0	32.7	13.1	13.1
0.15fpuB	19.6	91.5	-58.9	-19.6
0.15fpuT	6.5	65.4	-52.3	-26.2
0.45fpuB	26.2	98.1	91.6	19.6
0.45fpuT	78.5	156.9	104.7	19.6
0.75fpuB	78.5	183.1	542.9	72.0
0.75fpuT	104.7	248.5	516.8	104.7
APB-50psi	-91.6	98.1	457.9	19.6
APT-50psi	-91.6	104.6	451.4	26.2
APB-75psi	-78.5	222.3	425.2	65.4
APT-75psi	-78.5	222.3	418.6	72.0
APB-100psi	-72.0	307.3	1314.8	111.2
APT-100psi	-65.4	307.3	1282.1	111.2
APB-125psi	-52.3	490.4	1550.3	163.6
APT-125psi	-39.3	490.4	1543.8	163.6
0.85fpuB	104.7	732.4	1779.3	229.0
0.85fpuT	117.8	804.3	1825.0	229.0
APB-50psi	-19.6	660.5	1883.9	235.6
APT-50psi	-19.6	660.5	1890.5	242.1
APB-75psi	-19.6	660.5	1903.5	248.6
APT-75psi	-19.6	667.0	1910.1	242.1
APB-100psi	-13.1	693.2	1903.5	255.2
APT-100psi	-6.5	693.2	1897.0	255.2
APB-125psi	-6.5	738.9	1923.2	301.0
APT-125psi	-6.5	738.9	1923.2	287.9

Appendix B: Experimental Figures

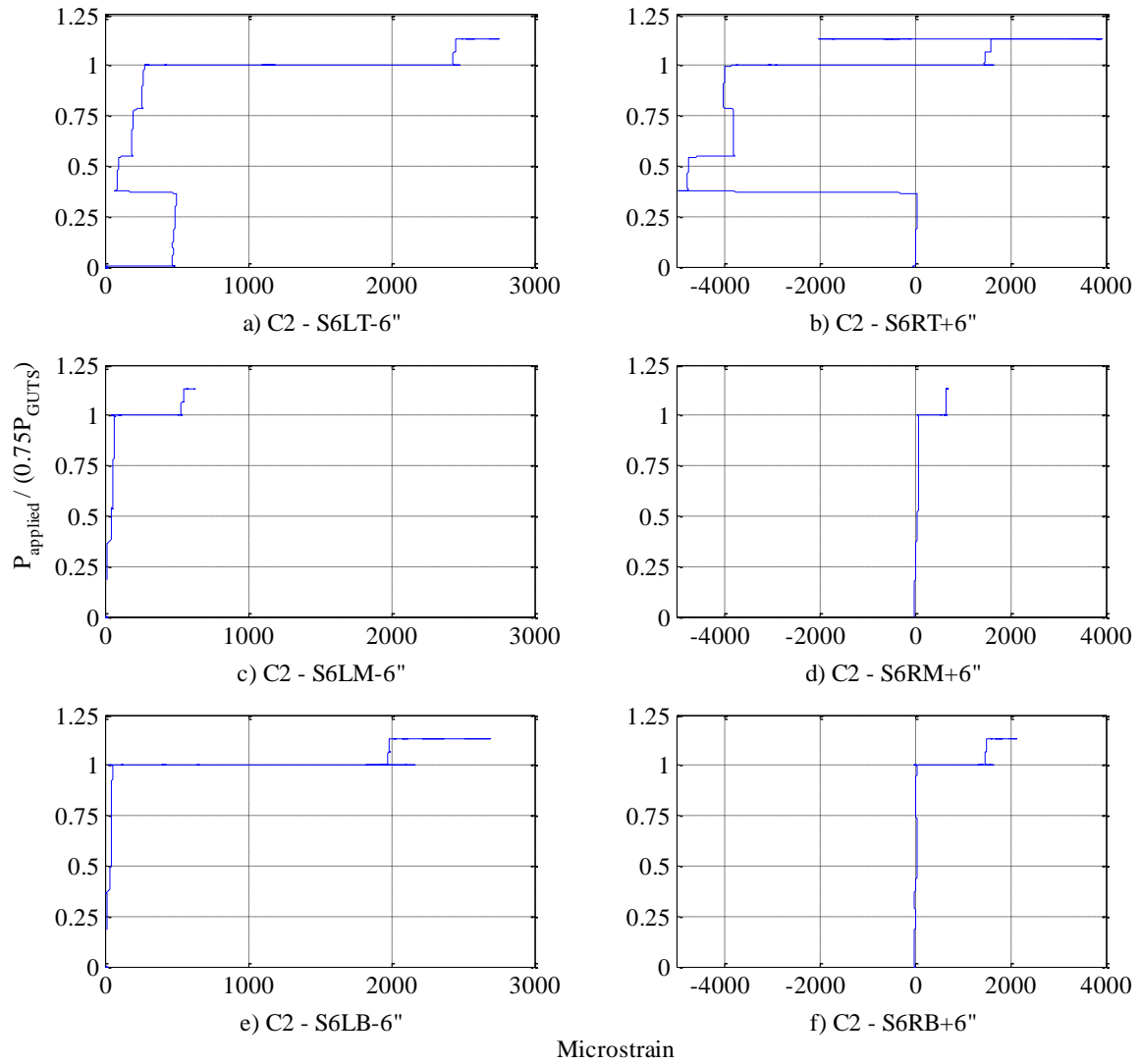


Figure B-1: C2 shear reinforcement.

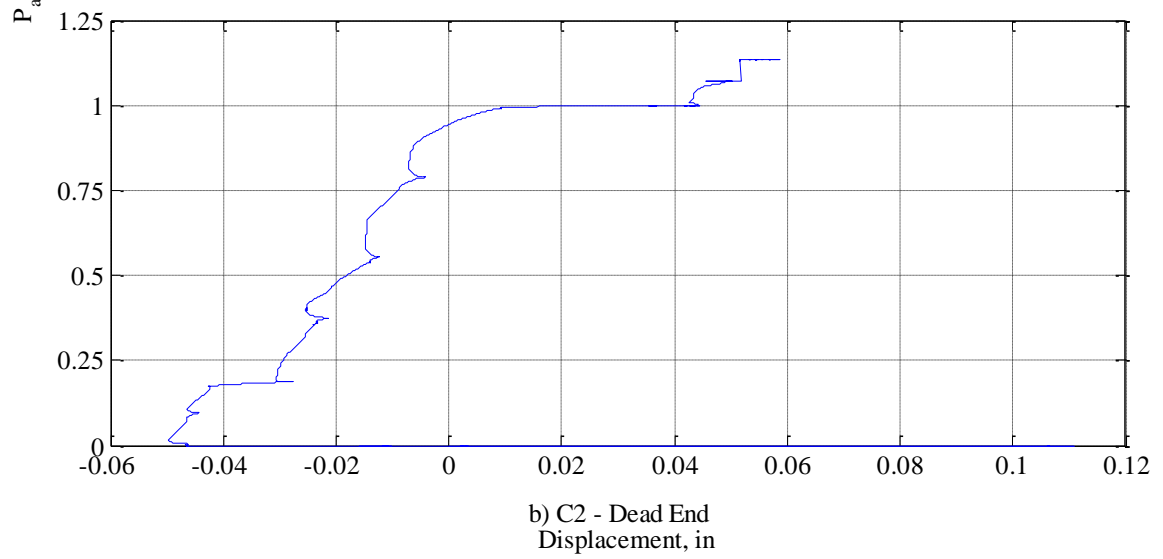
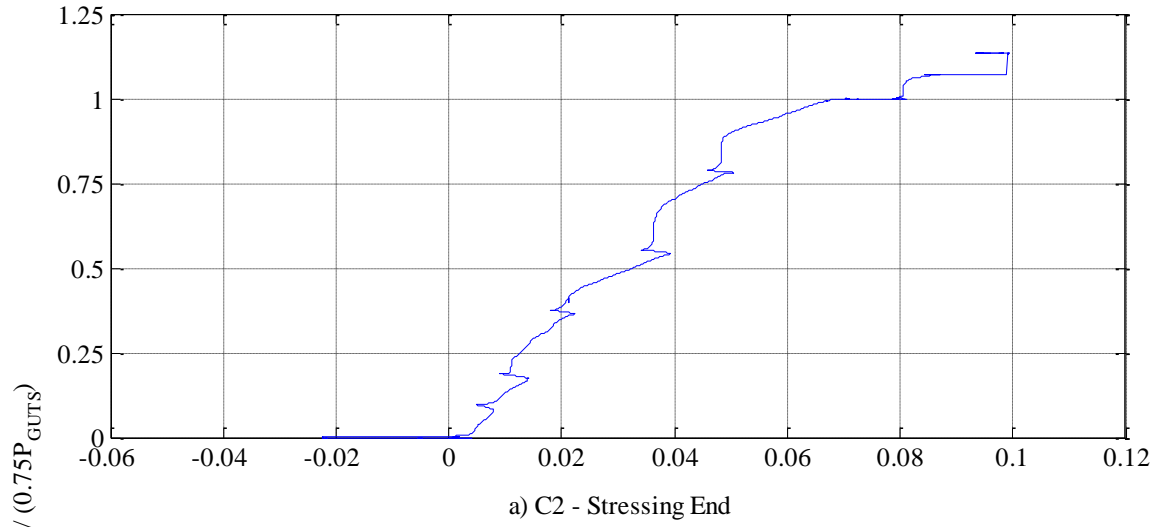


Figure B-2: C2 beam end displacement.

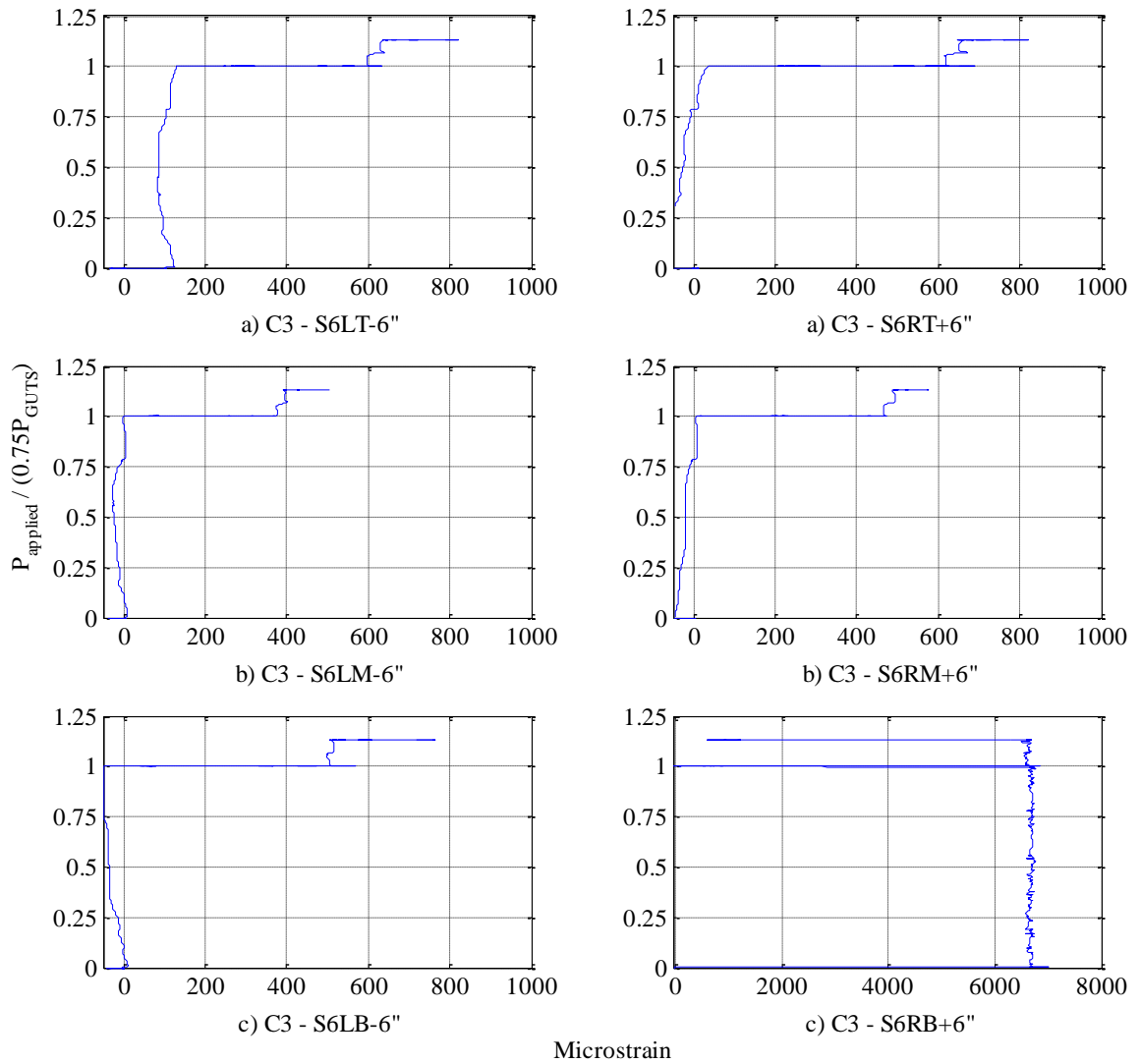


Figure B-3: C3 shear reinforcement.

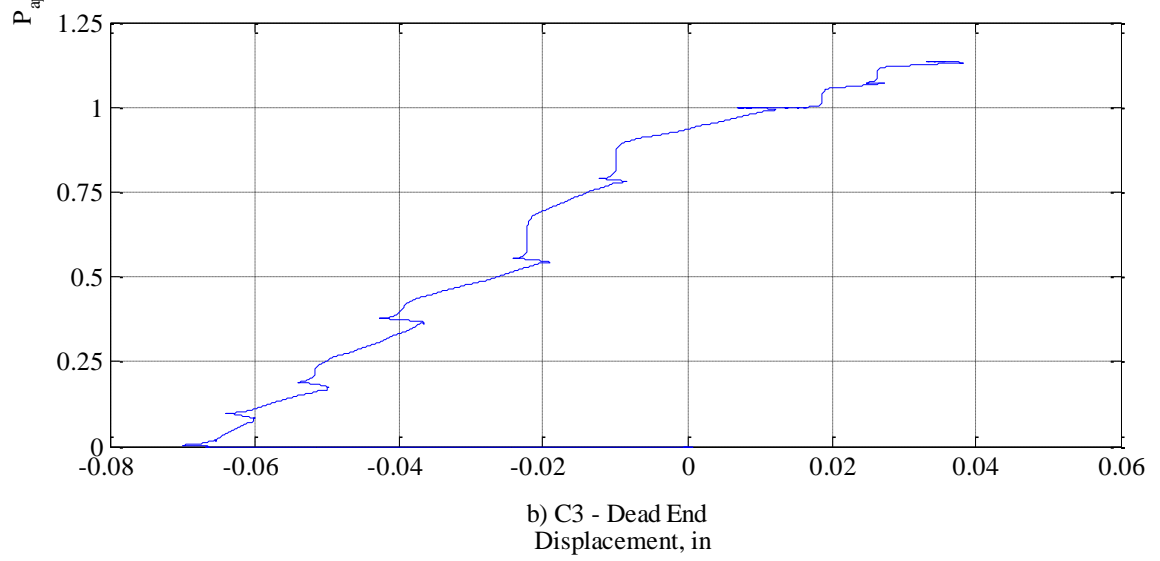
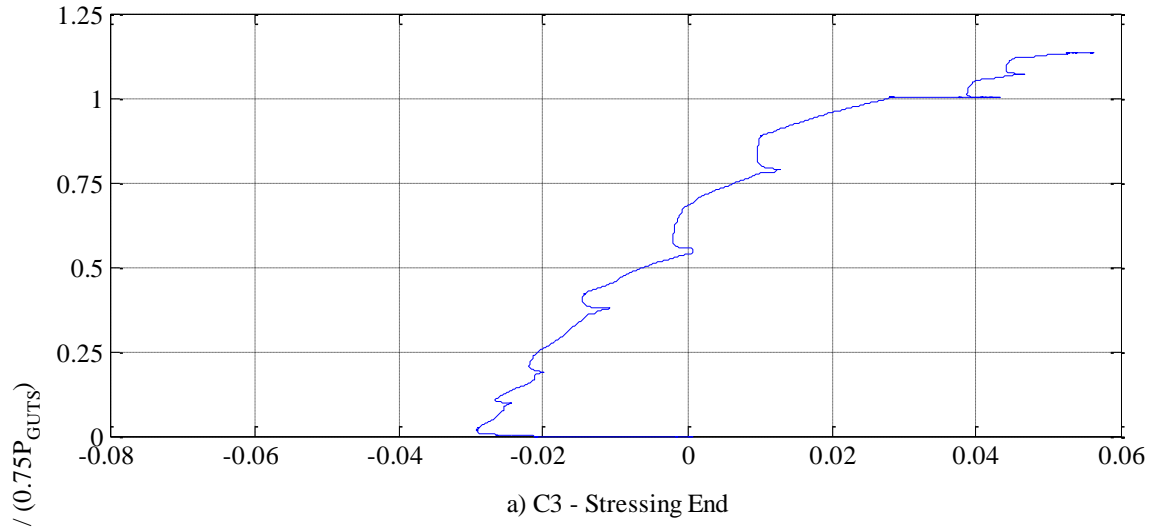


Figure B-4: C3 beam end displacements.

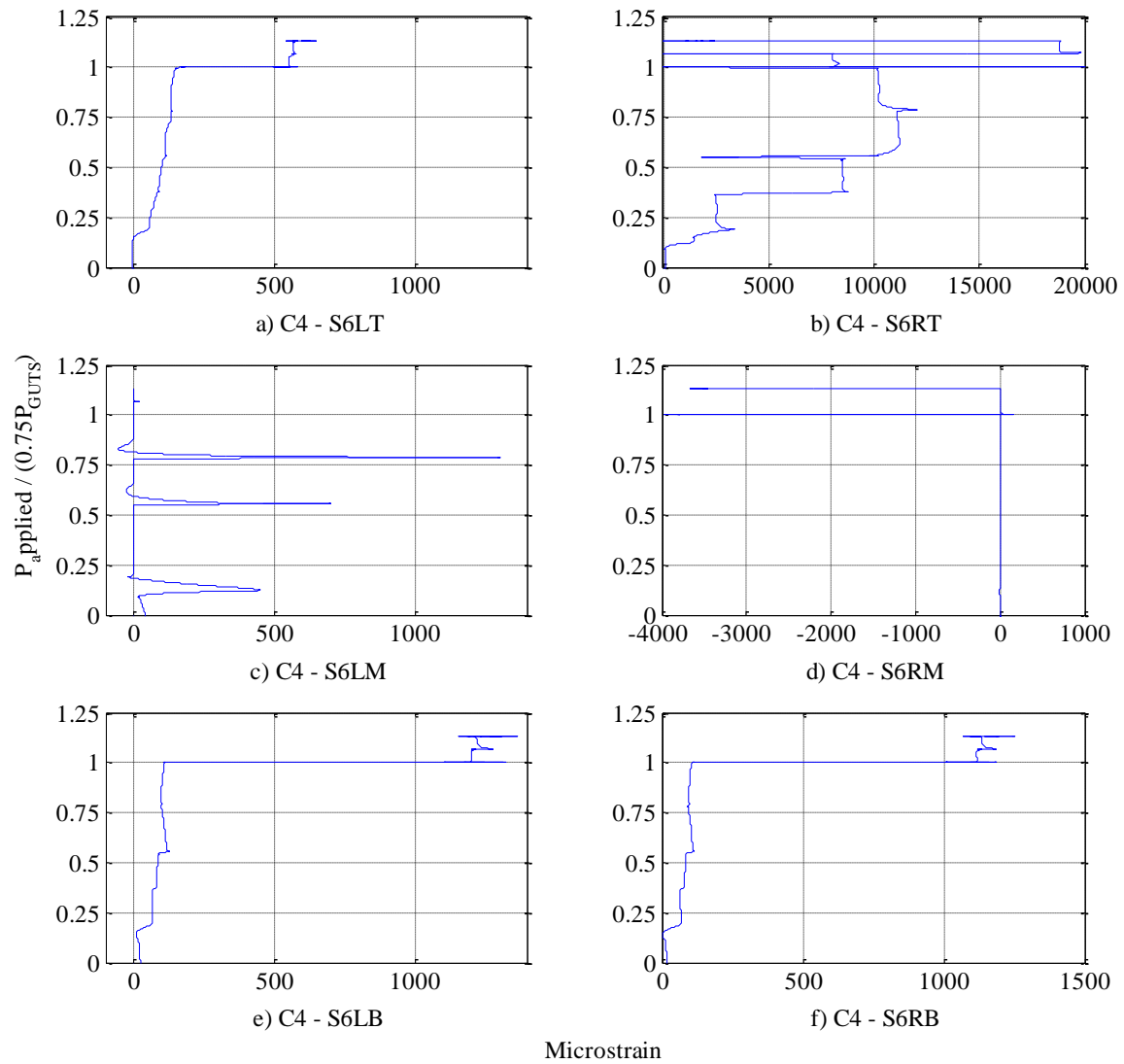


Figure B-5: C4 shear reinforcement.

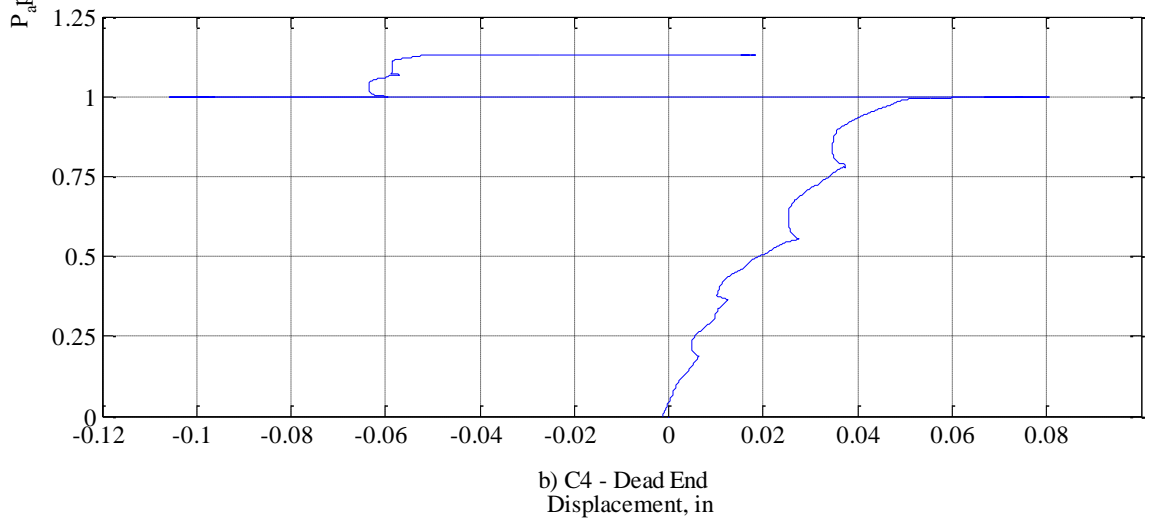
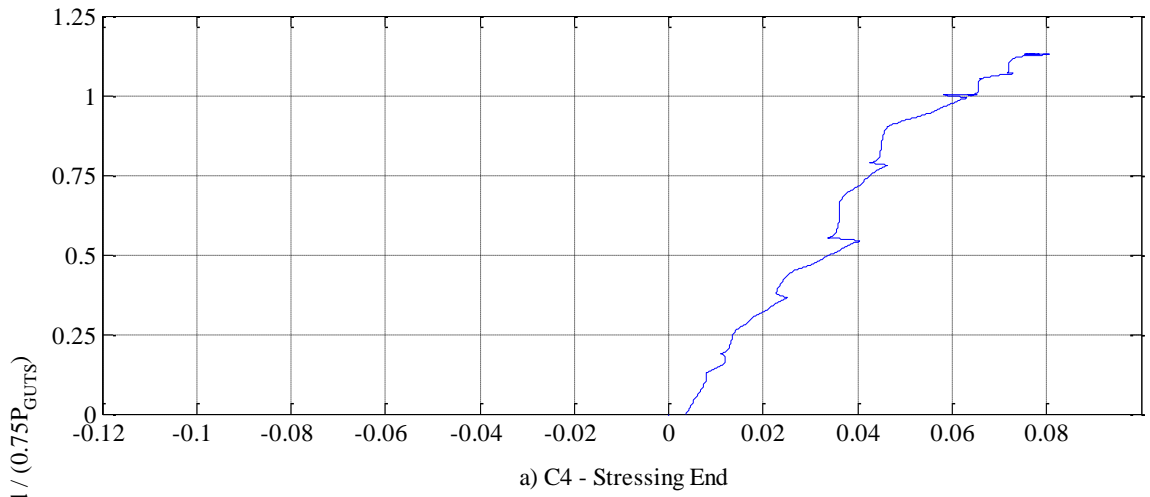


Figure B-6: C4 beam end displacements.

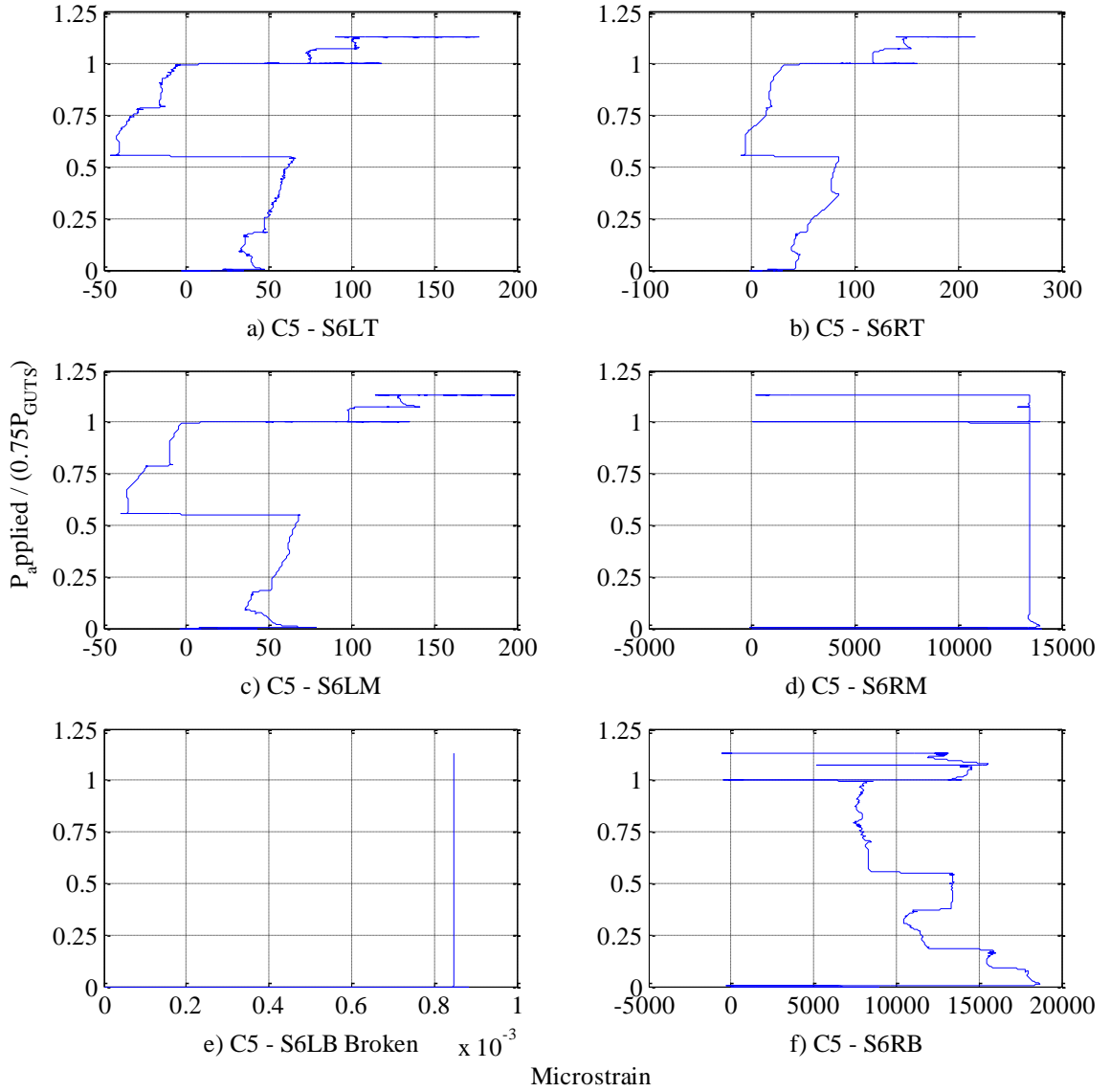


Figure B-7: C5 shear reinforcement.

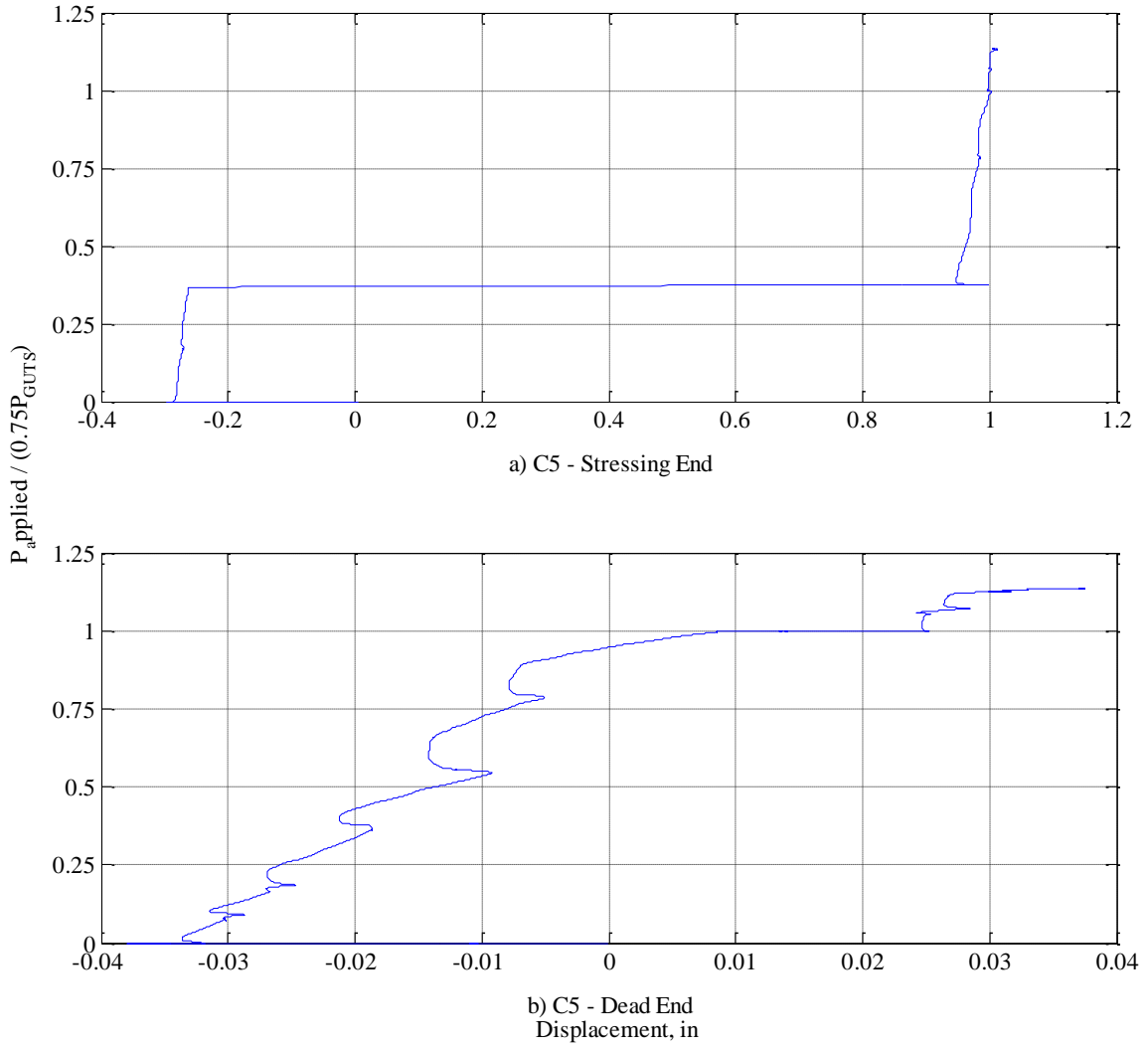


Figure B-8: C5 beam end displacements.

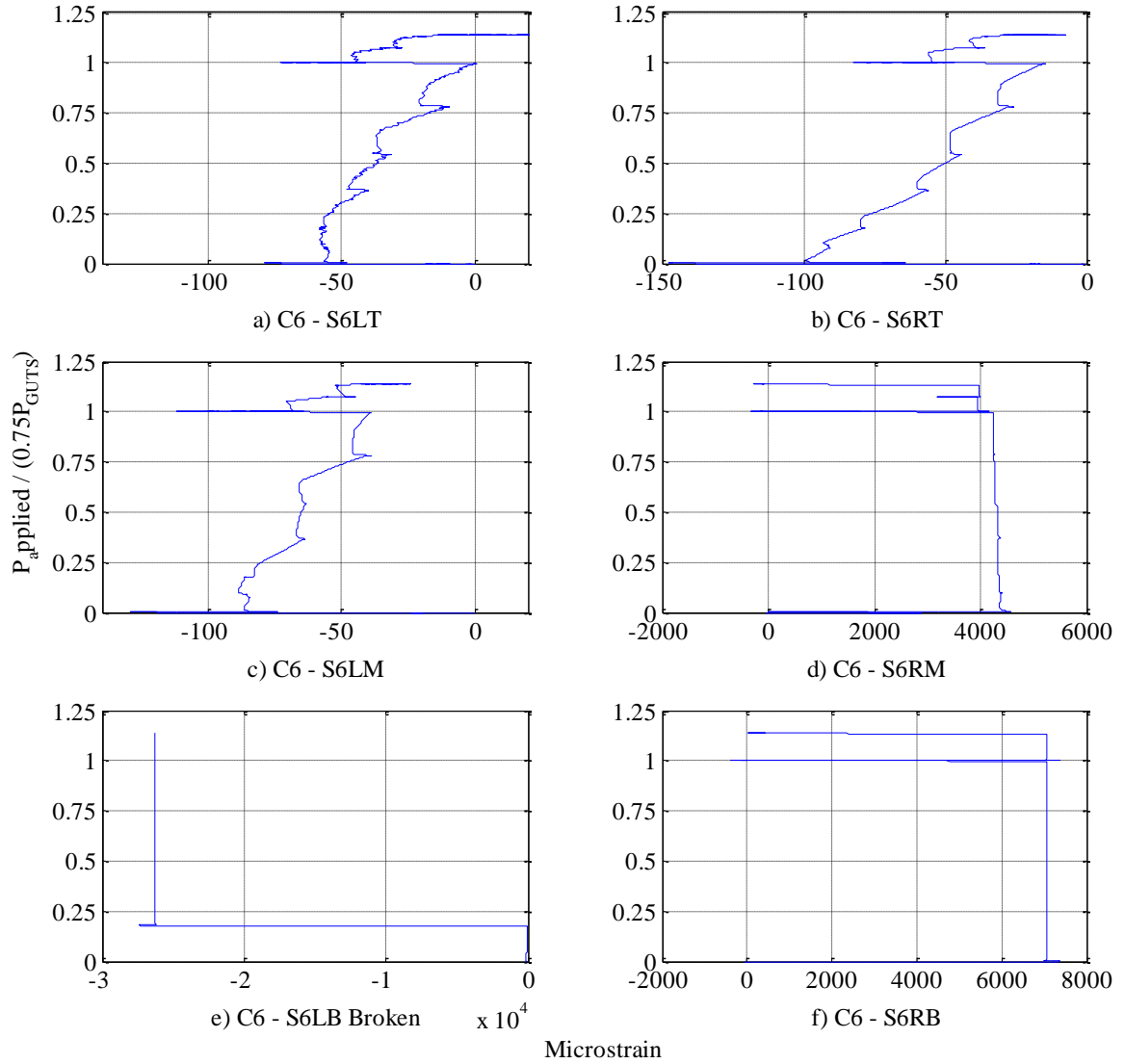


Figure B-9: C6 shear reinforcement.

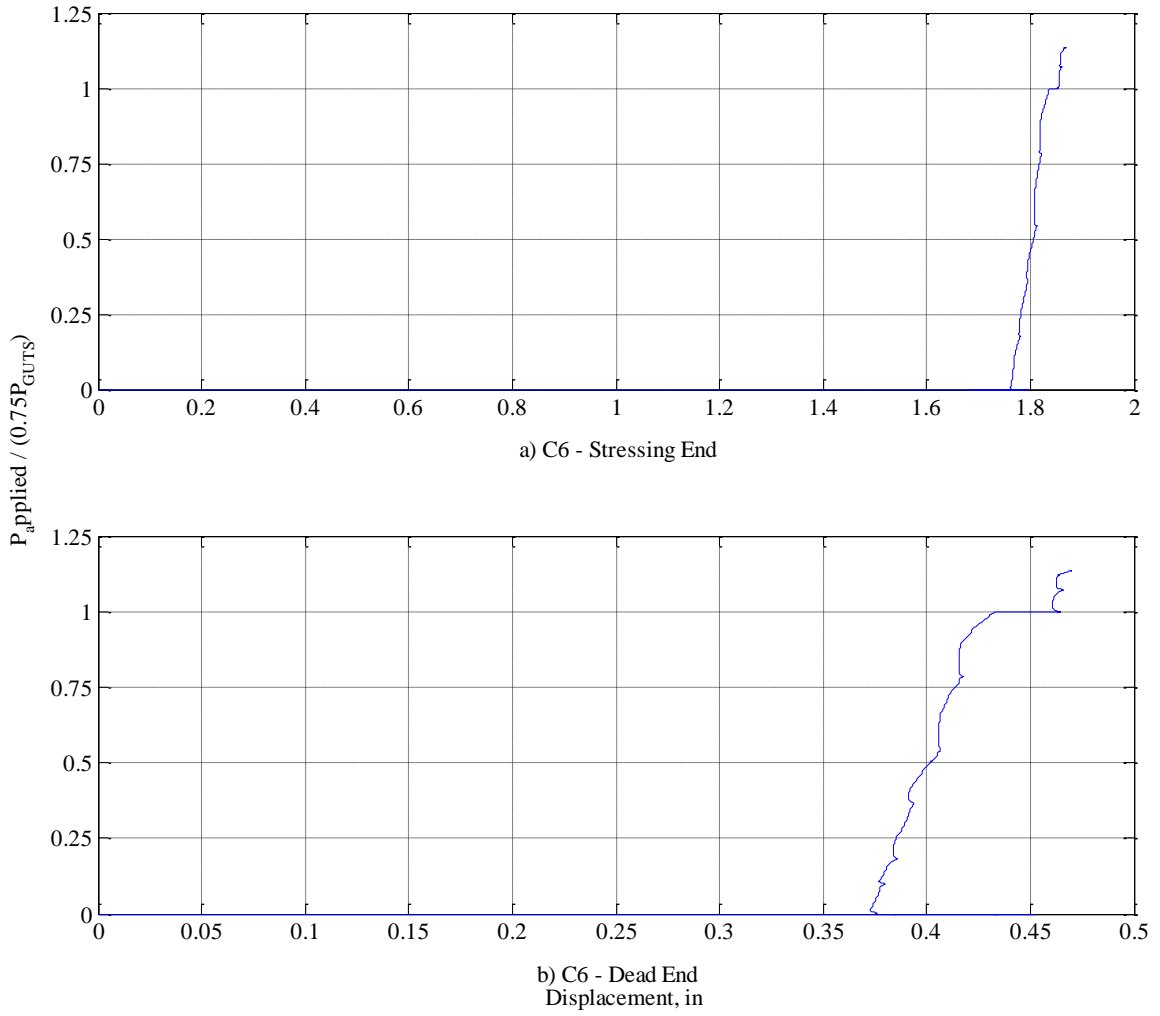


Figure B-10: C6 beam end displacements.

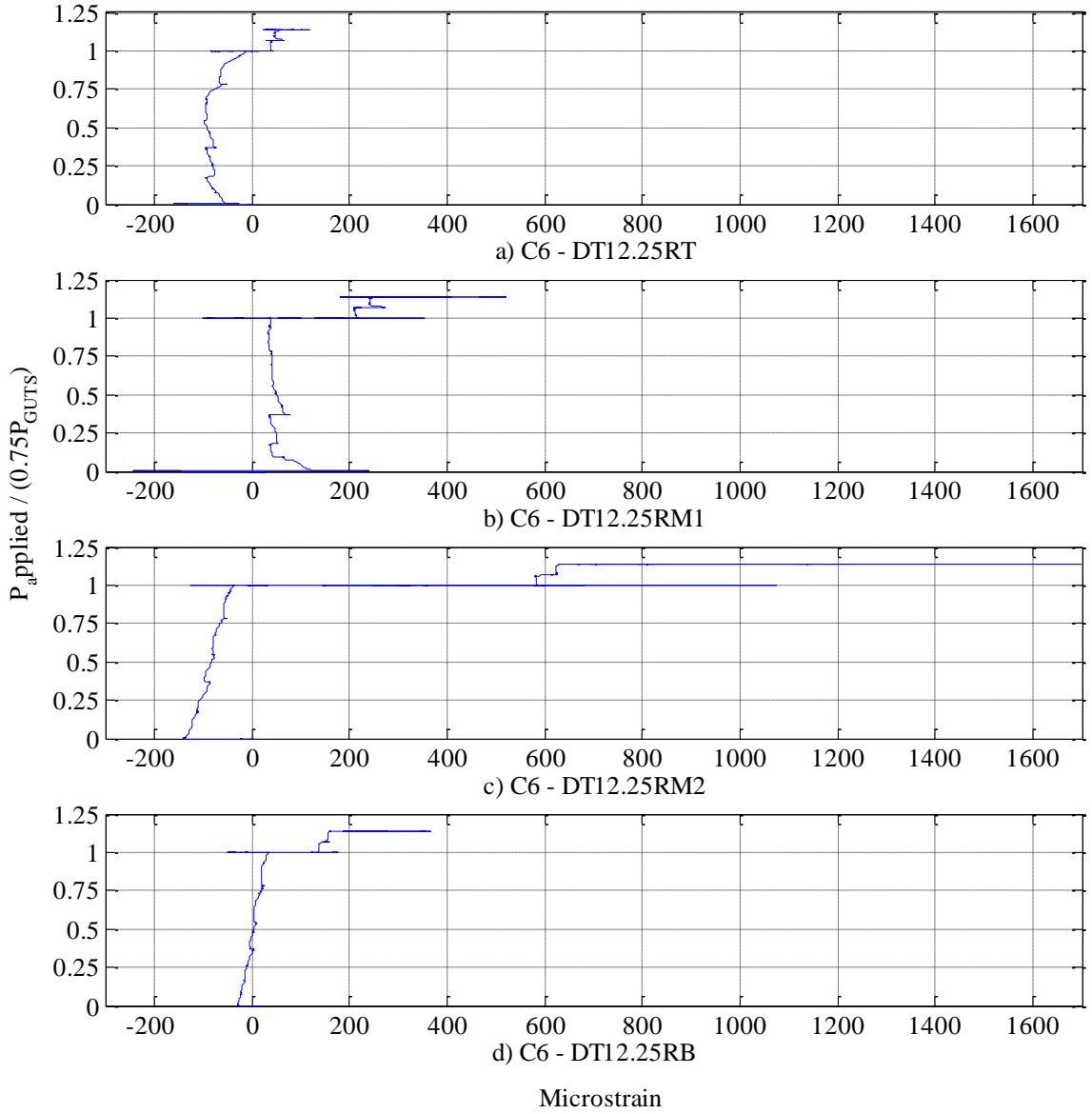


Figure B-11: C6 duct tie reinforcement 12.25" right of centerline.

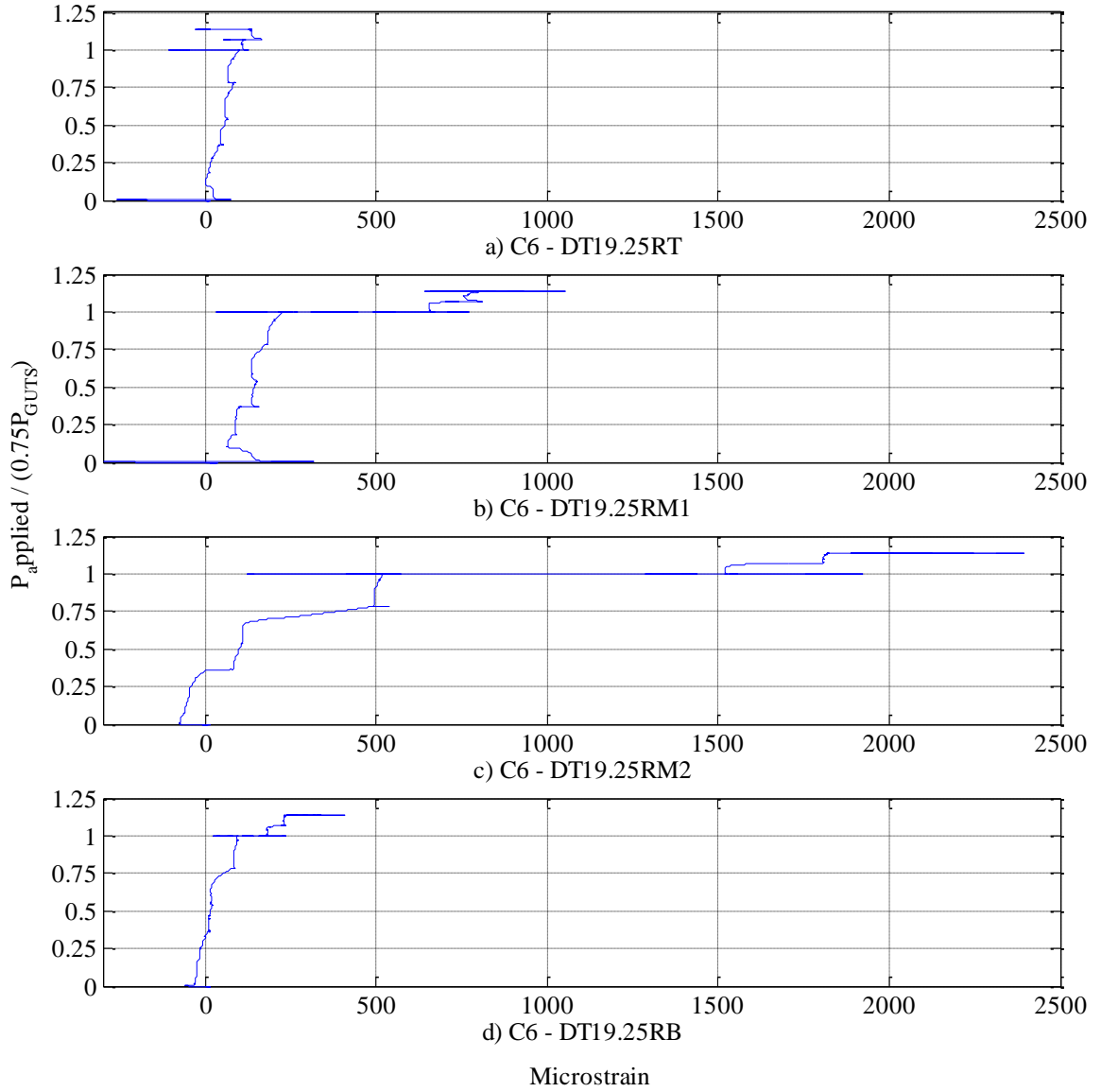


Figure B-12: C6 duct tie reinforcement 19.25" right of centerline.

Appendix C: Atena Results

Table C-1: Load and associated steps in Atena software.

Load	Step
DL	6
0.4B	19
0.80B	31
0.40T	43
0.80T	56
50psiB	66
75psiB	71
100psiB	76
APB off	77
50psiT	87
75psiT	92
100psiT	97
APT off	98

Appendix C - No Artificial Crack

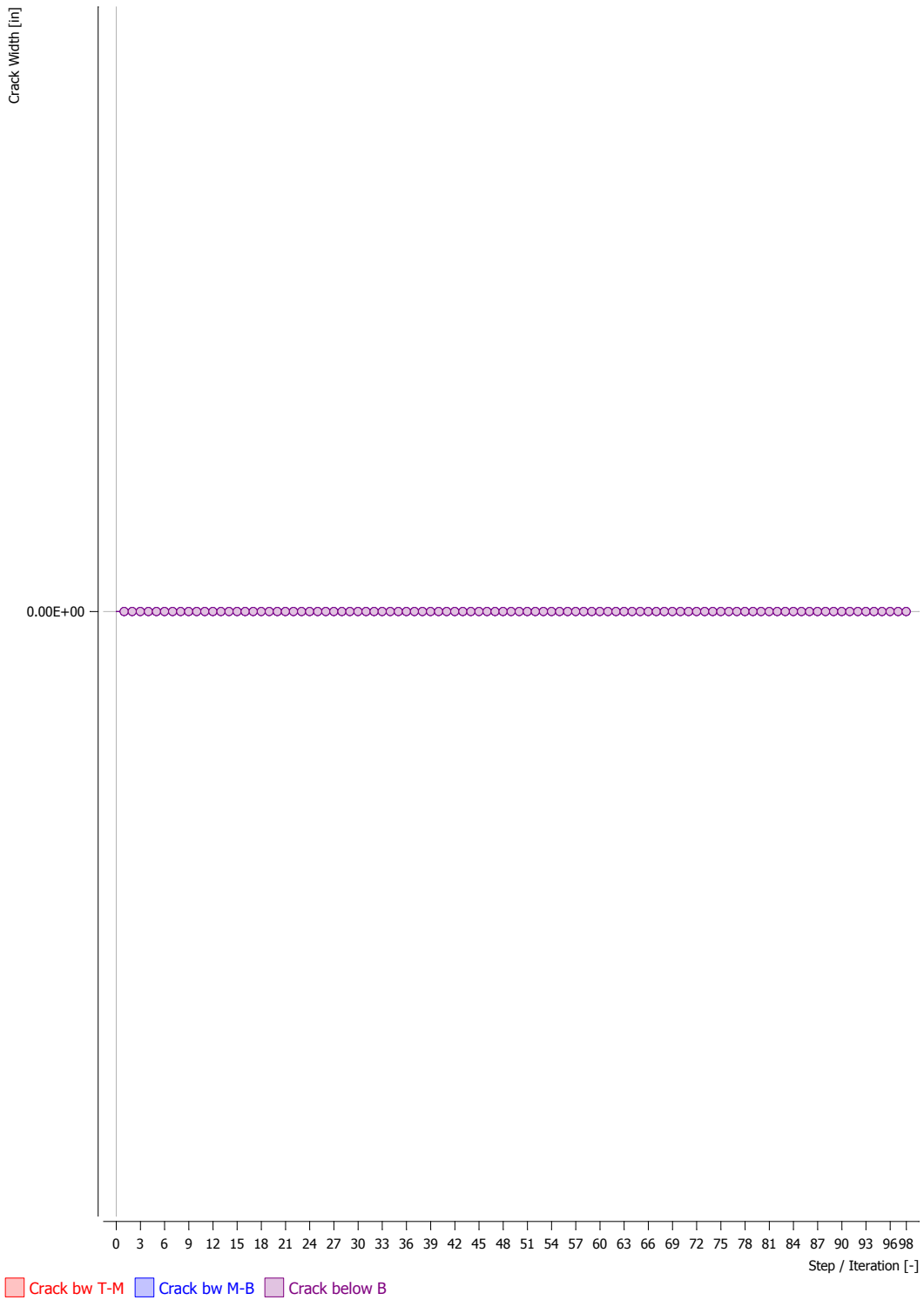


Figure C-1: C1 (11.5 k/ft.) crack width at CL between ducts (no duct ties).

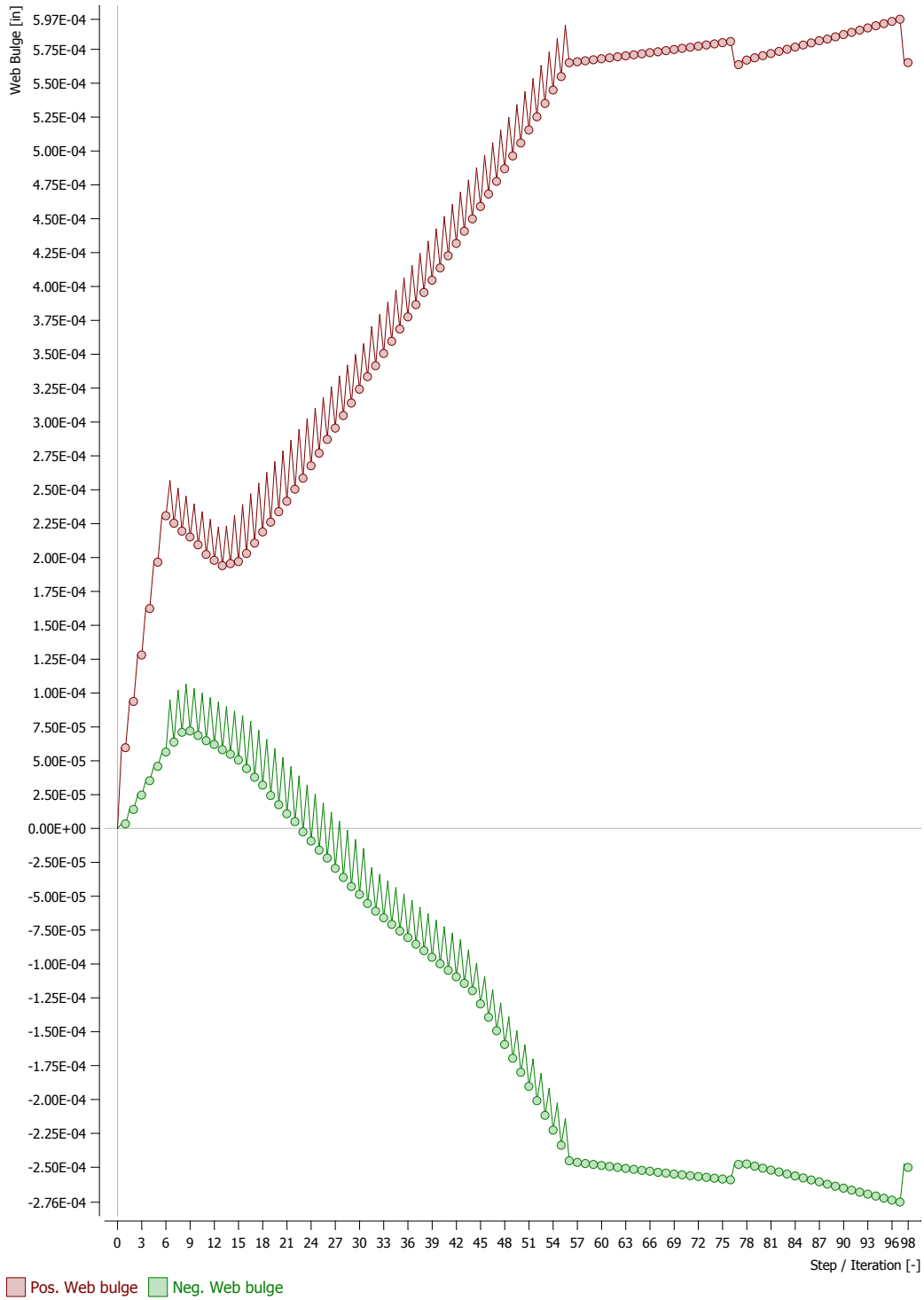


Figure C-2: C1 (11.5 k/ft.) max. web bulge on each face (no duct ties).

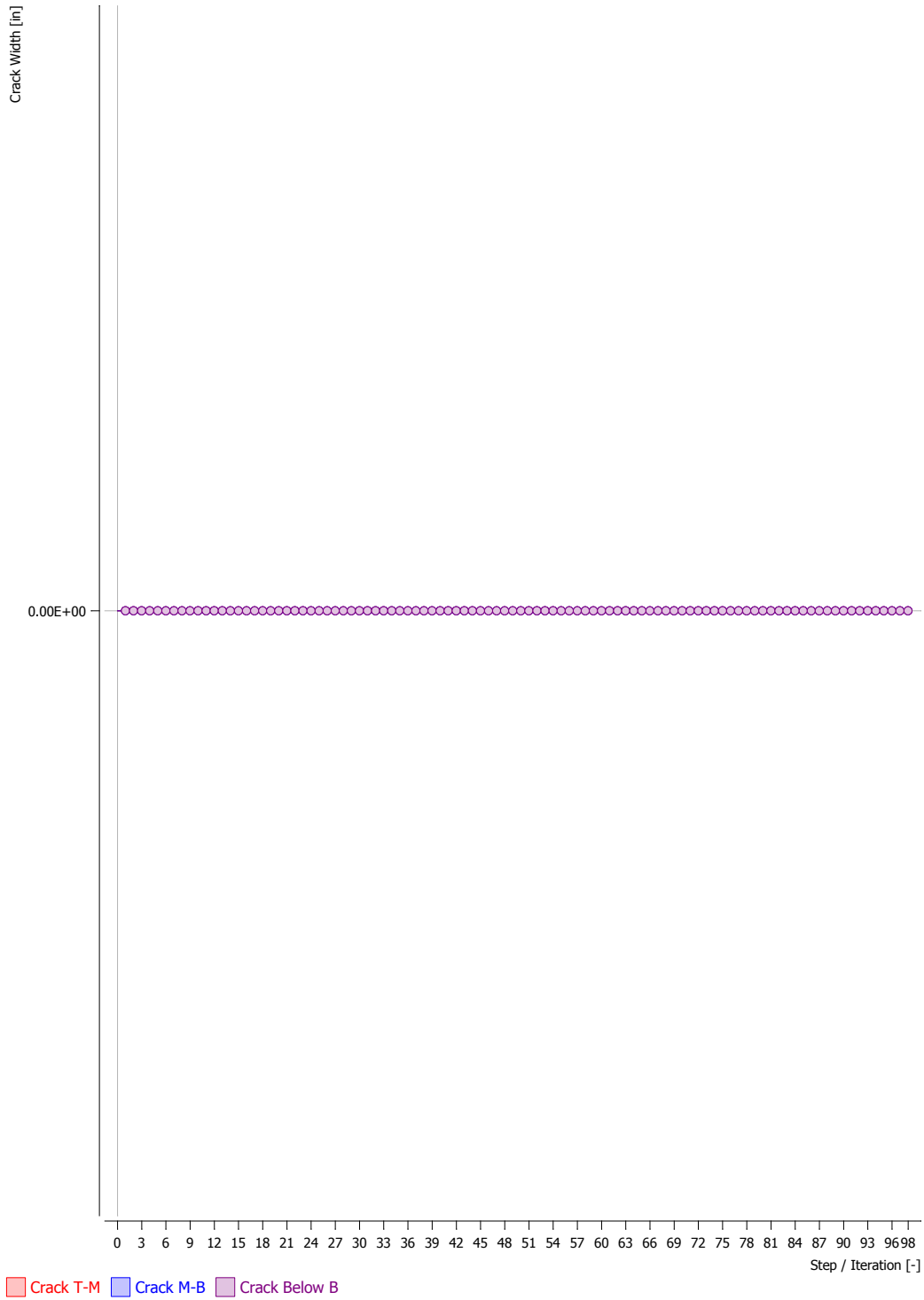


Figure C-3: C1 (11.5 k/ft.) crack width at CL between ducts (1.05" spacing).

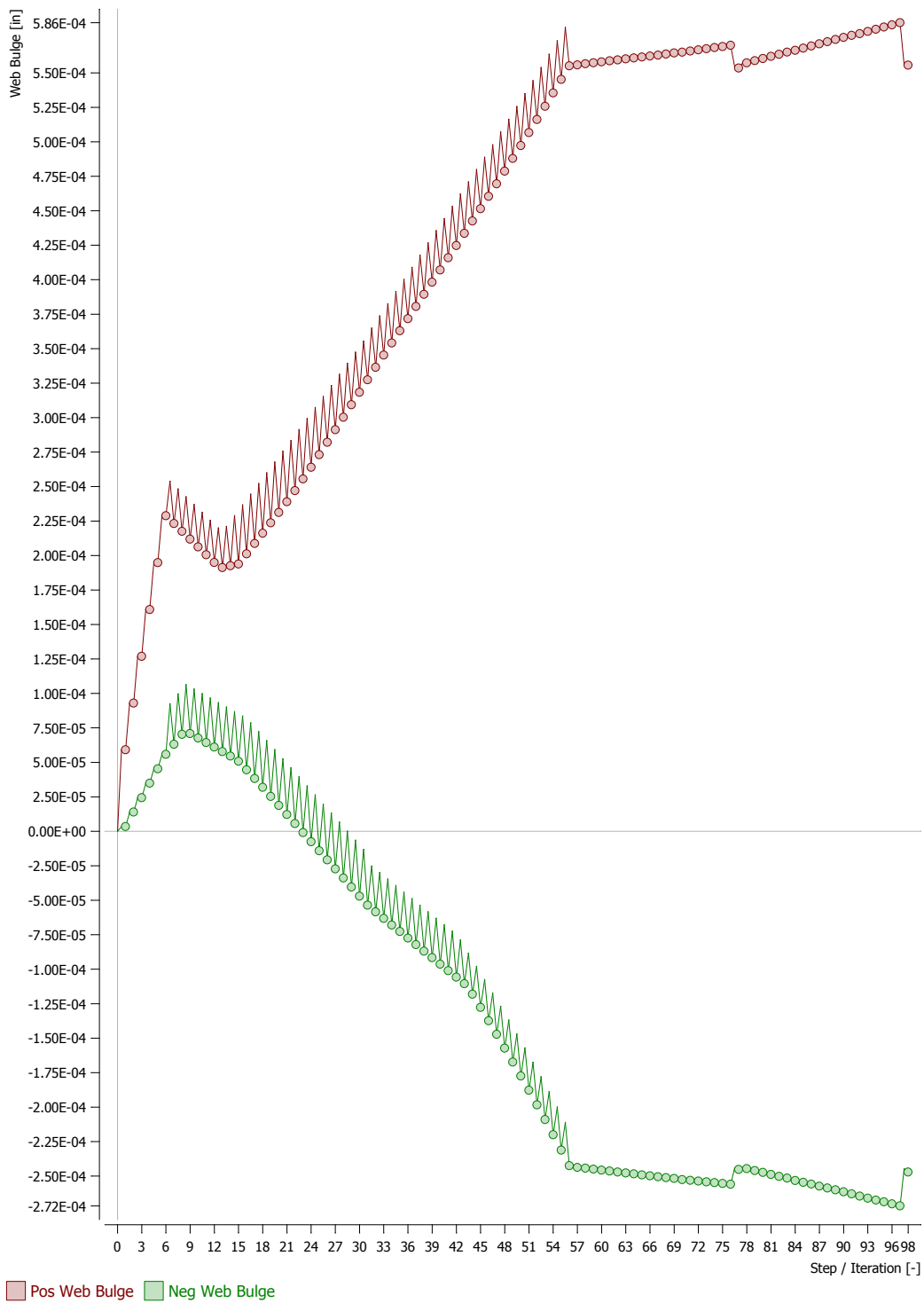


Figure C-4: C1 (11.5 k/ft.) max. web bulge on each face (1.05" spacing).

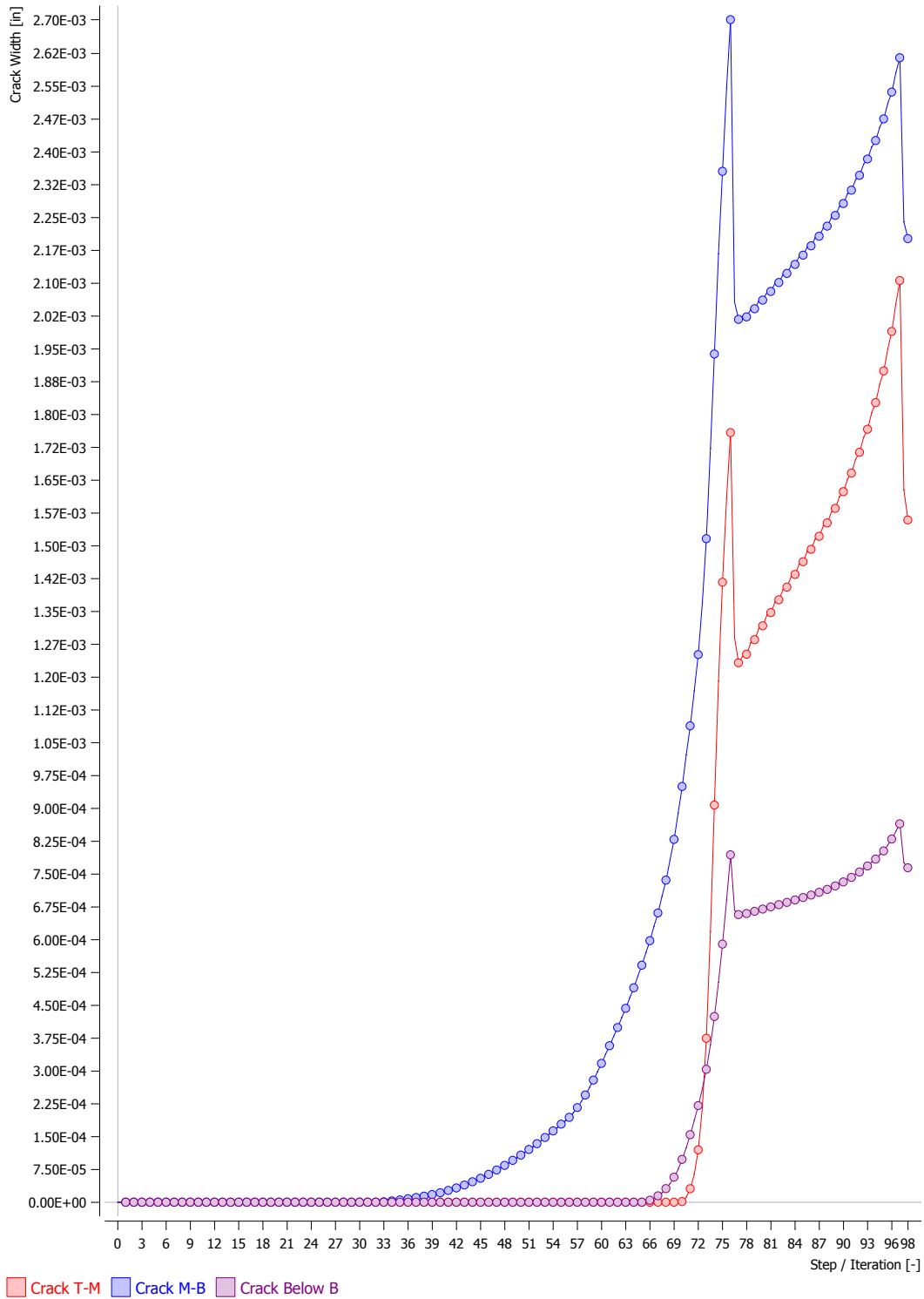


Figure C-5: C2 (19.12 k/ft.) crack width at CL between ducts (no duct ties).

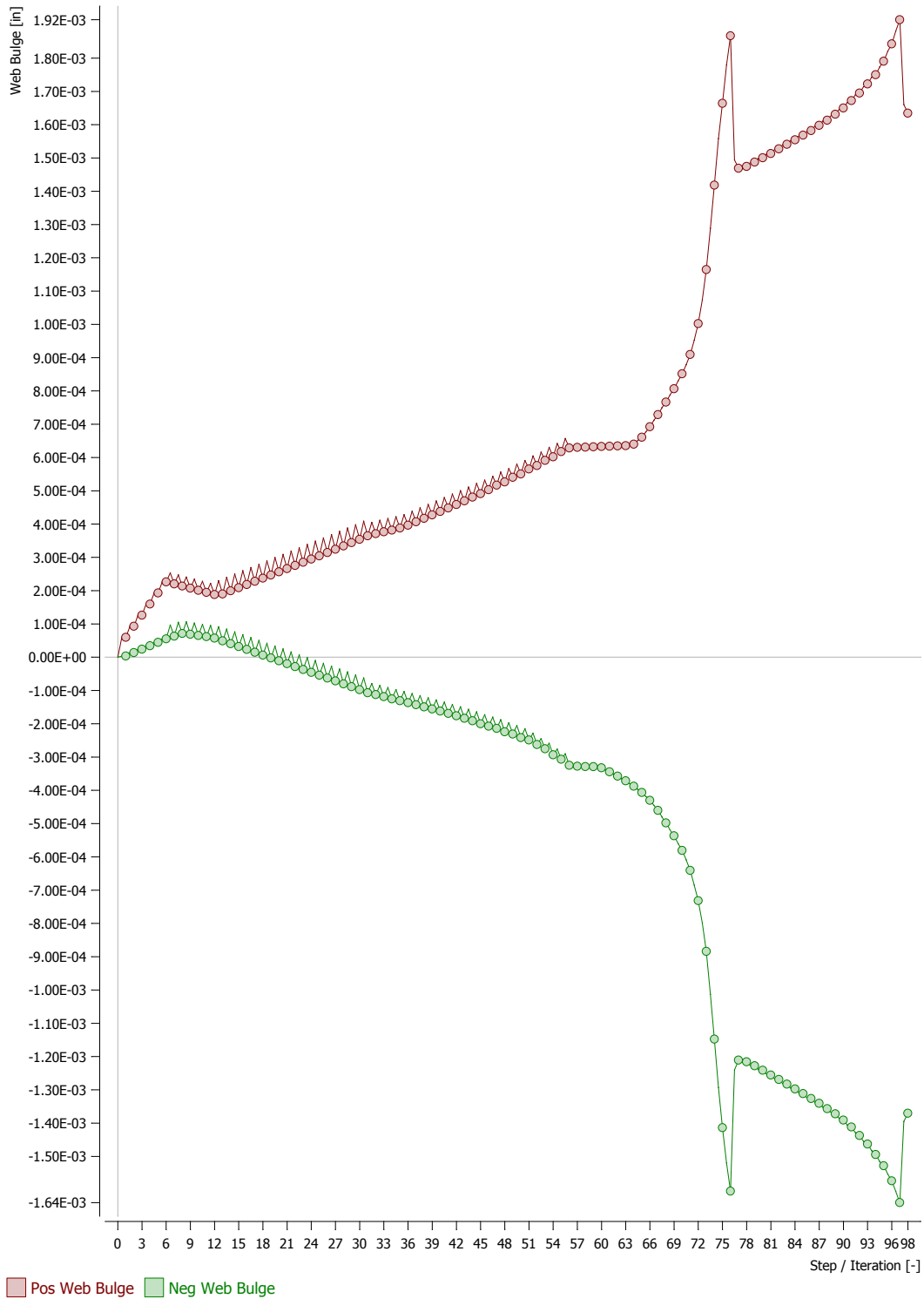


Figure C-6: C2 (19.12 k/ft.) max. web bulge on each face (no duct ties).

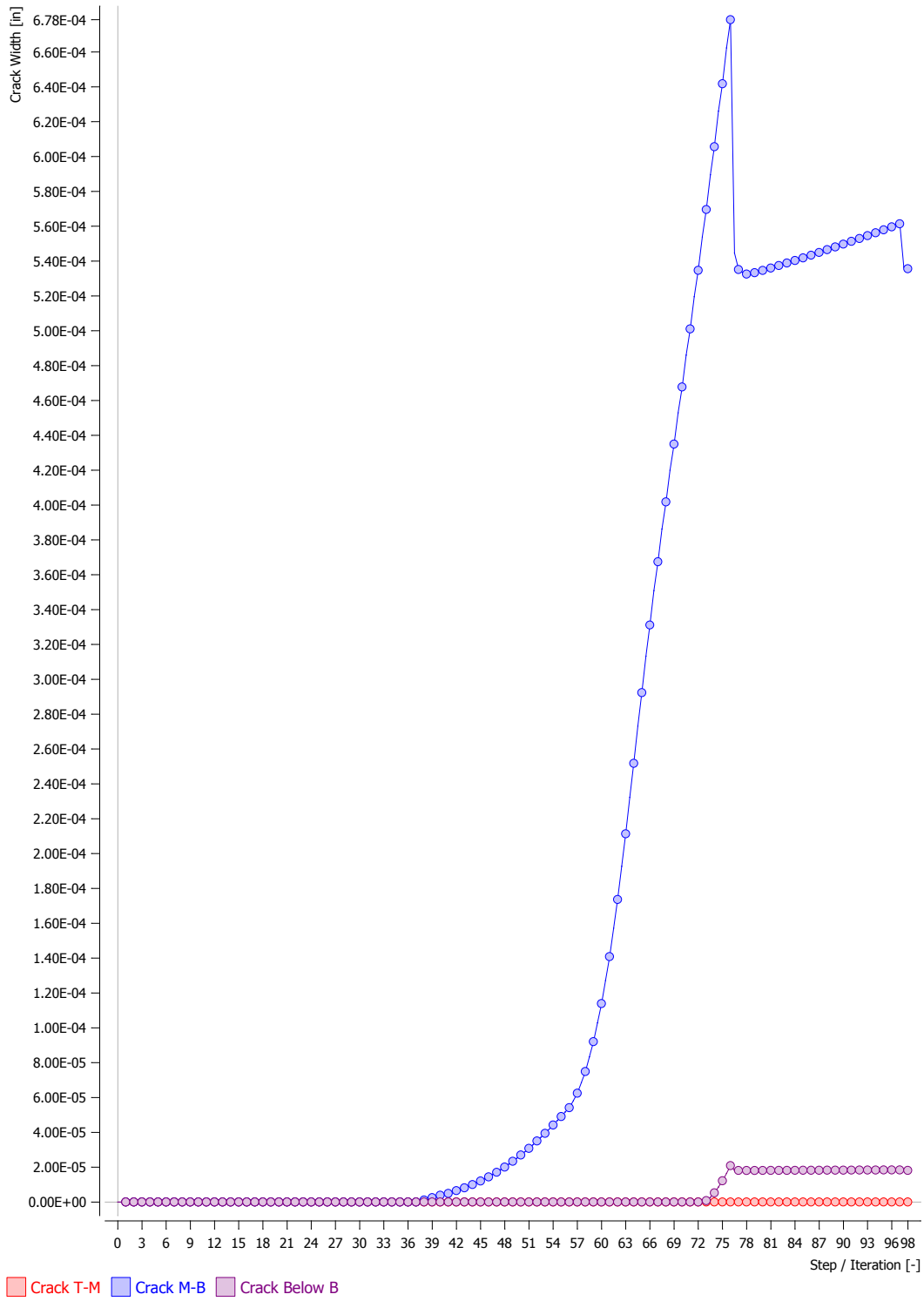


Figure C-7: C2 (19.12 k/ft.) crack width at CL between ducts (1.05" spacing).

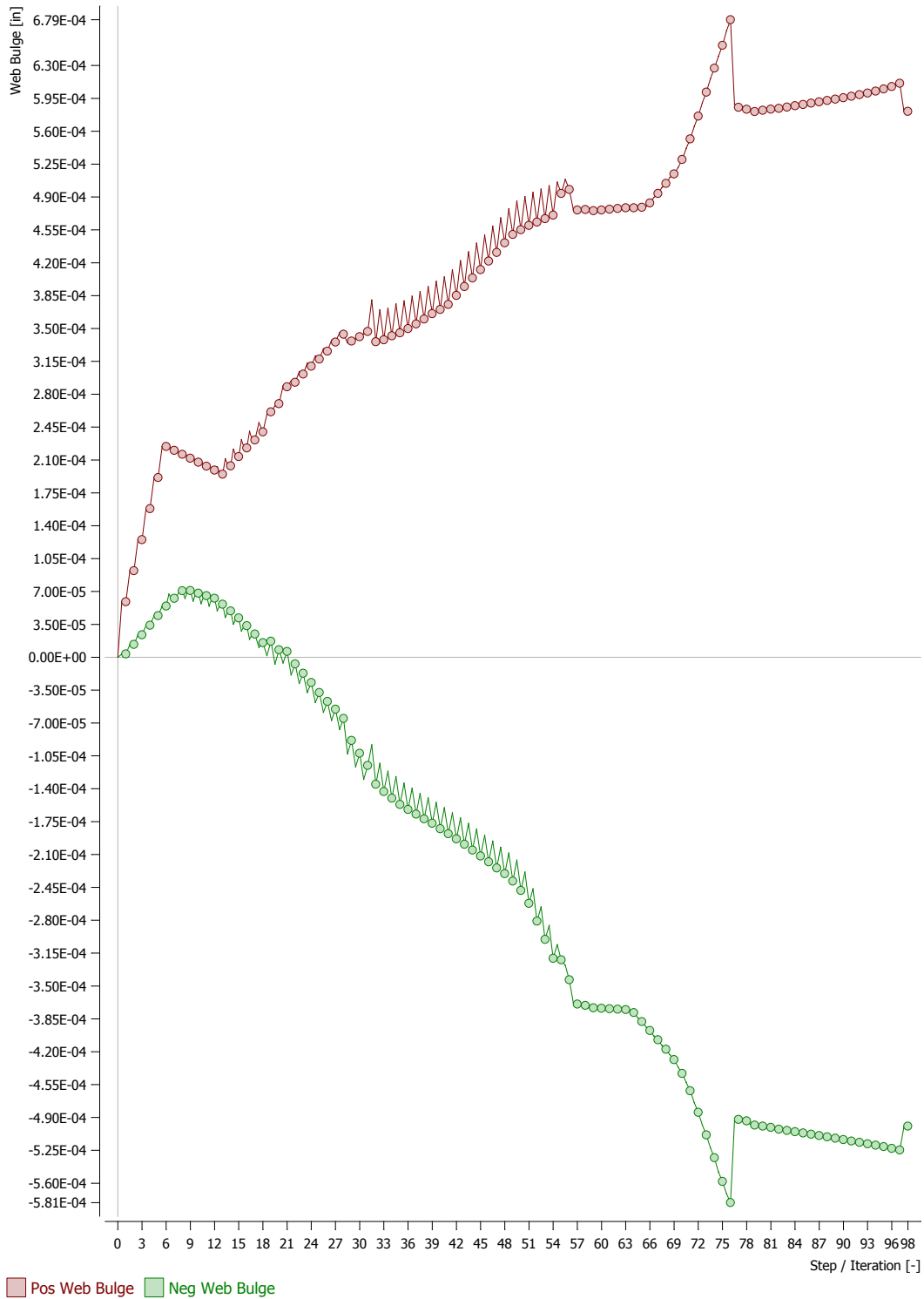


Figure C-8: C2 (19.12 k/ft.) max. web bulge on each face (1.05'' spacing).

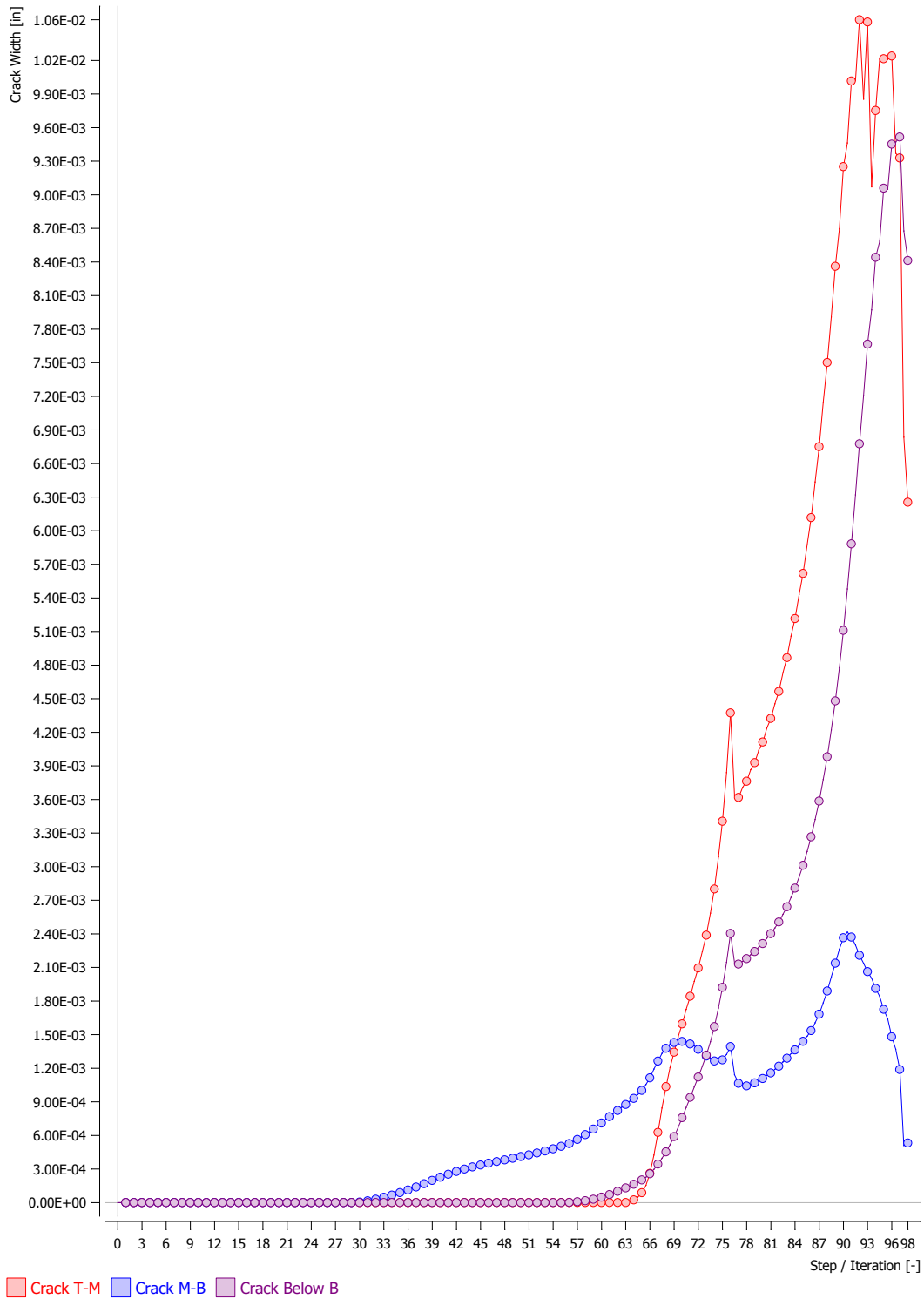


Figure C-9: Avg. C2 & C3 (22.60 k/ft.) crack width at CL (no duct ties).

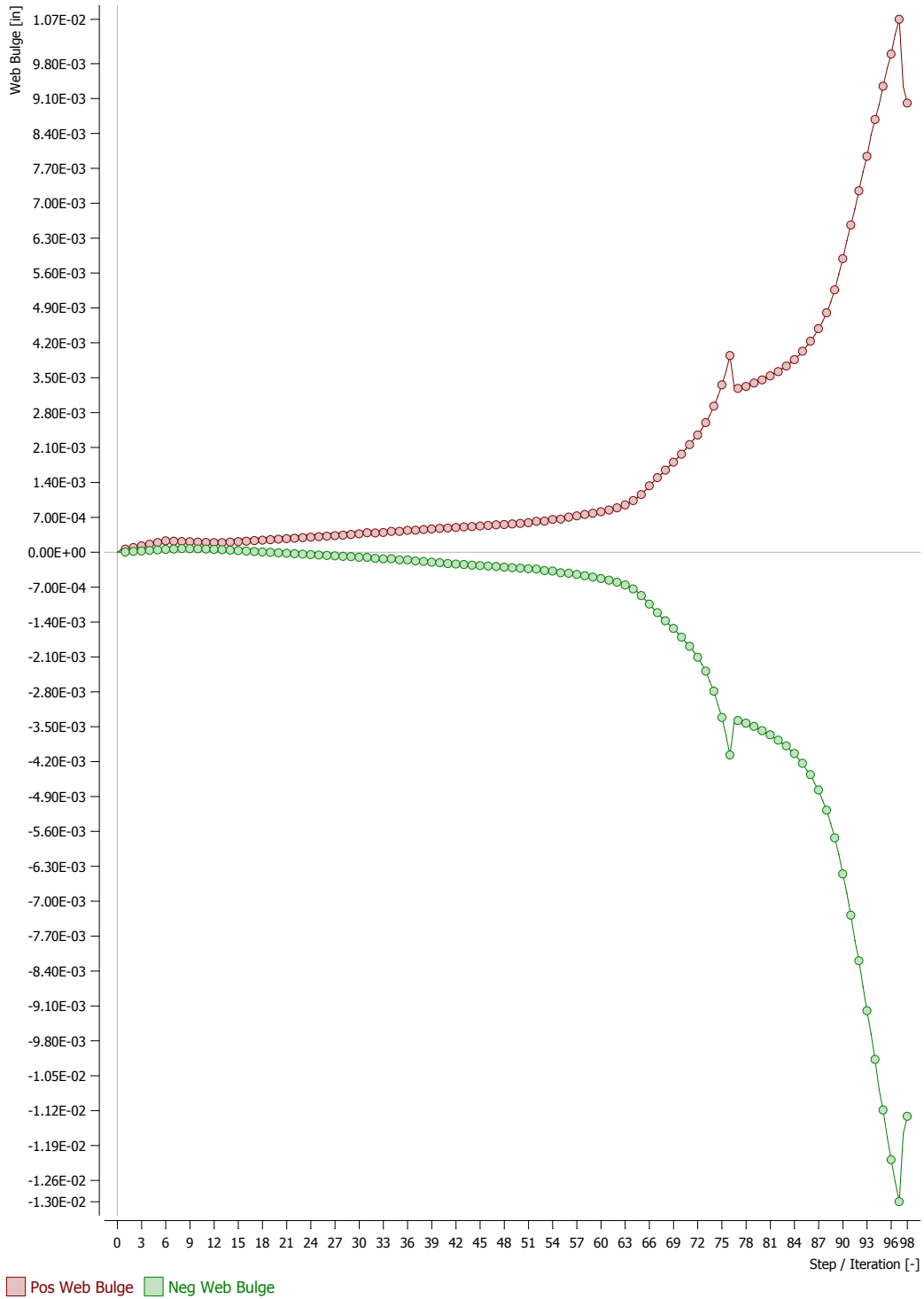


Figure C-10: Avg. C2 & C3 (22.60 k/ft.) max. web bulge (no duct ties).

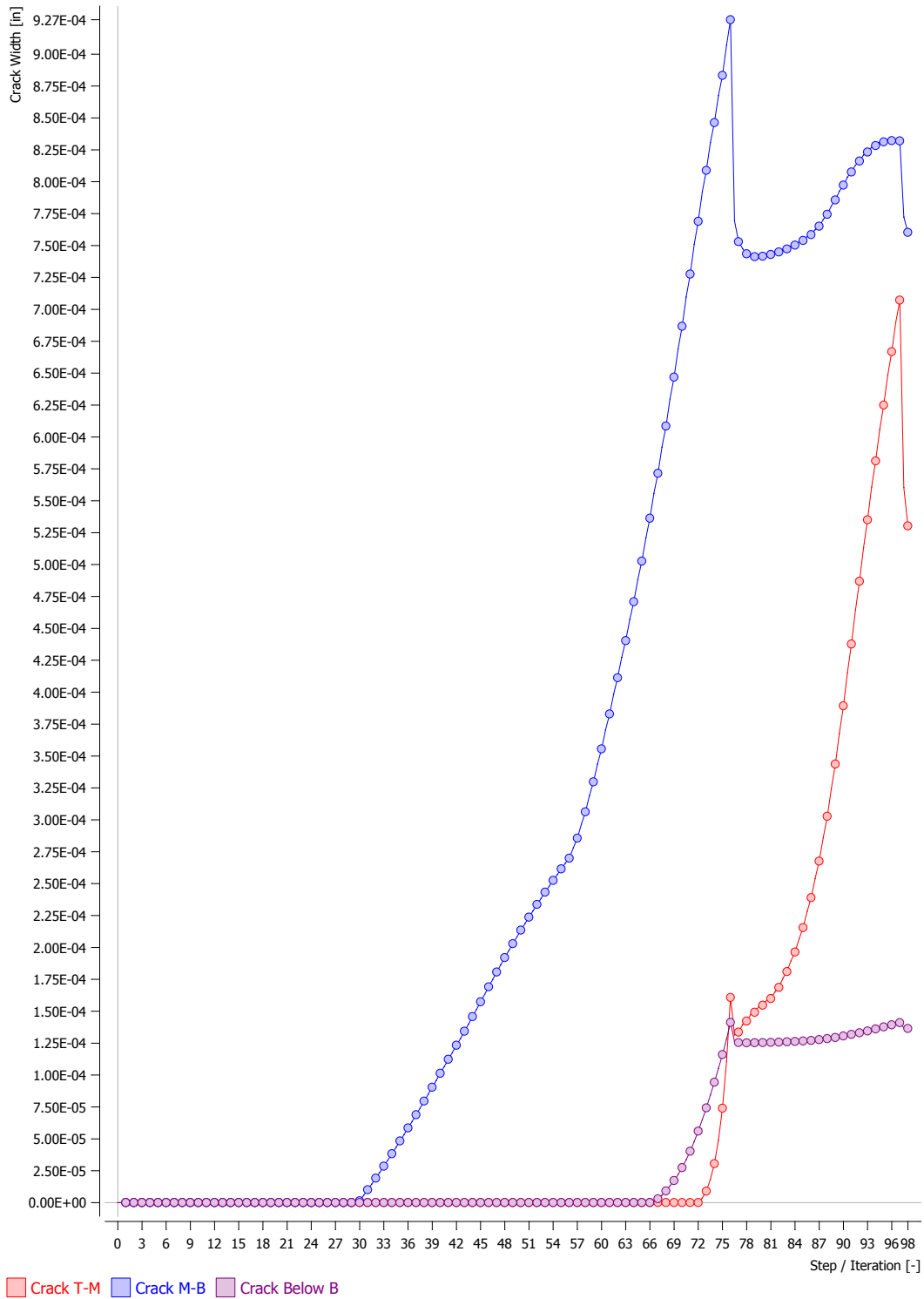


Figure C-11: Avg. C2 & C3 (22.60 k/ft.) crack width at CL (1.05" spacing).

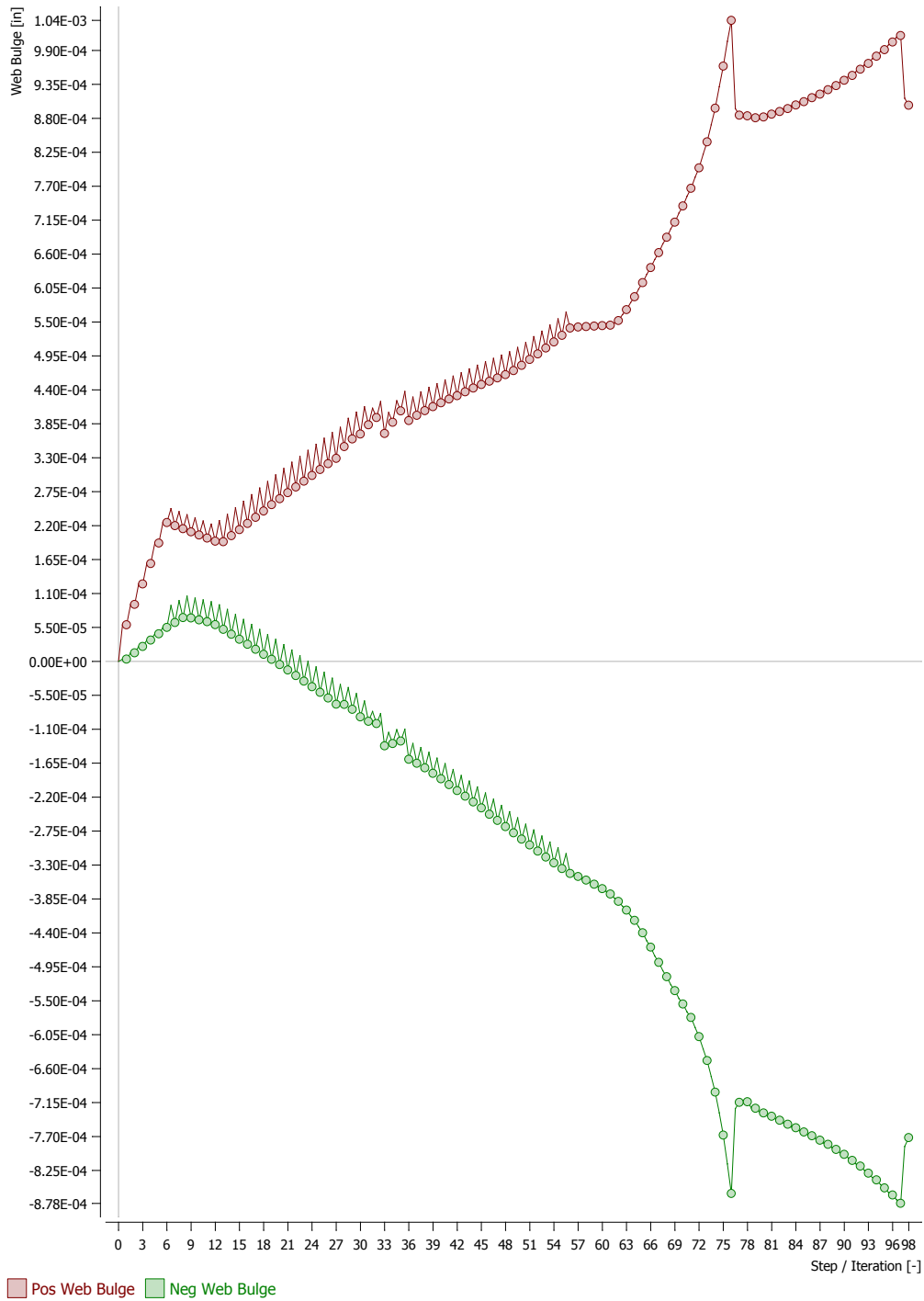


Figure C-12: Avg. of C2 & C3 (22.60 k/ft.) max. web bulge (1.05" spacing).

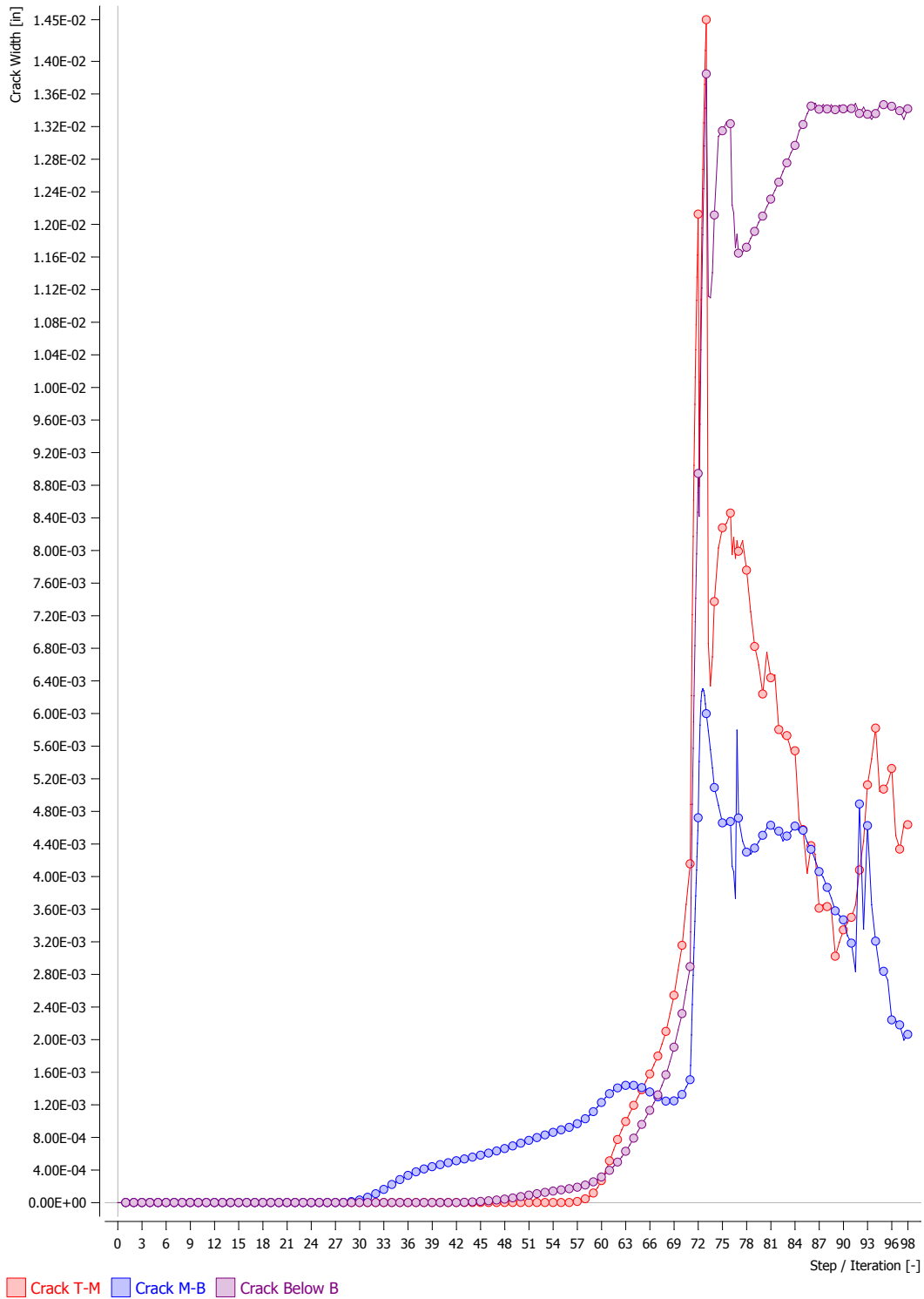


Figure C-13: C3 (26.10 k/ft.) crack width at CL between ducts (no duct ties).

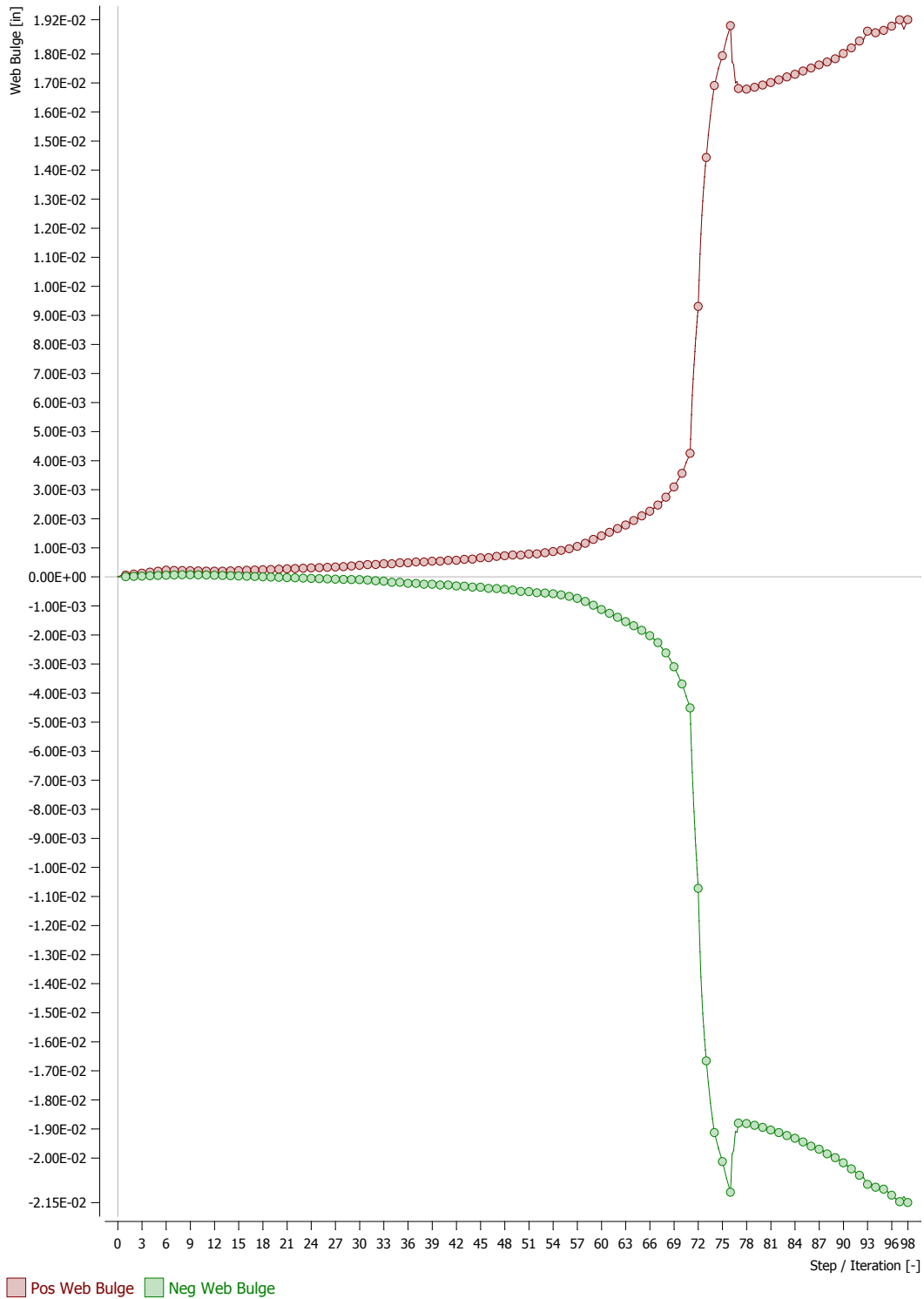


Figure C-14: C3 (26.10 k/ft.) max. web bulge on each face (no duct ties).

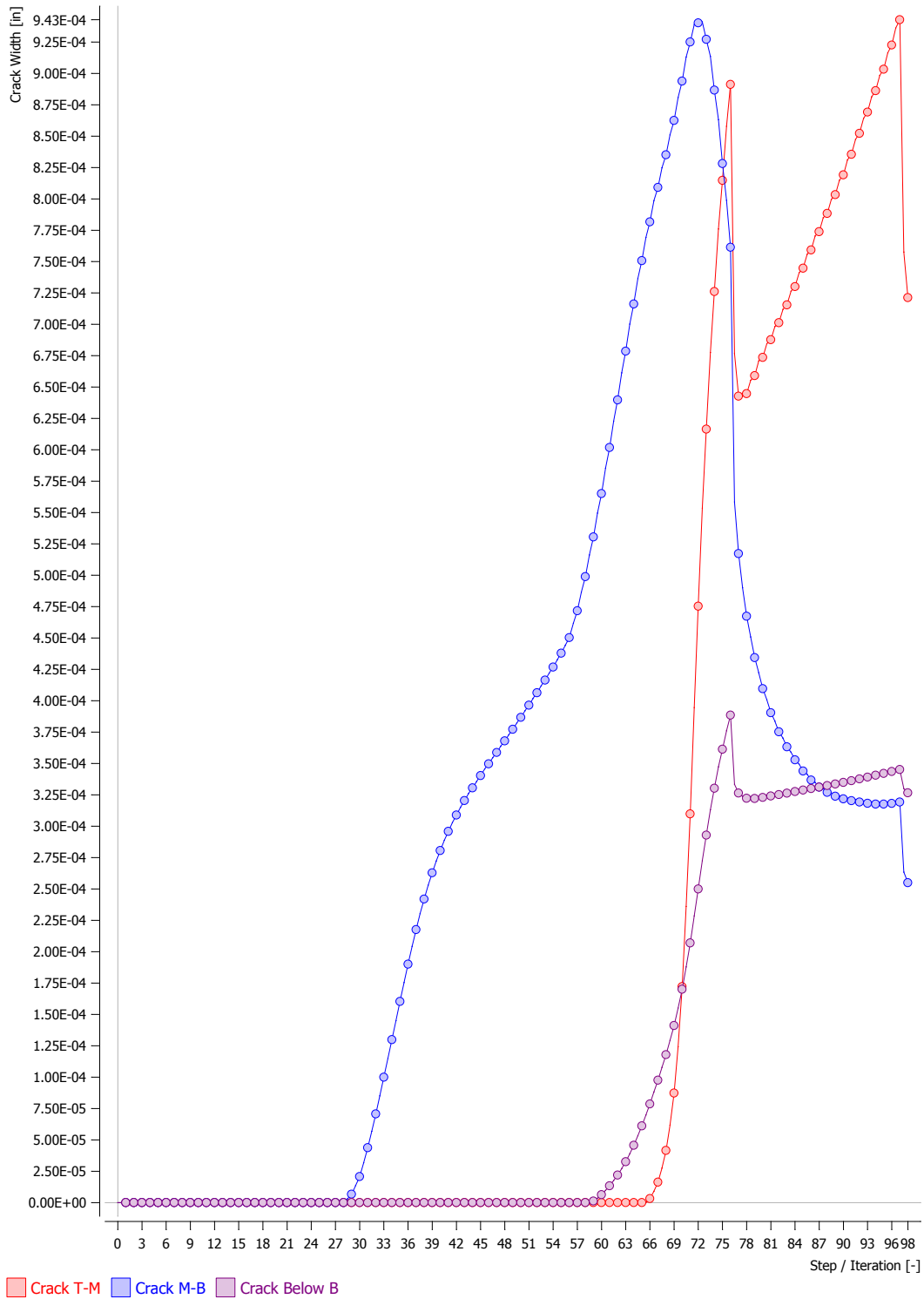


Figure C-15: C3 (26.10 k/ft.) crack width at CL between ducts (1.05" spacing).

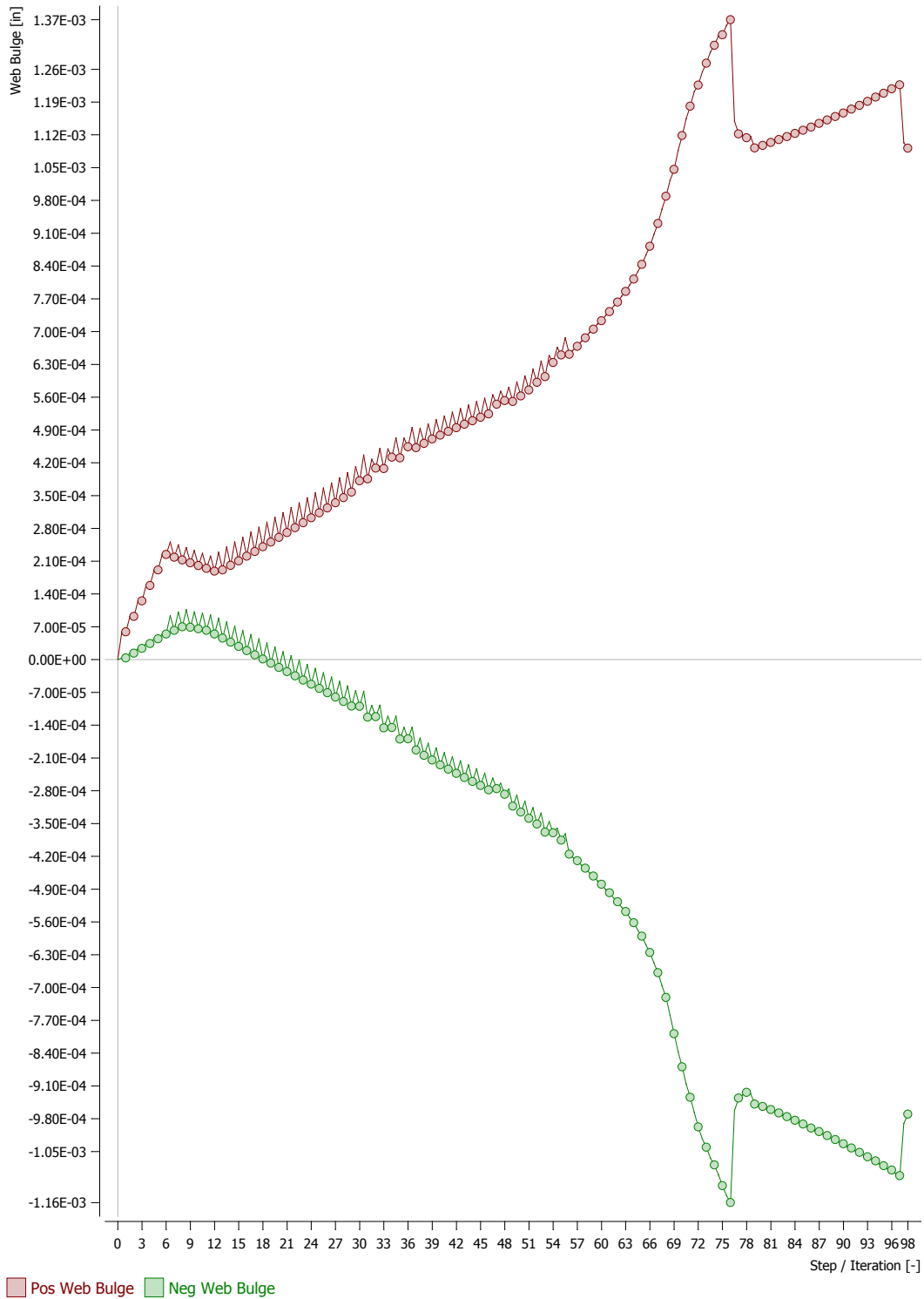


Figure C-16: C3 (26.10 k/ft.) max. web bulge on each face (1.05'' spacing).

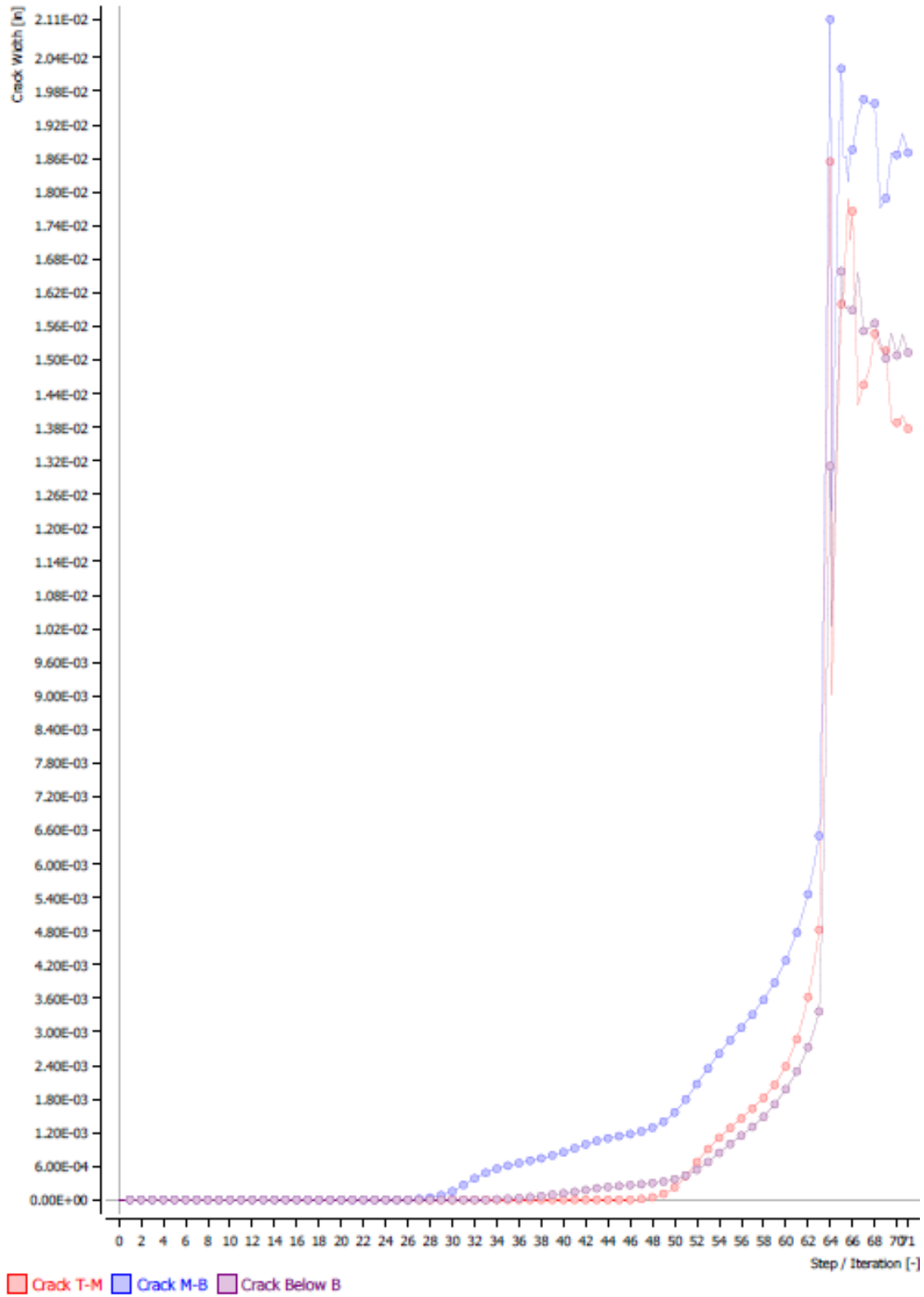


Figure C-17: C3+ (29.7 k/ft.) crack at CL between ducts (no duct ties).

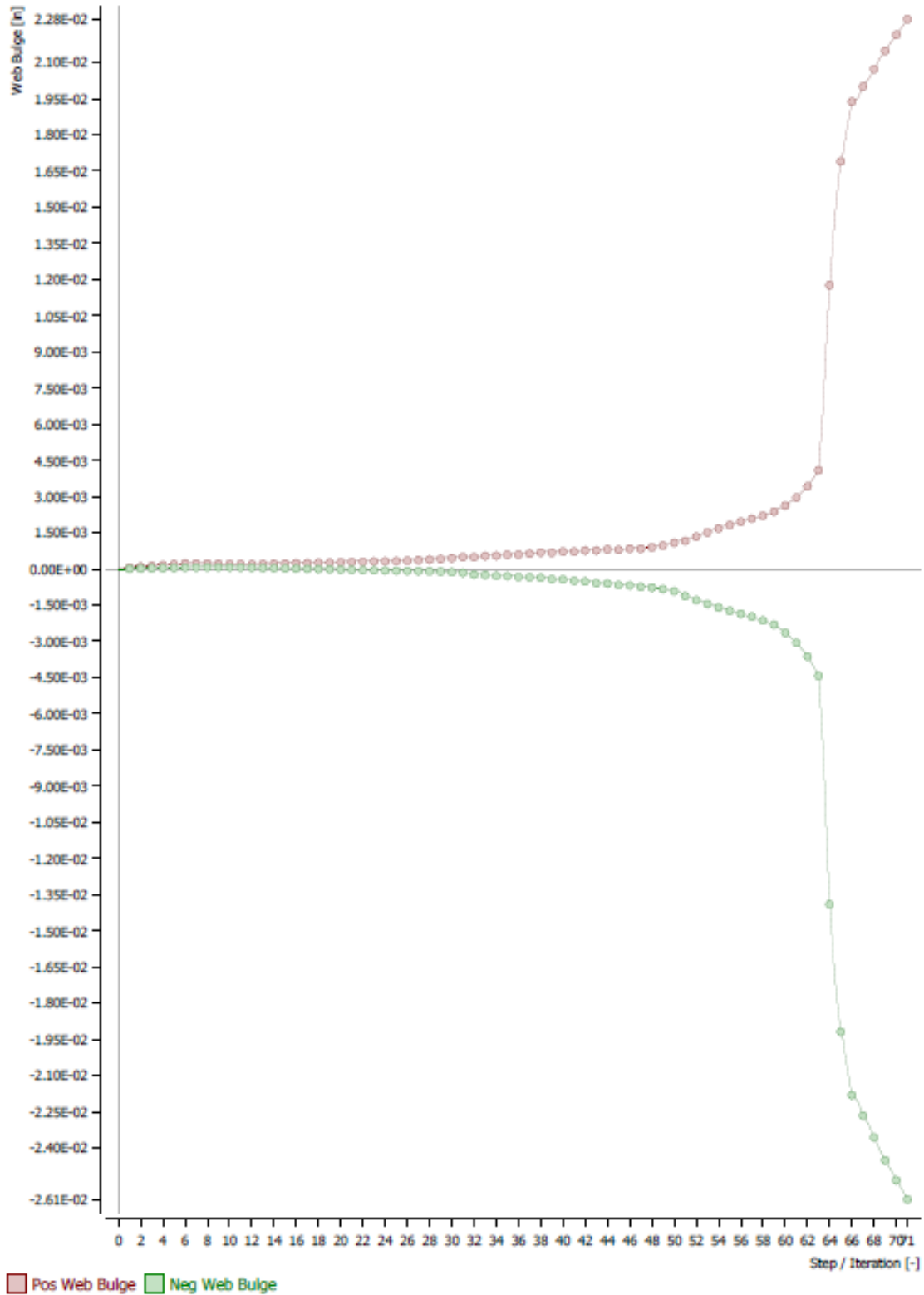


Figure C-18: C3+ (29.7 k/ft.) max. web bulge on each face (no duct ties).

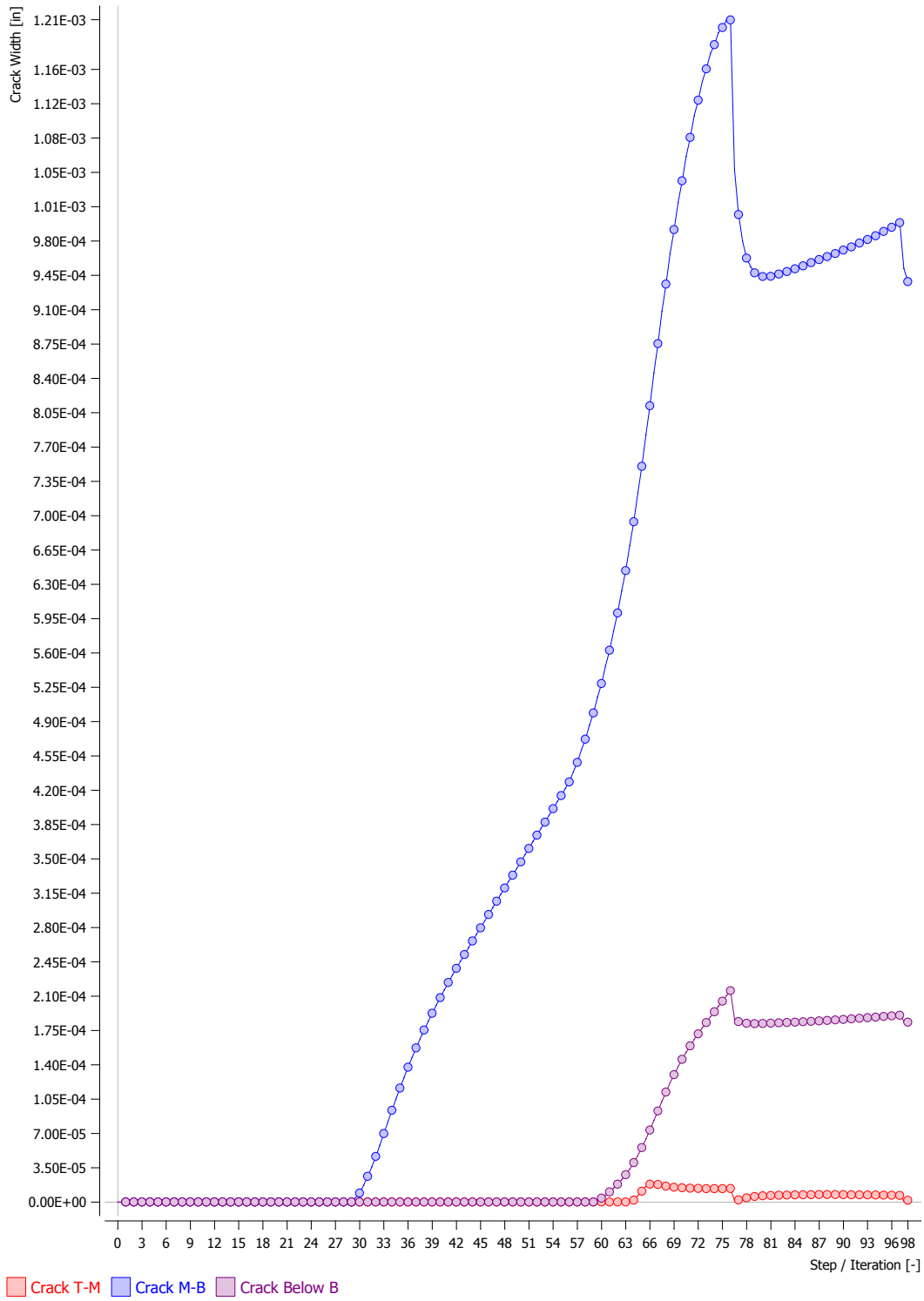


Figure C-19: C3+ (29.7 k/ft.) crack width at CL between the ducts (1.05" spacing).

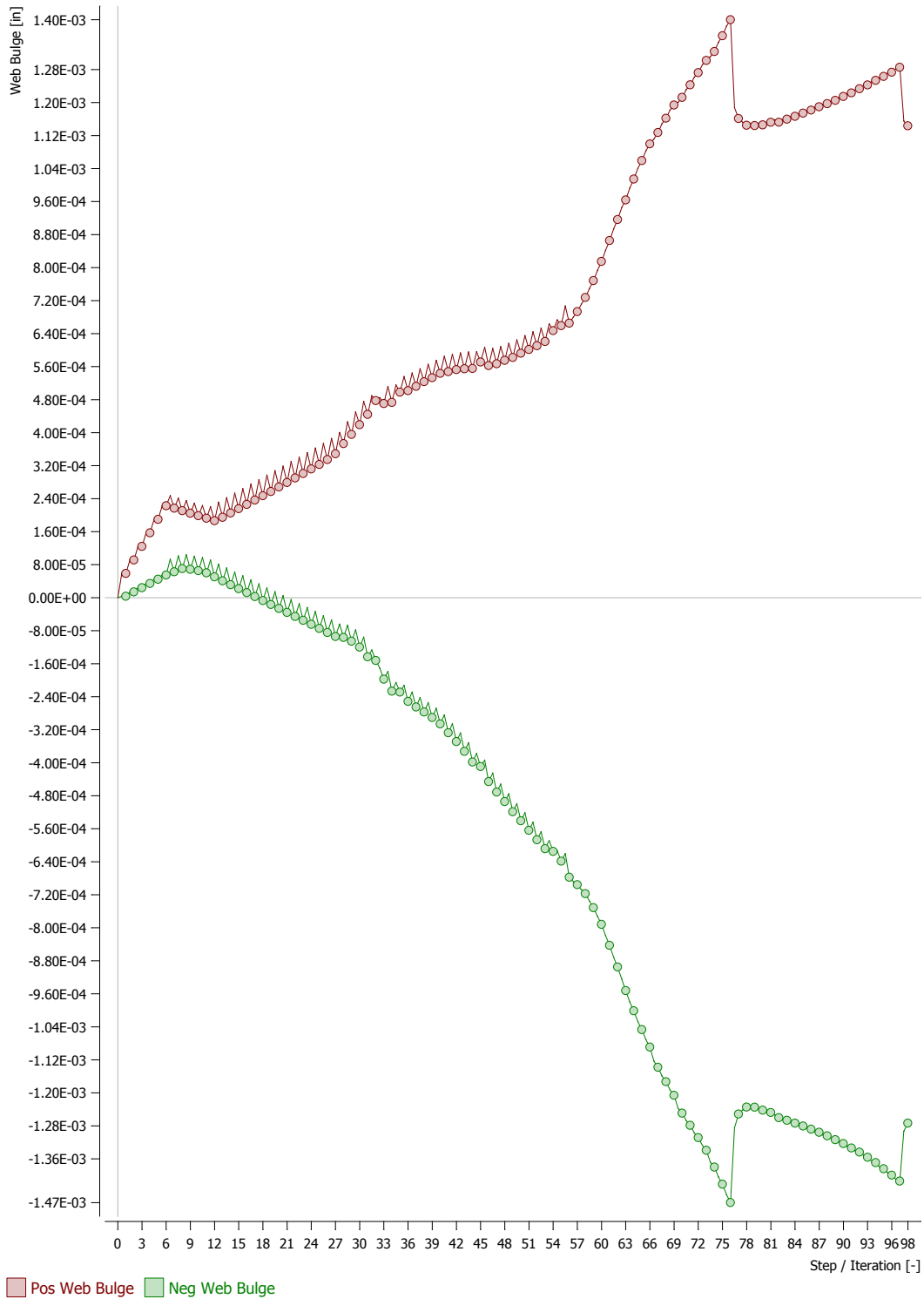


Figure C-20: C3+ (29.7 k/ft.) max. web bulge on each face (1.05" spacing).

Appendix C - Artificial Cracks

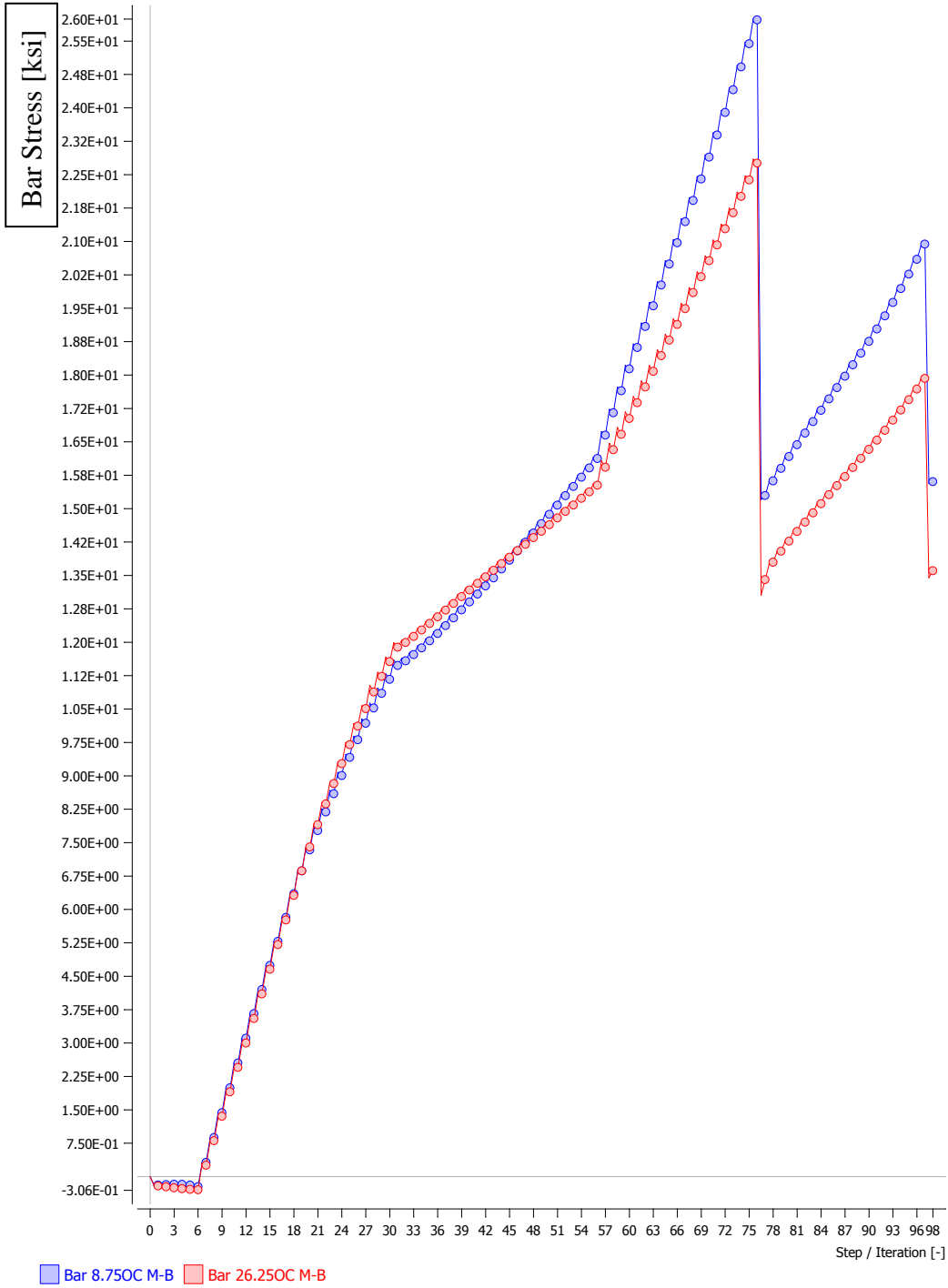


Figure C-21: C1 (11.5 k/ft.) AC bar stress MB (17.5" spacing).

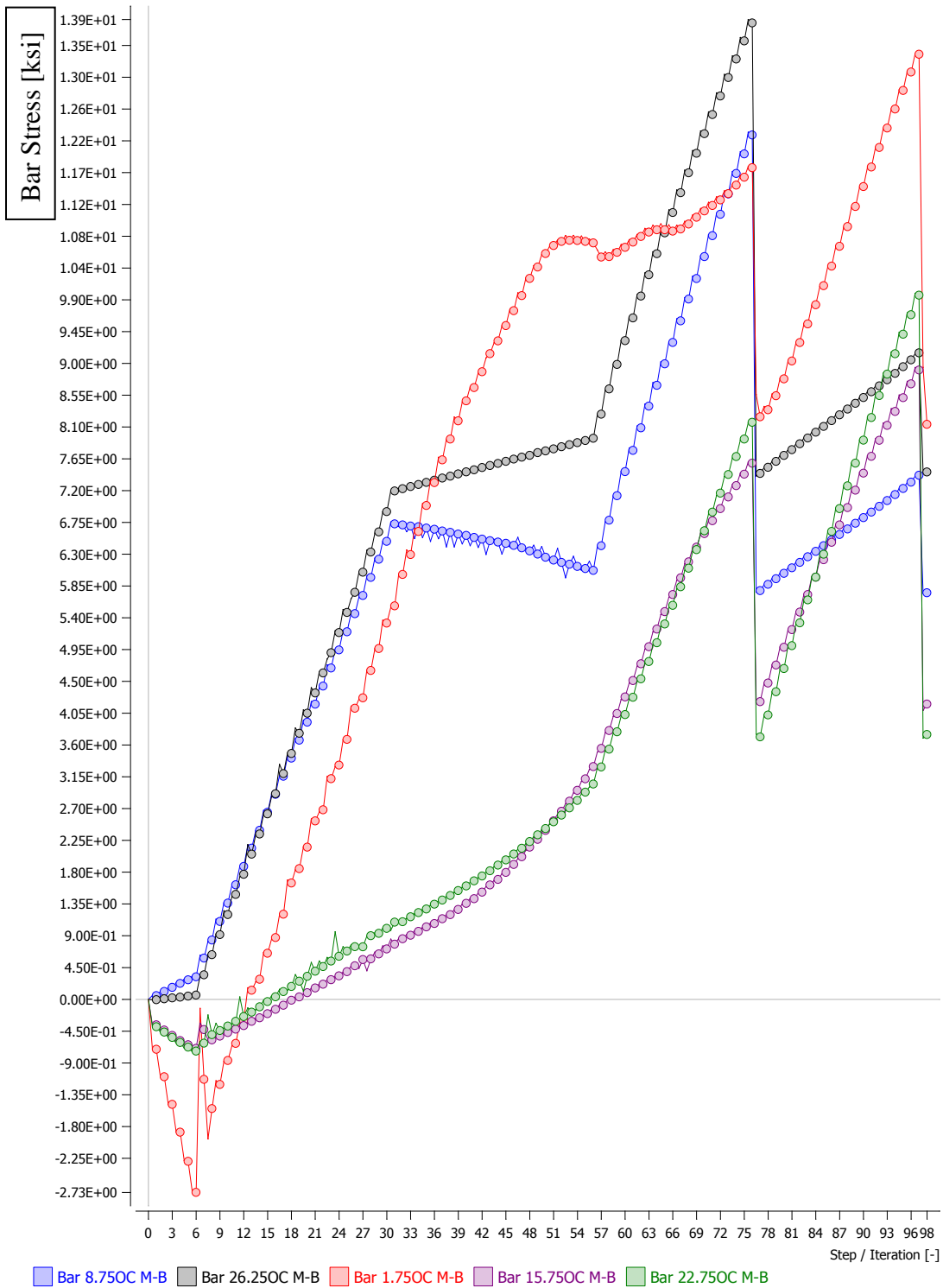


Figure C-22: C1 (11.5 k/ft.) AC bar stress MB (7" spacing).

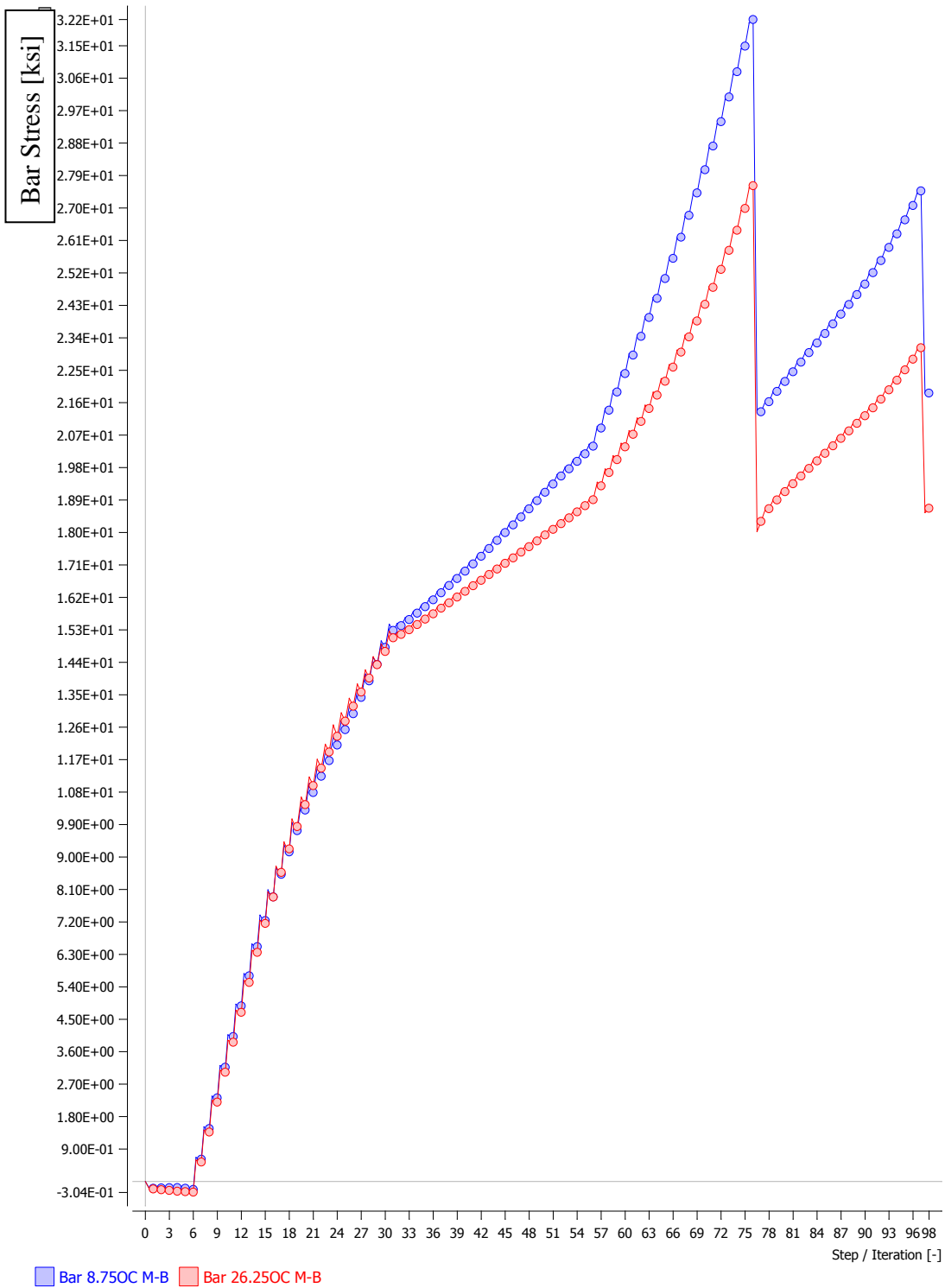


Figure C-23: C2 (19.12 k/ft.) AC bar stress MB (17.5" spacing).

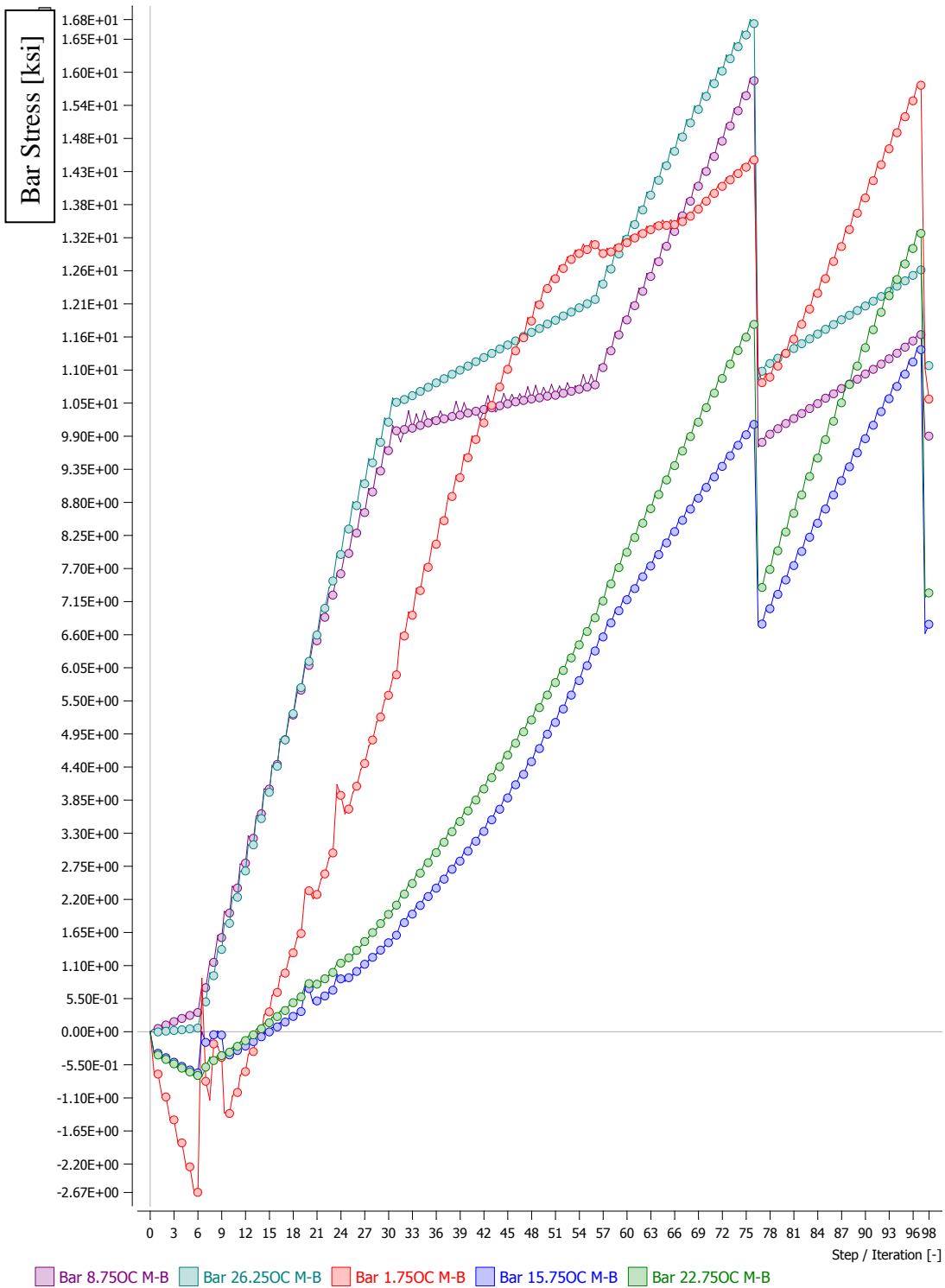


Figure C-24: C2 (19.12 k/ft.) AC bar stress MB (3.5" spacing).

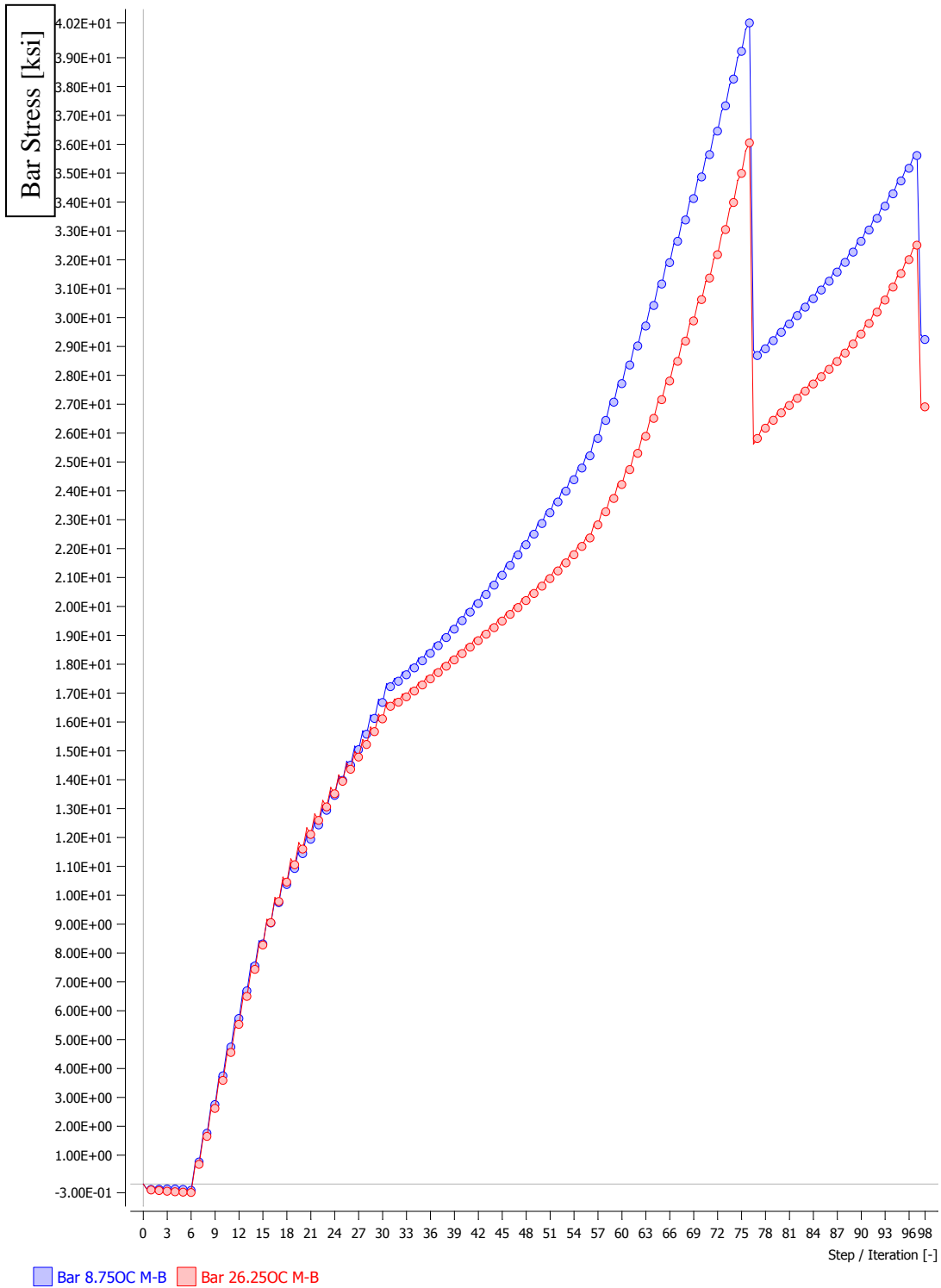


Figure C-25: C3 (26.10 k/ft.) AC bar stress MB (17.5" spacing).

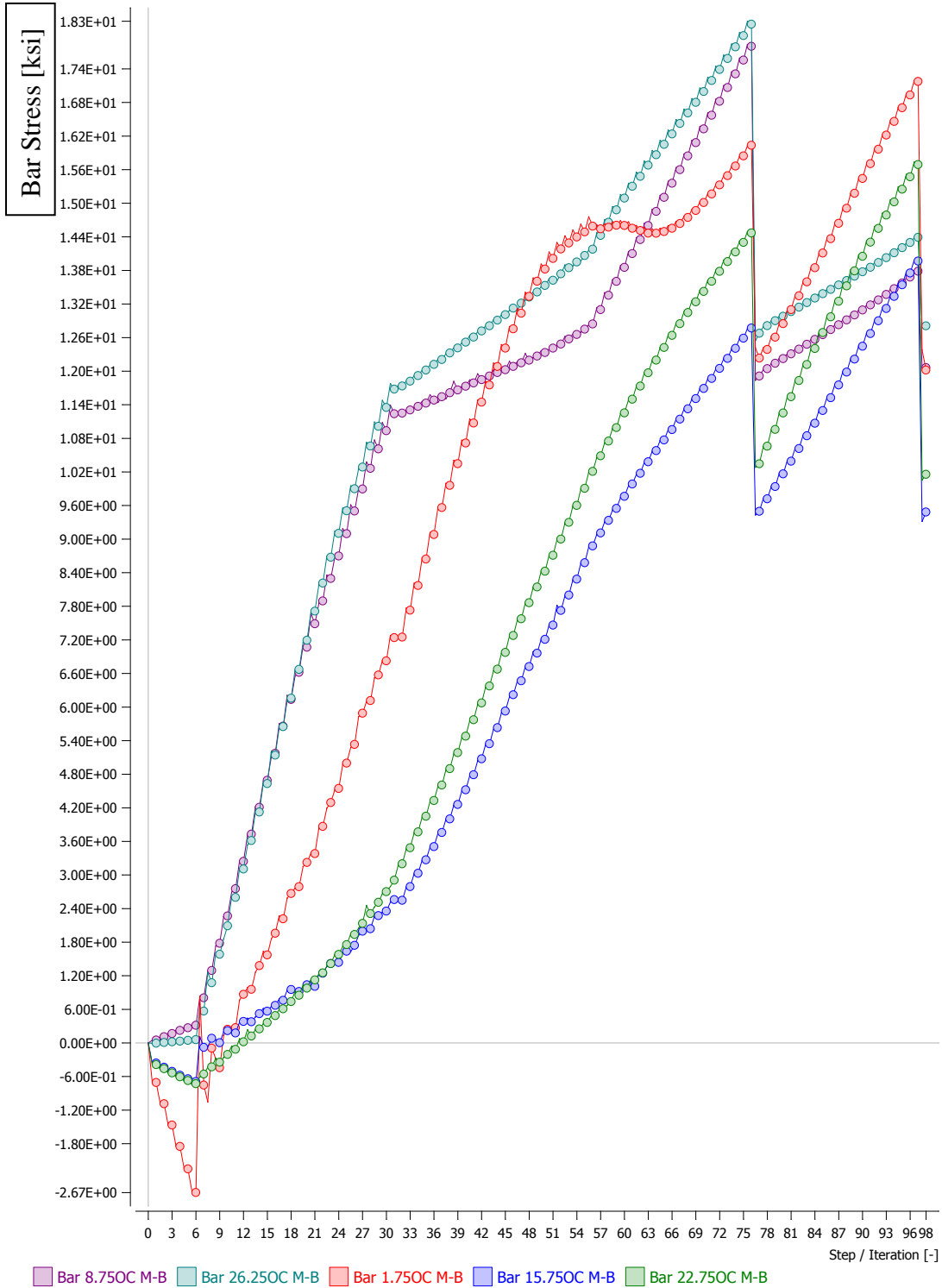


Figure C-26: C3 (26.10 k/ft.) AC bar stress MB (3.5" spacing).

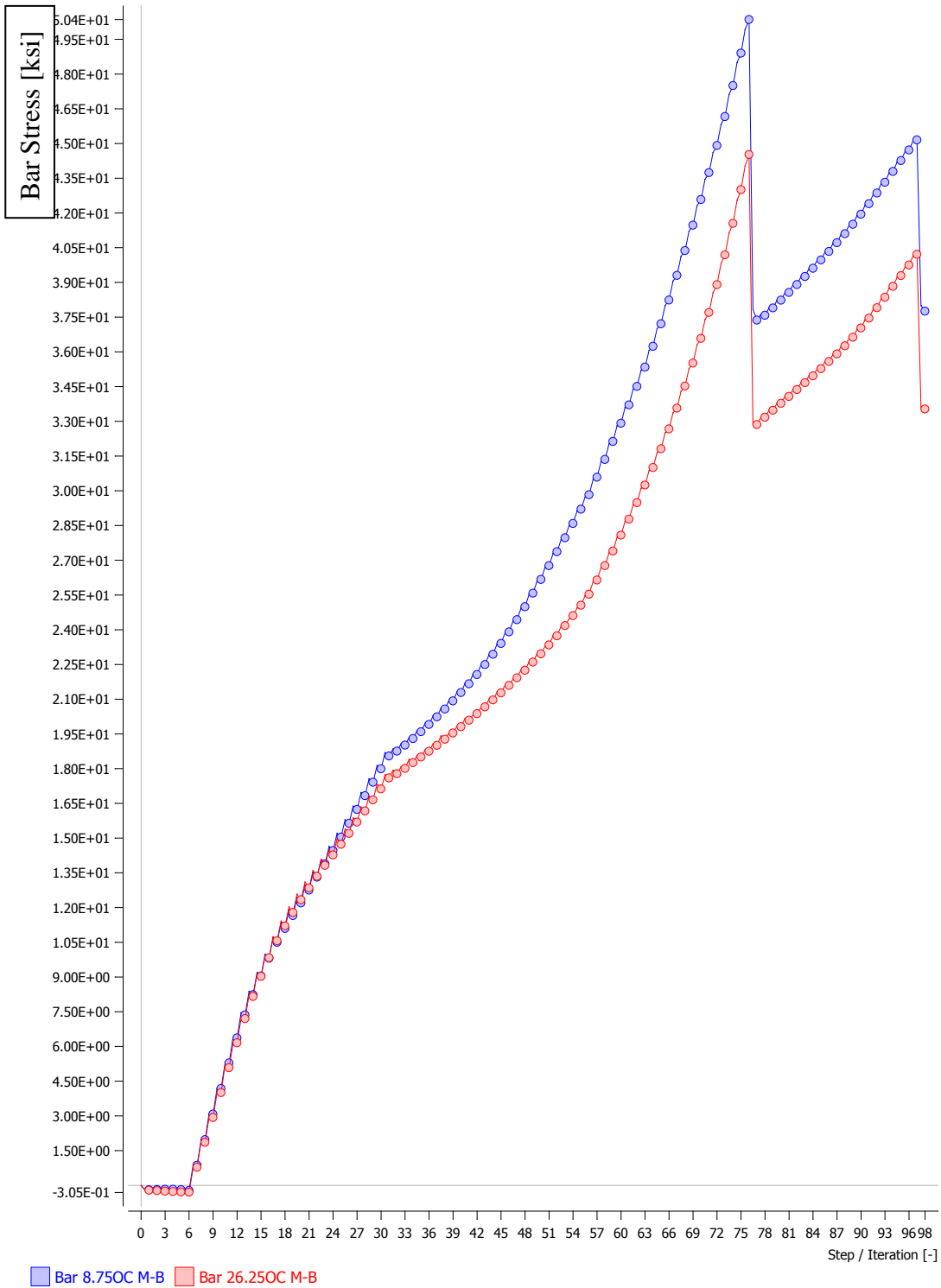
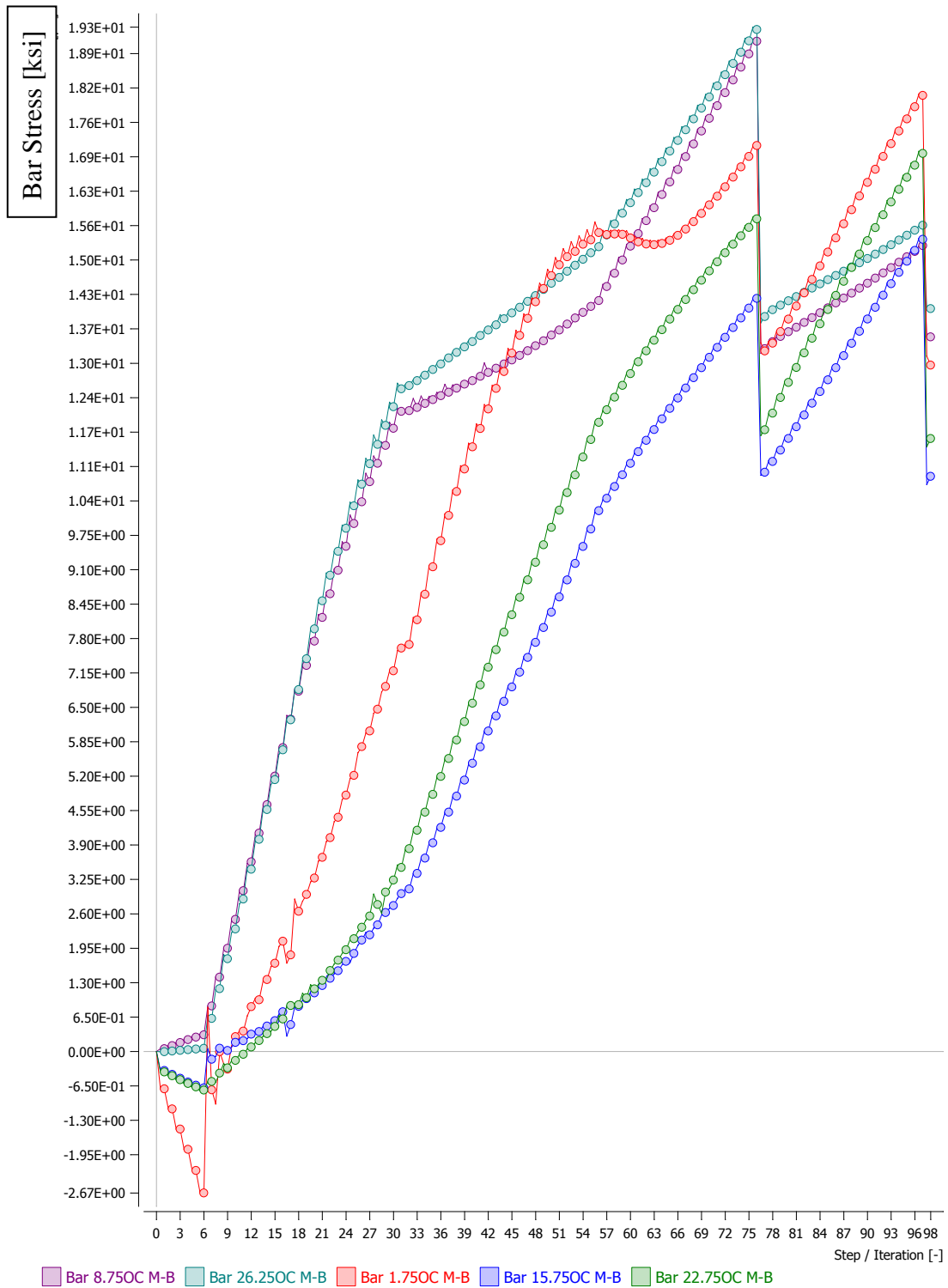


Figure C-27: C3+ (29.7 k/ft.) AC bar stress MB (17.5" spacing).



S

Figure C-28: C3+ (29.7 k/ft.) AC bar stress MB (3.5" spacing).

LIST OF CCEER PUBLICATIONS

Report No.	Publication
CCEER-84-1	Saiidi, M., and R. Lawver, "User's Manual for LZAK-C64, A Computer Program to Implement the Q-Model on Commodore 64," Civil Engineering Department, Report No. CCEER-84-1, University of Nevada, Reno, January 1984.
CCEER-84-1 Reprint	Douglas, B., Norris, G., Saiidi, M., Dodd, L., Richardson, J. and Reid, W., "Simple Bridge Models for Earthquakes and Test Data," Civil Engineering Department, Report No. CCEER-84-1 Reprint, University of Nevada, Reno, January 1984.
CCEER-84-2	Douglas, B. and T. Iwasaki, "Proceedings of the First USA-Japan Bridge Engineering Workshop," held at the Public Works Research Institute, Tsukuba, Japan, Civil Engineering Department, Report No. CCEER-84-2, University of Nevada, Reno, April 1984.
CCEER-84-3	Saiidi, M., J. Hart, and B. Douglas, "Inelastic Static and Dynamic Analysis of Short R/C Bridges Subjected to Lateral Loads," Civil Engineering Department, Report No. CCEER-84-3, University of Nevada, Reno, July 1984.
CCEER-84-4	Douglas, B., "A Proposed Plan for a National Bridge Engineering Laboratory," Civil Engineering Department, Report No. CCEER-84-4, University of Nevada, Reno, December 1984.
CCEER-85-1	Norris, G. and P. Abdollaholizadeh, "Laterally Loaded Pile Response: Studies with the Strain Wedge Model," Civil Engineering Department, Report No. CCEER-85-1, University of Nevada, Reno, April 1985.
CCEER-86-1	Ghusn, G. and M. Saiidi, "A Simple Hysteretic Element for Biaxial Bending of R/C in NEABS-86," Civil Engineering Department, Report No. CCEER-86-1, University of Nevada, Reno, July 1986.
CCEER-86-2	Saiidi, M., R. Lawver, and J. Hart, "User's Manual of ISADAB and SIBA, Computer Programs for Nonlinear Transverse Analysis of Highway Bridges Subjected to Static and Dynamic Lateral Loads," Civil Engineering Department, Report No. CCEER-86-2, University of Nevada, Reno, September 1986.
CCEER-87-1	Siddharthan, R., "Dynamic Effective Stress Response of Surface and Embedded Footings in Sand," Civil Engineering Department, Report No. CCEER-86-2, University of Nevada, Reno, June 1987.
CCEER-87-2	Norris, G. and R. Sack, "Lateral and Rotational Stiffness of Pile Groups for Seismic Analysis of Highway Bridges," Civil Engineering Department, Report No. CCEER-87-2, University of Nevada, Reno, June 1987.
CCEER-88-1	Orie, J. and M. Saiidi, "A Preliminary Study of One-Way Reinforced Concrete Pier Hinges Subjected to Shear and Flexure," Civil Engineering Department, Report No. CCEER-88-1, University of Nevada, Reno, January 1988.
CCEER-88-2	Orie, D., M. Saiidi, and B. Douglas, "A Micro-CAD System for Seismic Design of Regular Highway Bridges," Civil Engineering Department, Report No. CCEER-88-2, University of Nevada, Reno, June 1988.
CCEER-88-3	Orie, D. and M. Saiidi, "User's Manual for Micro-SARB, a Microcomputer Program for Seismic Analysis of Regular Highway Bridges," Civil Engineering Department, Report

No. CCEER-88-3, University of Nevada, Reno, October 1988.

- CCEER-89-1 Douglas, B., M. Saiidi, R. Hayes, and G. Holcomb, "A Comprehensive Study of the Loads and Pressures Exerted on Wall Forms by the Placement of Concrete," Civil Engineering Department, Report No. CCEER-89-1, University of Nevada, Reno, February 1989.
- CCEER-89-2 Richardson, J. and B. Douglas, "Dynamic Response Analysis of the Dominion Road Bridge Test Data," Civil Engineering Department, Report No. CCEER-89-2, University of Nevada, Reno, March 1989.
- CCEER-89-2 Vrontinos, S., M. Saiidi, and B. Douglas, "A Simple Model to Predict the Ultimate Response of R/C Beams with Concrete Overlays," Civil Engineering Department, Report NO. CCEER-89-2, University of Nevada, Reno, June 1989.
- CCEER-89-3 Ebrahimpour, A. and P. Jagadish, "Statistical Modeling of Bridge Traffic Loads - A Case Study," Civil Engineering Department, Report No. CCEER-89-3, University of Nevada, Reno, December 1989.
- CCEER-89-4 Shields, J. and M. Saiidi, "Direct Field Measurement of Prestress Losses in Box Girder Bridges," Civil Engineering Department, Report No. CCEER-89-4, University of Nevada, Reno, December 1989.
- CCEER-90-1 Saiidi, M., E. Maragakis, G. Ghush, Y. Jiang, and D. Schwartz, "Survey and Evaluation of Nevada's Transportation Infrastructure, Task 7.2 - Highway Bridges, Final Report," Civil Engineering Department, Report No. CCEER 90-1, University of Nevada, Reno, October 1990.
- CCEER-90-2 Abdel-Ghaffar, S., E. Maragakis, and M. Saiidi, "Analysis of the Response of Reinforced Concrete Structures During the Whittier Earthquake 1987," Civil Engineering Department, Report No. CCEER 90-2, University of Nevada, Reno, October 1990.
- CCEER-91-1 Saiidi, M., E. Hwang, E. Maragakis, and B. Douglas, "Dynamic Testing and the Analysis of the Flamingo Road Interchange," Civil Engineering Department, Report No. CCEER-91-1, University of Nevada, Reno, February 1991.
- CCEER-91-2 Norris, G., R. Siddharthan, Z. Zafir, S. Abdel-Ghaffar, and P. Gowda, "Soil-Foundation-Structure Behavior at the Oakland Outer Harbor Wharf," Civil Engineering Department, Report No. CCEER-91-2, University of Nevada, Reno, July 1991.
- CCEER-91-3 Norris, G., "Seismic Lateral and Rotational Pile Foundation Stiffnesses at Cypress," Civil Engineering Department, Report No. CCEER-91-3, University of Nevada, Reno, August 1991.
- CCEER-91-4 O'Connor, D. and M. Saiidi, "A Study of Protective Overlays for Highway Bridge Decks in Nevada, with Emphasis on Polyester-Styrene Polymer Concrete," Civil Engineering Department, Report No. CCEER-91-4, University of Nevada, Reno, October 1991.
- CCEER-91-5 O'Connor, D.N. and M. Saiidi, "Laboratory Studies of Polyester-Styrene Polymer Concrete Engineering Properties," Civil Engineering Department, Report No. CCEER-91-5, University of Nevada, Reno, November 1991.
- CCEER-92-1 Straw, D.L. and M. Saiidi, "Scale Model Testing of One-Way Reinforced Concrete Pier Hinges Subject to Combined Axial Force, Shear and Flexure," edited by D.N. O'Connor, Civil Engineering Department, Report No. CCEER-92-1, University of Nevada, Reno, March 1992.

- CCEER-92-2 Wehbe, N., M. Saiidi, and F. Gordaninejad, "Basic Behavior of Composite Sections Made of Concrete Slabs and Graphite Epoxy Beams," Civil Engineering Department, Report No. CCEER-92-2, University of Nevada, Reno, August 1992.
- CCEER-92-3 Saiidi, M. and E. Hutchens, "A Study of Prestress Changes in A Post-Tensioned Bridge During the First 30 Months," Civil Engineering Department, Report No. CCEER-92-3, University of Nevada, Reno, April 1992.
- CCEER-92-4 Saiidi, M., B. Douglas, S. Feng, E. Hwang, and E. Maragakis, "Effects of Axial Force on Frequency of Prestressed Concrete Bridges," Civil Engineering Department, Report No. CCEER-92-4, University of Nevada, Reno, August 1992.
- CCEER-92-5 Siddharthan, R., and Z. Zafir, "Response of Layered Deposits to Traveling Surface Pressure Waves," Civil Engineering Department, Report No. CCEER-92-5, University of Nevada, Reno, September 1992.
- CCEER-92-6 Norris, G., and Z. Zafir, "Liquefaction and Residual Strength of Loose Sands from Drained Triaxial Tests," Civil Engineering Department, Report No. CCEER-92-6, University of Nevada, Reno, September 1992.
- CCEER-92-6-A Norris, G., Siddharthan, R., Zafir, Z. and Madhu, R. "Liquefaction and Residual Strength of Sands from Drained Triaxial Tests," Civil Engineering Department, Report No. CCEER-92-6-A, University of Nevada, Reno, September 1992.
- CCEER-92-7 Douglas, B., "Some Thoughts Regarding the Improvement of the University of Nevada, Reno's National Academic Standing," Civil Engineering Department, Report No. CCEER-92-7, University of Nevada, Reno, September 1992.
- CCEER-92-8 Saiidi, M., E. Maragakis, and S. Feng, "An Evaluation of the Current Caltrans Seismic Restrainer Design Method," Civil Engineering Department, Report No. CCEER-92-8, University of Nevada, Reno, October 1992.
- CCEER-92-9 O'Connor, D., M. Saiidi, and E. Maragakis, "Effect of Hinge Restrainers on the Response of the Madrone Drive Undercrossing During the Loma Prieta Earthquake," Civil Engineering Department, Report No. CCEER-92-9, University of Nevada, Reno, February 1993.
- CCEER-92-10 O'Connor, D., and M. Saiidi, "Laboratory Studies of Polyester Concrete: Compressive Strength at Elevated Temperatures and Following Temperature Cycling, Bond Strength to Portland Cement Concrete, and Modulus of Elasticity," Civil Engineering Department, Report No. CCEER-92-10, University of Nevada, Reno, February 1993.
- CCEER-92-11 Wehbe, N., M. Saiidi, and D. O'Connor, "Economic Impact of Passage of Spent Fuel Traffic on Two Bridges in Northeast Nevada," Civil Engineering Department, Report No. CCEER-92-11, University of Nevada, Reno, December 1992.
- CCEER-93-1 Jiang, Y., and M. Saiidi, "Behavior, Design, and Retrofit of Reinforced Concrete One-way Bridge Column Hinges," edited by D. O'Connor, Civil Engineering Department, Report No. CCEER-93-1, University of Nevada, Reno, March 1993.
- CCEER-93-2 Abdel-Ghaffar, S., E. Maragakis, and M. Saiidi, "Evaluation of the Response of the Aptos Creek Bridge During the 1989 Loma Prieta Earthquake," Civil Engineering Department, Report No. CCEER-93-2, University of Nevada, Reno, June 1993.
- CCEER-93-3 Sanders, D.H., B.M. Douglas, and T.L. Martin, "Seismic Retrofit Prioritization of Nevada Bridges," Civil Engineering Department, Report No. CCEER-93-3, University of Nevada, Reno, July 1993.

- CCEER-93-4 Abdel-Ghaffar, S., E. Maragakis, and M. Saiidi, "Performance of Hinge Restrainers in the Huntington Avenue Overhead During the 1989 Loma Prieta Earthquake," Civil Engineering Department, Report No. CCEER-93-4, University of Nevada, Reno, June 1993 (in final preparation).
- CCEER-93-5 Maragakis, E., M. Saiidi, S. Feng, and L. Flournoy, "Effects of Hinge Restrainers on the Response of the San Gregorio Bridge during the Loma Prieta Earthquake," (in final preparation) Civil Engineering Department, Report No. CCEER-93-5, University of Nevada, Reno.
- CCEER-93-6 Saiidi, M., E. Maragakis, S. Abdel-Ghaffar, S. Feng, and D. O'Connor, "Response of Bridge Hinge Restrainers during Earthquakes -Field Performance, Analysis, and Design," Civil Engineering Department, Report No. CCEER-93-6, University of Nevada, Reno, May 1993.
- CCEER-93-7 Wehbe, N., Saiidi, M., Maragakis, E., and Sanders, D., "Adequacy of Three Highway Structures in Southern Nevada for Spent Fuel Transportation," Civil Engineering Department, Report No. CCEER-93-7, University of Nevada, Reno, August 1993.
- CCEER-93-8 Roybal, J., Sanders, D.H., and Maragakis, E., "Vulnerability Assessment of Masonry in the Reno-Carson City Urban Corridor," Civil Engineering Department, Report No. CCEER-93-8, University of Nevada, Reno, May 1993.
- CCEER-93-9 Zafir, Z. and Siddharthan, R., "MOVLOAD: A Program to Determine the Behavior of Nonlinear Horizontally Layered Medium Under Moving Load," Civil Engineering Department, Report No. CCEER-93-9, University of Nevada, Reno, August 1993.
- CCEER-93-10 O'Connor, D.N., Saiidi, M., and Maragakis, E.A., "A Study of Bridge Column Seismic Damage Susceptibility at the Interstate 80/U.S. 395 Interchange in Reno, Nevada," Civil Engineering Department, Report No. CCEER-93-10, University of Nevada, Reno, October 1993.
- CCEER-94-1 Maragakis, E., B. Douglas, and E. Abdelwahed, "Preliminary Dynamic Analysis of a Railroad Bridge," Report CCEER-94-1, January 1994.
- CCEER-94-2 Douglas, B.M., Maragakis, E.A., and Feng, S., "Stiffness Evaluation of Pile Foundation of Cazenovia Creek Overpass," Civil Engineering Department, Report No. CCEER-94-2, University of Nevada, Reno, March 1994.
- CCEER-94-3 Douglas, B.M., Maragakis, E.A., and Feng, S., "Summary of Pretest Analysis of Cazenovia Creek Bridge," Civil Engineering Department, Report No. CCEER-94-3, University of Nevada, Reno, April 1994.
- CCEER-94-4 Norris, G.M., Madhu, R., Valceschini, R., and Ashour, M., "Liquefaction and Residual Strength of Loose Sands from Drained Triaxial Tests," Report 2, Vol. 1&2, Civil Engineering Department, Report No. CCEER-94-4, University of Nevada, Reno, August 1994.
- CCEER-94-5 Saiidi, M., Hutchens, E., and Gardella, D., "Prestress Losses in a Post-Tensioned R/C Box Girder Bridge in Southern Nevada," Civil Engineering Department, CCEER-94-5, University of Nevada, Reno, August 1994.
- CCEER-95-1 Siddharthan, R., El-Gamal, M., and Maragakis, E.A., "Nonlinear Bridge Abutment Verification, and Design Curves," Civil Engineering Department, CCEER-95-1, University of Nevada, Reno, January 1995.

- CCEER-95-2 Ashour, M. and Norris, G., "Liquefaction and Undrained Response Evaluation of Sands from Drained Formulation," Civil Engineering Department, Report No. CCEER-95-2, University of Nevada, Reno, February 1995.
- CCEER-95-3 Wehbe, N., Saiidi, M., Sanders, D. and Douglas, B., "Ductility of Rectangular Reinforced Concrete Bridge Columns with Moderate Confinement," Civil Engineering Department, Report No. CCEER-95-3, University of Nevada, Reno, July 1995.
- CCEER-95-4 Martin, T., Saiidi, M. and Sanders, D., "Seismic Retrofit of Column-Pier Cap Connections in Bridges in Northern Nevada," Civil Engineering Department, Report No. CCEER-95-4, University of Nevada, Reno, August 1995.
- CCEER-95-5 Darwish, I., Saiidi, M. and Sanders, D., "Experimental Study of Seismic Susceptibility Column-Footing Connections in Bridges in Northern Nevada," Civil Engineering Department, Report No. CCEER-95-5, University of Nevada, Reno, September 1995.
- CCEER-95-6 Griffin, G., Saiidi, M. and Maragakis, E., "Nonlinear Seismic Response of Isolated Bridges and Effects of Pier Ductility Demand," Civil Engineering Department, Report No. CCEER-95-6, University of Nevada, Reno, November 1995.
- CCEER-95-7 Acharya, S., Saiidi, M. and Sanders, D., "Seismic Retrofit of Bridge Footings and Column-Footing Connections," Civil Engineering Department, Report No. CCEER-95-7, University of Nevada, Reno, November 1995.
- CCEER-95-8 Maragakis, E., Douglas, B., and Sandirasegaram, U., "Full-Scale Field Resonance Tests of a Railway Bridge," A Report to the Association of American Railroads, Civil Engineering Department, Report No. CCEER-95-8, University of Nevada, Reno, December 1995.
- CCEER-95-9 Douglas, B., Maragakis, E. and Feng, S., "System Identification Studies on Cazenovia Creek Overpass," Report for the National Center for Earthquake Engineering Research, Civil Engineering Department, Report No. CCEER-95-9, University of Nevada, Reno, October 1995.
- CCEER-96-1 El-Gamal, M.E. and Siddharthan, R.V., "Programs to Computer Translational Stiffness of Seat-Type Bridge Abutment," Civil Engineering Department, Report No. CCEER-96-1, University of Nevada, Reno, March 1996.
- CCEER-96-2 Labia, Y., Saiidi, M. and Douglas, B., "Evaluation and Repair of Full-Scale Prestressed Concrete Box Girders," A Report to the National Science Foundation, Research Grant CMS-9201908, Civil Engineering Department, Report No. CCEER-96-2, University of Nevada, Reno, May 1996.
- CCEER-96-3 Darwish, I., Saiidi, M. and Sanders, D., "Seismic Retrofit of R/C Oblong Tapered Bridge Columns with Inadequate Bar Anchorage in Columns and Footings," A Report to the Nevada Department of Transportation, Civil Engineering Department, Report No. CCEER-96-3, University of Nevada, Reno, May 1996.
- CCEER-96-4 Ashour, M., Pilling, R., Norris, G. and Perez, H., "The Prediction of Lateral Load Behavior of Single Piles and Pile Groups Using the Strain Wedge Model," A Report to the California Department of Transportation, Civil Engineering Department, Report No. CCEER-96-4, University of Nevada, Reno, June 1996.
- CCEER-97-1-A Rimal, P. and Itani, A. "Sensitivity Analysis of Fatigue Evaluations of Steel Bridges," Center for Earthquake Research, Department of Civil Engineering, University of Nevada, Reno, Nevada Report No. CCEER-97-1-A, September, 1997.

- CCEER-97-1-B Maragakis, E., Douglas, B., and Sandirasegaram, U. "Full-Scale Field Resonance Tests of a Railway Bridge," A Report to the Association of American Railroads, Civil Engineering Department, University of Nevada, Reno, May, 1996.
- CCEER-97-2 Wehbe, N., Saiidi, M., and D. Sanders, "Effect of Confinement and Flares on the Seismic Performance of Reinforced Concrete Bridge Columns," Civil Engineering Department, Report No. CCEER-97-2, University of Nevada, Reno, September 1997.
- CCEER-97-3 Darwish, I., M. Saiidi, G. Norris, and E. Maragakis, "Determination of In-Situ Footing Stiffness Using Full-Scale Dynamic Field Testing," A Report to the Nevada Department of Transportation, Structural Design Division, Carson City, Nevada, Report No. CCEER-97-3, University of Nevada, Reno, October 1997.
- CCEER-97-4-A Itani, A. "Cyclic Behavior of Richmond-San Rafael Tower Links," Center for Civil Engineering Earthquake Research, Department of Civil Engineering, University of Nevada, Reno, Nevada, Report No. CCEER-97-4, August 1997.
- CCEER-97-4-B Wehbe, N., and M. Saiidi, "User's Manual for RCMC v. 1.2: A Computer Program for Moment-Curvature Analysis of Confined and Unconfined Reinforced Concrete Sections," Center for Civil Engineering Earthquake Research, Department of Civil Engineering, University of Nevada, Reno, Nevada, Report No. CCEER-97-4, November, 1997.
- CCEER-97-5 Isakovic, T., M. Saiidi, and A. Itani, "Influence of new Bridge Configurations on Seismic Performance," Department of Civil Engineering, University of Nevada, Reno, Report No. CCEER-97-5, September, 1997.
- CCEER-98-1 Itani, A., Vesco, T. and Dietrich, A., "Cyclic Behavior of "as Built" Laced Members With End Gusset Plates on the San Francisco Bay Bridge," Center for Civil Engineering Earthquake Research, Department of Civil Engineering, University of Nevada, Reno, Nevada Report No. CCEER-98-1, March, 1998.
- CCEER-98-2 G. Norris and M. Ashour, "Liquefaction and Undrained Response Evaluation of Sands from Drained Formulation," Center for Civil Engineering Earthquake Research, Department of Civil Engineering, University of Nevada, Reno, Nevada, Report No. CCEER-98-2, May, 1998.
- CCEER-98-3 Qingbin, Chen, B. M. Douglas, E. Maragakis, and I. G. Buckle, "Extraction of Nonlinear Hysteretic Properties of Seismically Isolated Bridges from Quick-Release Field Tests," Center for Civil Engineering Earthquake Research, Department of Civil Engineering, University of Nevada, Reno, Nevada, Report No. CCEER-98-3, June, 1998.
- CCEER-98-4 Maragakis, E., B. M. Douglas, and C. Qingbin, "Full-Scale Field Capacity Tests of a Railway Bridge," Center for Civil Engineering Earthquake Research, Department of Civil Engineering, University of Nevada, Reno, Nevada, Report No. CCEER-98-4, June, 1998.
- CCEER-98-5 Itani, A., Douglas, B., and Woodgate, J., "Cyclic Behavior of Richmond-San Rafael Retrofitted Tower Leg," Center for Civil Engineering Earthquake Research, Department of Civil Engineering, University of Nevada, Reno. Report No. CCEER-98-5, June 1998
- CCEER-98-6 Moore, R., Saiidi, M., and Itani, A., "Seismic Behavior of New Bridges with Skew and Curvature," Center for Civil Engineering Earthquake Research, Department of Civil Engineering, University of Nevada, Reno. Report No. CCEER-98-6, October, 1998.

- CCEER-98-7 Itani, A and Dietrich, A, "Cyclic Behavior of Double Gusset Plate Connections," Center for Civil Engineering Earthquake Research, Department of Civil Engineering, University of Nevada, Reno, Nevada, Report No. CCEER-98-5, December, 1998.
- CCEER-99-1 Caywood, C., M. Saiidi, and D. Sanders, "Seismic Retrofit of Flared Bridge Columns with Steel Jackets," Civil Engineering Department, University of Nevada, Reno, Report No. CCEER-99-1, February 1999.
- CCEER-99-2 Mangoba, N., M. Mayberry, and M. Saiidi, "Prestress Loss in Four Box Girder Bridges in Northern Nevada," Civil Engineering Department, University of Nevada, Reno, Report No. CCEER-99-2, March 1999.
- CCEER-99-3 Abo-Shadi, N., M. Saiidi, and D. Sanders, "Seismic Response of Bridge Pier Walls in the Weak Direction," Civil Engineering Department, University of Nevada, Reno, Report No. CCEER-99-3, April 1999.
- CCEER-99-4 Buzick, A., and M. Saiidi, "Shear Strength and Shear Fatigue Behavior of Full-Scale Prestressed Concrete Box Girders," Civil Engineering Department, University of Nevada, Reno, Report No. CCEER-99-4, April 1999.
- CCEER-99-5 Randall, M., M. Saiidi, E. Maragakis and T. Isakovic, "Restrainer Design Procedures For Multi-Span Simply-Supported Bridges," Civil Engineering Department, University of Nevada, Reno, Report No. CCEER-99-5, April 1999.
- CCEER-99-6 Wehbe, N. and M. Saiidi, "User's Manual for RCMC v. 1.2, A Computer Program for Moment-Curvature Analysis of Confined and Unconfined Reinforced Concrete Sections," Civil Engineering Department, University of Nevada, Reno, Report No. CCEER-99-6, May 1999.
- CCEER-99-7 Burda, J. and A. Itani, "Studies of Seismic Behavior of Steel Base Plates," Civil Engineering Department, University of Nevada, Reno, Report No. CCEER-99-7, May 1999.
- CCEER-99-8 Ashour, M. and G. Norris, "Refinement of the Strain Wedge Model Program," Civil Engineering Department, University of Nevada, Reno, Report No. CCEER-99-8, March 1999.
- CCEER-99-9 Dietrich, A., and A. Itani, "Cyclic Behavior of Laced and Perforated Steel Members on the San Francisco-Oakland Bay Bridge," Civil Engineering Department, University, Reno, Report No. CCEER-99-9, December 1999.
- CCEER 99-10 Itani, A., A. Dietrich, "Cyclic Behavior of Built Up Steel Members and their Connections," Civil Engineering Department, University of Nevada, Reno, Report No. CCEER-99-10, December 1999.
- CCEER 99-10-A Itani, A., E. Maragakis and P. He, "Fatigue Behavior of Riveted Open Deck Railroad Bridge Girders," Civil Engineering Department, University of Nevada, Reno, Report No. CCEER-99-10-A, August 1999.
- CCEER 99-11 Itani, A., J. Woodgate, "Axial and Rotational Ductility of Built Up Structural Steel Members," Civil Engineering Department, University of Nevada, Reno, Report No. CCEER-99-11, December 1999.
- CCEER-99-12 Sgambelluri, M., Sanders, D.H., and Saiidi, M.S., "Behavior of One-Way Reinforced Concrete Bridge Column Hinges in the Weak Direction," Department of Civil Engineering, University of Nevada, Reno, Report No. CCEER-99-12, December 1999.

- CCEER-99-13 Laplace, P., Sanders, D.H., Douglas, B, and Saiidi, M, “Shake Table Testing of Flexure Dominated Reinforced Concrete Bridge Columns”, Department of Civil Engineering, University of Nevada, Reno, Report No. CCEER-99-13, December 1999.
- CCEER-99-14 Ahmad M. Itani, Jose A. Zepeda, and Elizabeth A. Ware “Cyclic Behavior of Steel Moment Frame Connections for the Moscone Center Expansion,” Department of Civil Engineering, University of Nevada, Reno, Report No. CCEER-99-14, December 1999.
- CCEER 00-1 Ashour, M., and Norris, G. “Undrained Lateral Pile and Pile Group Response in Saturated Sand,” Civil Engineering Department, University of Nevada, Reno, Report No. CCEER-00-1, May 1999. January 2000.
- CCEER 00-2 Saiidi, M. and Wehbe, N., “A Comparison of Confinement Requirements in Different Codes for Rectangular, Circular, and Double-Spiral RC Bridge Columns,” Civil Engineering Department, University of Nevada, Reno, Report No. CCEER-00-2, January 2000.
- CCEER 00-3 McElhaney, B., M. Saiidi, and D. Sanders, “Shake Table Testing of Flared Bridge Columns With Steel Jacket Retrofit,” Civil Engineering Department, University of Nevada, Reno, Report No. CCEER-00-3, January 2000.
- CCEER 00-4 Martinovic, F., M. Saiidi, D. Sanders, and F. Gordaninejad, “Dynamic Testing of Non-Prismatic Reinforced Concrete Bridge Columns Retrofitted with FRP Jackets,” Civil Engineering Department, University of Nevada, Reno, Report No. CCEER-00-4, January 2000.
- CCEER 00-5 Itani, A., and M. Saiidi, “Seismic Evaluation of Steel Joints for UCLA Center for Health Science Westwood Replacement Hospital,” Civil Engineering Department, University of Nevada, Reno, Report No. CCEER-00-5, February 2000.
- CCEER 00-6 Will, J. and D. Sanders, “High Performance Concrete Using Nevada Aggregates,” Civil Engineering Department, University of Nevada, Reno, Report No. CCEER-00-6, May 2000.
- CCEER 00-7 French, C., and M. Saiidi, “A Comparison of Static and Dynamic Performance of Models of Flared Bridge Columns,” Civil Engineering Department, University of Nevada, Reno, Report No. CCEER-00-7, October 2000.
- CCEER 00-8 Itani, A., H. Sedarat, “Seismic Analysis of the AISI LRFD Design Example of Steel Highway Bridges,” Civil Engineering Department, University of Nevada, Reno, Report No. CCEER 00-08, November 2000.
- CCEER 00-9 Moore, J., D. Sanders, and M. Saiidi, “Shake Table Testing of 1960’s Two Column Bent with Hinges Bases,” Civil Engineering Department, University of Nevada, Reno, Report No. CCEER 00-09, December 2000.
- CCEER 00-10 Asthana, M., D. Sanders, and M. Saiidi, “One-Way Reinforced Concrete Bridge Column Hinges in the Weak Direction,” Civil Engineering Department, University of Nevada, Reno, Report No. CCEER 00-10, April 2001.
- CCEER 01-1 Ah Sha, H., D. Sanders, M. Saiidi, “Early Age Shrinkage and Cracking of Nevada Concrete Bridge Decks,” Civil Engineering Department, University of Nevada, Reno, Report No. CCEER 01-01, May 2001.

- CCEER 01-2 Ashour, M. and G. Norris, "Pile Group program for Full Material Modeling a Progressive Failure," Civil Engineering Department, University of Nevada, Reno, Report No. CCEER 01-02, July 2001.
- CCEER 01-3 Itani, A., C. Lanaud, and P. Dusicka, "Non-Linear Finite Element Analysis of Built-Up Shear Links," Civil Engineering Department, University of Nevada, Reno, Report No. CCEER 01-03, July 2001.
- CCEER 01-4 Saiidi, M., J. Mortensen, and F. Martinovic, "Analysis and Retrofit of Fixed Flared Columns with Glass Fiber-Reinforced Plastic Jacketing," Civil Engineering Department, University of Nevada, Reno, Report No. CCEER 01-4, August 2001.
- CCEER 01-5 Not Published
- CCEER 01-6 Laplace, P., D. Sanders, and M. Saiidi, "Experimental Study and Analysis of Retrofitted Flexure and Shear Dominated Circular Reinforced Concrete Bridge Columns Subjected to Shake Table Excitation," Civil Engineering Department, University of Nevada, Reno, Report No. CCEER 01-6, June 2001.
- CCEER 01-7 Reppi, F., and D. Sanders, "Removal and Replacement of Cast-in-Place, Post-tensioned, Box Girder Bridge," Civil Engineering Department, University of Nevada, Reno, Report No. CCEER 01-7, December 2001.
- CCEER 02-1 Pulido, C., M. Saiidi, D. Sanders, and A. Itani, "Seismic Performance and Retrofitting of Reinforced Concrete Bridge Bents," Civil Engineering Department, University of Nevada, Reno, Report No. CCEER 02-1, January 2002.
- CCEER 02-2 Yang, Q., M. Saiidi, H. Wang, and A. Itani, "Influence of Ground Motion Incoherency on Earthquake Response of Multi-Support Structures," Civil Engineering Department, University of Nevada, Reno, Report No. CCEER 02-2, May 2002.
- CCEER 02-3 M. Saiidi, B. Gopalakrishnan, E. Reinhardt, and R. Siddharthan, "A Preliminary Study of Shake Table Response of A Two-Column Bridge Bent on Flexible Footings," Civil Engineering Department, University of Nevada, Reno, Report No. CCEER 02-03, June 2002.
- CCEER 02-4 Not Published
- CCEER 02-5 Banghart, A., Sanders, D., Saiidi, M., "Evaluation of Concrete Mixes for Filling the Steel Arches in the Galena Creek Bridge," Civil Engineering Department, University of Nevada, Reno, Report No. CCEER 02-05, June 2002.
- CCEER 02-6 Dusicka, P., Itani, A., Buckle, I. G., "Cyclic Behavior of Shear Links and Tower Shaft Assembly of San Francisco – Oakland Bay Bridge Tower," Civil Engineering Department, University of Nevada, Reno, Report No. CCEER 02-06, July 2002.
- CCEER 02-7 Mortensen, J., and M. Saiidi, "A Performance-Based Design Method for Confinement in Circular Columns," Civil Engineering Department, University of Nevada, Reno, Report No. CCEER 02-07, November 2002.
- CCEER 03-1 Wehbe, N., and M. Saiidi, "User's manual for SPMC v. 1.0 : A Computer Program for Moment-Curvature Analysis of Reinforced Concrete Sections with Interlocking Spirals," Center for Civil Engineering Earthquake Research, Department of Civil Engineering, University of Nevada, Reno, Nevada, Report No. CCEER-03-1, May, 2003.

- CCEER 03-2 Wehbe, N., and M. Saiidi, "User's manual for RCMC v. 2.0: A Computer Program for Moment-Curvature Analysis of Confined and Unconfined Reinforced Concrete Sections," Center for Civil Engineering Earthquake Research, Department of Civil Engineering, University of Nevada, Reno, Nevada, Report No. CCEER-03-2, June, 2003.
- CCEER 03-3 Nada, H., D. Sanders, and M. Saiidi, "Seismic Performance of RC Bridge Frames with Architectural-Flared Columns," Civil Engineering Department, University of Nevada, Reno, Report No. CCEER 03-3, January 2003.
- CCEER 03-4 Reinhardt, E., M. Saiidi, and R. Siddharthan, "Seismic Performance of a CFRP/ Concrete Bridge Bent on Flexible Footings," Civil Engineering Department, University of Nevada, Reno, Report No. CCEER 03-4, August 2003.
- CCEER 03-5 Johnson, N., M. Saiidi, A. Itani, and S. Ladhany, "Seismic Retrofit of Octagonal Columns with Pedestal and One-Way Hinge at the Base," Center for Civil Engineering Earthquake Research, Department of Civil Engineering, University of Nevada, Reno, Nevada, and Report No. CCEER-03-5, August 2003.
- CCEER 03-6 Mortensen, C., M. Saiidi, and S. Ladhany, "Creep and Shrinkage Losses in Highly Variable Climates," Center for Civil Engineering Earthquake Research, Department of Civil Engineering, University of Nevada, Reno, Report No. CCEER-03-6, September 2003.
- CCEER 03-7 Ayoub, C., M. Saiidi, and A. Itani, "A Study of Shape-Memory-Alloy-Reinforced Beams and Cubes," Center for Civil Engineering Earthquake Research, Department of Civil Engineering, University of Nevada, Reno, Nevada, Report No. CCEER-03-7, October 2003.
- CCEER 03-8 Chandane, S., D. Sanders, and M. Saiidi, "Static and Dynamic Performance of RC Bridge Bents with Architectural-Flared Columns," Center for Civil Engineering Earthquake Research, Department of Civil Engineering, University of Nevada, Reno, Nevada, Report No. CCEER-03-8, November 2003.
- CCEER 04-1 Olaegbe, C., and Saiidi, M., "Effect of Loading History on Shake Table Performance of A Two-Column Bent with Infill Wall," Center for Civil Engineering Earthquake Research, Department of Civil Engineering, University of Nevada, Reno, Nevada, Report No. CCEER-04-1, January 2004.
- CCEER 04-2 Johnson, R., Maragakis, E., Saiidi, M., and DesRoches, R., "Experimental Evaluation of Seismic Performance of SMA Bridge Restrainers," Center for Civil Engineering Earthquake Research, Department of Civil Engineering, University of Nevada, Reno, Nevada, Report No. CCEER-04-2, February 2004.
- CCEER 04-3 Moustafa, K., Sanders, D., and Saiidi, M., "Impact of Aspect Ratio on Two-Column Bent Seismic Performance," Center for Civil Engineering Earthquake Research, Department of Civil Engineering, University of Nevada, Reno, Nevada, Report No. CCEER-04-3, February 2004.
- CCEER 04-4 Maragakis, E., Saiidi, M., Sanchez-Camargo, F., and Elfass, S., "Seismic Performance of Bridge Restrainers At In-Span Hinges," Center for Civil Engineering Earthquake Research, Department of Civil Engineering, University of Nevada, Reno, Nevada, Report No. CCEER-04-4, March 2004.
- CCEER 04-5 Ashour, M., Norris, G. and Elfass, S., "Analysis of Laterally Loaded Long or Intermediate Drilled Shafts of Small or Large Diameter in Layered Soil," Center for Civil Engineering Earthquake Research, Department of Civil Engineering, University of Nevada, Reno, Nevada, Report No. CCEER-04-5, June 2004.

- CCEER 04-6 Correal, J., Saiidi, M. and Sanders, D., "Seismic Performance of RC Bridge Columns Reinforced with Two Interlocking Spirals," Center for Civil Engineering Earthquake Research, Department of Civil Engineering, University of Nevada, Reno, Nevada, Report No. CCEER-04-6, August 2004.
- CCEER 04-7 Dusicka, P., Itani, A. and Buckle, I., "Cyclic Response and Low Cycle Fatigue Characteristics of Plate Steels," Center for Civil Engineering Earthquake Research, Department of Civil Engineering, University of Nevada, Reno, Nevada, Report No. CCEER-04-7, November 2004.
- CCEER 04-8 Dusicka, P., Itani, A. and Buckle, I., "Built-up Shear Links as Energy Dissipaters for Seismic Protection of Bridges," Center for Civil Engineering Earthquake Research, Department of Civil Engineering, University of Nevada, Reno, Nevada, Report No. CCEER-04-8, November 2004.
- CCEER 04-9 Sureshkumar, K., Saiidi, S., Itani, A. and Ladkany, S., "Seismic Retrofit of Two-Column Bents with Diamond Shape Columns," Center for Civil Engineering Earthquake Research, Department of Civil Engineering, University of Nevada, Reno, Nevada, Report No. CCEER-04-9, November 2004.
- CCEER 05-1 Wang, H. and Saiidi, S., "A Study of RC Columns with Shape Memory Alloy and Engineered Cementitious Composites," Center for Civil Engineering Earthquake Research, Department of Civil Engineering, University of Nevada, Reno, Nevada, Report No. CCEER-05-1, January 2005.
- CCEER 05-2 Johnson, R., Saiidi, S. and Maragakis, E., "A Study of Fiber Reinforced Plastics for Seismic Bridge Restrainers," Center for Civil Engineering Earthquake Research, Department of Civil Engineering, University of Nevada, Reno, Nevada, Report No. CCEER-05-2, January 2005.
- CCEER 05-3 Carden, L.P., Itani, A.M., Buckle, I.G., "Seismic Load Path in Steel Girder Bridge Superstructures," Center for Civil Engineering Earthquake Research, Department of Civil Engineering, University of Nevada, Reno, Nevada, Report No. CCEER-05-3, January 2005.
- CCEER 05-4 Carden, L.P., Itani, A.M., Buckle, I.G., "Seismic Performance of Steel Girder Bridge Superstructures with Ductile End Cross Frames and Seismic Isolation," Center for Civil Engineering Earthquake Research, Department of Civil Engineering, University of Nevada, Reno, Nevada, Report No. CCEER-05-4, January 2005.
- CCEER 05-5 Goodwin, E., Maragakis, M., Itani, A. and Luo, S., "Experimental Evaluation of the Seismic Performance of Hospital Piping Subassemblies," Center for Civil Engineering Earthquake Research, Department of Civil Engineering, University of Nevada, Reno, Nevada, Report No. CCEER-05-5, February 2005.
- CCEER 05-6 Zadeh M. S., Saiidi, S, Itani, A. and Ladkany, S., "Seismic Vulnerability Evaluation and Retrofit Design of Las Vegas Downtown Viaduct," Center for Civil Engineering Earthquake Research, Department of Civil Engineering, University of Nevada, Reno, Nevada, Report No. CCEER-05-6, February 2005.
- CCEER 05-7 Phan, V., Saiidi, S. and Anderson, J., "Near Fault (Near Field) Ground Motion Effects on Reinforced Concrete Bridge Columns," Center for Civil Engineering Earthquake Research, Department of Civil Engineering, University of Nevada, Reno, Nevada, Report No. CCEER-05-7, August 2005.

- CCEER 05-8 Carden, L., Itani, A. and Laplace, P., "Performance of Steel Props at the UNR Fire Science Academy subjected to Repeated Fire," Center for Civil Engineering Earthquake Research, Department of Civil Engineering, University of Nevada, Reno, Nevada, Report No. CCEER-05-8, August 2005.
- CCEER 05-9 Yamashita, R. and Sanders, D., "Shake Table Testing and an Analytical Study of Unbonded Prestressed Hollow Concrete Column Constructed with Precast Segments," Center for Civil Engineering Earthquake Research, Department of Civil Engineering, University of Nevada, Reno, Nevada, Report No. CCEER-05-9, August 2005.
- CCEER 05-10 Not Published
- CCEER 05-11 Carden, L., Itani, A., and Peckan, G., "Recommendations for the Design of Beams and Posts in Bridge Falsework," Center for Civil Engineering Earthquake Research, Department of Civil Engineering, University of Nevada, Reno, Nevada, Report No. CCEER-05-11, October 2005.
- CCEER 06-01 Cheng, Z., Saiidi, M., and Sanders, D., "Development of a Seismic Design Method for Reinforced Concrete Two-Way Bridge Column Hinges," Center for Civil Engineering Earthquake Research, Department of Civil Engineering, University of Nevada, Reno, Nevada, Report No. CCEER-06-01, February 2006.
- CCEER 06-02 Johnson, N., Saiidi, M., and Sanders, D., "Large-Scale Experimental and Analytical Studies of a Two-Span Reinforced Concrete Bridge System," Center for Civil Engineering Earthquake Research, Department of Civil Engineering, University of Nevada, Reno, Nevada, Report No. CCEER-06-02, March 2006.
- CCEER 06-03 Saiidi, M., Ghasemi, H. and Tiras, A., "Seismic Design and Retrofit of Highway Bridges," Proceedings, Second US-Turkey Workshop, Center for Civil Engineering Earthquake Research, Department of Civil Engineering, University of Nevada, Reno, Nevada, Report No. CCEER-06-03, May 2006.
- CCEER 07-01 O'Brien, M., Saiidi, M. and Sadrossadat-Zadeh, M., "A Study of Concrete Bridge Columns Using Innovative Materials Subjected to Cyclic Loading," Center for Civil Engineering Earthquake Research, Department of Civil Engineering, University of Nevada, Reno, Nevada, Report No. CCEER-07-01, January 2007.
- CCEER 07-02 Sadrossadat-Zadeh, M. and Saiidi, M., "Effect of Strain rate on Stress-Strain Properties and Yield Propagation in Steel Reinforcing Bars," Center for Civil Engineering Earthquake Research, Department of Civil Engineering, University of Nevada, Reno, Nevada, Report No. CCEER-07-02, January 2007.
- CCEER 07-03 Sadrossadat-Zadeh, M. and Saiidi, M., "Analytical Study of NEESR-SG 4-Span Bridge Model Using OpenSees," Center for Civil Engineering Earthquake Research, Department of Civil Engineering, University of Nevada, Reno, Nevada, Report No. CCEER-07-03, January 2007.
- CCEER 07-04 Nelson, R., Saiidi, M. and Zadeh, S., "Experimental Evaluation of Performance of Conventional Bridge Systems," Center for Civil Engineering Earthquake Research, Department of Civil Engineering, University of Nevada, Reno, Nevada, Report No. CCEER-07-04, October 2007.
- CCEER 07-05 Bahen, N. and Sanders, D., "Strut-and-Tie Modeling for Disturbed Regions in Structural Concrete Members with Emphasis on Deep Beams," Center for Civil Engineering Earthquake Research, Department of Civil Engineering, University of Nevada, Reno, Nevada, Report No. CCEER-07-05, December 2007.

- CCEER 07-06 Choi, H., Saiidi, M. and Somerville, P., "Effects of Near-Fault Ground Motion and Fault-Rupture on the Seismic Response of Reinforced Concrete Bridges," Center for Civil Engineering Earthquake Research, Department of Civil Engineering, University of Nevada, Reno, Nevada, Report No. CCEER-07-06, December 2007.
- CCEER 07-07 Ashour M. and Norris, G., "Report and User Manual on Strain Wedge Model Computer Program for Files and Large Diameter Shafts with LRFD Procedure," Center for Civil Engineering Earthquake Research, Department of Civil Engineering, University of Nevada, Reno, Nevada, Report No. CCEER-07-07, October 2007.
- CCEER 08-01 Doyle, K. and Saiidi, M., "Seismic Response of Telescopic Pipe Pin Connections," Center for Civil Engineering Earthquake Research, Department of Civil Engineering, University of Nevada, Reno, Nevada, Report No. CCEER-08-01, February 2008.
- CCEER 08-02 Taylor, M. and Sanders, D., "Seismic Time History Analysis and Instrumentation of the Galena Creek Bridge," Center for Civil Engineering Earthquake Research, Department of Civil Engineering, University of Nevada, Reno, Nevada, Report No. CCEER-08-02, April 2008.
- CCEER 08-03 Abdel-Mohti, A. and Pekcan, G., "Seismic Response Assessment and Recommendations for the Design of Skewed Post-Tensioned Concrete Box-Girder Highway Bridges," Center for Civil Engineering Earthquake Research, Department of Civil and Environmental Engineering, University of Nevada, Reno, Nevada, Report No. CCEER-08-03, September 2008.
- CCEER 08-04 Saiidi, M., Ghasemi, H. and Hook, J., "Long Term Bridge Performance Monitoring, Assessment & Management," Proceedings, FHWA/NSF Workshop on Future Directions," Center for Civil Engineering Earthquake Research, Department of Civil and Environmental Engineering, University of Nevada, Reno, Nevada, Report No. CCEER 08-04, September 2008.
- CCEER 09-01 Brown, A., and Saiidi, M., "Investigation of Near-Fault Ground Motion Effects on Substandard Bridge Columns and Bents," Center for Civil Engineering Earthquake Research, Department of Civil and Environmental Engineering, University of Nevada, Reno, Nevada, Report No. CCEER-09-01, July 2009.
- CCEER 09-02 Linke, C., Pekcan, G., and Itani, A., "Detailing of Seismically Resilient Special Truss Moment Frames," Center for Civil Engineering Earthquake Research, Department of Civil and Environmental Engineering, University of Nevada, Reno, Nevada, Report No. CCEER-09-02, August 2009.
- CCEER 09-03 Hillis, D., and Saiidi, M., "Design, Construction, and Nonlinear Dynamic Analysis of Three Bridge Bents Used in a Bridge System Test," Center for Civil Engineering Earthquake Research, Department of Civil and Environmental Engineering, University of Nevada, Reno, Nevada, Report No. CCEER-09-03, August 2009.
- CCEER 09-04 Bahrami, H., Itani, A., and Buckle, I., "Guidelines for the Seismic Design of Ductile End Cross Frames in Steel Girder Bridge Superstructures," Center for Civil Engineering Earthquake Research, Department of Civil and Environmental Engineering, University of Nevada, Reno, Nevada, Report No. CCEER-09-04, September 2009.
- CCEER 10-01 Zaghi, A. E., and Saiidi, M., "Seismic Design of Pipe-Pin Connections in Concrete Bridges," Center for Civil Engineering Earthquake Research, Department of Civil and Environmental Engineering, University of Nevada, Reno, Nevada, Report No. CCEER-10-01, January 2010.

- CCEER 10-02 Pooranampillai, S., Elfass, S., and Norris, G., "Laboratory Study to Assess Load Capacity Increase of Drilled Shafts through Post Grouting," Center for Civil Engineering Earthquake Research, Department of Civil and Environmental Engineering, University of Nevada, Reno, Nevada, Report No. CCEER-10-02, January 2010.
- CCEER 10-03 Itani, A., Grubb, M., and Monzon, E., "Proposed Seismic Provisions and Commentary for Steel Plate Girder Superstructures," Center for Civil Engineering Earthquake Research, Department of Civil and Environmental Engineering, University of Nevada, Reno, Nevada, Report No. CCEER-10-03, June 2010.
- CCEER 10-04 Cruz-Noguez, C., Saiidi, M., "Experimental and Analytical Seismic Studies of a Four-Span Bridge System with Innovative Materials," Center for Civil Engineering Earthquake Research, Department of Civil and Environmental Engineering, University of Nevada, Reno, Nevada, Report No. CCEER-10-04, September 2010.
- CCEER 10-05 Vosooghi, A., Saiidi, M., "Post-Earthquake Evaluation and Emergency Repair of Damaged RC Bridge Columns Using CFRP Materials," Center for Civil Engineering Earthquake Research, Department of Civil and Environmental Engineering, University of Nevada, Reno, Nevada, Report No. CCEER-10-05, September 2010.
- CCEER 10-06 Ayoub, M., Sanders, D., "Testing of Pile Extension Connections to Slab Bridges," Center for Civil Engineering Earthquake Research, Department of Civil and Environmental Engineering, University of Nevada, Reno, Nevada, Report No. CCEER-10-06, October 2010.
- CCEER 10-07 Builes-Mejia, J. C. and Itani, A., "Stability of Bridge Column Rebar Cages during Construction," Center for Civil Engineering Earthquake Research, Department of Civil and Environmental Engineering, University of Nevada, Reno, Nevada, Report No. CCEER-10-07, November 2010.
- CCEER 10-08 Monzon, E.V., "Seismic Performance of Steel Plate Girder Bridges with Integral Abutments," Center for Civil Engineering Earthquake Research, Department of Civil and Environmental Engineering, University of Nevada, Reno, Nevada, Report No. CCEER-10-08, November 2010.
- CCEER 11-01 Motaref, S., Saiidi, M., and Sanders, D., "Seismic Response of Precast Bridge Columns with Energy Dissipating Joints," Center for Civil Engineering Earthquake Research, Department of Civil and Environmental Engineering, University of Nevada, Reno, Nevada, Report No. CCEER-11-01, May 2011.
- CCEER 11-02 Harrison, N. and Sanders, D., "Preliminary Seismic Analysis and Design of Reinforced Concrete Bridge Columns for Curved Bridge Experiments," Center for Civil Engineering Earthquake Research, Department of Civil and Environmental Engineering, University of Nevada, Reno, Nevada, Report No. CCEER-11-02, May 2011.
- CCEER 11-03 Vallejera, J. and Sanders, D., "Instrumentation and Monitoring the Galena Creek Bridge," Center for Civil Engineering Earthquake Research, Department of Civil and Environmental Engineering, University of Nevada, Reno, Nevada, Report No. CCEER-11-03, September 2011.
- CCEER 11-04 Levi, M., Sanders, D., and Buckle, I., "Seismic Response of Columns in Horizontally Curved Bridges," Center for Civil Engineering Earthquake Research, Department of Civil and Environmental Engineering, University of Nevada, Reno, Nevada, Report No. CCEER-11-04, December 2011.

- CCEER 12-01 Saiidi, M., “NSF International Workshop on Bridges of the Future – Wide Spread Implementation of Innovation,” Center for Civil Engineering Earthquake Research, Department of Civil and Environmental Engineering, University of Nevada, Reno, Nevada, Report No. CCEER-12-01, January 2012.
- CCEER 12-02 Larkin, A.S., Sanders, D., and Saiidi, M., “Unbonded Prestressed Columns for Earthquake Resistance,” Center for Civil Engineering Earthquake Research, Department of Civil and Environmental Engineering, University of Nevada, Reno, Nevada, Report No. CCEER-12-02, January 2012.
- CCEER 12-03 Arias-Acosta, J. G., Sanders, D., “Seismic Performance of Circular and Interlocking Spirals RC Bridge Columns under Bidirectional Shake Table Loading Part 1,” Center for Civil Engineering Earthquake Research, Department of Civil and Environmental Engineering, University of Nevada, Reno, Nevada, Report No. CCEER-12-03, September 2012.
- CCEER 12-04 Cukrov, M.E., Sanders, D., “Seismic Performance of Prestressed Pile-To-Bent Cap Connections,” Center for Civil Engineering Earthquake Research, Department of Civil and Environmental Engineering, University of Nevada, Reno, Nevada, Report No. CCEER-12-04, September 2012.
- CCEER 13-01 Carr, T. and Sanders, D., “Instrumentation and Dynamic Characterization of the Galena Creek Bridge,” Center for Civil Engineering Earthquake Research, Department of Civil and Environmental Engineering, University of Nevada, Reno, Nevada, Report No. CCEER-13-01, January 2013.
- CCEER 13-02 Vosooghi, A. and Buckle, I., “Evaluation of the Performance of a Conventional Four-Span Bridge During Shake Table Tests,” Center for Civil Engineering Earthquake Research, Department of Civil and Environmental Engineering, University of Nevada, Reno, Nevada, Report No. CCEER-13-02, January 2013.
- CCEER 13-03 Amirhormozaki, E. and Pekcan, G., “Analytical Fragility Curves for Horizontally Curved Steel Girder Highway Bridges,” Center for Civil Engineering Earthquake Research, Department of Civil and Environmental Engineering, University of Nevada, Reno, Nevada, Report No. CCEER-13-03, February 2013.
- CCEER 13-04 Almer, K. and Sanders, D., “Longitudinal Seismic Performance of Precast Bridge Girders Integrally Connected to a Cast-in-Place Bentcap,” Center for Civil Engineering Earthquake Research, Department of Civil and Environmental Engineering, University of Nevada, Reno, Nevada, Report No. CCEER-13-04, April 2013.
- CCEER 13-05 Monzon, E.V., Itani, A.I., and Buckle, I.G., “Seismic Modeling and Analysis of Curved Steel Plate Girder Bridges,” Center for Civil Engineering Earthquake Research, Department of Civil and Environmental Engineering, University of Nevada, Reno, Nevada, Report No. CCEER-13-05, April 2013.
- CCEER 13-06 Monzon, E.V., Buckle, I.G., and Itani, A.I., “Seismic Performance of Curved Steel Plate Girder Bridges with Seismic Isolation,” Center for Civil Engineering Earthquake Research, Department of Civil and Environmental Engineering, University of Nevada, Reno, Nevada, Report No. CCEER-13-06, April 2013.
- CCEER 13-07 Monzon, E.V., Buckle, I.G., and Itani, A.I., “Seismic Response of Isolated Bridge Superstructure to Incoherent Ground Motions,” Center for Civil Engineering Earthquake Research, Department of Civil and Environmental Engineering, University of Nevada, Reno, Nevada, Report No. CCEER-13-07, April 2013.

- CCEER 13-08 Haber, Z.B., Saiidi, M.S., and Sanders, D.H., "Precast Column-Footing Connections for Accelerated Bridge Construction in Seismic Zones," Center for Civil Engineering Earthquake Research, Department of Civil and Environmental Engineering, University of Nevada, Reno, Nevada, Report No. CCEER-13-08, April 2013.
- CCEER 13-09 Ryan, K.L., Coria, C.B., and Dao, N.D., "Large Scale Earthquake Simulation of a Hybrid Lead Rubber Isolation System Designed under Nuclear Seismicity Considerations," Center for Civil Engineering Earthquake Research, Department of Civil and Environmental Engineering, University of Nevada, Reno, Nevada, Report No. CCEER-13-09, April 2013.
- CCEER 13-10 Wibowo, H., Sanford, D.M., Buckle, I.G., and Sanders, D.H., "The Effect of Live Load on the Seismic Response of Bridges," Center for Civil Engineering Earthquake Research, Department of Civil and Environmental Engineering, University of Nevada, Reno, Nevada, Report No. CCEER-13-10, May 2013.
- CCEER 13-11 Sanford, D.M., Wibowo, H., Buckle, I.G., and Sanders, D.H., "Preliminary Experimental Study on the Effect of Live Load on the Seismic Response of Highway Bridges," Center for Civil Engineering Earthquake Research, Department of Civil and Environmental Engineering, University of Nevada, Reno, Nevada, Report No. CCEER-13-11, May 2013.
- CCEER 13-12 Saad, A.S., Sanders, D.H., and Buckle, I.G., "Assessment of Foundation Rocking Behavior in Reducing the Seismic Demand on Horizontally Curved Bridges," Center for Civil Engineering Earthquake Research, Department of Civil and Environmental Engineering, University of Nevada, Reno, Nevada, Report No. CCEER-13-12, June 2013.
- CCEER 13-13 Ardakani, S.M.S. and Saiidi, M.S., "Design of Reinforced Concrete Bridge Columns for Near-Fault Earthquakes," Center for Civil Engineering Earthquake Research, Department of Civil and Environmental Engineering, University of Nevada, Reno, Nevada, Report No. CCEER-13-13, July 2013.
- CCEER 13-14 Wei, C. and Buckle, I., "Seismic Analysis and Response of Highway Bridges with Hybrid Isolation," Center for Civil Engineering Earthquake Research, Department of Civil and Environmental Engineering, University of Nevada, Reno, Nevada, Report No. CCEER-13-14, August 2013.
- CCEER 13-15 Wibowo, H., Buckle, I.G., and Sanders, D.H., "Experimental and Analytical Investigations on the Effects of Live Load on the Seismic Performance of a Highway Bridge," Center for Civil Engineering Earthquake Research, Department of Civil and Environmental Engineering, University of Nevada, Reno, Nevada, Report No. CCEER-13-15, August 2013.
- CCEER 13-16 Itani, A.M., Monzon, E.V., Grubb, M., and Amirhormozaki, E. "Seismic Design and Nonlinear Evaluation of Steel I-Girder Bridges with Ductile End Cross-Frames," Center for Civil Engineering Earthquake Research, Department of Civil and Environmental Engineering, University of Nevada, Reno, Nevada, Report No. CCEER-13-16, September 2013.
- CCEER 13-17 Kavianipour, F. and Saiidi, M.S., "Experimental and Analytical Seismic Studies of a Four-span Bridge System with Composite Piers," Center for Civil Engineering Earthquake Research, Department of Civil and Environmental Engineering, University of Nevada, Reno, Nevada, Report No. CCEER-13-17, September 2013.

- CCEER 13-18 Mohebbi, A., Ryan, K., and Sanders, D., "Seismic Response of a Highway Bridge with Structural Fuses for Seismic Protection of Piers," Center for Civil Engineering Earthquake Research, Department of Civil and Environmental Engineering, University of Nevada, Reno, Nevada, Report No. CCEER-13-18, December 2013.
- CCEER 13-19 Guzman Pujols, Jean C., Ryan, K.L., "Development of Generalized Fragility Functions for Seismic Induced Content Disruption," Center for Civil Engineering Earthquake Research, Department of Civil and Environmental Engineering, University of Nevada, Reno, Nevada, Report No. CCEER-13-19, December 2013.
- CCEER 14-01 Salem, M. M. A., Pekcan, G., and Itani, A., "Seismic Response Control Of Structures Using Semi-Active and Passive Variable Stiffness Devices," Center for Civil Engineering Earthquake Research, Department of Civil and Environmental Engineering, University of Nevada, Reno, Nevada, Report No. CCEER-14-01, May 2014.
- CCEER 14-02 Saini, A. and Saiidi, M., "Performance-Based Probabilistic Damage Control Approach for Seismic Design of Bridge Columns," Center For Civil Engineering Earthquake Research, Department Of Civil and Environmental Engineering, University of Nevada, Reno, Nevada, Report No. CCEER-14-02, May 2014.
- CCEER 14-03 Saini, A. and Saiidi, M., "Post Earthquake Damage Repair of Various Reinforced Concrete Bridge Components," Center For Civil Engineering Earthquake Research, Department Of Civil and Environmental Engineering, University of Nevada, Reno, Nevada, Report No. CCEER-14-03, May 2014.
- CCEER 14-04 Monzon, E.V., Itani, A.M., and Grubb, M.A., "Nonlinear Evaluation of the Proposed Seismic Design Procedure for Steel Bridges with Ductile End Cross Frames," Center For Civil Engineering Earthquake Research, Department Of Civil and Environmental Engineering, University of Nevada, Reno, Nevada, Report No. CCEER-14-04, July 2014.
- CCEER 14-05 Nakashoji, B. and Saiidi, M.S., "Seismic Performance of Square Nickel-Titanium Reinforced ECC Columns with Headed Couplers," Center For Civil Engineering Earthquake Research, Department Of Civil and Environmental Engineering, University of Nevada, Reno, Nevada, Report No. CCEER-14-05, July 2014.
- CCEER 14-06 Tazarv, M. and Saiidi, M.S., "Next Generation of Bridge Columns for Accelerated Bridge Construction in High Seismic Zones," Center For Civil Engineering Earthquake Research, Department Of Civil and Environmental Engineering, University of Nevada, Reno, Nevada, Report No. CCEER-14-06, August 2014.
- CCEER 14-07 Mehrsorouh, A. and Saiidi, M.S., "Experimental and Analytical Seismic Studies of Bridge Piers with Innovative Pipe Pin Column-Footing Connections and Precast Cap Beams," Center For Civil Engineering Earthquake Research, Department Of Civil and Environmental Engineering, University of Nevada, Reno, Nevada, Report No. CCEER-14-07, December 2014.
- CCEER 15-01 Dao, N.D. and Ryan, K.L., "Seismic Response of a Full-scale 5-story Steel Frame Building Isolated by Triple Pendulum Bearings under 3D Excitations," Center For Civil Engineering Earthquake Research, Department Of Civil and Environmental Engineering, University of Nevada, Reno, Nevada, Report No. CCEER-15-01, January 2015.
- CCEER 15-02 Allen, B.M. and Sanders, D.H., "Post-Tensioning Duct Air Pressure Testing Effects on Web Cracking," Center For Civil Engineering Earthquake Research, Department Of Civil and Environmental Engineering, University of Nevada, Reno, Nevada, Report No. CCEER-15-02, January 2015.



Nevada Department of Transportation
Rudy Malfabon, P.E. Director
Ken Chambers, Research Division Chief
(775) 888-7220
kchambers@dot.nv.gov
1263 South Stewart Street
Carson City, Nevada 89712